# Predictive energy management for fuel cell hybrid electric vehicle

Yang Zhou

**THÈSE DE DOCTORAT DE L'ETABLISSEMENT UNIVERSITÉ BOURGOGNE FRANCHE-COMTÉ**

**PRÉPARÉE A L'UNIVERSITÉ DE TECHNOLOGIE DE BELFORT-MONTBÉLIARD**

Ecole doctorale n°37

Sciences Pour l'Ingénieur et Microtechniques

Doctorat de Génie électrique

Par

Yang ZHOU

# Gestion de l'énergie prédictive appliquée aux véhicules hybrides pile à combustible

Thèse présentée et soutenue à Belfort, le 12/11/2020

Composition du Jury :

| | | |
|---|---|---|
| M. Rachid Outbib | Professeur à l'Université d'Aix-Marseille | Président |
| M. Olivier Sename | Professeur à l'Institut Polytechnique de Grenoble | Rapporteur |
| Mme. Florence Ossart | Professeure à Sorbonne Université | Rapportrice |
| M. Ali Sari | Professeur à Université Claude Bernard Lyon 1 | Examinateur |
| M. Simon Morando | Spécialiste diagnostique et pronostique de PEMFC chez Symbio | Examinateur |
| M. Marco Sorrentino | Maitre de conférences à l'Université de Salerno | Examinateur |
| Mme. Marie-Cécile Péra | Professeure à l'Université de Franche-Comté | Directeur de thèse |
| M. Alexandre Ravey | Maitre de conférences à l'Université de Technologie de Belfort-Montbéliard | Codirecteur de thèse |

**PH.D. THESIS OF THE UNIVERSITY BOURGOGNE FRANCHE-COMTÉ**

**PREPARED AT THE UNIVERSITY OF TECHNOLOGY OF BELFORT-MONTBÉLIARD**

Doctoral School n°37

Engineering Sciences and Microtechnologies

Doctor of Philosophy (Ph.D.) in Electrical Engineering

by

Yang ZHOU

# Predictive energy management for fuel cell hybrid electric vehicle

Thesis presented and defended in Belfort, on 12/11/2020

Composition of Jury:

| | | |
|---|---|---|
| M. Rachid Outbib | Professor at Aix-Marseilles University | President |
| M. Olivier Sename | Professor at Grenoble Institute of Technology | Reviewer |
| Mme. Florence Ossart | Professor at Sorbonne University | Reviewer |
| M. Ali Sari | Professor at University Claude Bernard Lyon 1 | Examiner |
| M. Simon Morando | PEMFC diagnosis and prognosis specialist at Symbio corporation | Examiner |
| M. Marco Sorrentino | Associate Professor at University of Salerno | Examiner |
| Mme. Marie-Cécile Péra | Professor at University of Franche-Comté | Supervisor |
| M. Alexandre Ravey | Associate professor at University of Technology of Belfort-Montbéliard | Co-supervisor |

**Titre:** Gestion de l'énergie prédictive appliquée aux véhicules hybrides pile à combustible

**Mots clés :** véhicule électrique hybride, gestion de l'énergie, pile à combustible

**Résumé :** Les véhicules électriques hybrides à pile à combustible ont été largement considérés comme la substitution prometteuse par rapport aux véhicules traditionnels à moteur à combustion interne. Pour réduire les coûts d'exploitation des véhicules, une solution pratique au stade actuel consiste à utiliser efficacement et sainement les systèmes de propulsion hybrides. Une telle tâche peut être remplie via des stratégies de gestion d'énergie fiables, qui coordonnent les sorties de plusieurs sources d'énergie pour satisfaire la demande de puissance des véhicules.

Dans un tel contexte, cette thèse vise à concevoir des stratégies de gestion intelligente de l'énergie pour les véhicules électriques hybrides à pile à combustible. Par rapport aux stratégies de contrôle existantes, cette thèse se concentre particulièrement sur la possibilité de combiner les informations de conduite prévues avec le cadre de contrôle optimal en temps réel.

Plusieurs techniques de prédiction de conduite sont développées pour estimer les conditions de conduite à venir, comme la vitesse du véhicule, la référence de l'état de charge de la batterie et les informations sur le modèle de conduite. Ensuite, la model predictive control est sélectionnée pour la prise de décision en temps réel, car elle est capable de gérer les systèmes contraints variant dans le temps et est pratique pour l'intégration des informations prédictives de pilotage. Sur la base des résultats prévus et model predictive control, plusieurs stratégies de gestion prédictive de l'énergie sont établies, visant à économiser la consommation d'hydrogène et à améliorer la durabilité des piles à combustible par rapport aux stratégies de référence.

La simulation hors ligne et les tests logiciels en boucle ont vérifié la fonctionnalité et l'adéquation en temps réel des stratégies proposées.

**Title:** Predictive energy management for fuel cell hybrid electric vehicle

**Keywords:** hybrid electric vehicle, energy management, fuel cells

**Abstract:** Fuel cell electric vehicles have been widely deemed as the promising substitution against traditional internal combustion engine-based vehicles. To reduce the vehicular operating costs, a practical solution at current stage is to efficiently and healthily use the hybrid propulsion systems. Such task can be fulfilled via reliable energy management strategies, which coordinate the outputs of multiple energy sources to satisfy the vehicular power request.

In such context, this PhD thesis intends to devise intelligent energy management strategies for fuel cell hybrid electric vehicles. Compared to existing control strategies, this thesis especially focuses on the possibility of combining the forecasted driving information with the real-time optimal control framework.

Several driving prediction techniques are developed to estimate the upcoming driving conditions, like the vehicle's speed, battery state-of-charge reference and driving pattern information. Thereafter, model predictive control is selected for real-time decision-making, since it is capable of handling the time-varying constrained systems and is convenient for the integration of driving predictive information. Based on the forecasted results and model predictive control, several predictive energy management strategies are established, aiming at saving hydrogen consumption and enhancing fuel cell durability versus benchmark strategies.

Both offline simulation and software-in-the-loop testing have verified the functionality and real-time suitability of the proposed strategies.

Université Bourgogne Franche-Comté
32, avenue de l'Observatoire
25000 Besançon

# Acknowledgement

First of all, I am very grateful to Prof. Olivier Sename and Prof. Florence Ossart for their agreements in review of this thesis, despite their very busy schedule. The constructive feedbacks they have given are of great help in improving the quality of this thesis. Besides, I also want to thank Prof. Rachid Outbib, Prof. Ali Sari, Dr. Marco Sorrentino and Dr. Simon Morando for their kindly assistances in preparation for thesis defense.

I would like to express my special appreciations to my supervisor and co-supervisor, Prof. Marie-Cécile Péra and Dr. Alexandre Ravey, respectively. I still remember that, at the beginning of my PhD study, I know nothing about fuel cells, hybrid electric vehicles and optimization, let alone how to initiate innovative researches or how to write high-quality scientific articles. Throughout my three-year PhD study, it is their constant support and patient guidance that encourage me to find the truth in scientific researches. They set up themselves as the real models to show me how to become an independent and professional researcher. Moreover, the critical thoughts and insightful suggestions they have proposed have generated profound impacts not only on this PhD thesis but also on my future career. It is my great privilege to work with them during the last three years.

I want to specially thank Prof. Fei Gao for his selfless help and constant support during my PhD study. His motivation and perseverance towards scientific researches greatly inspire me during the past three years. Moreover, I would like to express my sincere appreciations to Prof. Ruiqing Ma and Prof. Yigeng Huangfu from Northwestern Polytechnical University for their guidance and suggestions towards my future scientific career.

Wherever you go, friends are always here. I would like to convey my sincere appreciations to my friends: Mr. Weizhu QIAN, Mr. Shengrong ZHUO, Mr. Hongjian WU, Mr. Shiming XIE, Miss Bingcong JIAN, Miss Linrunjia LIU, Miss Shuangshuang Meng, Miss Yue ZHOU, Dr. Rui MA, Dr. Chen LIU, Dr. Hao BAI, Dr. Hanqing WANG, Dr. Hailong WU, Dr. Yu WU, Dr. Huan LI, Dr. Jian ZHANG, Dr. Bei LI, Dr. Meiling Yue, Dr. Dan ZHU, Dr. Suyao Kong, Mr. Zhiguang HUA, Mr. Xinyang HAO, Mr. Tianhong WANG, Mr. Qian LI and many other friends in France and China. Besides, I would also like to thank my dear colleagues in UTBM: Dr. Berk Celik, Dr. Salah Soued and Dr. Loic Vichard.

It takes time from resisting, accepting, towards slowly falling in love with a place. The people and endless memories encountered here are the most effective catalyst for this process. Three-year is enough to ferment my emotions. Thank you, Belfort, for always embracing me and being my second hometown.

Family accompany is my biggest treasure all the way. My deepest love goes to my families.

Finally, the financial support from China Scholarship Council (CSC) during my PhD study is sincerely appreciated.

# Table of contents

# General Introduction

For mitigating the dependencies on fossil fuels, advanced technologies regarding Electric Vehicles (EVs), Hybrid Electric Vehicles (HEVs) and Plug-in Hybrid Electric Vehicles (PHEVs) have been widely regarded as one of promising technologies towards future cleaner transportations. Most recently, with the rapid development of fuel cell (FC) technologies, onboard fuel cell systems (FCS) are becoming the competitive alternative to conventional internal combustion engines (ICEs) in automotive industries, considering its higher system efficiency and zero-local-emission property. Combined with these technical advancements, the birth of Fuel Cell Hybrid Electric Vehicles (FCHEVs) has brought a new research hotspot to both industry and academia.

Although the powertrain hybridization is helpful to improve the vehicles' dynamic and economic performance via combining the benefits of multiple energy sources, the additional flexibility in powertrain topology would intensify the complexity in control aspect accordingly. To effectively coordinate the output behaviors of multiple energy sources, a reliable control strategy (usually termed as energy management strategy (EMS)) should be intensively investigated. Specifically, the basic objective of EMSs is to satisfy the vehicular power demand while respecting the constraints imposed by powertrain operating limitations. Nevertheless, the high manufacturing costs and limited FCS lifetime greatly hinder the massive promotion of FCHEVs. To further reduce the operation costs of a FCHEV, other optimization objectives, like the reduction on fuel consumption and the enhancement on powertrain durability, should be simultaneously included in the EMS control framework.

In order to achieve these objectives, two types of EMSs are widely studied in previous works. Given the complete route information *a priori*, global optimization-based approaches (e.g. Dynamic Programming (DP), Genetic Algorithm (GA)) derives the optimal control actions via minimizing the predefined objective function over the entire driving cycle. Nevertheless, the major drawback of this type of EMS is that the required fully previewed route knowledge is hard to obtain before departure, thus preventing its online implementations. In contrast, real-time control-based EMSs are developed based on the preset rules (e.g. Thermostat strategy, Fuzzy Logic Controller (FLC)) or instantaneous optimization results (e.g. Equivalent Consumption Minimization Strategy (ECMS)), which do not rely on the full driving cycle information and thus can be used for real-time control. However, this type of EMS may lead to the sub-optimal performance under changeable driving conditions.

Nowadays, the maturation of modern telematics systems as well as the development of driving prediction techniques (DPTs) make it possible to acquire the previewed information regarding the vehicle's future driving conditions, such as the traffic flow speed and the road slope. Benefiting from the previewed information, there would be more chances for the predictive energy management strategies (PEMSs) to further enhance the vehicles' performance (e.g. fuel economy) compared to traditional non-predictive EMSs. Compared to existing studies, this thesis will especially focus on the

development of PEMS for fuel cell/battery-based hybrid electric vehicles, so as to explore the potential performance improvement imposed by driving prediction integration.

The structure of this thesis is sketched as follows. **Chapter 1** presents the introduction of the PhD thesis, including the research background illustration, the development status on FCHEVs, EMSs and DPTs, the knowledge gaps against the existing studies, and the major objectives of the PhD thesis.

**Chapter 2** presents a detailed comparative study on EMSs for FCHEVs, including rule-based, global optimization-based and real-time optimization-based strategies. Afterwards, the model predictive control (MPC) framework is selected for EMS development of FCHEVs.

**Chapter 3** develops the DPTs applied to EMSs. Specifically, three improved data-driven approaches for velocity prediction are developed. Besides, an adaptive state-of-charge (SoC) reference estimation method is proposed for guiding the future battery depletion. In addition, a Markov Chain-based driving pattern recognition (DPR) method is designed to identify the real-time driving patterns, which establishes a basis for the realization of multi-mode EMSs.

Benefiting from the proposed driving prediction techniques, **Chapter 4** provides with several ways of combining the predictive information with the real-time MPC decision-making framework, leading to the birth of multiple integrated MPC-based PEMSs, whose performances are validated through simulation studies. Moreover, to explore the fuel economy impacts brought by sizing discrepancy, a numerical analysis regarding the vehicle's operational costs under different powertrain sizing configurations is conducted.

Software-in-the-loop (SIL) test is conducted in **Chapter 5** to verify the proposed PEMSs. The validation results show that the proposed strategy is operational in real-time environment, with the expected objectives realized. Specifically, the proposed PEMSs outperform the lower benchmark strategy in terms of fuel economy and fuel cell durability. Moreover, the proposed PEMSs perform close to the upper benchmark DP-based strategy.

**Chapter 6** summarizes the research works that have been done during this PhD thesis, briefs the major conclusions and indicates the future working directions.

# Chapter 1. Introduction

**Chapter 1** presents a thorough introduction of the PhD thesis, including the research background illustration, the development status on fuel cell hybrid electric vehicles (FCHEVs), energy management strategies (EMSs) and driving prediction techniques (DPTs). Specifically, based on the analyses of existing vehicle configurations, the powertrain topology of the studied FCHEVs is determined, which is composed of a fuel cell and battery. Thereafter, the operating characteristics of proton exchange membrane fuel cells (PEMFC) and lithium-ion batteries are analyzed, thus indicating the optimization objectives that should be included in the energy management framework. Then, the research progresses on EMSs and DPTs are illustrated to facilitate the establishment of the predictive EMSs (PEMSs). In the end, the un-well-solved issues in existing studies are specified and the corresponding solutions are put forwarded accordingly, so as to highlight the contributions of this thesis.

## 1.1. Fuel cell hybrid electric vehicles

In general, the term "Hybrid Electric Vehicle (HEV)" refers to the vehicles powered by a traditional internal combustion engines (ICE) system and an electric propulsion system [1]. The conception of HEVs is to seek the possibility of combining the benefits of two types of vehicles, namely the high energy and power density of the ICE-based vehicles as well as the zero-emission property of the pure electric vehicles (PEV) [2]. Modern HEVs have multiple types of variants and they take advantage of many energy-saving techniques for achieving better performance compared to conventional ICE-based vehicles. For example, HEVs' regenerative braking systems permit a portion of vehicles' kinetic energy to be recovered and stored in battery packs or supercapacitors for future use [1]. Some HEVs can reduce the emission of exhausted gases by shutting down the engine under idling or low-speed conditions, thus improving fuel economy [1]. However, traditional HEVs still lead to carbon emissions owing to the use of fossil fuels.

Nowadays, serious environmental issues like air pollution, energy shortage and global warming require the acceleration of decarbonization in automotive sector [3]. In accordance with this trend, fuel cell systems (FCS) gradually become the competitive alternatives to thermal engines within traditional HEVs. This is because, on the one hand, FCS can directly transform the chemical energy into the useful electricity power. Compared with ICEs, the FCS's efficiency is not restricted by the Carnot efficiency, since there are no intermediate conversion processes, namely from chemical energy to thermal energy and finally to mechanical energy [1]. On the other hand, when using hydrogen as fuel, the FCS can generate electrical power through electrochemical reaction Eq. (1.1), with the pure water and heat as its only byproducts [4].

$$\mathrm{H_2} + \frac{1}{2}\mathrm{O_2} \rightarrow \mathrm{H_2O} + \mathrm{Electricity} + \mathrm{Heat} \tag{1.1}$$

Hence, two overwhelming advantages, namely the higher system efficiency and the zero local emission property, make the FCS a proper substitution to conventional ICE system in vehicles' powertrain.

Actually, there are many different types of fuel cells, including alkaline fuel cells (AFC), proton exchange membrane fuel cells (PEMFC), phosphoric-acid fuel cells (PAFC), molten-carbonate fuel cells (MCFC) and Solid-oxide fuel cells (SOFC) [4]. The features of each fuel cell deviate in many aspects, such as the types of electrolyte, the operation temperature range, the peak system efficiency and the output power level, resulting in different suitable application fields, as indicated in TABLE 1.1. Considering the advanced properties like the quick start-up capacity and the high-power density, PEMFCs are especially suitable for automotive applications [4]. Hence, throughout this thesis, the term "fuel cell" refers in particular to PEMFC, if no additional statement is made.

TABLE 1.1. Comparison of different types of fuel cells [1]

| **Fuel Cell Type** | **Electrolyte Type** | **Operation Temperature Range ($C^o$)** | **System Output Power Level** | **System Efficiency (%)** | **Typical Application Fields** |
|---|---|---|---|---|---|
| PEMFC | Ionic membrane | $[50-80]$ | 1 to 250 kW | 50 to 60 | Automotive |
| AFC | KOH, NaOH | $[65-200]$ | 300 to 5000 W | 50 to 65 | Aerospace |
| PAFC | $H_3PO_4$ | $[180-250]$ | 100 to 1000 kW | 35 to 45 | Power Generation |
| MCFC | $KLiCO_3$ | $[600-700]$ | 10 kW to 2 MW | 40 to 60 | Power Generation |
| SOFC | $ZrO_2, Y_2O_3$ | $[750-1000]$ | $<100$ kW | $\sim 50$ | Power Generation |

As mentioned before, onboard fuel cell systems generate electrical power via a series of electrochemical reactions. Usually, the current variation of fuel cell systems is limited since it takes time to increase or decrease the amount of gas in the stack, making it hard to meet the rapid-changing power demands in realistic driving environments. In this case, using fuel cells as the sole energy source may compromise the drivability of the commercial fuel cell electric vehicles (FCEVs). To address this issue, secondary energy sources (e.g. batteries, supercapacitors (SC)) are integrated into the powertrain to form the fuel cell hybrid electric vehicles (FCHEVs). Typically, secondary energy sources are used to provide the peak power during the acceleration phases or to recover the power during regenerative braking phases. Hence, the onboard FCSs can be downsized concerning the average power requests, thus reducing the overall vehicles' manufacturing costs. In addition, the stationary operation of fuel cell is not only instrumental in improving the system working efficiency but also in extending its lifetime [1].

The HEV's powertrain design, the sizing of components and the development of corresponding EMSs affect each other, which thus deserves substantial attentions when devising control strategies for HEVs, especially for fuel-cell-based ones [5]. Considering the major objective of this thesis, it is better to determine the vehicle's powertrain structure as the basis for further control strategy development. To this end, a survey regarding the proper powertrain structures for commercial FCHEVs from 1997 to 2018 is conducted to obtain the suggestions from car manufacturers, where the detailed results are presented in TABLE 1.2. As can be seen, there are mainly three configurations adopted by car

manufacturers, namely “FC (fuel cell) only”, “FC (fuel cell) + B (battery)” and “FC (fuel cell) + SC (supercapacitor)”, where more than 62% products use the “FC+B” configuration. The major reason for the popularity of such configuration is given as follows.

TABLE 1.2. Powertrain structure comparison among commercial FCHEVs

| Vehicle model | Type | Date | Powertrain | Vehicle model | Type | Date | Powertrain |
|---|---|---|---|---|---|---|---|
| Mazda Demio FC-EV | Concept | 1997 | FC+B | Chang'an Z-SHINE FCV | Prototype | 2010 | FC+B |
| Mercedes-Benz F-Cell | Concept | 2002 | Fc only | FAW Besturn B70 FCV | Prototype | 2010 | FC+B |
| Nissan X-Trail FCV | Prototype | 2003 | FC+B | Ford Focus FCV | Prototype | 2010 | FC+B |
| Jeep Treo-Fuel cell | Concept | 2004 | FC Only | VW Golf Sport Wagen HyMotion | Concept | 2010 | FC+B |
| Suzuki SX4-FCV Fuel Cell Vehicle | Concept | 2004 | FC+SC | Nissan Terra FCEV SUV | Concept | 2012 | FC only |
| Suzuki Wagon R-FCV | Concept | 2005 | FC only | Kia Borrego FCEV | Concept | 2012 | FC only |
| Peugeot 207 Epure | Concept | 2006 | FC+B | BMW i8 Hydrogen Car | Concept | 2012 | FC+B |
| Ford F-250 Super Chief | Concept | 2006 | FC+ICE | Nissan TeRRA SUV Concept | Concept | 2012 | FC+B |
| Fiat Panda Hydrogen | Prototype | 2006 | FC only | Honda FCX clarity | Product | 2014 | FC only |
| Fiat Phyllis | Prototype | 2008 | FC+B | Audi Sportback A7h-tron Quattro | Concept | 2014 | FC+B |
| Mitsubishi Grandis FCV | Concept | 2008 | FC+B | Roewe 950 Fuel Cell | Concept | 2014 | FC+B |
| Morgan LIFEcar | Concept | 2008 | FC+SC | Volkswagen Golf Hymotion | Concept | 2014 | FC+B |
| Peugeot H2Origin | Concept | 2008 | FC+B | Hyundai ix35 fuel cell | product | 2015 | FC+B |
| Scenic ZEV H2 | Concept | 2008 | FC+B | Riversimple | Concept | 2016 | FC+B |
| Ronn Motor Scorpion | Concept | 2008 | FC+ICE | Honda Clarity Fuel Cell | Product | 2017 | FC+B |
| Suzuki SX4-FCV | Concept | 2008 | FC+SC | Toyota Mirai | Product | 2017 | FC+B |
| Audi Q5 FCEV | Concept | 2009 | FC+B | Hyundai Tucson Fuel cell | Product | 2017 | FC+B |
| Chevrolet Equinox Fuel Cell | Concept | 2009 | FC+B | BMW 5 series Gran fuel cell vehicle | Concept | 2017 | FC+B |
| Mazda Premacy Hydrogen RE Hybrid | Concept | 2009 | FC+B+ ICE | Alfa Romeo MiTo FCEV | Concept | 2017 | FC+B |
| Mercedes-Benz F800 | Product | 2010 | FC only | Mercedes Benz New GLC-Fuel Cell | Product | 2018 | FC+B |
| BMW 1 Series Fuel Cell Hybrid | Concept | 2010 | ICE+FC+SC | Hyundai Nexo | Concept | 2018 | FC+B |

Based on the number of energy/power sources (PEMFC, battery, supercapacitor) within the powertrain and the way of connection to the DC bus (direct connection or connection via DC/DC converters), six different topologies (T1 to T6) can be found in existing studies [6], as indicated in figure 1.1. Specifically, there are two energy sources, PEMFC and battery (or supercapacitor), within in topologies T1 to T4, whereas three energy sources, PEMFC, battery and supercapacitor, can be found within topologies T5 and T6. Generally, cutting down the number of energy sources and power converters is favorable for reducing the powertrain weights, mitigating the complexity in control strategies, restricting power losses from devices, decreasing the manufacturing cost and improving the system reliability. However, the simple powertrain topologies may degrade the EMS control performance. For instance, within T2 topology, the DC voltage is determined by the state-of-charge (SoC) of battery (or supercapacitor) due to its direct link to the DC bus. Compared to T4 topology, without the voltage regulation by a DC/DC converter, the output of battery is not controllable so advanced EMSs cannot take advantage of the full

degree of freedom of the energy source use [6]. Furthermore, the advantages and disadvantages of six topologies are listed in TABLE 1.3. Among six different topologies, T2 achieves a well balance among following metrics: the complexity in powertrain structure and corresponding control strategies, the powertrain weight and volume, the protection of high-cost PEMFC system and the system reliability. Hence, considering its popularity in both industry and academia, we decide to use T2 topology for control strategy development in the rest of this thesis.

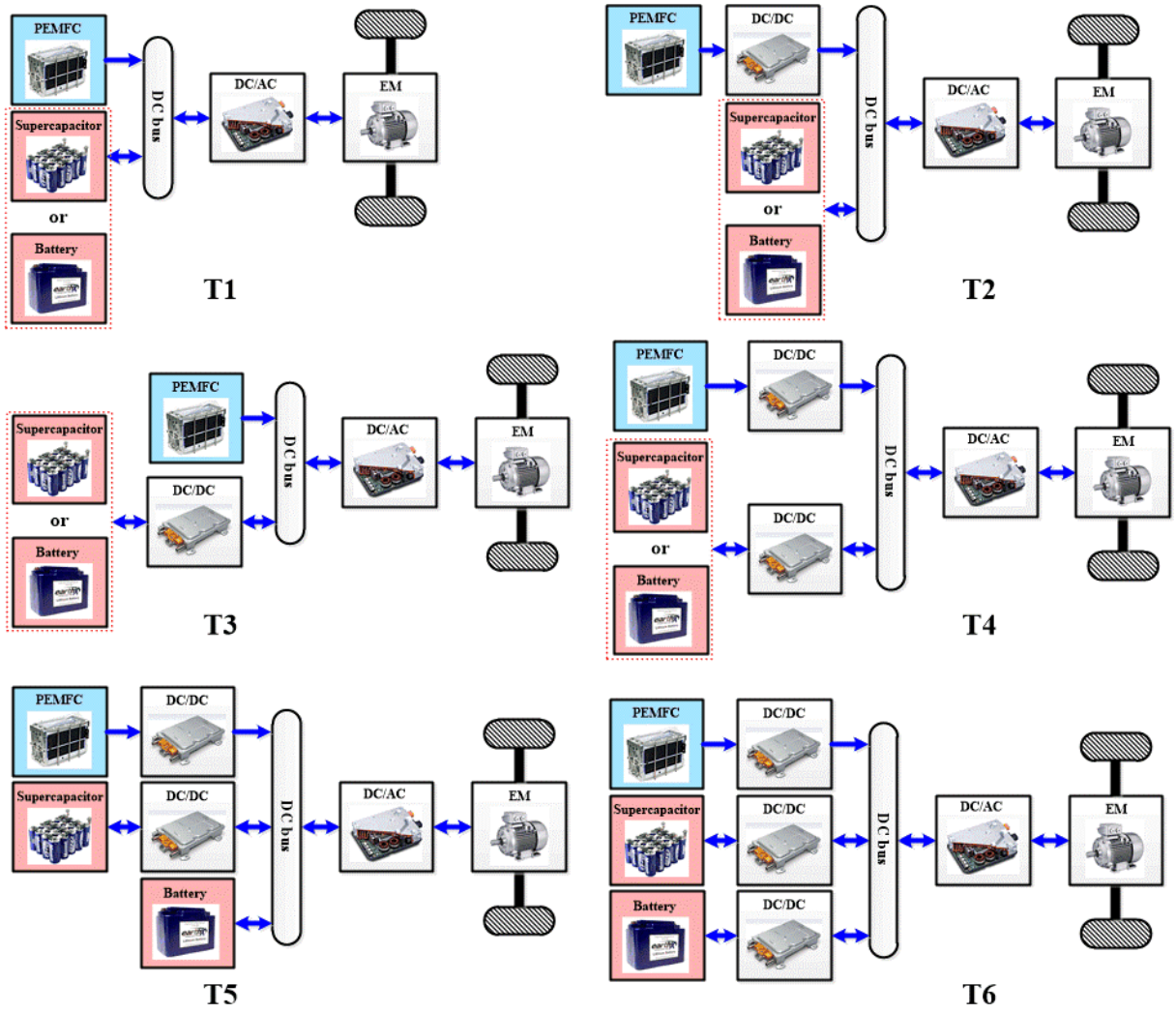


Figure 1.1. Comparison of six different FCHEV powertrain topologies.

Yet, whether to use battery or supercapacitor as the energy storage system in T2 still remains a question. To make a proper decision, the characteristics of several commonly used energy storage systems are carefully compared, as listed in TABLE 1.4. Generally, these devices are employed for assisting the vehicles' acceleration as well as the recovery of braking energy. Compared to batteries, the higher power density of supercapacitor makes it especially suitable for handling the high dynamic power requests. Moreover, the extremely long-life cycle times ensure the system reliability and greatly reduce the vehicle's maintenance costs. In contrast, supercapacitors have much lower energy density than batteries.

Hence, the huge energy density gap versus batteries would make the weight of powertrain greatly growing when using supercapacitors rather than batteries as the sole energy storage system.

TABLE 1.3. Comparative results among different FCHEV powertrain topologies [6]

| Topology | Benefits | Drawbacks | Remark |
|---|---|---|---|
| **T1** | 1. Simplest structure<br>2. Less mass and volume | 1. Hard to effectively split the power flow<br>2. Risk of DC bus current injection back to FCS | Seldom used |
| **T2** | 1. Easy to split the power flow<br>2. Better FCS efficiency and durability. | 1. Floating DC voltage | Widely used |
| **T3** | 1. Accurately control the power flow among secondary energy sources (magnitude and direction) | 1. Compromised FCS performance<br>2. Increased complexity in control strategy than T2 | Seldom used |
| **T4** | 1. Both energy sources can be controlled<br>2. Stable DC bus voltage<br>3. Reduced complexity in motor driving system | 1. Increased powertrain weight and volume<br>2. Increased complexity in control than T1 – T3<br>3. Lower system efficiency (additional DC/DC converter) | Widely used |
| **T5** | 1. Combined advantages of three energy sources<br>2. Flexibility in energy distribution | 1. Increased complexity in powertrain configuration<br>2. Increased complexity in control strategy than T1 – T3 | Preferred by researchers |
| **T6** | 1. Combined merits of all energy sources<br>2. Flexibility in energy distribution<br>3. Better protection for energy sources | 1. Most complex configuration and control strategy<br>2. Highest level of the mass and volume<br>3. Lowest system efficiency (three DC/DC converters) | Preferred by researchers |

TABLE 1.4. Comparison of commonly used energy storage systems: batteries and supercapacitor [7]

| Type | Energy Density | Power Density | Life Cycles (times) | Efficiency (%) | Benefits | Drawbacks |
|---|---|---|---|---|---|---|
| Lead-acid Battery | 30-40 Wh/kg | 0.2-0.3 kW/kg | 300-400 | 75 | 1. Low cost<br>2. High discharging/charging rate | 1. Poor low-temperature performance |
| Ni-MH Battery | 60-80 Wh/kg | 0.8-1.5 kW/kg | >1000 | 75 | 1. High discharging/charging rate<br>2. Long life cycle | 1. High self-discharging rate<br>2. Higher manufacturing costs<br>3. Necessity of cooling system |
| Lithium Battery | 100-135 Wh/kg | 0.6-2.0 kW/kg | >1000 | 90 | 1. High voltage/ Long life cycle<br>2. Light weight/ No memory effect<br>3. Low self-discharging rate | 1. Reduced lifetime at high temperature<br>2. High security requirement |
| Super-capacitor | 4-15 Wh/kg | 1.0-10.0 kW/kg | >100000 | 85-98 | 1. Fast charging and discharging rate<br>2. Extremely long-life cycle | 1. Low energy density |

Based on the aforementioned analyses, battery is finally selected as the energy storage system in this thesis, with the studied FCHEVs' powertrain schematically depicted in figure 1.2.

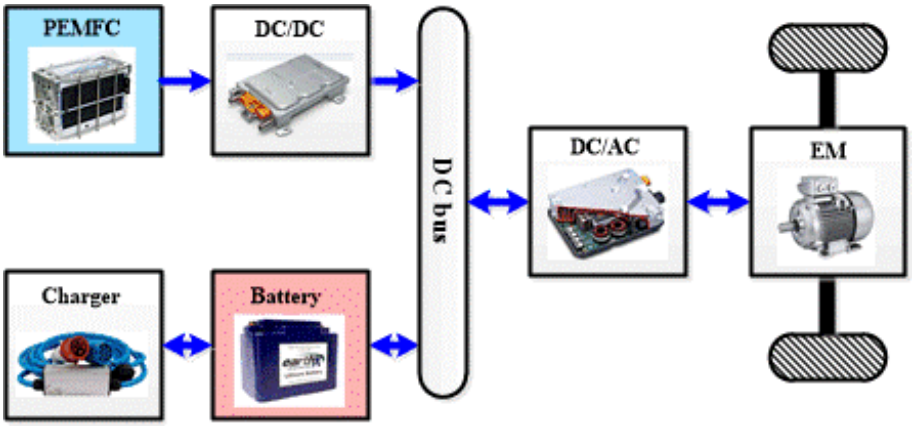


Figure 1.2. Architecture of the studied FCHEVs' powertrain.

The major advantages of the studied hybrid powertrain are given as follows. Under this powertrain structure, it is easy to control the power flow between PEMFC and battery, since the only manipulated variable is the output power (or current) of fuel cell. Besides, the battery can be charged either by PEMFC through the DC bus or by grid power through the onboard charger. In addition, this topology permits both PEMFC and battery to directly power the vehicle, leading to the flexibility in selecting the operating modes of FCHEVs in face of different working scenarios. For example, if its SoC is high, battery can work under charge depleting (CD) mode to deplete the low-cost electricity energy for vehicle propulsion, so as to enhance the fuel economy. If SoC is low, PEMFC can provide the majority of traction power and sustain the SoC level within a safety range (charge sustaining mode, CS).

## 1.2. Energy management strategy for fuel cell/battery-based HEV

As analyzed previously, the powertrain hybridization could be helpful to boost the vehicles' overall operation efficiency through combining the advantages of multiple energy sources [1]. Nevertheless, the correspondingly increased structural complexity against traditional ICE-based vehicles also bring numerous challenges for powertrain control. To make full use of the hybrid powertrain as well as to enhance the vehicles' drivability, the development of reliable energy management strategies (EMS) to coordinate the outputs of multiple power sources deserves substantial attentions. Hence, this subsection presents a brief review on the recent research progress on EMS for FCHEVs.

### 1.2.1 Characteristics of powertrain energy sources

Subsection 1.2.1 specifies the characteristics of PEMFC and lithium-ion battery as well as indicates the related control objectives that should be included in EMS framework.

#### 1.2.1.1. Proton Exchange Membrane Fuel Cell

PEMFC is an electrochemical converter and continuously converts hydrogen energy into electricity power, heat and pure water [4]. The structural representation of a single PEMFC is depicted in figure 1.3 [8].

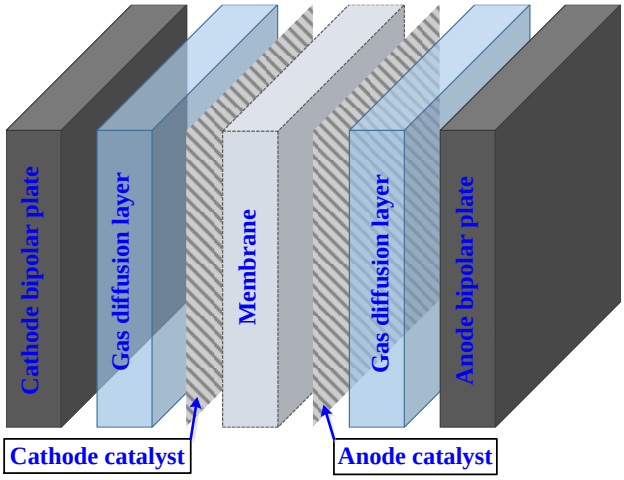


Figure 1.3. Structure representation of a single proton exchange membrane fuel cell.

Although the higher system efficiency and the zero-local-emission property versus thermal engines make PEMFC systems suitable for power generation in theory, many limitations in practical aspects, including the too high manufacturing costs, the too short durability as well as the shortage of hydrogen refueling infrastructures, greatly hinder its applications [9]. In other words, the high operation cost of vehicular PEMFC systems remains one major barrier towards the massive promotion of commercial FCHEVs. Although the efforts towards cost reduction of PEMFC systems can be made from structural design and material replacement perspectives (e.g. the development of more durable and cost-effective catalysts, etc.), breakthrough research progresses can hardly be made in a short time [10]. Hence, at current stage, a more practical solution is to use PEMFCs in an efficient and healthy manner for mitigating its operation costs [11].

Specifically, the operation costs of onboard PEMFC systems comprise two aspects: (1) the cost owing to hydrogen consumption and (2) the cost owing to fuel cell degradation. The hydrogen consumption costs can be effectively brought down by urging more fuel cell operation points towards the predefined high efficiency area [12]. Hence, the improved fuel cell working efficiency would lead to the reduction of hydrogen consumption and a better fuel economy.

In contrast, reducing the degradation costs of PEMFC requires a comprehensive understanding on the degradation mechanism of fuel cells, which is a complicated process involving multiple impact factors ranging from electrochemical to mechanical perspectives [10]-[14]. As reported in [13], the degradation of membrane electrode assembly (MEA) would greatly affect the normal operation of PEMFC, where the MEA degradation mainly originates from the following perspectives:

(a) **Catalyst layer degradation** mainly refers to the reduction of Electrochemical Active Surface Area (ECASA) [13]. One major reason for ECASA reduction is the platinum catalyst particles' agglomeration, sintering and detach from the support material [15]. Moreover, fuel starvation caused by several operation conditions, including running under high loading, transient loading and during start-stop

procedures, would intensify this process [16]. Another major cause of catalyst layer degradation appears when running at extremely low current densities, increasing the surface oxides on the platinum particles [17].

(b) **Membrane layer degradation** occurs mainly due to chemical attack, mechanical stress and/or thermal stress [16], [18], [19]. The former two are owing to the contaminants in the fuel [16] and the improper assembly or the congenital defects [18], respectively, where EMSs can do very little to prevent these defects. However, the thermal stress can be mitigated by properly regulating the PEMFC output power. This is because the high level of heat due to improper loading would reduce the membrane conductivity, increasing the fuel cell electrical resistance, thus compromising the fuel cell efficiency and generating more heats. Besides, excess heat can also cause the membrane drying, leading to the gas permeability [13].

(c) **Gas diffusion layer (GDL) degradation** shares the similar degradation mechanisms to the catalyst support materials [13]. For instance, fuel starvation at high or transient or on/off loading conditions intensify the oxidation of carbon. Besides, excess humidity at high current densities can cause flooding.

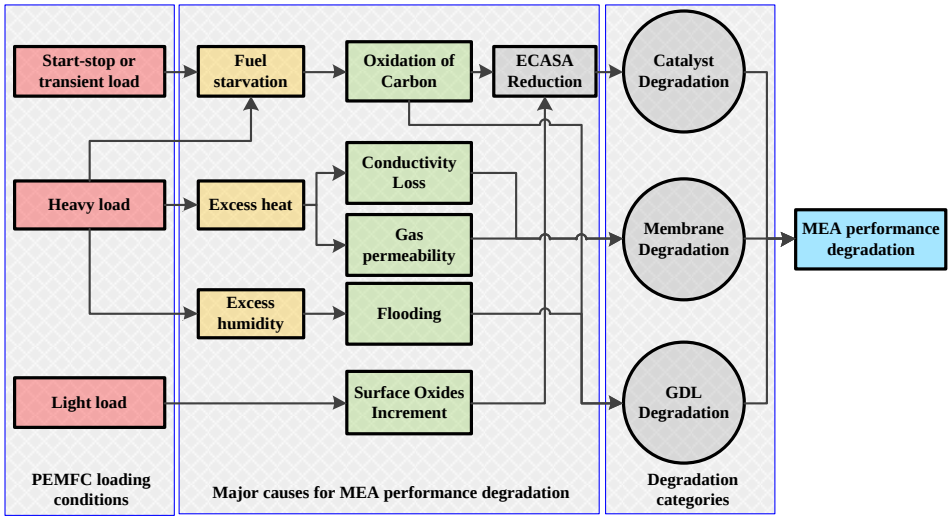


Figure 1.4. Relationship between PEMFC loading conditions and MEA performance degradation [14].

To sum up, the relationship between PEMFC loading conditions and MEA performance degradation is given in figure 1.4. Four PEMFC operating conditions, namely start-stop cycling [18], transient loading [10], heavy [20] and light loading [17], would intensify the MEA performance degradation, leading to the compromised fuel cell durability [14]. Therefore, to reduce the cost owing to fuel cell degradation, EMSs should prevent the occurrence of these operating conditions by controlling the power flow between fuel cell and battery. Specifically, for fuel cell lifetime prolongation, following suggestions should be systematically considered by the EMS designer:

(a) Avoiding frequent fuel cell on-off cycling.

(b) Limiting the duration of fuel cell idling (working at extremely low load).

(c) Restricting the changing rate of fuel cell output power/current.

(d) Preventing fuel cell working at extremely high loads.

#### 1.2.1.2. Rechargeable battery pack

As the important energy storage device in the hybrid powertrain, rechargeable battery pack acts not only as the energy buffer to hold the DC bus voltage in charge-sustaining (CS) mode but also as the energy provider to deliver electricity power in charge-depleting (CD) mode. Lithium-ion battery is one of the most representative traction batteries for electric vehicles applications [7], whose working principle is schematically depicted in figure 1.5.

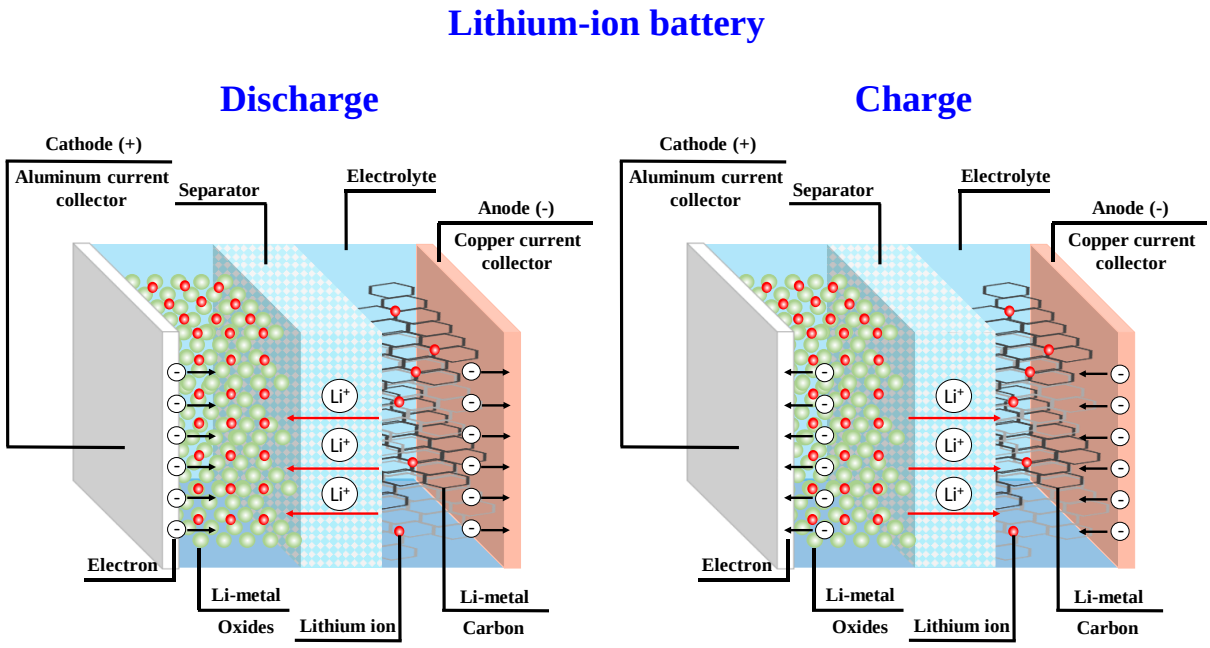


Figure 1.5. Schematic diagram of lithium-ion battery in discharge and charge mode.

Compared to PEMFCs, lithium-ion batteries have following two advantages:

(a) **Fast dynamic response**: Lithium-ion battery is a kind of energy storage systems, which directly converts the (stored) chemical energy into electricity power. Hence, in contrast to PEMFCs, it can more promptly response to the dynamic power requirement [1].

(b) **High working efficiency**: Due to the characteristic discrepancy in energy conversion processes between two power sources, the average efficiency of vehicular lithium-ion battery is about 90% [21], while the electrical efficiency for PEMFC is about 50% to 60% [1].

These advantages make Lithium-ion battery pack an ideal assistant power source within the hybrid powertrain especially during vehicle's acceleration or regenerative braking phases. However, improper

ways of battery usage could shorten its lifetime, compromise its working efficiency and thus threaten the vehicles' drivability. Hence, a well-designed EMS should be able to reduce the battery's operation costs and to prolong its onboard service time. According to previous studies [22], [23], following working conditions would affect the battery performance:

(a) **Extremely low temperature**: The performance of lithium-ion battery is very sensitive to the temperature. Low environmental temperature would slow down the battery's chemical-reaction activity [24], leading to the reduced ionic conductivity of the electrolyte and the limited diffusivity of lithium-ion with the electrodes [25]. However, this deficiency is related to the characteristic and working principle of lithium-ion battery and thus can be hardly mitigated by the EMSs.

(b) **Extremely high temperature:** In contrast, high temperature would intensify the side reactions within the battery [22], leading to the loss of capacity [26] and the decrement of battery efficiency [27]. Furthermore, if the temperature is out of control, battery self-ignition and even explosion could happen in some cases [28]. Please note that, in most cases, high temperature effects are attributed to the high internal temperature of lithium-ion batteries during operation instead of the environmental temperature, which can thus be mitigated by properly governing the output behavior of battery [23].

(c) **Over-charge [22]**: On the one hand, this would increase the opportunity for electrolyte to decompose and have side reaction with the positive electrode. On the other hand, it is easy for lithium-ions to be reduced at the negative electrode.

(d) **Over-discharge [22]**: It is easy for the copper foil of the negative electrode to corrode and for the active material lattice of the positive electrode to collapse.

(e) **High charge/discharge rate [29]**: this would cause the rise of battery internal temperature, lead to the intensification of side reactions, and result in the fatigue and collapse of the active material crystal lattice.

Therefore, to extend the lifetime of lithium-ion batteries, it is necessary for EMS to limit the occurrence of the above-mentioned working conditions. Specifically, following control objectives should be integrated into the EMS framework:

(a) Maintain battery SoC within the predefined range to prevent battery over-charge or over-discharge.

(b) Set upper limits for battery charge/discharge current to retard the rise of internal temperature.

### 1.2.2. Research progress of energy management strategies

In general, the term "energy management strategy (EMS)" refers to the system-level control strategies for splitting the external power demand towards multiple energy sources within the hybrid powertrain. Obviously, satisfying the driver's power demand while respecting the physical constraints on each

component (e.g. the maximum output power limits of PEMFC etc.) is the basic goal of EMS. In parallel, the well-designed EMSs are expected to achieve multiple optimal objectives, where the predominant one is the fuel economy enhancement. Specially, for FCHEVs, prolonging the lifetime of PEMFC systems and ensuring the operation safety of battery pack are also regarded as the important objectives, since they are of great significance to bring down the vehicle's maintenance costs (as analyzed in subsection 1.2.1). Despite distinct objectives realized by various strategies, the working principle of EMSs keeps almost identical. Served as the supervisory controller, EMSs interact with the lower-level controllers (e.g. DC/DC controller). The lower-level controllers respect the commands from the EMSs to control the output behaviors of DC/DC converter, DC/AC inverter and electric machine etc. [30].

Although numerous EMSs have been developed in previous studies, how to design an intelligent EMS to tradeoff among multiple contradictory objectives and how to release the computation burden for better real-time suitability, still remain challenging tasks. To better understand the developing history and the future trend of EMSs, a survey on the proposed EMSs from 1993 to 2018 is conducted. Please note that the EMSs in the literatures deal with both ICE-based and fuel-cell-based HEVs.

Actually, the crucial discriminating factor for any EMS is the control algorithms used for energy distribution. From the literature review, we found fourteen major control algorithms for EMS, including deterministic or fuzzy rules, deterministic dynamic programming (DP), quadratic programming (QP), game theory (GT), genetic algorithm (GA), convex programming (CP), particle swarm optimization (PSO), neural network (NN), Pontryagin's Minimum Principle (PMP), equivalent consumption minimization strategy (ECMS), stochastic dynamic programming (SDP), model predictive control (MPC), reinforcement learning (RL) based strategy.

Figure 1.6 clearly depicts the EMS evolution details within the period from 1993 to 2018. Dating back to 1993, the basic EMS for HEVs was built based on the expertise knowledge and engineering experiences, for simply splitting power request between ICE and EM to bring down the tailpipe emission and fuel consumption [31]. However, those preset rules cannot guarantee the performance optimality until the assistance of DP to refine the rules [32] for EMSs or the employment of GA for multi-parametric tuning of fuzzy membership functions [33]. With the presence of DP, the global optimization results of EMS problem can be attained by minimizing the predefined cost function, given the knowledge of entire driving cycle [34]. Yet, the unavoidable computational burden, especially when a higher (discrete) grid resolution is required, makes DP-based strategy serve as the offline evaluation benchmark instead of being a real-time control strategy.

To overcome the deficiencies of DP, numerous researchers have switched their attentions to performing the optimal control in real-time, thus yielding three different real-time optimization-based EMSs, namely the instantaneous optimal control via PMP and ECMS [35], the approximate optimal control through NN [36] and SDP [37]. Afterwards, more advanced control strategies arose based on their

predecessors, including the improved-SDP [38], the adaptive-ECMS [39], the enhanced-NN [40] and MPC [41]. They were proven to be capable of further enhancing the vehicle's performance in face of real-world driving uncertainties. Meanwhile, compared to the single-objective optimization framework in previous studies, EMSs at this stage were evolving towards simultaneously achieving multiple objectives [42]. Most recently, with the rapid development of machine learning and artificial intelligence, Reinforcement learning (RL) was introduced as a novel model-free and adaptive control algorithm applied to EMS problems [43]. The performance of RL-based EMS may be far from global optimality at the trip beginning. However, it can eventually converge to the global optimality by stepwise updating the control policy through the action-reward interaction with driving environment [30].

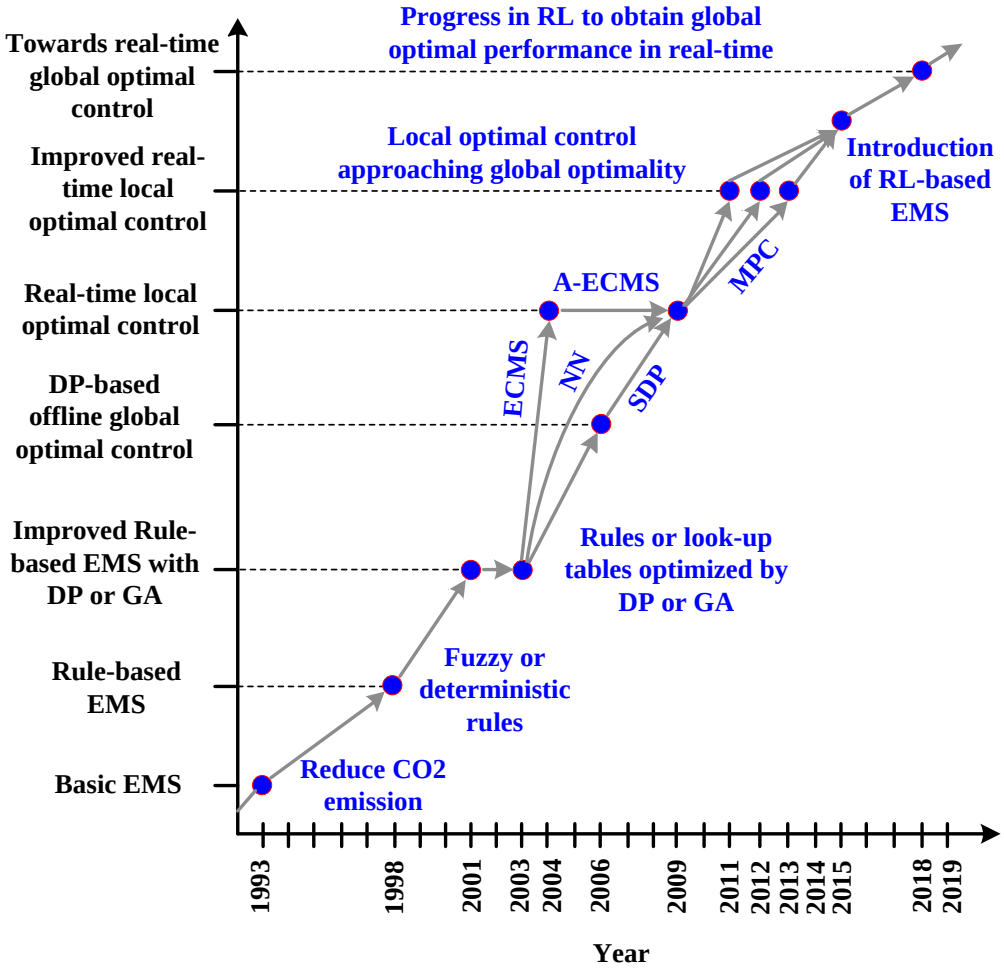


Figure 1.6. Evolution of EMSs for HEVs from 1993 to 2018 [30].

Though the advent of RL algorithm exhibits great potential in obtaining global optimal performance in real-time sophisticated driving conditions, several un-well-solved issues could be threaten to its online implementation, including how to select a proper immediate cost for global optimization [30]; how to tradeoff between the heavy computational burden and the limited resources in the contemporary vehicular electronic control units (ECUs) [30]; how to build a cooperation framework between the

onboard ECU and the modern telematics systems, e.g. intelligent transportation systems (ITS), global positioning systems (GPS) and cloud computing systems [44]. Thus, the author believes that, at the current stage, RL is not the most appropriate candidate to realize the real-time optimal control for EMSs, although its implementation seems to be appealing.

In contrast, originating from model predictive heuristic control (MPHC), model algorithm control (MAC) and dynamic matrix control (DMC) from 1970s, the theory of model predictive control (MPC) has been established and intensively studied by numerous scientific communities [45]. Moreover, it has been successfully applied to many different industrial fields, including chemical industry, aerospace industry, automotive industry, etc. Considering its proven capacity of handling the multivariate constrained systems, the author decides to employ MPC for real-time decision-making for EMS development in this thesis. Moreover, the performance of MPC-based EMS is largely dependent on two essential factors, namely the accurate reference information as the guidance for vehicular power allocation (especially for PHEV applications), and the precise modelling of future driving disturbances for estimating the vehicle's upcoming dynamics [45]. To provide with accurate predictive information for MPC decision-making, it is necessary to investigate the advanced driving prediction techniques, which would be discussed in detail in subsection 1.3.

## 1.3. Driving prediction techniques

Driving prediction techniques (DPT) refer to the algorithms that characterize the future distributions of various driving-related conditions, like vehicle speed, acceleration, driving pattern, etc. The predicted information is then integrated into the real-time optimization framework to form predictive energy management strategies (PEMS) and hence the quality of prediction would heavily affect the overall performance of PEMS [46].

### 1.3.1. Relationship between driving prediction techniques and predictive energy management strategies

Traditional classification on EMSs is based on different control algorithms for power allocation (e.g. rule-based, optimization-based etc.). To clearly illustrate the relationship between the EMS and DPT, a novel classification criterion on control strategies for HEVs/PHEVs is put forwarded, considering whether or not the control strategies are assisted by the predictive information, whose block diagram is given in figure 1.7.

PEMS can be further classified into three sub-categories. "Full-knowledge" based PEMSs distribute energy flow according to the completely previewed traffic information, whereas "zero-knowledge" based PEMSs benefit no information from telematics systems. Please note that the major discrepancy between "zero-knowledge" based PEMSs and "N-PEMSs" (non-predictive EMS) is that the former takes advantage of the estimation of future driving conditions from DPTs, while the latter depends not

on any predicted information but only on the preset rules, human intuitions and expert experiences.

Benefiting from the complete route-based information, "full-knowledge" based PEMSs could guarantee the global optimality to the utmost extent, but their performance can only be deemed as the offline benchmark rather than being used in real-time control. Therefore, as the major provider of predictive information in "partial-knowledge" and "zero-knowledge" based PEMSs, the DPTs would heavily affect the performance of these control strategies.

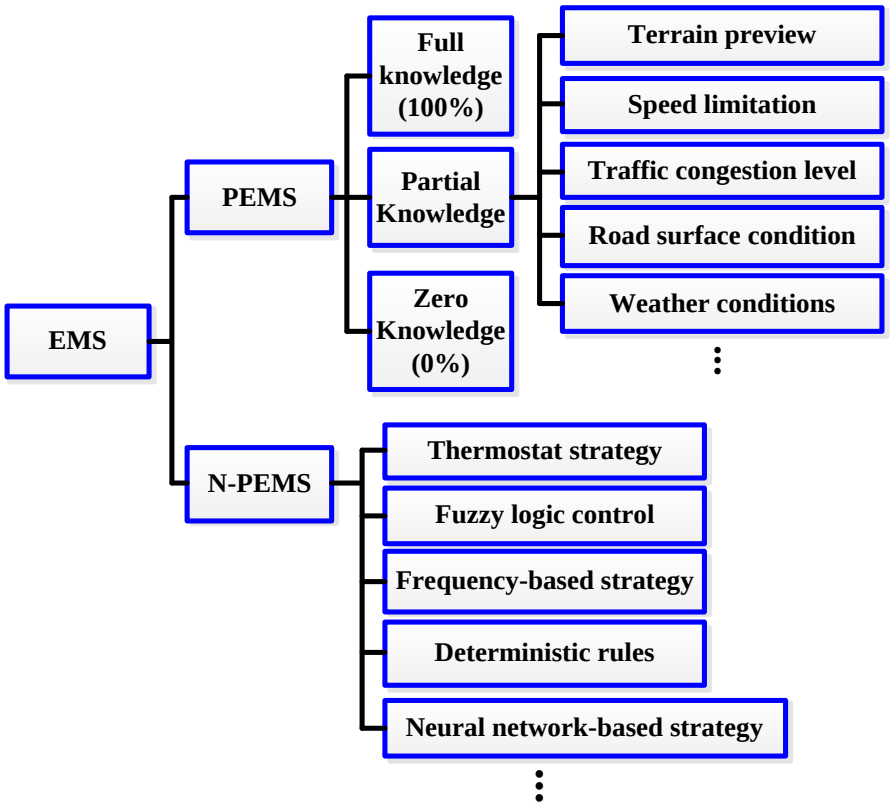


Figure 1.7. A novel classification of control strategy for HEVs/PHEVs.

### 1.3.2. Forecast objectives and algorithms

To enhance the PEMS performance, the precise characterization of future distribution of driving conditions is of great interests to researchers. Specifically, three major types of driving prediction objectives can be found within the existing literatures, namely driving cycle estimation, battery SoC reference prediction and driving pattern recognition.

#### 1.3.2.1. Driving cycle estimation

Typically, a driving cycle is a series of data points representing the speed of a vehicle versus time [47], while a power profile is a series of data points denoting the vehicular traction power demand versus time. When the vehicle is running on a non-horizontal road (figure 1.8), its traction power demand $P_{tra}$ can be calculated by Eq. (1.2) [1], where $c_r$ denotes the rolling resistance drag coefficient, $\rho_{air}$ the air density, $S_f$ the vehicle front surface area, $c_d$ the aerodynamic drag coefficient, $\theta$ the road slope angle,

$M$ and $v$ respectively the vehicle weight and velocity.

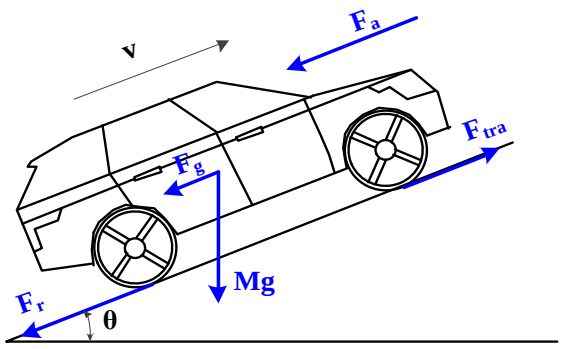


Figure 1.8. Vehicle's dynamics on a non-horizontal road.

$$P_{tra} = v \cdot F_{tra} = v \cdot \left( \underbrace{Mg\sin(\theta)}_{\mathbf{F_g}} + \underbrace{c_r Mg\cos(\theta)}_{\mathbf{F_r}} + \underbrace{0.5\rho_{air} S_f c_d v^2}_{\mathbf{F_a}} + M\dot{v} \right) \tag{1.2}$$

As seen from Eq. (1.2), $P_{tra}$ is closely related to the vehicular parameters (e.g. $S_f, c_d, M$ and $c_r$ etc.), the driving cycles ($e.g.\, v$ and $\dot{v}$) and the road slope information ($e.g.\ \theta$). The vehicular parameters are specified once the vehicle model is selected, while the road slope information can be previewed with the help of telematics systems or mobile applications. However, the driving cycle cannot be precisely estimated by the telematics systems since there are plenty of uncertainties on roads, like the stochastic distribution of traffic lights and the unexpected pedestrian movements [46]. To this end, it is important to carefully model the upcoming vehicle speed (or acceleration) trajectory. Generally, the algorithms for driving cycle estimation can be roughly categorized into three types:

**Artificial intelligence-based methods:** Due to its proven capacity in time-series forecasting field [48], artificial-intelligence based approaches are deemed as the proper candidate for driving cycle estimation, where neural network (NN) is one of the most representative approaches [49]. The general working principle of NN-based prediction model is depicted in figure 1.9. As can be seen, the typical NN-based predictor comprises an input layer, hidden layers and an output layer. The input layer receives the historical speed samples, the hidden layers approximate the nonlinear relationship in a speed-series via proper weight and bias vectors, and the output layer transforms the output from the hidden layers into the desired forecast results.

Mathematically, the NN-based predictor can be written as a multi-input-multi-output function $f_{NN}$, which maps $H_q$ historical speed samples at time step k into the future ones in $H_p$ steps ahead [49].

$$\left[v^*_{k+1}, \dots, v^*_{k+H_p}\right] = f_{NN}\left(v_{k+H_q-1}, \dots, v_k\right) \tag{1.3}$$

Moreover, the size of NN-based predictor is determined by the number of hidden layers and the number

of neurons in each layer. As far as known, there is no uniform guideline for the setting of these parameters, meaning they have to be tuned manually to tradeoff between NN generalization capacity and the overfitting phenomena [50].

After the NN size is specified, the associated weights and bias should be adjusted to optimize the given performance index over the available dataset, which is termed as NN training. Please note that the training database usually comprises standard driving cycles, like the Federal Test Procedure-75 (FTP-75), Urban Dynamometer Driving Schedule (UDDS), or the GPS-collected speed profiles in real missions [49]. Since NN attempts to describe the complex, multivariate, nonlinear relationships in time series, and thus the time-consuming training processes are usually accomplished offline.

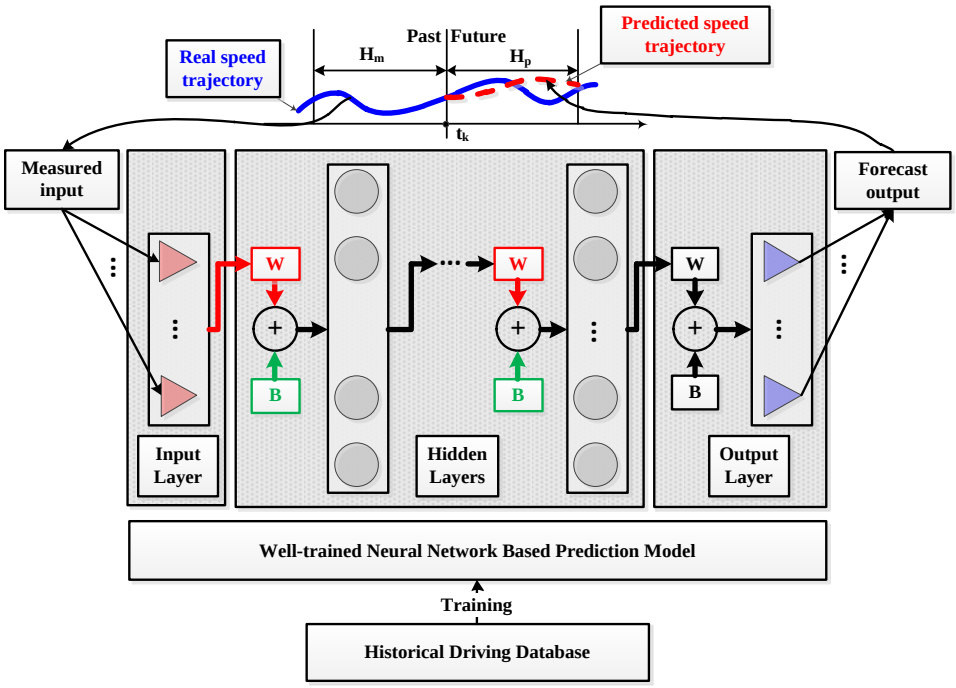


Figure 1.9. Schematic diagram of neural network-based velocity prediction model.

**Markov Chain based methods:** In realistic driving environment, vehicle's operation can be influenced by many uncertain factors [46]. Therefore, the future distribution of vehicle velocity can be deemed as a stochastic process. As a powerful tool for stochastic modeling, Markov Chain is a commonly used approach to forecast the driving cycle or the vehicle's power demand [49].

A Markov Chain (MC) is used to describe a stochastic sequence of possible events wherein the probability of each event depends only on the state obtained in the previous event [51]. The most important concept in Markov Chain is the transition probability matrix (TPM), as given in Eq. (1.4). TPM defines the future probability distribution of the Markov (stochastic) process, where its element in the $i^{th}$ row and $j^{th}$ column ($P_{i,j}$) is a conditional probability reflecting the occurrence of state transition event originating from state $i$ and ending at state $j$. For driving cycle prediction purpose, the Markov

state is usually defined as the velocity, acceleration, or velocity-acceleration pairs, etc.[46].

$$\mathrm{TPM} = \begin{bmatrix} P_{1,1} & P_{1,2} & \dots & P_{1,j} & \dots & P_{1,s} \\ P_{2,1} & P_{2,2} & \dots & P_{2,j} & \dots & P_{2,s} \\ \vdots & \vdots & \ddots & \vdots & \ddots & \vdots \\ P_{i,1} & P_{i,2} & \dots & P_{i,j} & \dots & P_{i,s} \\ \vdots & \vdots & \ddots & \vdots & \ddots & \vdots \\ P_{s,1} & P_{s,2} & \dots & P_{s,j} & \dots & P_{s,s} \end{bmatrix} \text{ with } \sum_{j=1}^{s} P_{i,j} = 1 \tag{1.4}$$

The overall working flow of MC based prediction model is depicted in figure 1.10, including three working stages, where stage I (TPM group estimation) is conducted offline based on the available driving database, while stage II (driving data sample & encoding) and stage III (state transition estimation & decoding) are realized online for driving cycle prediction.

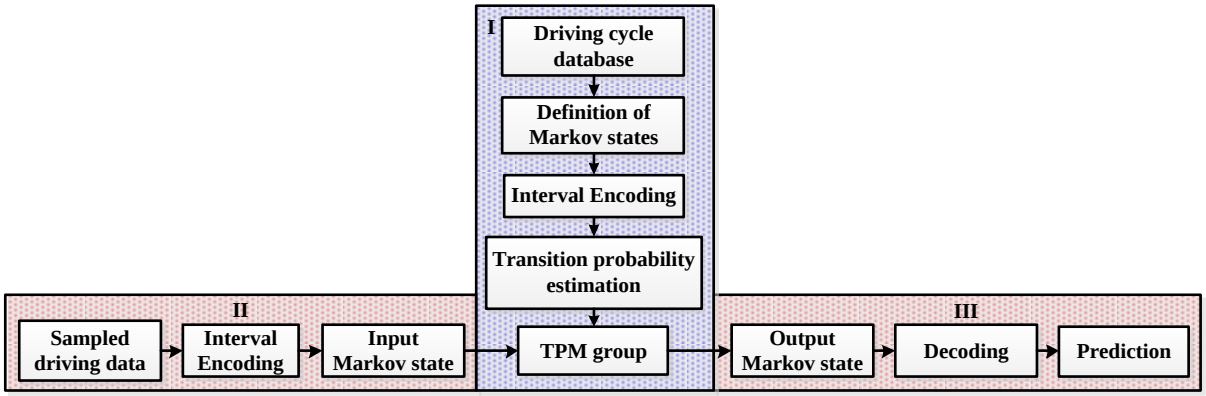


Figure 1.10. Working flow of Markov Chain based prediction model.

**Exponentially decreasing model:** Another simple but effective approach for driving cycle estimation is the exponentially decreasing model (EDM), which was originally proposed by H. Borhan in [52] and applied to MPC-based EMS for HEVs. This method forecasts the vehicle velocity by assuming the vehicle torque demand $\tau_{tra}$ will decrease exponentially over the prediction horizon, as indicated by Eq. (1.5).

$$\begin{aligned} &\tau_{tra}[(k+i)T] = \tau_{tra}(kT) \cdot \exp\left(\frac{-i \cdot T}{T_d}\right) && (a) \\ &v[(k+i)T] = v(kT) + \frac{1}{M}\int_{kT}^{(k+i)T} \left[\frac{\tau_{tra}(t) \cdot \exp\left(\frac{-t}{T_d}\right)}{R_{tire}} - F_g(t) - F_r(t) - F_a(t)\right] dt && (b) \\ &i = 1,2,\dots,H_p. && (c) \end{aligned} \tag{1.5}$$

Where $\tau_{tra}(kT)$ is the known torque requirement at the beginning of the preview horizon, $v(kT)$ the sampled speed at the beginning of the prediction horizon, $R_{tire}$ the vehicle tire radius and the detail expressions of $\mathrm{F_g}$, $\mathrm{F_r}$ and $\mathrm{F_a}$ are given in Eq. (1.2). Please note $T_d$ denotes the torque decay coefficient, and it is the only parameter that needs to be tuned before online application. A larger $T_d$ contributes to a slower torque decay rate. To enhance the speed forecast performance, the value of $T_d$ should be

carefully adjusted under different driving patterns [53].

**Telematics based methods:** Thanks to the rapid development of modern telematics systems (e.g. GPS, ITS, Vehicle-to-Vehicle (V2V) communications), the forecast of future driving conditions can be made with higher credibility. Specifically, the preview of route-based information like upcoming traffic light distributions [54], speed limits [55], average traffic flow speed [56], future road grade [57], movement of preceding vehicles [58], drivers' driving styles [59] and traffic congestion level [60] are utilized to reduce the prediction uncertainty, so as to improve the overall performance for HEV control strategies. For example, a higher prediction accuracy for future driving condition can be reached when considering the previewed topographic information [61]. Benefiting from such predictive information, the related EMSs for HEVs not only improve the fuel economy but also extend the lifetime of battery. Moreover, an ITS-enabled vehicle velocity-planning algorithm is proposed, aiming at scheduling the vehicles speed profiles based on the preview of traffic light distributions, so as to reduce the idle time of engine for better fuel economy [62].

#### 1.3.2.2. Battery SoC reference estimation

Compared to HEVs, the plug-in property of PHEVs allows its onboard battery to be recharged by the external grid power, which, hence, enables a way towards better fuel economy by consuming the low-cost electricity energy. More importantly, for PHEVs, its global optimal fuel economy is closely related to the way of battery energy depletion. Therefore, an explicit SoC reference trajectory is indispensable as the guidance for battery energy allocation within the PEMS framework [63]. Please note that the global optimal SoC profile varies accordingly with different driving routes, and thus the estimation of SoC reference trajectory should take the previewed route information into account. From the related literatures, it can be found that the approaches for SoC reference estimation can roughly be categorized into three types:

**Linear SoC reference model:** The linear SoC reference model only requires the trip length $L_{trip}$ [64] (or duration $T_{trip}$ [65]) information for SoC reference planning. Typically, the reference SoC is designed to linearly decline from the initial (maximum) value to the terminal (minimum) one, implying the single SoC depleting rate over the entire trip.

**Telematics-based SoC reference model:** The second type of SoC reference planning method takes advantage of the real-time updated route information from modern telematics system (e.g. ITS, GPS, etc.). For example, in [56], the authors assumed that the average traffic flow speed on the selected routes can be previewed by the onboard GPS. Thereafter, dynamic programming (DP) is utilized to search for the optimal SoC trajectory on the previewed routes, where the obtained SoC trajectory is then used as the reference for MPC energy allocation control. The overall working flow of telematics-based SoC reference calculation approach is depicted in figure 1.11.

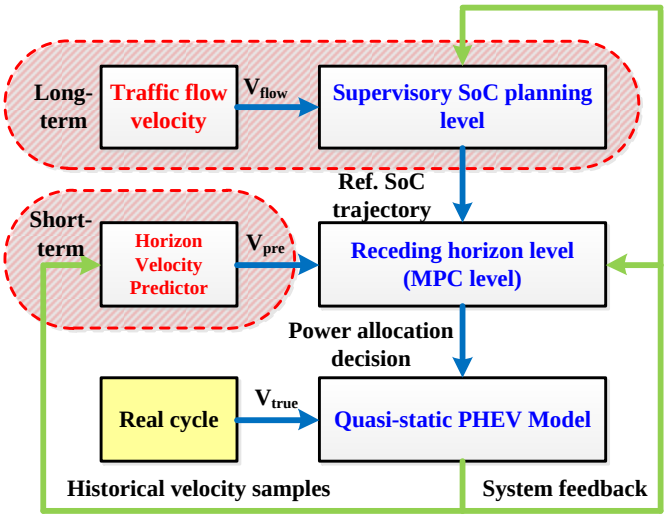


Figure 1.11. Working flow of telematics based SoC planning approach: the supervisory level utilizes the real-time traffic flow speed to compute the global optimal SoC trajectory. The lower level MPC control takes the extracted SoC trajectory as reference for energy distribution [56].

**Data-driven SoC reference model:** Existing data-driven approaches for SoC reference generation are largely designed for the vehicles with relatively fixed running routes and repetitive driving patterns, like city buses [66]-[68], commuter cars [69], etc. In this case, the past driving experience is valuable for guiding the future battery energy distribution, since there is a great chance for these vehicles to follow the past driving patterns in future tasks. Therefore, data-driven based methods, like neural network [66]-[68] and multivariate regression algorithm [70], [71], are naturally regarded as the proper candidates because of their proven capacity in learning from available dataset and then reproducing the similar behaviors.

For example, authors in [66] devise a NN-based SoC reference planning method for plug-in hybrid electric buses, attempting to characterize the relationship among average route speed, route segment length and optimal SoC traces, where figure 1.12(a) depicts the proposed three-layer NN structure. Assisted by ITS and onboard navigation system, it is assumed that the average speed of each driving segment, the remaining length percentage and the current segment length percentage can be obtained. Thereafter, the NN plans the macroscopic battery energy depletion by generating SoC trajectory outline. Between each two consecutive SoC outline points, the linear SoC reference model is adopted to generate the SoC reference points for integrated control, by assuming the battery energy depleting linearly with the increment of the traveled distance.

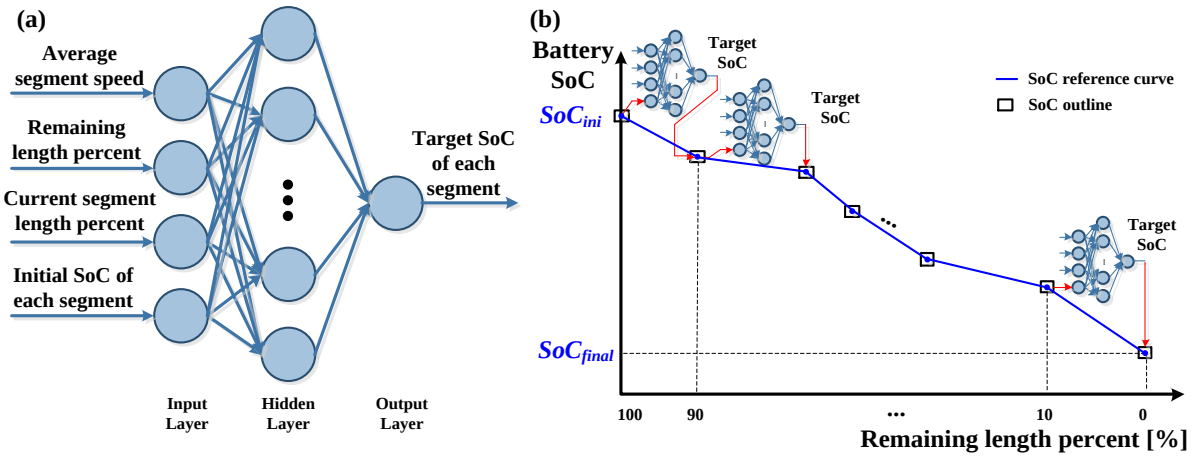


Figure 1.12. (a) Structure of NN-based SoC reference generator. (b) Working flow of SOC reference outline construction [66].

### 1.3.2.3. Driving pattern recognition

Driving pattern is a comprehensive description of the combination of road environment and the state of vehicles [46], where congested urban, flowing urban, suburban and highway are four typical driving patterns defined by Environmental Protection Agency [72]. As shown in figure 1.13, taken INRETS standard driving cycle as an example, it is a combined driving cycle including multiple driving patterns [46], wherein each driving pattern has its own characteristics, like the average speed and number of vehicles stops.

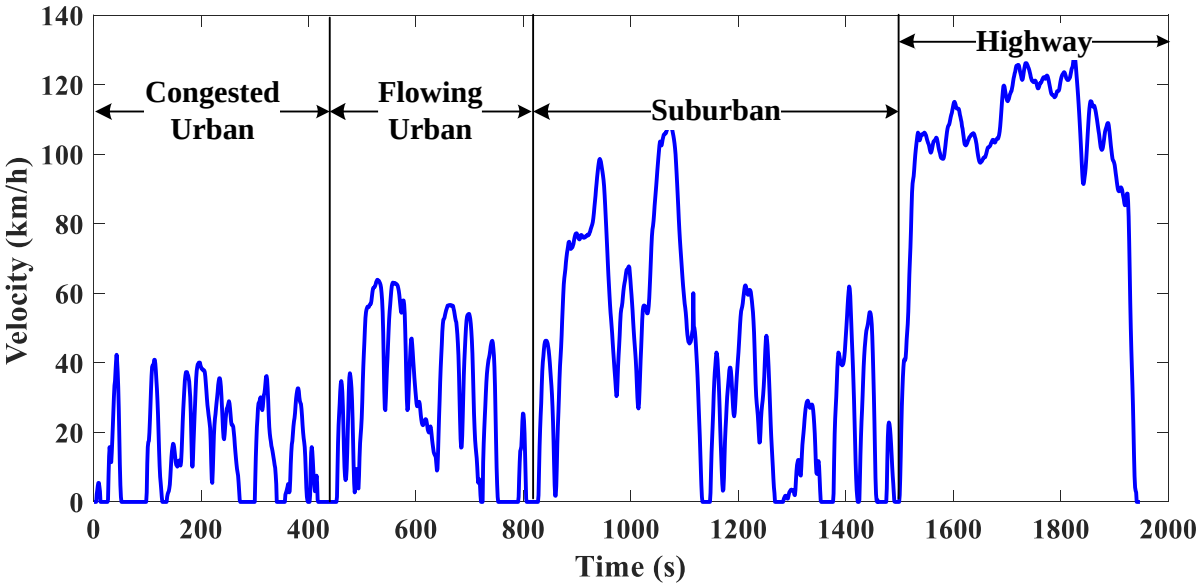


Figure 1.13. Representation of different driving patterns.

Due to such driving discrepancies, the control parameters optimized for one driving pattern may not be optimal for another one anymore [73]. Hence, it is necessary to consider the driving pattern impacts when devising EMSs for HEVs/PHEVs. This yields the necessity of investigating driving pattern

recognition (DPR) techniques, which can classify the real-time driving segment into one of several predefined types based on the extracted feature parameters [74]. In this way, benefiting from the periodically updated DPR results, the EMS can better adapt to the changeable driving environment. A typical working flow for DRP-based EMS is depicted in figure 1.14 [46].

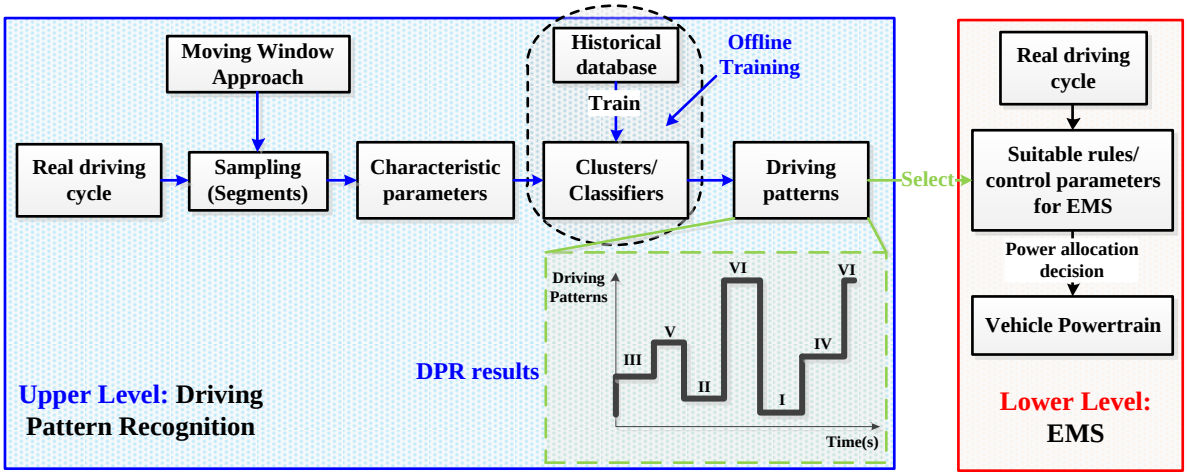


Figure 1.14. Control framework of driving pattern recognition-based energy management strategy.

Mathematically, the DPR problem can be regarded as a classification (or supervised learning) task. Numerous algorithms can be used to tackle such problem, like neural network (NN) [75]-[77], support vector machine (SVM) [46], [53], [78], and k-nearest neighbor (KNN) algorithm [79]. Before online pattern identification, the selected classifiers should be trained offline based on the historical driving database. Thereafter, the driving characteristic parameters (e.g. average speed, maximum acceleration, etc.) extracted in each moving window are imported into the well-trained classifiers for mapping the real-time driving segment into one of preset types. Finally, the DPR results are served as the selection criteria for proper control parameters/rules of EMSs. Overall, within the DPR-based EMS control framework, the DPR technique acts as the upper level controller to estimate the real-time driving patterns, while the EMS is the lower level controller for executing corresponding energy allocation decisions with respect to different driving conditions [46].

Based on the discussion in subsection 1.4, the benefits, drawbacks and application scenarios of existing driving prediction techniques are summarized in TABLE 1.5, where the abbreviation EDM stands for exponentially decreasing model, NN for neural network, ARIMA for auto-regressive integrated moving average [80], GSDM for gain scheduled driver model [81], HACM for hierarchical agglomerative clustering method [82], FDP for frequency-domain based prediction [83], SD for similarity degree [84], FL for fuzzy logic recognizer [72] and PSVM for probabilistic support vector machine [12].

TABLE 1.5. Comparison of existing driving prediction techniques

| Method | Benefits | Drawbacks | Application scenarios |
|---|---|---|---|
| **EDM** | 1. Easy and robust to implement;<br>2. Less computation burden and data requirements.<br>3. Good benchmark. | 1. Fixed model structures lead to poor adaptation to changeable driving cycles; | 1. Driving cycle estimation |
| **NN** | 1. Nonlinear multivariate relationship approximation;<br>2. Potential of integrating preview knowledge;<br>3. Strong learning capacity from available dataset. | 1. Performance relies heavily on training accuracy.<br>2. Conflicts between NN generalization and over-fitting;<br>3. Forecast robustness loss under novel driving conditions. | 1. Driving cycle estimation;<br>2. Battery SoC reference estimation;<br>3. Driving pattern recognition. |
| **Telematics** | 1. Real-time updated & historical statistic traffic information (e.g. average traffic flow speed).<br>2. Data communication with modern telematics systems;<br>3. Previewed route information. | 1. Heavy computation load, sometimes cloud computing involved;<br>2. Early stage of ITS and traffic flow modeling techniques; | 1. Driving cycle estimation;<br>2. Battery SoC reference estimation;<br>3. Driving pattern recognition. |
| **Linear model** | 1. Computation-efficient;<br>2. Preview route information (trip length or trip duration) easy to obtain. | 1. Compromised battery energy distribution performance dealing with complex driving conditions. | 1. Battery SoC reference estimation. |
| **Markov Chain** | 1. Suitable for modeling stochastic process.<br>2. Reasonable accuracy on similar driving conditions.<br>3. Easy to enable online leaning technique. | 1. Single-order MC model is difficult to model blended driving conditions, leading to low prediction accuracy.<br>2. High memory burden for high-order MC model. | 1. Driving cycle estimation. |
| **ARIMA** | 1.Advances in forecasting time-series sequences;<br>2. Potential to reduce “non-stationary” characteristics in data; | 1. Less adaptability due to relatively fixed structures;<br>2. Huge dependency on historical database. | 1. Driving cycle estimation. |
| **GSDM** | 1. Less computation & memory burden;<br>2. Adaptability to real driving conditions ensured by online recursive least square approaches. | 1. Forecast only based on the single vehicle state may compromise the prediction accuracy. | 1. Driving cycle estimation. |
| **HACM** | 1. Unsupervised learning technique, where the number of clusters need not to be specified in advance;<br>2. Both driving conditions and uncertainties of the exact final position could be modeled. | 1. Highly dependent on servers where complicated computation and large data storage space were required.<br>2. Highly dependent on corresponding route-based techniques, like route identification approaches. | 1. Driving pattern recognition. |
| **FDP** | 1. Reduce prediction difficulty by forecasting future speed in frequency domain rather than in time domain. | 1. The predicted driving profile is not available in time-domain, limiting the potential for further performance improvement. | 1. Driving cycle estimation. |
| **SD** | 1. Computation-efficient compared to traditional DPR techniques;<br>2. Easy to understand. | 1. Difficult to choose driving feature parameters;<br>2. Weight factor of each driving characteristic parameters is hard to tune. | 1. Driving pattern recognition. |
| **FL** | 1. Less computation burden and robust to external disturbances; | 1. Parameters of membership functions need to be re-tuned in different driving scenarios. | 1. Driving pattern recognition. |
| **PSVM** | 1. Quantify driving pattern by probability vector, rather than specifying the deterministic pattern identification result.<br>2. Potential to be combined with data fusion techniques. | 1. Performance highly depends on several pre-set known cases.<br>2. Time-consuming training process. | 1. Driving pattern recognition. |

## 1.4. PhD project objectives

Based on the aforementioned discussions, this subsection summarizes the limitations in previous studies, so as to better underline the contributions of this PhD thesis towards the pool of existing knowledge.

### 1.4.1. Knowledge gap in existing studies

According to the literature review, the limitations of existing energy management strategies (EMSs) for fuel cell hybrid electric vehicles (FCHEVs) are summarized in the following aspects:

**(i) Extend single-objective EMS into multi-objective EMS**: In most of previous studies, fuel economy is generally taken as the primary EMS objective for traditional ICE-based HEVs [85]. Nevertheless, improper fuel cell/battery operations would compromise their durability, shorten their onboard service time and eventually threaten the vehicle's operation safety. Therefore, control strategies for FCPHEVs should also attempt to reduce the vehicle's maintenance costs imposed by the performance degradations of powertrain energy sources [14]. This yields a challenging task, that is, to devise an intelligent multi-objective EMS for FCPHEVs, which can systematically guarantee the following performance indices, namely hydrogen consumption saving, fuel cell lifetime extension, battery SoC tracking capacity and battery operation safety.

**(ii) Improve real-time suitability for EMS**: Computation efficiency is a significant aspect for the real-time practicality of EMSs in automotive field. Within the MPC-based EMS framework, although using nonlinear dynamic model permits a more accurate estimation of system future behaviors and thus improve the EMS performance, the additional computation burden for handling the nonlinearities would be a great threat to its online implementation [86]. Besides, the MPC cost function formulation would also affect the calculation efficiency of control strategies. For example, the existence of nonlinear cost terms (or constraints) in optimization problem requires the employment of nonlinear solvers (e.g. DP) to compute the desired control actions, whose computation time increases exponentially with the growth of discrete grid resolution [87]. In contrast, if the MPC cost function could be formulated into some specific types (e.g. quadratic form), the well-established commercial solvers (e.g. QP solvers) can tackle the optimization problem with acceptable calculation burden [88]. Therefore, how to enhance the real-time suitability of the devised EMS without over compromising its performance still deserves further investigations.

**(iii) Integrate DPR results into MPC-based EMS**: Most existing studies combine the DPR results with multiple sets of deterministic (or fuzzy) rules, where, specifically, several rule-based strategies are optimized in offline to cope with corresponding predefined driving patterns [74]. In this way, with the real-time updated DPR results, the rules for power allocation switch accordingly with the change of recognized driving pattern, so as to realize the adaptive EMS framework [75]. Nevertheless, few studies utilize MPC for decision-making within the adaptive EMS framework, nor propose the suitable way of

integrating pattern identification results into MPC control framework. Therefore, how to devise a multi-mode MPC-based EMS, which can both recognize the real-time driving pattern and then perform suitable control strategies in different driving conditions, needs further studies.

**(iv) Enhance the quality of speed prediction:** Tow major drawbacks can be found within the existing driving cycle estimation approaches. Firstly, most of existing data-driven approaches acquire predictive knowledge from historical stationary driving database. However, if the realistic driving conditions were divergent significantly from the historical ones, the forecast performance would be greatly compromised. Therefore, the online-learning techniques, which can update the structure of offline-trained prediction models according to the recent driving changes, should be intensively studied [89]. Secondly, drivers' intentions would change accordingly with vehicles' operation stages. For instance, aggressive driving behaviors with large acceleration would be detected in vehicle's start-up phases, whereas mild driving behaviors tend to appear during the vehicles' cruising phases. Apparently, various driving intentions would lead to huge discrepancies in terms of future velocity distributions. Hence, the conventional single-mode velocity-forecast approaches may compromise the prediction reliability when handling multiple driving stages. Thus, it is necessary to investigate a multi-mode speed predictor for adapting to different driving intentions [85].

**(v) An integrable battery SoC reference estimation approach:** In linear SoC reference model, the single SoC declining rate may be improper for the realistic cycles with multiple driving patterns [63]. Besides, the real-time updated traffic information required by telematics-based approaches [56], the abundant historical driving data required by data-driven approaches [67] as well as the corresponding extra computation and memory burden greatly hinder their real-time implementations. Hence, an adaptive real-time applicable solution for generating SoC reference should be further studied, which has suitable computational burden and less dependency on telematics systems, so as to enhance its integration possibility into the onboard ECUs.

**(vi) Recognize driving patterns with high reliability:** From existing studies, it can be found that challenges for DPR techniques exists in the following aspects: (1) the conflicts between recognition accuracy and computation burden [46]; (2) the determination of the moving window length for both driving data collection and driving pattern duration [79], and (3) the DPR accuracy compensation during driving pattern shifting phases [90]. Consequently, to address these issues, it is necessary to explore advanced DPR techniques for providing reliable pattern identification results for EMSs.

### 1.4.2. Innovation and contribution

The aim of this PhD thesis is to design a predictive EMS for FCHEV, for optimally allocating the power flow among energy sources regarding the vehicle's power requirement. Compared to existing strategies, this study will especially attempt to embed the driving predictive information into the optimization-based EMS framework, so as to explore the performance enhancement imposed by the predictive

information integration. To achieve this goal, the primary task is to advance the driving prediction techniques (DPTs) by addressing the following issues:

- What kind of physical quantities should be predicted for energy management purpose;
- Which specific algorithms can be used to forecast the future driving conditions;
- How to enhance the prediction quality under complex, rapid-changing driving conditions;
- How to plan the depletion of battery energy with the help of route preview information;
- How to identify real-time driving patterns with high credibility.

Likewise, several challenges also exist from the viewpoint of control strategy development:

- How to choose a suitable control framework for predictive information integration;
- How to simultaneously realize multiple control objectives (e.g. H2 saving, fuel cell lifetime extension, battery SoC reference tracking ability, etc.) within the proposed EMS framework;
- How to guarantee the robustness of the proposed strategy in face of mis-predictions.
- Finally, a suitable validation approach is required to verify both the functionality and real-time suitability of the proposed strategy, so as to further demonstrate the potential of the proposed strategy to be embedded into the vehicular electronic control units (ECU).

To bridge these research gaps, this thesis proposes predictive energy management strategies for fuel cell/battery-based HEVs, including following major contributions:

- To improve the performance of model predictive control (MPC), the prediction quality of vehicles' future speed should be enhanced. Hence, three improved speed-forecasting methods are proposed, including an online-learning enhanced Markov predictor (OL-MC), a fuzzy C-means clustering enhanced Markov predictor (FCM-MC) and a Layer-Recurrent Neural Network based predictor (LRNN), where the forecast precision and robustness are improved compared to the conventional predictors;
- To perform proper control strategies in different driving conditions (e.g. urban, suburban, highway), driving pattern recognition (DPR) techniques should be intensively investigated. In this thesis, a novel DPR approach based on self-learning Markov Chain is proposed. The periodically updated DPR results are instrumental in selecting the appropriate EMS control parameters for adapting to changeable driving scenarios;
- To effectively allocate PEHV battery energy under different driving scenarios, an explicit SoC reference trajectory is necessary as a guidance in PEMSs. In this thesis, an integrable driving-pattern-conscious SoC reference generator is proposed, leading to the enhanced battery energy distribution performance versus the existing linear SoC reference model;
- Combined with the predictive information, several ways of integrating the predictive information into the real-time MPC framework are proposed, leading to the birth of multiple

PEMSs. For example, with the assistance of the Markov driving pattern recognizer, a multi-mode EMS is proposed for power distribution under changeable driving patterns. Besides, an integrated PEMS based on the FCM-MC predictor and the adaptive SoC reference generator is presented for a light-duty mail-delivery FCHEV. Furthermore, to improve the EMS performances under newly encountered driving conditions, a multi-objective PEMS assisted by the OL-MC predictor is developed for a fuel cell/battery-based PHEV.

- Software-in-the-loop validation results demonstrate the functionality and real-time practicality of the proposed strategies.

## 1.5. Publication List

This PhD thesis has contributed to nine publications, which are listed as below:

**Papers published in international journals:**

**Y. Zhou**, A. Ravey, M.C. Péra, A survey on driving prediction techniques for predictive energy management of plug-in hybrid electric vehicles, ***Journal of Power Sources***, Volume 412, 2019, Pages 480-495, https://doi.org/10.1016/j.jpowsour.2018.11.085. **[Q1, IF = 8.247]**

**Y. Zhou**, A. Ravey, M.C. Péra, Multi-mode predictive energy management for fuel cell hybrid electric vehicles using Markov driving pattern recognizer, ***Applied Energy***, Volume 258, 2020, 114057, https://doi.org/10.1016/j.apenergy.2019.114057. **[ESI highly-cited paper, Q1, IF = 8.848]**

**Y. Zhou**, H. Li, A. Ravey, M.C. Péra, An integrated predictive energy management for light-duty range-extended plug-in fuel cell electric vehicle, ***Journal of Power Sources***, Volume 451, 2020, 227780, https://doi.org/10.1016/j.jpowsour.2020.227780. **[Q1, IF = 8.247]**

**Y. Zhou**, A. Ravey, M.C. Péra, Multi-objective energy management for fuel cell electric vehicles using online-learning enhanced Markov speed predictor, ***Energy conversion and Management***, Volume 213, 2020, 112821, https://doi.org/10.1016/j.enconman.2020.112821. **[Q1, IF = 8.208]**

H. Li, **Y. Zhou**, H. Gualous, H. Chaoui, L. Boulon, Optimal Cost Minimization Strategy for Fuel Cell Hybrid Electric Vehicles Based on Decision Making Framework, ***IEEE Transactions on Industrial Informatics***, doi: 10.1109/TII.2020.3003554. **[Q1, IF = 9.112]**

**Papers presented at international/national conferences:**

**Y. Zhou**, A. Ravey, M.C. Péra, Review and analysis of algorithms for the driving condition prediction and its applications, ***SYMPOSIUM DE GÉNIE ELECTRIQUE (SGE 2018)***, Jul. 2018, Nancy, France. [**Available online**]

**Y. Zhou**, A. Ravey, M.C. Péra, "A Velocity Prediction Method based on Self-Learning Multi-Step Markov Chain," ***IECON 2019 - 45th Annual Conference of the IEEE Industrial Electronics Society***,

Lisbon, Portugal, 2019, pp. 2598-2603. doi: 10.1109/IECON.2019.8927191. [**Available online**]

**Y. Zhou**, A. Ravey, M.C. Péra, Real-time Multi-Objective Energy Management for Fuel Cell Hybrid Electric Vehicles, ***IESES 2020 - IEEE 2ND International Conference on Industrial Electronics for Sustainable Energy Systems***, Cagliari, Italy, 2020. [**Accepted**]

**Y. Zhou**, A. Ravey, M.C. Péra, Operational cost analysis of fuel cell electric vehicles under different powertrain-sizing configurations, ***IEEE VPPC 2020 - The IEEE Vehicular Power and Propulsion Conference 2020***, Gijon, Spain, 2020. [**Accepted**]

## References


[1]. Guzzella L, Sciarretta A. Vehicle Propulsion systems: introduction to modeling and optimization. ***Berlin: Springer-Verlag***; 2005.

[2]. X. Lü, Y. Wu, J. Lian, Y. Zhang, C. Chen, P. Wang, L. Meng, Energy management of hybrid electric vehicles: A review of energy optimization of fuel cell hybrid power system based on genetic algorithm, ***Energy Conversion and Management***, Volume 205, 2020, 112474, https://doi.org/10.1016/j.enconman.2020.112474.

[3]. D. Tran, M. Vafaeipour, M.E. Baghdadi, R. Barrero, J.V. Mierlo, O. Hegazy, Thorough state-of-the-art analysis of electric and hybrid vehicle powertrains: Topologies and integrated energy management strategies, ***Renewable and Sustainable Energy Reviews***, Volume 119, 2020, 109596, https://doi.org/10.1016/j.rser.2019.109596.

[4]. M.C. Péra, D. Hissel, H. Gualous, C. Turpin. Electrochemical components. ***John Wiley & Sons, Inc.*** 2013.

[5]. A. Ravey, N. Watrin, B. Blunier, D. Bouquain, A. Miraoui, "Energy-Source-Sizing Methodology for Hybrid Fuel Cell Vehicles Based on Statistical Description of Driving Cycles," in ***IEEE Transactions on Vehicular Technology***, vol. 60, no. 9, pp. 4164-4174, Nov. 2011. doi: 10.1109/TVT.2011.2158567.

[6]. H.S. Das, C.W. Tan, A.H.M. Yatim, Fuel cell hybrid electric vehicles: A review on power conditioning units and topologies, ***Renewable and Sustainable Energy Reviews***, Volume 76, 2017, Pages 268-291, https://doi.org/10.1016/j.rser.2017.03.056.

[7]. H. Li. Energy consumption minimization strategy for fuel cell hybrid electric vehicles. ***PhD Thesis. Université Bourgogne Franche-Comté***, 2018. English. NNT: 2018UBFCA034. tel-02084175. https://tel.archives-ouvertes.fr/tel-02084175.

[8]. D. Zhou, A. Al-Durra, K. Zhang, A. Ravey, F. Gao, Online remaining useful lifetime prediction of proton exchange membrane fuel cells using a novel robust methodology, ***Journal of Power Sources***, Volume 399, 2018, Pages 314-328, https://doi.org/10.1016/j.jpowsour.2018.06.098.

[9]. N. Sulaiman, M.A. Hannan, A. Mohamed, P.J. Ker, E.H. Majlan, W. Daud, Optimization of energy management system for fuel-cell hybrid electric vehicles: Issues and recommendations, ***Applied Energy***, Vol. 228, 2018, Pages 2061-2079, https://doi.org/10.1016/j.apenergy.2018.07.087.

[10]. C.H. Zheng, G.Q. Xu, Y.I. Park, W.S. Lim, S.W. Cha, Prolonging fuel cell stack lifetime based on Pontryagin's Minimum Principle in fuel cell hybrid vehicles and its economic influence evaluation, ***Journal of Power Sources***, Vol. 248, 2014, Pages 533-544, https://doi.org/10.1016/j.jpowsour.2013.09.110.

[11]. M. Yue, S. Jemei, R. Gouriveau, N. Zerhouni, Review on health-conscious energy management strategies for fuel cell hybrid electric vehicles: Degradation models and strategies, ***International Journal of Hydrogen Energy***, Volume 44, Issue 13, 2019, Pages 6844-6861, https://doi.org/10.1016/j.ijhydene.2019.01.190.

[12]. D. Zhou, A. Durra, F. Gao, A. Ravey, I. Matraji, M. G. Simões, Online energy management strategy of fuel cell hybrid electric vehicles based on data fusion approach, ***Journal of Power Sources***, Volume 366, 2017, Pages 278-291, https://doi.org/10.1016/j.jpowsour.2017.08.107.

[13]. T. Fletcher, R. Thring, M. Watkinson, An Energy Management Strategy to concurrently optimize fuel consumption & PEM fuel cell lifetime in a hybrid vehicle, ***International Journal of Hydrogen Energy***, Volume 41, Issue 46, 2016, Pages 21503-21515, https://doi.org/10.1016/j.ijhydene.2016.08.157.

[14]. X. Hu, C. Zou, X. Tang, T. Liu and L. Hu, "Cost-Optimal Energy Management of Hybrid Electric Vehicles Using Fuel Cell/Battery Health-Aware Predictive Control," in ***IEEE Transactions on Power Electronics***, vol.

35, no. 1, pp. 382-392, Jan. 2020. doi: 10.1109/TPEL.2019.2915675.
[15]. J. Wu, X. Yuan, J.J. Martin, H. Wang, D. Yang, J. Qiao, J. Ma, Proton exchange membrane fuel cell degradation under close to open-circuit conditions: Part I: In situ diagnosis, ***Journal of Power Sources***, Volume 195, Issue 4, 2010, Pages 1171-1176, https://doi.org/10.1016/j.jpowsour.2009.08.095.
[16]. L. Placca, R. Kouta, Fault tree analysis for PEM fuel cell degradation process modelling, ***International Journal of Hydrogen Energy***, Volume 36, Issue 19, 2011, Pages 12393-12405, https://doi.org/10.1016/j.ijhydene.2011.06.093.
[17]. Avakov, V.B., Bogdanovskaya, V.A., Kapustin, A.V. et al. Lifetime prediction for the hydrogen–air fuel cells. ***Russian Journal of Electrochemistry***, Vol. 51, 2015, Pages 570–586. https://doi.org/10.1134/S1023193515060026.
[18]. X. Yuan, H. Li, S. Zhang, J. Martin, H. Wang, A review of polymer electrolyte membrane fuel cell durability test protocols, ***Journal of Power Sources***, Volume 196, Issue 22, 2011, Pages 9107-9116, https://doi.org/10.1016/j.jpowsour.2011.07.082.
[19]. S. Zhang, X. Yuan, H. Wang, W. Mérida, H. Zhu, J. Shen, S. Wu, J. Zhang, A review of accelerated stress tests of MEA durability in PEM fuel cells, ***International Journal of Hydrogen Energy***, Volume 34, Issue 1, 2009, Pages 388-404, https://doi.org/10.1016/j.ijhydene.2008.10.012.
[20]. J. Sun, I. V. Kolmanovsky, "Load governor for fuel cell oxygen starvation protection: a robust nonlinear reference governor approach," in ***IEEE Transactions on Control Systems Technology***, vol. 13, no. 6, pp. 911-920, Nov. 2005. doi: 10.1109/TCST.2005.854323.
[21]. H. Wang, Q. Wang, B. Hu, A review of developments in energy storage systems for hybrid excavators, ***Automation in Construction***, Volume 80, 2017, Pages 1-10, https://doi.org/10.1016/j.autcon.2017.03.010.
[22]. L. Lu, X. Han, J. Li, J. Hua, M. Ouyang, A review on the key issues for lithium-ion battery management in electric vehicles, ***Journal of Power Sources***, Volume 226, 2013, Pages 272-288, https://doi.org/10.1016/j.jpowsour.2012.10.060.
[23]. S. Ma, M. Jiang, P. Tao, C. Song, J. Wu, J. Wang, T. Deng, W. Shang, Temperature effect and thermal impact in lithium-ion batteries: A review, ***Progress in Natural Science: Materials International***, Vol. 28, Issue 6, 2018, Pages 653-666, https://doi.org/10.1016/j.pnsc.2018.11.002.
[24]. Y. Ji, Y. Zhang, C. Wang, Li-Ion Cell operation at low temperatures, ***Journal of the electrochemical society***, Vol. 160, Issue 4, Pages: 636-649, 2013, https://doi.org/10.1149/2.047304jes.
[25]. H.-C. (Alex) Shiao, D. Chua, H. Lin, S. Slane, M. Salomon, Low temperature electrolytes for Li-ion PVDF cells, ***Journal of Power Sources***, Volume 87, Issues 1–2, 2000, Pages 167-173, https://doi.org/10.1016/S0378-7753(99)00470-X.
[26]. G. Ning, Bala Haran, Branko N. Popov, Capacity fade study of lithium-ion batteries cycled at high discharge rates, ***Journal of Power Sources***, Volume 117, Issues 1–2, 2003, Pages 160-169, https://doi.org/10.1016/S0378-7753(03)00029-6.
[27]. Y. Zhang, C. Wang, X. Tang, Cycling degradation of an automotive LiFePO4 lithium-ion battery, ***Journal of Power Sources,*** Volume 196, Issue 3, 2011, Pages 1513-1520, https://doi.org/10.1016/j.jpowsour.2010.08.070.
[28]. Q. Wang, P. Ping, X. Zhao, G. Chu, J. Sun, C. Chen, Thermal runaway caused fire and explosion of lithium ion battery, ***Journal of Power Sources***, Volume 208, 2012, Pages 210-224, https://doi.org/10.1016/j.jpowsour.2012.02.038.
[29]. S. S. Choi, H. S. Lim, Factors that affect cycle-life and possible degradation mechanisms of a Li-ion cell based on LiCoO2, ***Journal of Power Sources***, Volume 111, Issue 1, 2002, Pages 130-136, https://doi.org/10.1016/S0378-7753(02)00305-1.
[30]. A. Biswas, A. Emadi, "Energy Management Systems for Electrified Powertrains: State-of-the-Art Review and Future Trends," in ***IEEE Transactions on Vehicular Technology***, vol. 68, no. 7, pp. 6453-6467, July 2019. doi: 10.1109/TVT.2019.2914457.
[31]. S. D. Farrall, R. P. Jones, "Energy management in an automotive electric/heat engine hybrid powertrain using fuzzy decision making," ***Proceedings of 8th IEEE International Symposium on Intelligent Control***, Chicago, IL, USA, 1993, pp. 463-468. doi: 10.1109/ISIC.1993.397669.
[32]. C. Lin, H. Peng, J. W. Grizzle, Jun-Mo Kang, "Power management strategy for a parallel hybrid electric truck," in ***IEEE Transactions on Control Systems Technology***, vol. 11, no. 6, pp. 839-849, Nov. 2003. doi:

10.1109/TCST.2003.815606.
[33]. A. Piccolo, L. Ippolito, V. zo Galdi, A. Vaccaro, "Optimization of energy flow management in hybrid electric vehicles via genetic algorithms," ***2001 IEEE/ASME International Conference on Advanced Intelligent Mechatronics***. Proceedings (Cat. No.01TH8556), Como, Italy, 2001, pp. 434-439 vol.1. doi: 10.1109/AIM.2001.936493.
[34]. Laura V. Pérez, Guillermo R. Bossio, Diego Moitre, Guillermo O. García, Optimization of power management in a hybrid electric vehicle using dynamic programming, ***Mathematics and Computers in Simulation***, Volume 73, Issues 1–4, 2006, Pages 244-254, https://doi.org/10.1016/j.matcom.2006.06.016.
[35]. A. Sciarretta, M. Back and L. Guzzella, "Optimal control of parallel hybrid electric vehicles," in ***IEEE Transactions on Control Systems Technology***, vol. 12, no. 3, pp. 352-363, May 2004. doi: 10.1109/TCST.2004.824312.
[36]. J. Park et al., "Intelligent Vehicle Power Control Based on Machine Learning of Optimal Control Parameters and Prediction of Road Type and Traffic Congestion," in ***IEEE Transactions on Vehicular Technology***, vol. 58, no. 9, pp. 4741-4756, Nov. 2009. doi: 10.1109/TVT.2009.2027710.
[37]. C. Lin, H. Peng, J. W. Grizzle, "A stochastic control strategy for hybrid electric vehicles," ***Proceedings of the 2004 American Control Conference***, Boston, MA, USA, 2004, pp. 4710-4715 vol.5. doi: 10.23919/ACC.2004.1384056.
[38]. Opila, D. F., Wang, X., McGee, R., and Grizzle, J. W., "Real-Time Implementation and Hardware Testing of a Hybrid Vehicle Energy Management Controller Based on Stochastic Dynamic Programming." ***Journal of Dynamic Systems, Measurement, and Control***. March 2013; 135(2): 021002. https://doi.org/10.1115/1.4007238.
[39]. V. Sezer, M. Gokasan and S. Bogosyan, "A Novel ECMS and Combined Cost Map Approach for High-Efficiency Series Hybrid Electric Vehicles," in ***IEEE Transactions on Vehicular Technology***, vol. 60, no. 8, pp. 3557-3570, Oct. 2011. doi: 10.1109/TVT.2011.2166981.
[40]. Y. L. Murphey et al., "Intelligent Hybrid Vehicle Power Control—Part II: Online Intelligent Energy Management," in ***IEEE Transactions on Vehicular Technology***, vol. 62, no. 1, pp. 69-79, Jan. 2013. doi: 10.1109/TVT.2012.2217362.
[41]. A. Taghavipour, N. L. Azad, J. Mcphee, "An optimal power management strategy for power-split plug-in hybrid electric vehicles," ***International Journal of Vehicle Design***. Vol. 604, no. 34, pp. 286–304, 2012.
[42]. T. Nüesch, M. Wang, P. Isenegger, C. H. Onder, R. Steiner, P. Macri-Lassus, L. Guzzella, Optimal energy management for a diesel hybrid electric vehicle considering transient PM and quasi-static NOx emissions, ***Control Engineering Practice***, Volume 29, 2014, Pages 266-276, https://doi.org/10.1016/j.conengprac.2014.01.020.
[43]. X. Lin, Y. Wang, P. Bogdan, N. Chang, M. Pedram, "Reinforcement learning based power management for hybrid electric vehicles," ***2014 IEEE/ACM International Conference on Computer-Aided Design (ICCAD)***, San Jose, CA, 2014, pp. 33-38. doi: 10.1109/ICCAD.2014.7001326.
[44]. J. Hou, Z. Song, A hierarchical energy management strategy for hybrid energy storage via vehicle-to-cloud connectivity, ***Applied Energy***, Volume 257, 2020, 113900, https://doi.org/10.1016/j.apenergy.2019.113900.
[45]. Y. Huang, H. Wang, A. Khajepour, H. He, J. Ji, Model predictive control power management strategies for HEVs: A review, ***Journal of Power Sources***, Vol. 341, 2017, Pages 91-106, https://doi.org/10.1016/j.jpowsour.2016.11.106.
[46]. Y. Zhou, A. Ravey, M.C. Péra, A survey on driving prediction techniques for predictive energy management of plug-in hybrid electric vehicles, ***Journal of Power Sources***, Volume 412, 2019, Pages 480-495, https://doi.org/10.1016/j.jpowsour.2018.11.085.
[47]. H. Achour, A.G. Olabi, Driving cycle developments and their impacts on energy consumption of transportation, ***Journal of Cleaner Production***, Vol. 112, Part 2, 2016, Pages 1778-1788, https://doi.org/10.1016/j.jclepro.2015.08.007.
[48]. G. P. Zhang, Time series forecasting using a hybrid ARIMA and neural network model, ***Neurocomputing***, Vol. 50, 2003, Pages 159-175, ISSN 0925-2312, https://doi.org/10.1016/S0925-2312(01)00702-0.
[49]. C. Sun, X. Hu, S. J. Moura, F. Sun, "Velocity Predictors for Predictive Energy Management in Hybrid Electric Vehicles," in ***IEEE Transactions on Control Systems Technology***, vol. 23, no. 3, pp. 1197-1204, May 2015. doi: 10.1109/TCST.2014.2359176.

[50]. Liu, K., Asher, Z., Gong, X., Huang, M. et al., "Vehicle Velocity Prediction and Energy Management Strategy Part 1: Deterministic and Stochastic Vehicle Velocity Prediction Using Machine Learning," ***SAE Technical Paper,*** 2019-01-1051, 2019, https://doi.org/10.4271/2019-01-1051.

[51]. D. P. Filev, I. Kolmanovsky, "Generalized Markov Models for Real-Time Modeling of Continuous Systems," in ***IEEE Transactions on Fuzzy Systems***, vol. 22, no. 4, pp. 983-998, Aug. 2014. doi: 10.1109/TFUZZ.2013.2279535.

[52]. H. A. Borhan, A. Vahidi, A. M. Phillips, M. L. Kuang, I. V. Kolmanovsky, "Predictive energy management of a power-split hybrid electric vehicle," ***2009 American Control Conference***, St. Louis, MO, 2009, pp. 3970-3976. doi: 10.1109/ACC.2009.5160451.

[53]. Z. Lei, D. Sun, J. Liu, D. Chen, Y. Liu, Z. Chen, "Trip-Oriented Model Predictive Energy Management Strategy for Plug-in Hybrid Electric Vehicles," in ***IEEE Access***, vol. 7, pp. 113771-113785, 2019. doi: 10.1109/ACCESS.2019.2933015.

[54]. L. Guo, B. Gao, Y. Gao, H. Chen, "Optimal Energy Management for HEVs in Eco-Driving Applications Using Bi-Level MPC," in ***IEEE Transactions on Intelligent Transportation Systems***, vol. 18, no. 8, pp. 2153-2162, Aug. 2017. doi: 10.1109/TITS.2016.2634019.

[55]. S. Kelouwani, N. Henao, K. Agbossou, Y. Dube, L. Boulon, "Two-Layer Energy-Management Architecture for a Fuel Cell HEV Using Road Trip Information," in ***IEEE Transactions on Vehicular Technology***, vol. 61, no. 9, pp. 3851-3864, Nov. 2012. doi: 10.1109/TVT.2012.2214411.

[56]. C. Sun, S. J. Moura, X. Hu, J. K. Hedrick, F. Sun, "Dynamic Traffic Feedback Data Enabled Energy Management in Plug-in Hybrid Electric Vehicles," in ***IEEE Transactions on Control Systems Technology***, vol. 23, no. 3, pp. 1075-1086, May 2015. doi: 10.1109/TCST.2014.2361294.

[57]. X. Zeng, J. Wang, "A Parallel Hybrid Electric Vehicle Energy Management Strategy Using Stochastic Model Predictive Control With Road Grade Preview," in ***IEEE Transactions on Control Systems Technology***, vol. 23, no. 6, pp. 2416-2423, Nov. 2015. doi: 10.1109/TCST.2015.2409235.

[58]. S. Zhang, Y. Luo, K. Li, J. Wang, "Predictive energy management strategy for fully electric vehicles based on hybrid model predictive control," ***2017 American Control Conference (ACC)***, Seattle, WA, 2017, pp. 3625-3630. doi: 10.23919/ACC.2017.7963508.

[59]. C. Marina Martinez, M. Heucke, F. Wang, B. Gao, D. Cao, "Driving Style Recognition for Intelligent Vehicle Control and Advanced Driver Assistance: A Survey," in ***IEEE Transactions on Intelligent Transportation Systems***, vol. 19, no. 3, pp. 666-676, March 2018. doi: 10.1109/TITS.2017.2706978.

[60]. Y. L. Murphey et al., "Neural learning of driving environment prediction for vehicle power management," ***2008 IEEE International Joint Conference on Neural Networks***, Hong Kong, 2008, pp. 3755-3761. doi: 10.1109/IJCNN.2008.4634337.

[61]. C. Zhang, A. Vahidi, P. Pisu, X. Li, K. Tennant, "Role of Terrain Preview in Energy Management of Hybrid Electric Vehicles," in ***IEEE Transactions on Vehicular Technology***, vol. 59, no. 3, pp. 1139-1147, March 2010. doi: 10.1109/TVT.2009.2038707.

[62]. B. Asadi, A. Vahidi, "Predictive Cruise Control: Utilizing Upcoming Traffic Signal Information for Improving Fuel Economy and Reducing Trip Time," in ***IEEE Transactions on Control Systems Technology***, vol. 19, no. 3, pp. 707-714, May 2011. doi: 10.1109/TCST.2010.2047860.

[63]. S. Xie, X. Hu, Z. Xin, L. Li, "Time-Efficient Stochastic Model Predictive Energy Management for a Plug-In Hybrid Electric Bus With an Adaptive Reference State-of-Charge Advisory," in ***IEEE Transactions on Vehicular Technology***, vol. 67, no. 7, pp. 5671-5682, July 2018. doi: 10.1109/TVT.2018.2798662.

[64]. M. Sivertsson, L. Eriksson. Design and evaluation of energy management using map-based ECMS for the PHEV benchmark. ***Oil & Gas Science and Technology***, Vol. 70, No. 1, Jan 2014. https://doi.org/10.2516/ogst/2014018.

[65]. G. Li, J. Zhang, H. He, Battery SOC constraint comparison for predictive energy management of plug-in hybrid electric bus, ***Applied Energy***, Volume 194, 2017, Pages 578-587, https://doi.org/10.1016/j.apenergy.2016.09.071.

[66]. H. Tian, X. Wang, Z. Lu, Y. Huang, G. Tian, "Adaptive Fuzzy Logic Energy Management Strategy Based on Reasonable SOC Reference Curve for Online Control of Plug-in Hybrid Electric City Bus," in ***IEEE Transactions on Intelligent Transportation Systems***, vol. 19, no. 5, pp. 1607-1617, May 2018. doi: 10.1109/TITS.2017.2729621.

[67]. H. Tian, S. E. Li, X. Wang, Y. Huang, G. Tian, Data-driven hierarchical control for online energy management of plug-in hybrid electric city bus, ***Energy***, Volume 142, 2018, Pages 55-67, https://doi.org/10.1016/j.energy.2017.09.061.

[68]. He T., Z. Lu, X. Wang, X. Zhang, Y. Huang, G. Tian, A length ratio based neural network energy management strategy for online control of plug-in hybrid electric city bus, ***Applied Energy***, Volume 177, 2016, Pages 71-80, https://doi.org/10.1016/j.apenergy.2016.05.086.

[69]. M. Montazeri-Gh, Z. Pourbafarani, "Near-Optimal SOC Trajectory for Traffic-Based Adaptive PHEV Control Strategy," in ***IEEE Transactions on Vehicular Technology***, vol. 66, no. 11, pp. 9753-9760, Nov. 2017. doi: 10.1109/TVT.2017.2757604.

[70]. D. Hou, Q. Sun, C. Bao, X. Cheng, H. Guo, Y. Zhao, An all-in-one design method for plug-in hybrid electric buses considering uncertain factor of driving cycles, ***Applied Energy***, Volume 253, 2019, 113499, https://doi.org/10.1016/j.apenergy.2019.113499.

[71]. H. Guo, S. Lu, H. Hui, C. Bao, J. Shangguan, Receding horizon control-based energy management for plug-in hybrid electric buses using a predictive model of terminal SOC constraint in consideration of stochastic vehicle mass, ***Energy***, Volume 176, 2019, Pages 292-308, https://doi.org/10.1016/j.energy.2019.03.192.

[72]. S. Zhang, R. Xiong, Adaptive energy management of a plug-in hybrid electric vehicle based on driving pattern recognition and dynamic programming, ***Applied Energy***, Volume 155, 2015, Pages 68-78, https://doi.org/10.1016/j.apenergy.2015.06.003.

[73]. A. Ravey, B. Blunier, A. Miraoui, "Control Strategies for Fuel-Cell-Based Hybrid Electric Vehicles: From Offline to Online and Experimental Results," in ***IEEE Transactions on Vehicular Technology***, vol. 61, no. 6, pp. 2452-2457, July 2012. doi: 10.1109/TVT.2012.2198680.

[74]. Y. Zhou, A. Ravey, M.C. Péra, Multi-mode predictive energy management for fuel cell hybrid electric vehicles using Markov driving pattern recognizer, ***Applied Energy***, Volume 258, 2020, 114057, https://doi.org/10.1016/j.apenergy.2019.114057.

[75]. K. Song, F. Li, X. Hu, l. He, W. Niu, S. Lu, T. Zhang, Multi-mode energy management strategy for fuel cell electric vehicles based on driving pattern identification using learning vector quantization neural network algorithm, ***Journal of Power Sources***, Volume 389, 2018, Pages 230-239, https://doi.org/10.1016/j.jpowsour.2018.04.024.

[76]. R. Zhang, J. Tao, H. Zhou, "Fuzzy Optimal Energy Management for Fuel Cell and Supercapacitor Systems Using Neural Network Based Driving Pattern Recognition," in ***IEEE Transactions on Fuzzy Systems***, vol. 27, no. 1, pp. 45-57, Jan. 2019. doi: 10.1109/TFUZZ.2018.2856086.

[77]. F. Soriano, M. Moreno-Eguilaz, J. Álvarez-Flórez, "Drive Cycle Identification and Energy Demand Estimation for Refuse-Collecting Vehicles," in ***IEEE Transactions on Vehicular Technology***, vol. 64, no. 11, pp. 4965-4973, Nov. 2015. doi: 10.1109/TVT.2014.2382591.

[78]. X. Li, Y. W., D. Yang, Z. Chen, Adaptive energy management strategy for fuel cell/battery hybrid vehicles using Pontryagin's Minimal Principle, ***Journal of Power Sources***, Volume 440, 2019, 227105, https://doi.org/10.1016/j.jpowsour.2019.227105.

[79]. X. Huang, Y. Tan, X. He, "An Intelligent Multifeature Statistical Approach for the Discrimination of Driving Conditions of a Hybrid Electric Vehicle," in ***IEEE Transactions on Intelligent Transportation Systems***, vol. 12, no. 2, pp. 453-465, June 2011. doi: 10.1109/TITS.2010.2093129.

[80]. J. Guo, H. He and C. Sun, "ARIMA-Based Road Gradient and Vehicle Velocity Prediction for Hybrid Electric Vehicle Energy Management," in ***IEEE Transactions on Vehicular Technology***, vol. 68, no. 6, pp. 5309-5320, June 2019. doi: 10.1109/TVT.2019.2912893.

[81]. Frank A. Bender, Hakan Uzuner, Oliver Sawodny, An Adaptive Driver Model for Driving Cycle Prediction in the Intelligent Truck, ***IFAC Proceedings Volumes***, Volume 47, Issue 3, 2014, Pages 10682-10687, https://doi.org/10.3182/20140824-6-ZA-1003.00285.

[82]. V. Larsson, L. Johannesson Mårdh, B. Egardt, S. Karlsson, "Commuter Route Optimized Energy Management of Hybrid Electric Vehicles," in ***IEEE Transactions on Intelligent Transportation Systems***, vol. 15, no. 3, pp. 1145-1154, June 2014. doi: 10.1109/TITS.2013.2294723.

[83]. S. Kermani, S. Delprat, T.M. Guerra, R. Trigui, B. Jeanneret, Predictive energy management for hybrid vehicle, ***Control Engineering Practice***, Volume 20, Issue 4, 2012, Pages 408-420, https://doi.org/10.1016/j.conengprac.2011.12.001.

[84]. Z. Wei, J. Xu, D. Halim, HEV power management control strategy for urban driving, ***Applied Energy***, Volume 194, 2017, Pages 705-714, https://doi.org/10.1016/j.apenergy.2016.10.023.

[85]. Y. Zhou, H. Li, A. Ravey, M.C. Péra, An integrated predictive energy management for light-duty range-extended plug-in fuel cell electric vehicle, ***Journal of Power Sources***, Volume 451, 2020, 227780, https://doi.org/10.1016/j.jpowsour.2020.227780.

[86]. H. Borhan, A. Vahidi, A. M. Phillips, M. L. Kuang, I. V. Kolmanovsky, S. Di Cairano, "MPC-Based Energy Management of a Power-Split Hybrid Electric Vehicle," in ***IEEE Transactions on Control Systems Technology***, vol. 20, no. 3, pp. 593-603, May 2012. doi: 10.1109/TCST.2011.2134852.

[87]. S. Di Cairano, W. Liang, I. V. Kolmanovsky, M. L. Kuang, A. M. Phillips, "Power Smoothing Energy Management and Its Application to a Series Hybrid Powertrain," in ***IEEE Transactions on Control Systems Technology***, vol. 21, no. 6, pp. 2091-2103, Nov. 2013. doi: 10.1109/TCST.2012.2218656.

[88]. S. D. Cairano, D. Bernardini, A. Bemporad, I. V. Kolmanovsky, "Stochastic MPC With Learning for Driver-Predictive Vehicle Control and its Application to HEV Energy Management," in ***IEEE Transactions on Control Systems Technology***, vol. 22, no. 3, pp. 1018-1031, May 2014. doi: 10.1109/TCST.2013.2272179.

[89]. Y. Zhou, A. Ravey, M. Pera, "A Velocity Prediction Method based on Self-Learning Multi-Step Markov Chain," ***IECON 2019 - 45th Annual Conference of the IEEE Industrial Electronics Society***, Lisbon, Portugal, 2019, pp. 2598-2603. doi: 10.1109/IECON.2019.8927191.

[90]. H. Xie et al., "A Hybrid Method Combining Markov Prediction and Fuzzy Classification for Driving Condition Recognition," in ***IEEE Transactions on Vehicular Technology***, vol. 67, no. 11, pp. 10411-10424, Nov. 2018. doi: 10.1109/TVT.2018.2868965.

# Chapter 2. Comparative study on energy management strategy for fuel cell electric vehicles

## 2.1. Introduction

Based on the discussions in **Chapter 1**, it is clear that the objective of this PhD thesis is to devise energy management strategies (EMS) for fuel cell/battery-based hybrid electric vehicles. Specifically, two different vehicle architectures are studied, namely fuel cell-based hybrid electric vehicles (FCHEVs) and fuel cell-based plug-in hybrid electric vehicles (FCPHEVs).

Due to their structural discrepancies, the major objectives of their control strategies are also different. Regarding the EMSs of FCHEVs, one of the important control objectives is to maintain the final battery state-of-charge (SoC) the same as or approximate to its initial value, since the onboard battery cannot be recharged via external grid power when trip ends. In contrast, since the battery of FCPHEVs can be recharged via the onboard charger, the EMSs attempt to use the cost-effective electricity power stored in battery for vehicle propulsion and balance its embedding cost. Due to the depletion of battery energy, there is normally an obvious discrepancy between the initial and the final battery SoC over the trip. Hence, the primary task for EMSs of FCPHEVs is to anticipate and control the decline of battery SoC, since the global optimal fuel economy is closely related to the way of battery energy usage.

Furthermore, existing EMSs diverge significantly in terms of the online computation efficiency and the optimal control performance. Therefore, how to choose a proper control framework to facilitate online optimization with reasonable computation efforts should be carefully considered. Moreover, another essential issue is to explore the potential EMS performance improvement imposed by predictive information integration, compared to conventional non-predictive EMSs. Hence, whether the selected control framework is convenient for predictive information integration, and whether it is capable of compensating for the performance losses imposed by mis-predictions should also be further evaluated.

**Chapter 2** presents a detailed comparative study on the state-of-the-art EMSs for FCHEVs/FCPHEVs, so as to help select the most appropriate control framework to realize the predictive energy management strategy (PEMS). Specifically, the structure of this chapter is given as follows: subsection 2.2 classifies the existing EMSs into three groups, illustrates their basic working principle, and then compares the benefits and drawbacks of each type of EMS. In subsection 2.3, the general theory of model predictive control (MPC) and its application in the vehicular EMS field are analyzed. Subsection 2.4 briefs the major conclusions in the end.

## 2.2. State-of-the-art review on energy management strategies

As depicted in figure 2.1, EMSs for FCHEVs can be categorized into rule-based, global optimization-based and real-time optimization-based strategies. Rule-based strategy constitutes of a series predefined deterministic (or fuzzy) rules. These rules for power allocation are largely designed based on human intuition, engineering experience or expertise knowledge, and seldom with the help of future driving cycle knowledge [1]. In contrast, global optimization-based strategy derives the optimal power distribution decisions based on the complete driving cycle knowledge *a priori*. Although the global optimal results cannot be directly applied to real-time control, they are still valuable in terms of multi-parametric tuning [2] and offline benchmarking [3]. Due to the inaccessibility of the fully previewed route information in practice, real-time optimization-based strategy leads to local optimal results, and it derives control actions by minimizing the performance index concerning the instantaneous power demand or the forecasted power profile over the finite time horizon. Equivalent consumption minimization strategy and model predictive control are two widely used real-time optimization-based strategies. In the following part of subsection 2.2, the principle of commonly used strategies in each category is introduced.

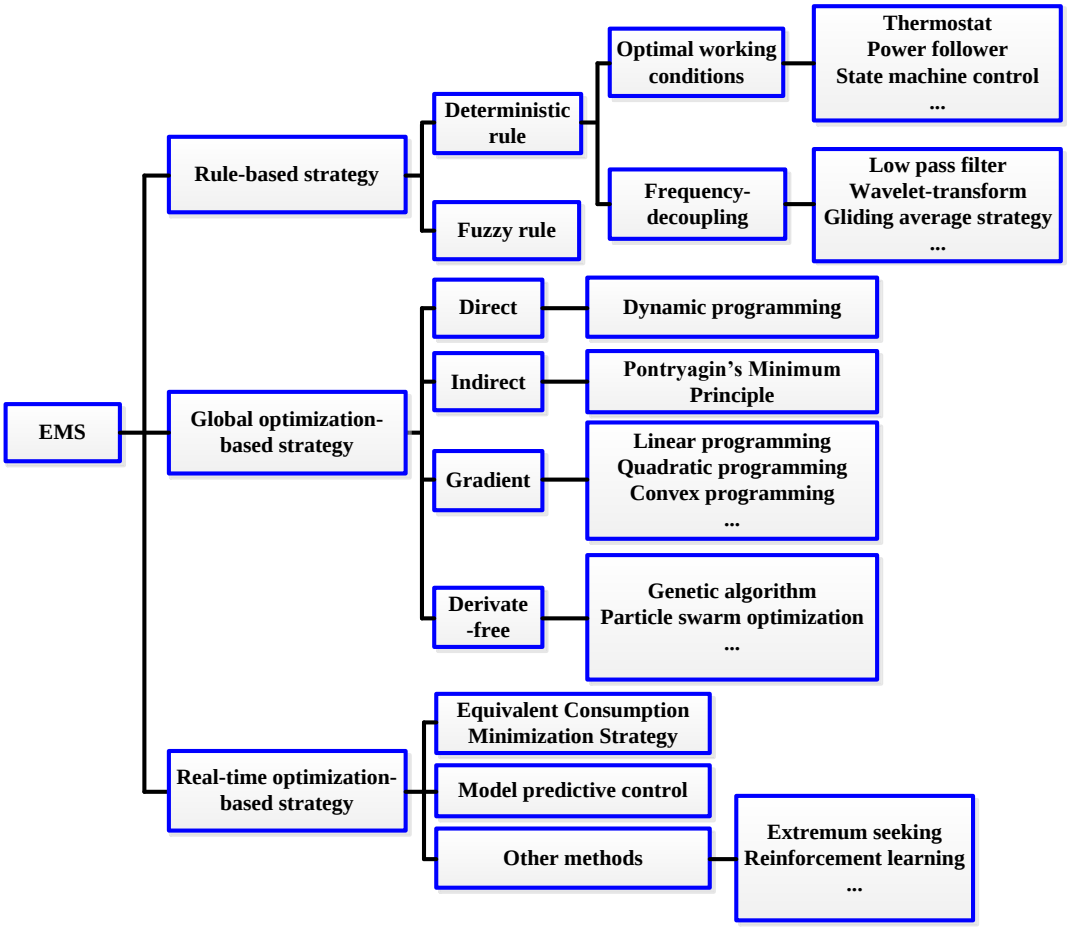


Figure 2.1. Classification of energy management strategies for fuel cell hybrid electric vehicles.

### 2.2.1. Rule-based strategies

Rule-based EMS can be further categorized into deterministic rule-based strategies and fuzzy rule-based strategies. The major advantage of this type of EMS lies in the simplicity and real-time suitability since the implementation of such control strategies requires no real-time optimization, but usually relies on the time-efficient ways, such as look-up table, state machine logic or on-off commands. Nevertheless, their deficiencies are also obvious: (a) the predefined rules can hardly bring the optimal or sub-optimal performance in realistic driving conditions, and (b) considerable parameter calibration efforts are needed towards the satisfied control performance.

#### 2.2.1.1. Deterministic rule-based strategies

Deterministic rule-based strategies split the required power demand among energy sources based on the preset rules extracted from the engineering experience. On the one hand, this type of strategies can be realized by urging the primary energy sources operating under their optimal working conditions (e.g. high efficiency region, etc.), so as to improve the overall fuel economy and reduce the vehicle's operation costs. On the other hand, frequency-decoupling control can also be used to achieve such power-splitting effect, wherein it coordinates the output behaviors of multiple energy sources based on frequency-separation results of original power demand signal. The working principle of several typical deterministic rule-based strategies are detailed as follows:

**Thermostat (on/off) strategy** controls fuel cell operating in on-off manner. The fuel cell turns on and works at its most efficient point [4], [5] or at the rated power point [6], when the battery state-of-charge (SoC) is below the preset lower threshold. When the battery SoC is higher than the upper threshold, the fuel cell shuts down. Normally, this strategy would lead to frequent fuel cell on-off cycles, especially in urban driving conditions, thus increasing the risk of fuel cell performance degradations [7].

**Power (load) follower strategy** controls the output power of fuel cell considering both the external power demand and the state of energy sources, where the rules for power allocation are set according to some heuristics rules and human reasoning. For example, when the power demand is high and battery SoC is low, fuel cell works towards its high-power level to meet the required power demand. When the power demand is low and SoC is high, fuel cell output power would be reduced and more propulsion power would be supplied by battery [8]. Moreover, based on the efficiency curve of fuel cell systems (FCS), the vehicle's powertrain can work under different operation modes. For example, figure 2.2 depicts the efficiency curve of a 45-kW FCS as a function of the net power of system [9]. Battery mode is activated when the FCS efficiency is extremely low ($P_{fc}$ < 5kW). When the FCS efficiency is in its optimal zone ($5\text{kW} < P_{fc} < 20\text{kW}$), the FCS is served as the primary mover (FCS mode). When $P_{fc} > 20\text{kW}$, the hybrid mode is triggered, where both energy sources work together for vehicle propulsion.

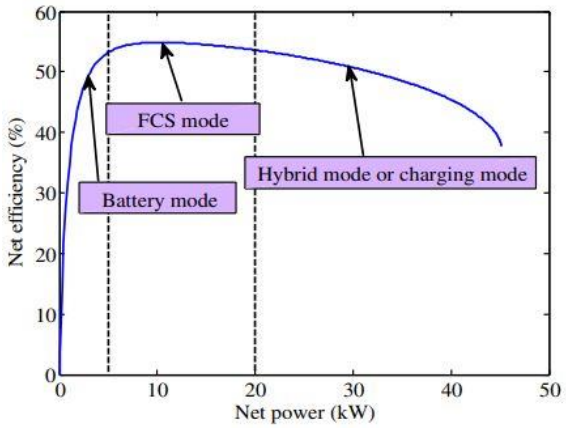


Figure 2.2. Representation of rule-based (power follower) strategy [9].

**State machine strategy (SMS)**, also known as multi-mode strategy, works on a specific operation or state of the vehicle using a flowchart or decision tree of the stationary conditions associated to the previous conditions and present input values. For instance, for a HEV propelled by a proton-exchange-membrane fuel cell (PEMFC) and a lithium-ion battery pack, Liangfei et al. in [10] have proposed a multi-mode real-time SMS-based EMS, which operates the FCS among three typical working states, namely start-up, shut-down and optimal power allocation processes. The FCS output power in start-up phases is determined by the dynamic heating process of the fuel cell system, while the FCS power in shut-down phase is calculated based on the maximal decreasing rate of fuel cell power. In optimal power allocation phase, the major EMS objective is to find a tradeoff decision among hydrogen consumption, battery SoC regulation and fuel cell degradation imposed by load dynamics. It should be mentioned that the transition among FCS operating states is determined by driver's acceleration/barking commands, and the status of electric machine, battery and fuel cell, as depicted in figure 2.3.

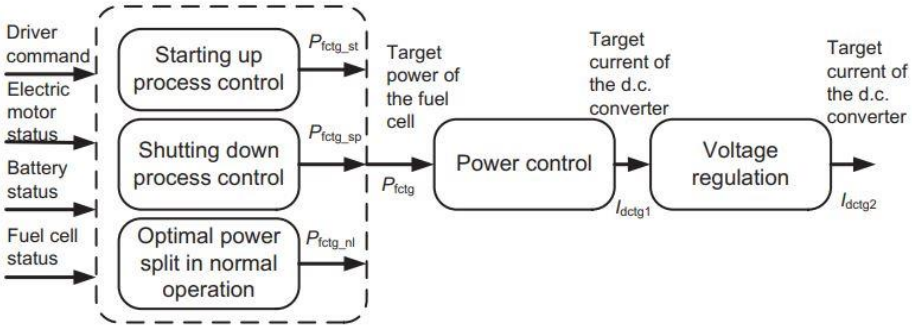


Figure 2.3. Control framework of the multi-mode SMS-based strategy [10].

Moreover, aiming at improving fuel efficiency without compromising the powertrain durability, a state machine-based EMS for a PEMFC-battery-supercapacitor hybrid tramway is reported in [11]. With the state defined as the SoC levels of battery and supercapacitor, the aim of state machine strategy is to decide the FCS reference power level with the state change. As shown in figure 2.4(a), according to the hysteresis cycles for SoC levels of batteries and supercapacitors, five operating states are defined to

facilitate the generation of the reference power signals for three energy sources in terms of power allocation. Moreover, as can be seen from figure 2.4(b), the transition from one state to another is triggered by certain conditions, which are denoted by the SoCs of batteries and supercapacitors. Thereafter, the PEMFC reference power in each state is determined based on the calculated DC bus power demand from droop control as well as the energy dissipation via the braking resistor.

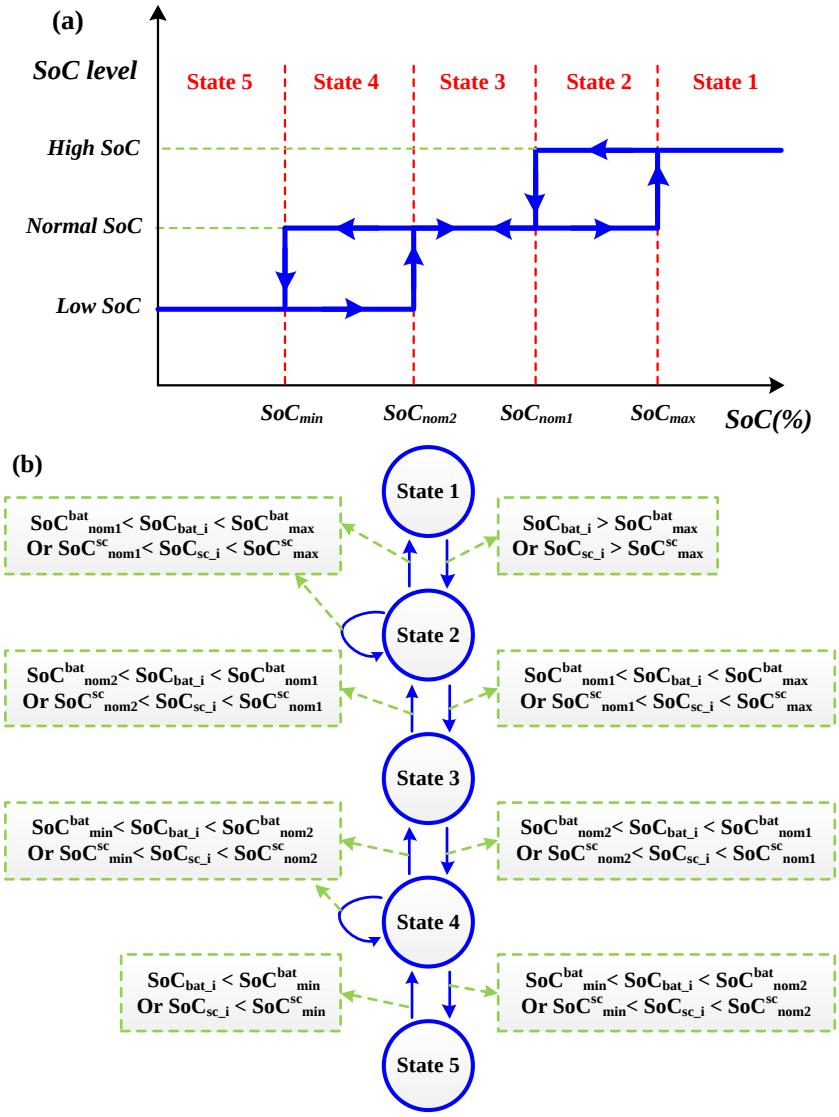


Figure 2.4. (a) Hysteresis cycles for SoC levels of batteries and supercapacitors and (b) state transition chart diagram of the SMS-based strategy [11].

**Frequency-decoupling strategy** splits the original power demand signal into low and high frequency components, and then allocates the low-frequency portion to the energy sources with relatively slow dynamic response (e.g. fuel cell), while utilizes the fast-dynamic power sources (e.g. battery or supercapacitor) to provide the high-frequency power requirement. Generally, low-pass filter [12], [13], moving average strategy [14] and wavelet-transform technique [15]-[17] can be used for signal frequency decoupling. For instance, the low-pass filter is used in the EMS of a fuel cell/battery-based

powertrain to release the burden of dynamic current demand on FCS [12]. Nevertheless, there is no general guidance on the setting of frequency decomposition depth of the low-pass filter and moving average strategy, leading to the trade-off of the battery SoC control performance (e.g. SoC variation range, final SoC value, etc.). Moreover, a wavelet transform (WT)-assisted rule-based control strategy is devised for a PEMFC-battery-supercapacitor HEV [15]. Figure 2.5 depicts the working principle of WT technique, which consists of signal decomposition and reconstruction phases. The symbols "g" and "h" respectively denote the coefficients for the high-pass and low-pass filters, the symbols "D" and "A" denote the detail signal and approximation signal components, respectively, and "*j*" is the signal decomposition level. The filter coefficients of detail and approximation are determined by Haar wavelet [15]. On this basis, the WT technique decomposes the original power demand signal into three levels, where the base frequency portion is assigned to fuel cell, the low and high frequency parts are assigned to battery and supercapacitor, respectively. With such power allocation, the proposed EMS not only can achieve efficient energy transfer but also can reduce the damage, caused by power rapid change and surge load, to the vehicular PEMFC system.

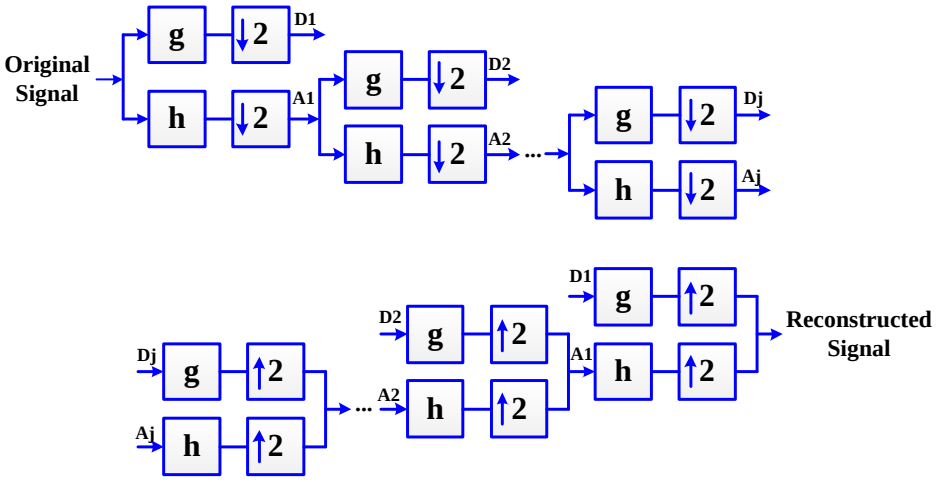


Figure 2.5. Schematic diagram of the wavelet transform: signal decomposition and reconstruction phases [15].

### 2.2.1.2. Fuzzy rule-based strategies

In contrast to Boolean logic ("true or false", "0,1" logic), fuzzy logic is capable of converting human experience into a series of IF-THEN rules, including five conversion stages: input quantization, fuzziness, fuzzy reasoning, de-fuzziness, and output quantification, as depicted in figure 2.6. Firstly, the original signal is converted into fuzzy values for each input fuzzy set by the fuzziness block. The universe of the input variables determines the required scaling for correct per-unit operation. Afterwards, the decision-making module determines how the fuzzy logic operations are performed, and together with the knowledge base determine the outputs of each IF-THEN rule. Finally, these are combined and then converted to the values with required scales by the de-fuzziness block [18].

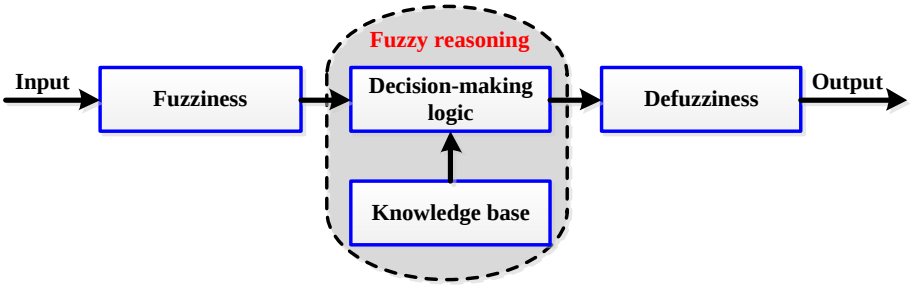


Figure 2.6. Block diagram of a fuzzy system.

The performance of fuzzy rule-based strategy is largely dependent on the formulation of fuzzy rules [18]. Since the fuzzy rules are extracted from the observation related to imprecise or non-numerical information, this type of strategy is thus independent of the precise system modelling, and such robustness makes it suitable for dealing with complex, nonlinear and time-varying systems, like vehicle propulsion system. For instance, Blunier et al. propose a fuzzy controller for a fuel cell/battery hybrid auxiliary power unit [18], aiming at fuel cell high efficiency utilization as well as keeping battery SoC within the predefined optimal zone. Moreover, a fuzzy controller is devised for a fuel cell/battery range-extended HEV [19], achieving the improved FCS working efficiency and the prolonged battery lifetime. To guarantee the normal operation of a FCHEV in powertrain degraded mode, the state-of-health of FCS is used as an additional input of fuzzy logic controller for coordinating the outputs of powertrain energy sources [20]. However, with manually-tuned fuzzy parameters, the basic fuzzy logic controllers could hardly lead to the optimal performance.

**Optimized fuzzy rules**: to improve the performance optimality of basic fuzzy rule based strategies, several optimization algorithms, like genetic algorithm (GA) [2], [21]-[24], teaching-learning based optimization [25], and direct algorithms [26], are adopted for optimally tuning the parameters of fuzzy membership function. For example, to improve the fuel economy performance, GA is adopted to tune multiple parameters of fuel cell current membership function for the basic fuzzy controller of a FCHEV [2]. Compared to a manually tuned fuzzy controller, the GA-optimized one can save more than 20% H2 consumption, thus indicating the effectiveness of genetic algorithm in multi-parametric tuning. Although these optimized fuzzy controllers can realize (near) optimal performance under one specific type of driving cycle, their performance could be degraded if the driving pattern changes [3]. Therefore, how to enhance their adaptability towards changeable driving conditions needs further investigations.

**Adaptive fuzzy rules**: to enhance the control adaptability, fuzzy rule-based strategies should be able to allocate power demand in different working scenarios (e.g. driving patterns [3], [27], fuel cell degradation levels [28], etc.). For example, as reported in [27], an adaptive fuzzy EMS combined with a neural network driving pattern recognizer is designed for a fuel cell/supercapacitor HEV, whose control framework is depicted in figure 2.7. In offline phase, the parameters of fuzzy membership functions and the adaptive coefficients are simultaneously optimized by genetic algorithm, aiming at

reducing H2 consumption and fuel cell current variation. In online phase, the power allocation decision of the basic fuzzy controller can be adjusted by the adaptive coefficients related to the pattern identification results, so as to adapt to the changeable driving patterns.

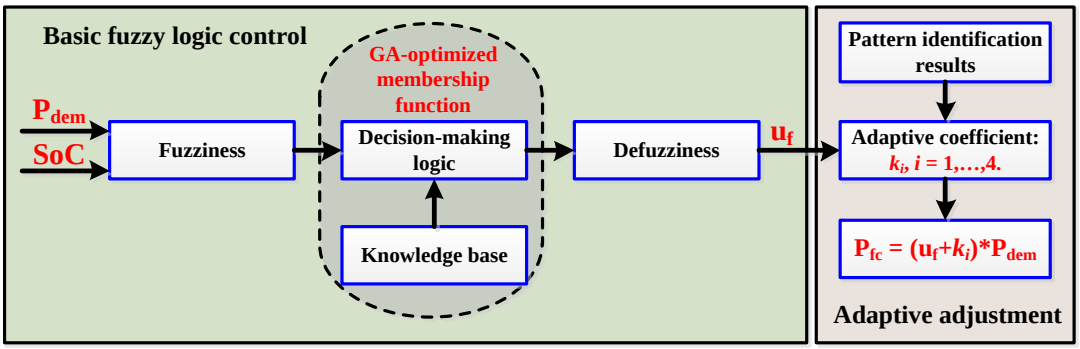


Figure 2.7. Framework of the adaptive fuzzy logic controller [27].

Moreover, a health-conscious EMS is proposed to realize power allocation for a light-duty FCHEV [28]. Fuzzy logic controllers are optimized offline by genetic algorithm under different FCS degradation states, and then, according to the periodically updated probabilistic classification results on fuel cell health states, offline-optimized fuzzy rules are aggregated for real-time control with the help of Dempster-Shafer theory. Validation results show that the proposed strategy can effectively improve the fuel cell lifetime by 56%, compared to a baseline fuzzy rule-based strategy.

In summary, the major advantage of rule-based strategies lies in their real-time practicality. However, their performance optimality could not be guaranteed under the realistic driving conditions.

### 2.2.2. Global optimization-based strategies

In contrast to rule-based strategies, global and real-time optimization-based strategies make power allocation decisions by optimizing the predefined performance index (or, objective/cost functions), while respecting the constraints imposed by the operating limitations on powertrain components.

Benefiting from the complete driving cycle knowledge *a priori*, global optimization-based strategies can solve the constrained optimization problems using a variety of algorithms. The cost function is a mathematical representation regarding the objectives that are expected to achieve by EMSs. Due to the discrepancies in terms of vehicle design purpose (e.g. racing cars or commercial cars) and powertrain structures (e.g. FC + Battery or FC + Supercapacitor), the formulation of cost function is also different. For example, the optimality is defined as to minimize the H2 mass consumption in [2], while the weighted sum of fuel cell current variation and H2 mass consumption is regarded as the optimal performance index in [23], [27]. Besides, the equality constraints are usually concerning the power balance equation and battery SoC dynamics, while the inequality constraints are largely used to specify the operation boundary of powertrain components. (e.g. the maximum fuel cell output power, etc.)

After the cost function and the constraints are specified, a proper algorithm is required to calculate the optimal control sequence. As indicated in [1], based on different types of problem-solving approaches, global optimization-based strategies can be further sub-categorized into four classes: direct, indirect, gradient and derivative-free. A classification of global optimization-based strategies (GOBS) is given in figure 2.8 using the problem-solving approaches as the criterion.

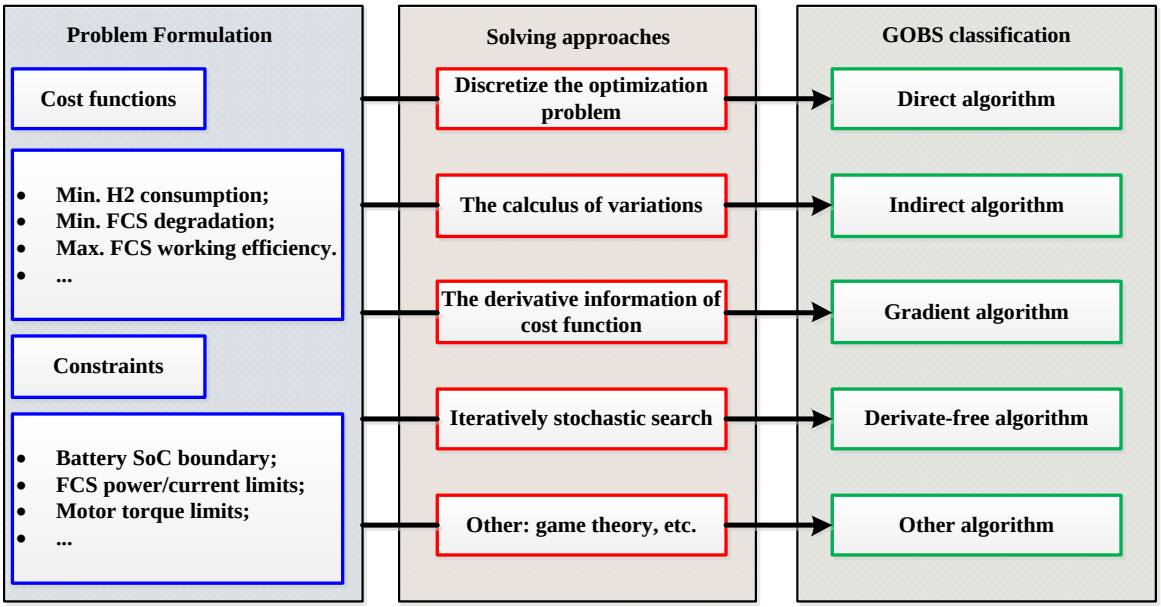


Figure 2.8. Classification of global optimization-based strategies based on problem-solving approaches [1].

**Direct algorithms**: Originally proposed by R. Bellman in 1950s, dynamic programming (DP), also known as deterministic DP (DDP), becomes one of the most representative direct algorithms to solve the EMS problem for HEVs. The basic idea of DP is to simplify the original complicated optimization problem by breaking it down into numerous simpler sub-problems. Specifically, DP evaluates the optimal cost-to-go function at every node in the discretized state-space domain by proceeding *backward* in time. Thereafter, in *forward* phase, the optimal control map attained in the *backward* phase is used to generate the optimal state trajectory, originating from a given initial state [29]. For example, Ravey et al. utilize DP to minimize the hydrogen consumption of a FCHEV over known driving cycles [2]. Moreover, Liangfei et al. use DP to minimize the operation cost of a FC-battery HEV, including the cost of H2 consumption, electricity consumption and final SoC deviation from the initial one [30]. Although DP can always lead to the global optimal performance, it cannot be directly applied to real-time control due to the following deficiencies: (a) the heavy computation burden for optima-searching imposed by the discretization of state and control variables, especially when a high discrete resolution is required; (b) the dependence on the complete driving cycle information beforehand. Despite these defects, the implementation of DP is still meaningful in terms of serving as the evaluation benchmark to other EMSs or as a powerful tool of multi-parametric tuning for rule-based strategies.

**Indirect algorithms**: Pontryagin's minimum principle (PMP), firstly introduced by Lev Pontryagin in

1956, is one of the commonly used indirectly algorithms to solve the global optimization problem in vehicular energy management field. PMP transforms the minimization of the cost function for global optimization problem into the minimization of local Hamiltonian [31]. The co-state is an important parameter of Hamiltonian function, which is usually interpreted as the equivalence factor between electricity energy consumption and primary fuel consumption (e.g. fossil fuel or H2). Only when the entire driving cycle information is available, the optimal value of initial co-state can be determined by the iterative calculation process. For instance, a PMP-based global optimal control strategy is devised for a FCHEV, which can minimize the H2 consumption over a given driving cycle [32]. Although PMP offers optimal or near-optimal solutions to constrained nonlinear optimization problems, it also suffers from heavy memory and computation burdens as DP does, thus making it impossible to be directly applied to real-time control.

**Gradient algorithms**: As analyzed previously, both direct and indirect algorithms suffer from heavy computation burdens. This is due to the complexity of optimization problems (e.g. nonlinearity of cost function and constraints), which are imposed by the nonlinearities of powertrain models. To mitigate such computation burdens, researchers attempt to simplify the original optimization problem, such as approximating the nonlinear cost terms/constraints by linear, piecewise linear or quadratic forms, so as to obtain the analytical solutions by the gradient algorithms. Therefore, gradient algorithms take advantage of the derivative information of analytical cost functions (which satisfy some specific mathematical conditions, like the continuity, differentiability, etc.) to resolve the optimization problems. Linear programming (LP) [33]-[35], quadratic programming (QP) [36]-[38] and convex programming (CP) [39]-[41] are three types of widely used gradient algorithms, where LP minimizes a linear cost function subject to linear constraints, QP tackles a quadratic cost function with linear constraints, while CP deals with a convex cost function and concave inequality constrains [39]. For instance, Dima et al. propose a LP-based power allocation strategy for FCHEV [33]. Specifically, the energy management problem is formulated as a constrained optimization problem, which comprises a linear performance index that is proportional to the price-weighted sum of fuel cell power, battery power and mechanical braking power, and several linear constraints describing the limitations on powertrain components. Compared to a rule-based strategy, it can improve the vehicle's operation efficiency by coordinating the following metrics: H2 consumption, FCS utilization, electricity energy consumption and energy dissipation by mechanical braking. Moreover, Xiaosong et al. present a sequential QP (SQP)-based cost optimal EMS for a FC-battery HEV, which attempts to minimize the vehicle's running cost, including the H2 consumption cost and the costs due to fuel cell and battery degradation [37]. Since the cost terms quantifying the degradations of fuel cell and battery cannot be simply expressed as the linear functions of the manipulated variable, thus LP is not suitable to tackle such problem. To this end, SQP, as a widely used technique for handling the nonlinear constrained optimization problems is adopted in this work. It should be mentioned that SQP algorithm solves a sequence of optimization subproblems via specifying

a suitable search direction as a solution to the QP subproblem with linear constraints. In addition, a CP-based co-optimization framework is employed to simultaneously tackle the component-sizing and energy management problems for a plug-in FCHEV [39]. In contrast to LP and QP, CP deals with the optimization problems with convex objective function over the convex set. In other words, CP can solve more complicated optimization problems, wherein, for example, the cost functions and constraints are not limited to linear or quadratic forms. Moreover, although the solutions' optimality derived by CP may degrade compared to DP due to the model simplification and convexification, the corresponding improved calculation efficiency facilitates the online applications of CP-based EMSs [39]. The major advantages of gradient algorithms lie in: (1) higher computation efficiency compared to direct and indirect algorithms; (2) the availability of the well-established commercial solvers [42]. In contrast, their performance optimality may be compromised to some extent, due to the simplification of original nonlinear optimization problems.

**Derivative-free algorithms**: if the derivative information of cost functions is unavailable or impractical to acquire, gradient algorithms are no longer suitable for solving optimization problems. In this case, derivative-free algorithms, like simulated annealing [43], genetic algorithm [21] and particle swarm optimization [44], are capable of obtaining the optimal results for EMS problems via iterative stochastic search. Simulated annealing (SA), firstly introduced by Kirkpatrick in 1983, is inspired by the metal annealing process. This algorithm randomly searches for the solution to an optimization problem relying on the improvement of performance index. For example, to enhance the drivability of a battery-supercapacitor based electric vehicle, Ref. [43] reports a dynamically restricted search-space strategy combined with SA technique to minimize the discrepancy between the demand power and the power supplied by both energy sources. Genetic algorithm (GA) is another random search algorithm based on the law of biological evolution [45], comprising three major working phases: reproduction, crossover and mutation. It can obtain the global optimal solution to the nonlinear, non-convex, multimodal, and discontinuous-time optimization problems [42]. For example, for tuning multiple control parameters of the fuzzy controller for a FCHEV, Ahmadi et al. utilize GA to simultaneously minimize the operation cost of powertrain energy sources (e.g. fuel cell and battery), the SoC reference deviations and the discrepancy between the actual and reference vehicle speed [21]. Validation results demonstrate the improved performance in contrast to a non-optimized fuzzy controller under different driving cycles. Furthermore, as another stochastic population-based optimization method, particle swarm optimization (PSO) was firstly proposed by Kennedy and Eberhart in 1995 [46]. It solves an optimization problem by iteratively attempting to enhance a candidate solution (termed as "particle") quantified by a performance index: by creating a population of particles, randomly mapping them into the search-space, allowing interactions among particles regarding their best known locations, and eventually converging the swarm to the best solutions. For example, a dual-layer PSO-enhanced rule-based EMS for a fuel cell/supercapacitor HEV is proposed in [44], where the upper rule-based layer reduces the computation

effort by shrinking down the search-space of PSO, and the lower metaheuristic layer searches for the optimal fuel cell output current to minimize H2 consumtion. Validation results show that the proposed strategy performs close to a GA-enhanced EMS regarding the fuel economy, but reduces the online computation time per step from an average of 43.09 ms (GA-based) to 0.65 ms (PSO-based), proving the proposed strategy is more suitable for real-time applications. Due to the lack of derivative information of cost function, derivative-free algorithms usually require large amount of computation time or memory spaces for stochastic searching. Moreover, the searching results depend heavily on the initial population settings, and thus the risk of being trapped into local optima cannot be fully avoided [31].

### 2.2.3. Real-time optimization-based strategies

Due to the unpredictable traffic conditions in realistic driving environment, the complete driving cycle information is impossible to obtain beforehand, implying that the global optimal results cannot be directly applied to real-time control. Therefore, how to enhance the EMS performance to approximate the global optimality based on the limited computational and memory resources of onboard electronic control units attracts numerous research attentions [47]-[49]. Thus, it has led to the birth of a variety of real-time optimization-based strategies, with Equivalent Consumption Minimization Strategy (ECMS) and Model Predictive Control (MPC) being two types of commonly used strategies in both industry and academia. Figure 2.9 depicts the relationship of global and real-time optimization-based strategies.

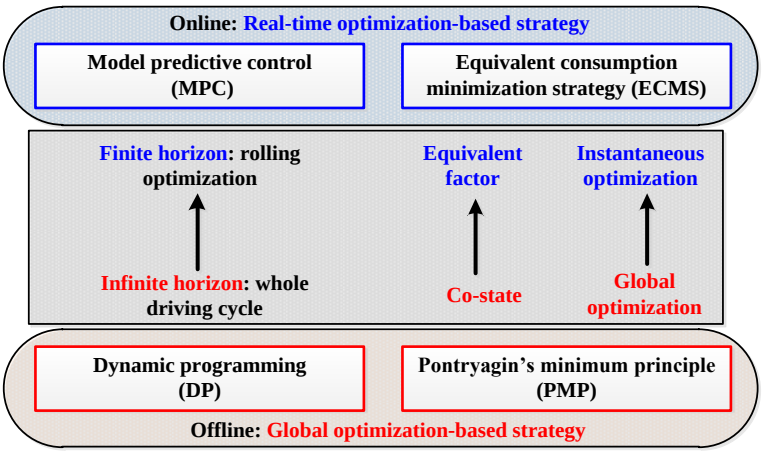


Figure 2.9. Optimization-based strategies for FCHEV: from offline to online [1].

Consider the major focus of this thesis, it should be mentioned that the performance of both ECMS and MPC can be enhanced by the integration of driving predictive information. For example, the real-time update of equivalence factor for ECMS and the estimation of upcoming disturbances over each rolling optimization horizon for MPC can be assisted by the speed forecasting techniques [42]. Thus, both ECMS and MPC frameworks are deemed as the potential candidates for the realization of predictive energy management strategies (PEMS) for FCHEVs, with their pros and cons detailed as follows.

### 2.2.3.1. Equivalent consumption minimization strategy

ECMS was firstly introduced by Paganelli for energy distribution within a parallel HEV operating under charge-sustaining (CS) conditions [50]. For a FCHEV, the equivalent H2 consumption comprises two parts: (i) the actual amount of H2 consumed by FCS, and (ii) the H2 consumption transformed from the electricity energy consumption by other energy sources (e.g. battery and/or supercapacitor (SC)). Therefore, ECMS derives power allocation decisions by minimizing the instantaneous equivalent H2 consumption per sampling time step. For example, an ECMS is designed for a PEMFC-battery-SC-based hybrid tramway [51]. Since the SC has low energy density compared to other power sources, the optimization problem is simplified to minimize the equivalent hydrogen consumption from PEMFC and battery. Under the real Urbos driving cycle for a tramway, the proposed strategy can effectively coordinate three power sources in real-time, leading to the reduction of total energy consumption compared to a rule-based strategy, with the SoCs of battery and SC maintained around the desired values, 65% and 75%, respectively. Moreover, Huan et al. propose a sequential quadratic programming based ECMS for a FCHEV propelled by fuel cell, battery and SC [38]. By using three dynamic penalty coefficients in cost function, the output behaviors of three energy sources can be effectively governed, resulting in the improved fuel economy and the smoothed fuel cell current, compared to a rule-based benchmark strategy.

According to the theory of Pontryagin's minimum principle, the equivalence factor (EF) in the Hamiltonian function quantifies the relative importance of the electricity consumption cost in contrast to H2 consumption cost. The optimal fuel economy of a given trip can only be realized via a perfect EF tuning [52]. Moreover, the optimal value of EF has strong relevance to the battery SoC boundary and the driving cycle information. Hence, numerous researches focus on the estimation of EF, which can be done in either online or offline mode, as illustrated in figure 2.10.

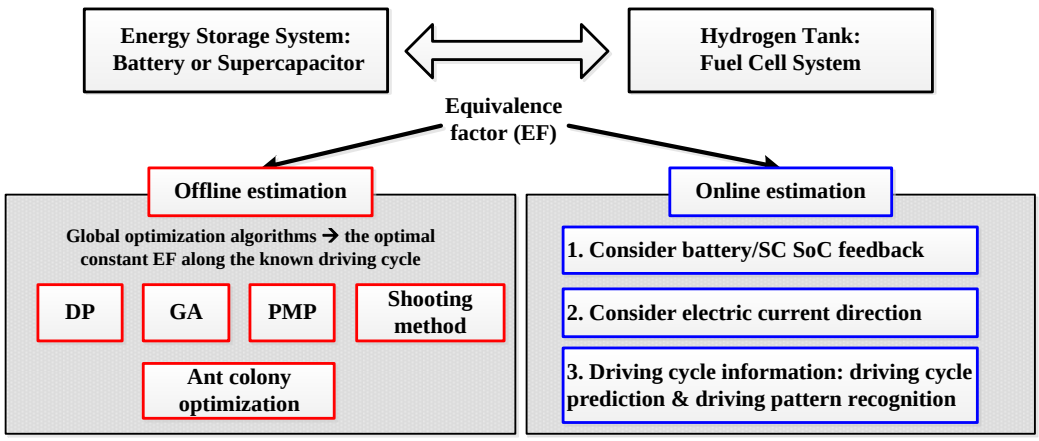


Figure 2.10. Estimation of EF in offline and online modes [1].

In offline mode, given the fully previewed driving cycle information, the estimation of constant EF can be described as a global optimization problem, which can be tackled by several algorithms, like dynamic

programming [53], genetic algorithm [53], Pontryagin's minimum principle [9], [54], shooting method [55]-[57] and ant colony optimization [58]. Nevertheless, the optimal constant EF needs to be re-calibrated when the driving cycle changes, and thus the poor adaptability towards changeable driving patterns is the major drawback of offline EF estimation.

In online mode, the real-time tuning of EF is the superior task of ECMS, leading to the birth of adaptive-ECMS (A-ECMS) framework, which can be realized with the assist of two techniques: driving cycle prediction and driving pattern recognition. Specifically, benefiting from the forecasted speed in an optimization horizon with fixed length, the estimation of EF is conducted over the current horizon, and the modified EF is adopted in the next horizon. In this way, the value of EF is updated once the optimization window has moved forward. By stepwise renewing EF, A-ECMS adapts to changeable driving conditions, and thus is capable of approximating the global optimal solution. For example, an adaptive PMP-based EMS is devised for a FCHEV, wherein the EF adaptation is realized by an improved Markov speed predictor [59]. Validation results indicate the proposed strategy perform close to the offline-PMP and DP strategies in terms of H2 consumption and average fuel cell power transients. In contrast, driving pattern recognition techniques can differentiate the real-time driving pattern, to select the most appropriate EFs from the offline-optimized candidates for the identified driving pattern. For example, a novel EF updating method assisted by driving pattern recognition is reported in [60] for a fuel cell/battery based HEV. By using proper EFs in different driving patterns, the presented adaption law can effectively extend the battery lifetime, guarantee the final SoC reaching the initial one and improve fuel economy in contrast to a non-adaptive ECMS.

#### 2.2.3.2. Model predictive control

Model predictive control (MPC) relies on the precise modeling of the controlled system and generates the desired control sequence by optimizing the performance index based on the anticipation of future system behaviors. Model distortions and disturbances, which lead to the discrepancy between the plant output and the output of the control-oriented model, can be compensated by refreshing measurements at each time step in MPC [61]. Owing to its strong capacity in handling constrained multivariate system and its potential for real-time applications, MPC is widely used in vehicular energy management field [62]. Figure 2.11 presents the control framework of MPC-based EMS.

MPC iteratively minimizes a series of objective functions over receding time horizons using a diversity of optimization solvers: quadratic programming [61], [63]-[65], deterministic dynamic programming [66]-[68], stochastic dynamic programming [69]-[71], nonlinear programming [72], [73], Pontryagin's Minimum Principle [74] and convex programming [75]. Specifically, quadratic programming, as the most widely used MPC solver, requires the optimization problem to be formulated with quadratic cost functions and linear constraints. For example, the EMS problem of a postal-delivery FCHEV is casted in the form of a quadratic MPC optimization problem, and the vehicle's future power demand is deemed

as the system disturbance and is estimated by a fuzzy C-means enhanced Markov predictor [64]. When nonlinear cost terms or constraints exist in MPC optimization problem, dynamic programming (DP) becomes a suitable problem solver in this case. For instance, a MPC-based power management strategy is built for a fuel cell/supercapacitor hybrid construction vehicle, wherein the upcoming vehicle power requirement is forecasted by a neural network predictor using historical power demand samples [66]. Within each prediction horizon, a nonlinear optimization problem is solved by DP to obtain the desired control sequence. Another commonly used MPC solver is stochastic dynamic programming, since it can find the optimal solution in EMS problem in face of future stochastic disturbances. For example, a stochastic MPC approach combined with road grade information modeled by a Markov Chain is used for power allocation in a parallel HEV, where the EMS problem is formulated as Markov decision process and solved by stochastic dynamic programming [71].

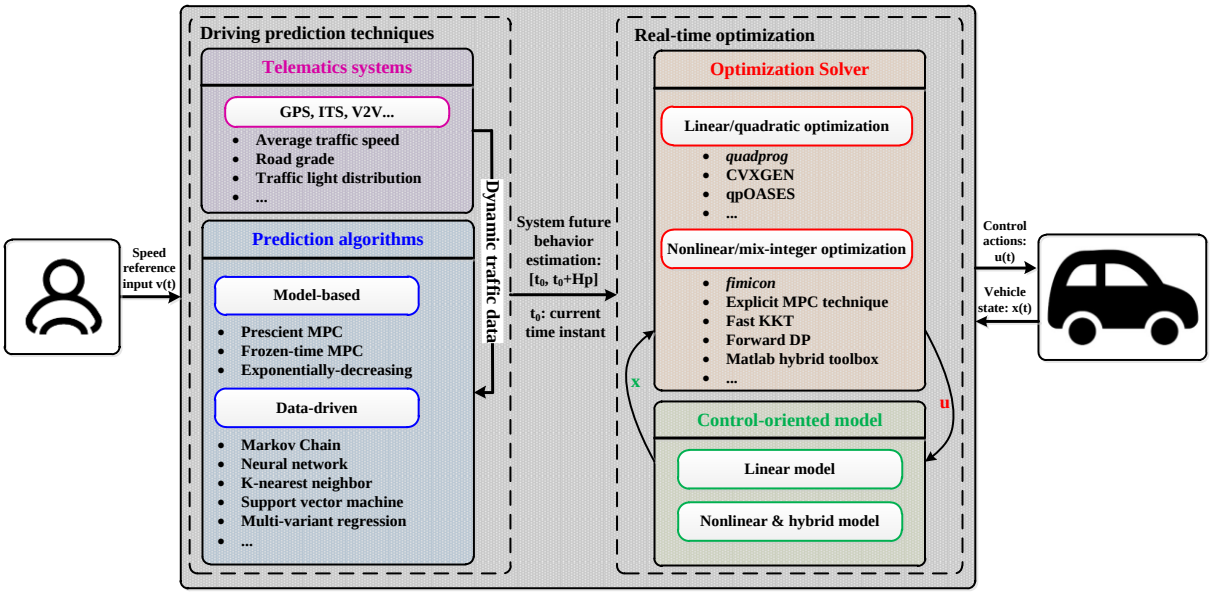


Figure 2.11. Representation of model predictive control-based energy management strategy.

As mentioned before, future driving disturbance and model distortion are two major factors that affect the performance of model predictive control. Hence, on the one hand, many researchers are dedicated to developing advanced driving prediction techniques to improve the estimation accuracy of system future behaviors [42]. Prescient and frozen-time MPC are two benchmark strategies where the former can preview the power demand profile within each moving horizon with 100% accuracy, and the latter makes the conservative prediction that the power request keeps unchanged within each rolling horizon [69]. Likewise, an exponentially decreasing model reported in [72] estimates the driver's torque request over each prediction horizon for an MPC-based EMS. Besides, data-driven approaches, like Markov Chain and neural network, also show the effectiveness in characterizing the distribution of future driving conditions [76]. Although numerous efforts have been done in previous studies, the quality of prediction (accuracy and robustness) needs to be further enhanced in future studies [77].

On the other hand, in vehicular EMS problems, a proper modelling of vehicle powertrain system would not only improve the control accuracy but also guarantee an affordable online computation burden. Due to the nonlinearity of powertrain components, the MPC control-oriented model is a nonlinear time-varying constrained system, causing a nonlinear optimization problem for MPC decision-making, which requires nonlinear solvers and, usually, consumes large amount of computation time. Several algorithms can be used to tackle such problems, like fuzzy MPC technique [61], explicit MPC technique [78], forward dynamic programming [79], and fast Karush-Kuhn-Tucker (KKT) approach [42], etc. Nevertheless, the computation efforts and stability issues imposed by these methods still need to be further studied and thus greatly hinder their online implementations at the current stage [42]. In contrast, the most common way is to linearize and discretize the model or even constraints, and transform the MPC optimization into a quadratic problem, which can be efficiently solved by many well-designed commercial solvers, like *quadprog*, GVXGEN, and qpOASES, etc. Specially, if discrete constraints on control or state variables are introduced, like the gear number selection, engine on/off commands or HEV operation modes, a hybrid MPC framework is established. The related mixed-integer optimization problems can be solved by using the hybrid toolbox in MATLAB [42].

#### 2.2.3.3. Other approaches

Other approaches like robust control [80], extremum seeking method (ESM) [81]-[83], decoupling control [84], [85], sliding mode control [86], and learning-based strategies [87]-[89] are also explored by many researchers to tackle the energy management problem for FCHEVs. Specifically, ESM, as a derivate-free algorithm, is capable of finding an extremum (maximum or minimum) value of a static nonlinear system in real-time. For example, the energy management problem for a fuel cell/battery based HEV is tackled by using a fractional-order ESM in [81]. Considering the nonlinear relationship between fuel cell power (current) and FCS efficiency, ESM can thus be utilized to control FCS operating towards its high efficiency region. In contrast to conventional integer-order ESM, the fractional-order ESM permits the faster convergence rate and the higher robustness due to the employment of Oustaloup approximation based fractional-order calculus. Compared to benchmark strategies, hardware-in-the-loop (HIL) tests confirm that the fractional-order ESM based strategy can improve average FCS working efficiency and FCS durability, while keeping battery SoC in the predefined zone.

In addition, with the rapid development of data-driven and artificial intelligence technologies in recent years, learning-based (particularly, reinforcement learning (RL)) EMSs have attracted considerable attentions in automotive industry, especially in vehicular energy management aspect. Compared to traditional EMSs, learning-based EMSs do not rely on the precise knowledge of the controlled system nor any predictive information for power allocation. In contrast, the control policy can be updated stepwise in real-time and ultimately reach the optima, through massive action-reward interactions between the learning agent and the driving environment. For example, a hierarchical RL-based EMS is

proposed for a hybrid electric vehicle propelled by fuel cell, battery and supercapacitor in [88]. To reduce the size of state-action space of Markov decision process, an adaptive fuzzy filter is adopted in the upper layer to decompose the historical power demand signal into different frequency components, where the negative power demand and high frequency positive power demand are directly assigned to supercapacitor, while the remaining portion goes to fuel cell and battery. Within the lower layer, an improved Q-learning algorithm combining with ECMS is developed to accelerate the convergence speed towards the optimal control policy in high-dimensional state-action space without over degrading the optimality of solution. Validation results have confirmed that it can improve computation efficiency, fuel cell working efficiency and fuel cell durability against existing learning-based EMSs.

### 2.2.4. Comparison of different energy management strategies

In the previous parts of this chapter, three types of control strategies for fuel-cell-based HEVs from the state-of-the-art literatures are comprehensively reviewed. Based on the aforementioned analysis, the benefits and drawbacks of existing EMSs for FCHEVs are summarized in TABLE 2.1.

TABLE 2.1. Comparison on control algorithms adopted in energy management strategies

| Classification | Algorithms | Benefits | Drawbacks |
|---|---|---|---|
| **Rule-based EMS** | **Deterministic Rule** | 1. Simple to implement;<br>2. Least computation burden. | 1. Depends on expertise knowledge or experience;<br>2. Less adaptability towards driving changes. |
| | **Fuzzy Rule** | 1. Free of precise system model;<br>2. Computation-friendly. | 1. Multiple fuzzy membership parameters need re-calibration in different driving cycles. |
| **Global-optimization based EMS** | **Dynamic Programming** | 1. Global optimality;<br>2. Benchmark to other strategies. | 1. Complete route information *a priori*;<br>2. High computation burden;<br>3. Curse of dimensionality. |
| | **Pontryagin's Minimum Principle** | 1. Near global optimality. | 1. System simplification for gaining analytical solution and better computation efficiency;<br>2. Complexity in mathematical theory. |
| | **Convex Programming** | 1. Sub-global optimality;<br>2. Less computation burden than DP. | 1. System must comply with convexification;<br>2. Hardly to achieve the global optimal results. |
| | **Quadratic Programming** | 1. Subset of convex optimization;<br>2. Less computation burden than DP;<br>3. Availability of commercial solver. | 1. Simplified model may degrade performance optimality. |
| | **Genetic Algorithm** | 1. Applicable to non-differentiable objective functions;<br>2. Support multiple objectives | 1. Time consuming;<br>2. Risk of stuck into local optima;<br>3. Searching results depend on the initial population. |
| | **Particle Swarm Optimization** | 1. Less parameter tuning;<br>2. Robust to initial population size. | 1. Extra memory requirement;<br>2. Less adaptability towards different driving cycles. |
| **Real-time optimization-based EMS** | **Equivalent Consumption Minimization Strategy** | 1. Solution to nonlinear constrained optimization problem in real-time. | 1. Optimal EF sensitive to driving cycle;<br>2. The sum of local optima ≠ global optima. |
| | **Model Predictive Control** | 1. Capacity of handling complex time-varying constrained system;<br>2. Real-time optimization. | 1. Performance compromised by model distortion;<br>2. Requirement & sensitivity of driving prediction. |
| **Others** | **Extreme Seeking Method** | 1. Near optimality;<br>2. Real-time suitable;<br>3. Capacity of handling nonlinearity. | 1. Complexity in mathematical theory;<br>2. Improper for multi-objective optimization. |
| | **Reinforcement Learning** | 1. Model-free control;<br>2. Self-learning capacity;<br>3. Free of previewed knowledge. | 1. No clear guidance in choosing immediate cost for multi-objective global optimization. |

Compared to other approaches, MPC framework is more suitable for realizing predictive EMSs for FCHEVs. The reasons are given as below:

- The major advantage of rule-based strategies is their computation efficiency. Nevertheless, the calibration of control parameters is achieved based on expertise knowledge or engineering experience, which may lead to following defects: (a) the performance optimality cannot be fully guaranteed, and (b) considerable parameter calibration efforts are required towards the satisfied performance. In contrast, MPC-based EMSs do not rely on predefined rules, but generate desired control policy by optimizing a performance index in real-time. It can better adapt to different driving conditions and disturbances by anticipating future system behaviors. Although the optimization is required per time step, by properly simplifying the powertrain model, the optimization problem can be tackled by available commercial solvers (e.g. qpOASES, *quadprog*, CVXGEN, etc.) with acceptable computation efforts.
- Given the complete route information *a priori*, global-optimization based strategies derive the optimal control sequence via minimizing the cost function over the entire driving cycle horizon, which offers the evaluation benchmark to other EMSs. Yet, the optimal control effects cannot be directly applied to real-time scenarios. In contrast, the optimization horizon of MPC is finite and moves forwards as the coming of the next sampling time instant. Hence, based on the anticipation of upcoming driving conditions, MPC generates the power-allocation decision at each time step by solving a finite-horizon optimization problem, whose real-time suitability is ensured by the well-established optimization algorithms [42].
- The major difference between MPC and conventional ECMS is that the former considers the upcoming vehicle power demand within a finite time horizon, while the latter allocates the power demand at current sampling time instant, implying the MPC-based EMS is more capable of handling future driving changes and may lead to better EMS performance [62]. Besides, the optimal value of equivalence factor (EF) is highly related to the entire driving cycle knowledge, which cannot be obtained beforehand. In this case, as an alternative solution, adaptive online EF estimation approaches should be integrated to the conventional ECMS framework, which requires the forecast of future driving conditions within each moving window horizon.
- Without any predictive results or precise system model information, reinforcement learning (RL)-based EMSs can improve its control performance and eventually converge towards the global optima. Although the realization of global optimal performance in real-time seems to be appealing, following issues should be further addressed before the online implementation of RL-based strategies: how to properly formulate a local cost function; how to guarantee a fast convergence speed in face of the high-dimensional state-action space; how to effectively coordinate with cloud-computing systems in order to mitigate the conflicts between limited resources of the onboard electronic control units and the heavy computation burdens. Thus, RL-based strategies may not be the most suitable candidate for

energy management problems of FCHEVs at the current stage.

## 2.3. Model predictive control-based energy management strategies

According to the above-mentioned analyzes, model predictive control (MPC) can achieve a well balance between performance optimality and computation efficiency among existing approaches for vehicular energy management problems. Besides, MPC framework is convenient for driving predictive information integration, which is very suitable concerning the subject of this PhD thesis. Thus, MPC is selected for real-time decision-making in the EMS for FCHEVs. To this end, subsection 2.3 presents a general introduction to the MPC-based EMS, including the brief to MPC theory and the formulation of MPC. Thereafter, based on the challenging issues for MPC-based EMSs in vehicular applications, the necessity and importance of developing advanced driving prediction techniques are illustrated.

### 2.3.1. Model predictive control: brief introduction to theory

Model predictive control, also referred to as moving horizon control or receding horizon control, is one of the most widely-used advanced control methods in multiple industrial sectors [90]. Despite the existence of multiple MPC variants, it should comprise following three basic elements, as shown in figure 2.12.

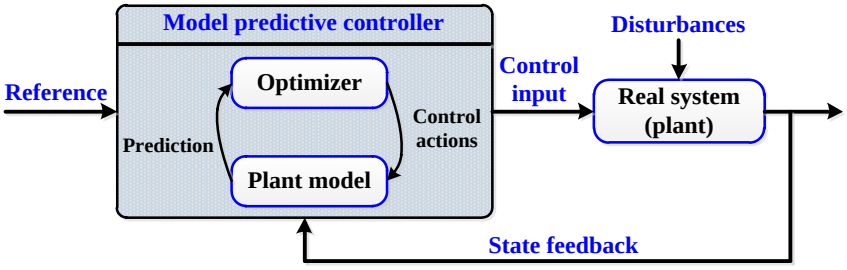


Figure 2.12. Illustration of model predictive control framework.

**(a) Predictive Model**: As a model-based control strategy, the term "model" in MPC refers to the control-oriented model (plant model), which is capable of representing the future dynamic behaviors of the real system (plant) according to the input information. In other words, MPC has the ability to anticipate future events and take control actions accordingly. The plant model is typically given in the form of state-space representation or transfer function, and the precision of system modelling can greatly affect the performance of MPC.

**(b) Rolling Optimization**: As an optimization-based control strategy, MPC takes control actions via optimizing the performance index (which is quantified by the cost function) over a finite time horizon. Specifically, with the plant state sampled at time instant t = k, MPC optimizes the performance index over the time horizon [k, k + $H_p$-1], where $H_p$ > 1 is the length of prediction horizon. At the next time instant, the time horizon shifts forward to [k + 1, k + $H_p$] with the optimization performed again. In this

way, the performance index optimization is repeatedly conducted online, instead of accomplishing at one time in offline, which is the biggest difference between MPC and traditional optimal control.

**(c) Feedback correction**: After obtaining the optimal control sequence, containing $H_p$ elements, at time instant $k$, MPC only implements the first one to the real system while discards the others. This measure can prevent the control performance losses imposed by model distortion or disturbances in environment. Then, at time instant $k+1$, the actual output is resampled to correct the plant model, and the updated state information is used for performance index optimization in the $(k+1)^{th}$ prediction horizon.

To sum up, the MPC working flow includes three steps: (i) Future system state trajectory estimation, (ii) MPC performance index optimization over finite time horizon, and (iii) Application of the first optimal control element to the real system. At any time instant, once the plant states are updated, step (i) to (iii) is sequentially carried out. Afterwards, the prediction horizon moves forward, the system states are resampled and the calculation (step (i) to (iii)) is repeated starting from the new states. Figure 2.13 provides a graphic representation of MPC working principle, where $H_m$ and $H_p$ denote the control and prediction horizon, respectively.

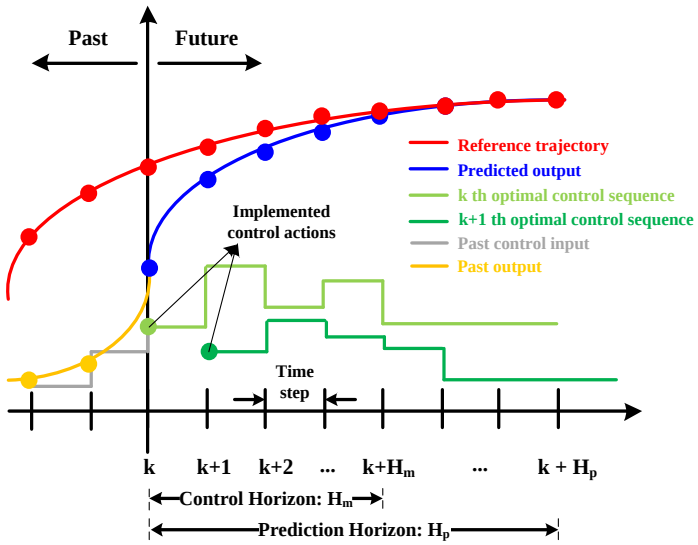


Figure 2.13. Representation of MPC working principle [42].

## 2.3.2. Model predictive control: application in vehicular energy management field

The mathematical formulation of MPC is presented in this subsection, including the establishment of control-oriented model, cost function and constraints.

### 2.3.2.1. Control-oriented model

Control-oriented model (also known as plant model) estimates the future behavior of a real system (plant) according to the input information. It is established based on the knowledge or observation of a nonlinear, time-varying system, and is used as the basis for the predictive control framework. If we consider a plant

model given in the form of state-space representation, with $\boldsymbol{x}, \boldsymbol{u}, \boldsymbol{\omega}$ and $\boldsymbol{y}$ respectively being the state, input (control), disturbance and output of the model, the plant model can be written as:

$$\dot{x} = f(x, u, \omega), y = g(x, u, \omega) \tag{2.1}$$

In vehicular EMS problems, the plant model formulation can be very different due to the discrepancies in terms of powertrain structure and definition of system variables. Moreover, due to the nonlinearity of the vehicular powertrain systems, the plant model is typically a nonlinear time-varying system, and corresponding MPC is termed as nonlinear MPC, indicating a nonlinear constrained optimization problem to be tackled over each prediction horizon. However, solving such a problem is very time-consuming: the calculation time, in some cases, is even two times larger in contrast to an optimization problem with the linearized plant model [72]. In light of the limited resources in electronic control units, the extra computational burden by nonlinear MPC would be a great threat to its real-time implementation. To address this issue, researchers attempt to linearize the nonlinear plant model Eq. (2.1) at each sampling time instant around the current operating conditions [72], as denoted by Eq. (2.2) and (2.3).

$$\begin{cases} \dot{x} = \tilde{A}x + \tilde{B}_u u + \tilde{B}_\omega \omega + \tilde{F} \\ y = \tilde{C}x + \tilde{D}_u u + \tilde{D}_\omega \omega + \tilde{G} \end{cases} \tag{2.2}$$

$$\begin{aligned} &\tilde{A} = \left(\frac{\partial f}{\partial x}\right)_{(x_0,u_0,\omega_0)}; \tilde{B}_u = \left(\frac{\partial f}{\partial u}\right)_{(x_0,u_0,\omega_0)}; \tilde{B}_\omega = \left(\frac{\partial f}{\partial \omega}\right)_{(x_0,u_0,\omega_0)} \\ &\tilde{C} = \left(\frac{\partial g}{\partial x}\right)_{(x_0,u_0,\omega_0)}; \tilde{D}_u = \left(\frac{\partial g}{\partial u}\right)_{(x_0,u_0,\omega_0)}; \tilde{D}_\omega = \left(\frac{\partial g}{\partial \omega}\right)_{(x_0,u_0,\omega_0)} \\ &\tilde{F} = f(x_0, u_0, \omega_0) - \tilde{A}x_0 - \tilde{B}_u u_0 - \tilde{B}_\omega \omega_0 \\ &\tilde{G} = g(x_0, u_0, \omega_0) - \tilde{C}x_0 - \tilde{D}_u u_0 - \tilde{D}_\omega \omega_0 \end{aligned} \tag{2.3}$$

Where $x_0, u_0$ and $\omega_0$ denote the current values of the state, input and disturbance to the system, respectively, $f(x_0, u_0, \omega_0)$ the estimation of system state dynamics, and $g(x_0, u_0, \omega_0)$ the vector of current measurements of system outputs. In fact, the plant model given in Eq. (2.2) and (2.3) represents a linear time-varying (LTV) system, and corresponding MPC is termed as LTV-MPC [72]. As a type of adaptive MPC approach, LTV-MPC permits the renew of the prediction model and the related nominal (initial) operating conditions at each control interval, and the updated model and operating conditions keep unchanged over the prediction horizon [91], [92]. Such measure helps the plant model in LTV-MPC adapt to the changes of operating conditions [93]. In addition, to eliminate the direct input-output feedthrough, the LTV system Eq. (2.2) is modified in accordance to the standard MPC formulation, through the model augmentation method presented in [72], leading to the birth of the following discrete representation of plant model, which is used for EMS development in this thesis.

$$\begin{cases} x(k+1) = A(k)x(k) + B_u(k)u(k) + B_\omega(k)\omega(k) \\ y(k) = C(k)x(k) + D_\omega(k)\omega(k) \end{cases} \tag{2.4}$$

#### 2.3.2.2. Cost function and constraints

In the standard MPC formulation, the LTV-MPC approach derives the $k$-th control sequence by solving the following quadratic finite-horizon optimization problem [72]:

$$\min_{\Delta U} J = \min \sum_{i=0}^{\mathrm{H_p}-1} \left\| u(k+i|k) - u_{target}(k) \right\|_{\rho_i^u}^2 + \left\| \Delta u(k+i|k) \right\|_{\rho_i^{\Delta u}}^2 + \left\| y(k+i+1|k) - r(r+i+1) \right\|_{\rho_{i+1}^y}^2 + \rho_\varepsilon \varepsilon^2 \tag{2.5}$$

subject to

$$\begin{cases} x(k+i+1|k) = Ax(k+i|k) + B_u u(k+i|k) + B_\omega \omega(k+i|k) \\ y(k+i|k) = Cx(k+i|k) + D_\omega \omega(k+i|k) \\ u_i^{\min} \le u(k+i|k) \le u_i^{\max} \\ \Delta u_i^{\min} \le \Delta u(k+i|k) \le \Delta u_i^{\max} \\ -\varepsilon + y_i^{\min} \le y(k+i+1|k) \le y_i^{\max} + \varepsilon \\ \Delta u(k+i|k) = 0 \text{ for } i = \mathrm{H_m}, \dots, \mathrm{H_p}. \\ \varepsilon \ge 0 \end{cases} \tag{2.6}$$

Where $\Delta U_k = [\Delta u(k|k), \dots, \Delta u(k+H_m-1|k)]^{\mathrm{T}}$ the sequence of control increments to be optimized, $\omega$ the vector of measured disturbances, $\rho_i^u, \rho_i^{\Delta u}, \rho_{i+1}^y$ and $\rho_\varepsilon$ the weighting factors at the $i$-th time step, $x(k+i|k) \in R^n$ the forecasted state vector, $u(k+i|k) \in R^m$ the input vector, $y(k+i|k)$ the vector of forecasted output, $r(k)$ the output reference trajectory, $u_{target}(k)$ the vector of input steady-state references, and $\varepsilon$ the slack coefficient for avoiding the infeasibility. Moreover, based on the discrete system model Eq. (2.4), the system outputs over a finite time horizon can be predicted by:

$$y(k+i+1|k) = C\left\{A^{i+1}x(k) + A^i \sum_{l=0}^{i} \left[B_u\left(u(k-1) + \sum_{j=0}^{l} \Delta u(k+j|k)\right) + B_\omega \omega(k+l|k)\right]\right\} + D_\omega \omega(k+i+1|k), i \in \{0, \dots, H_p - 1\}. \tag{2.7}$$

Hence, the forecasted output in both performance index $J$ and output constraints can be substituted using the results given in Eq. (2.7), and the optimization problem can be converted to a QP problem with linear inequality constraints:

$$\begin{aligned} [\Delta U^*, \varepsilon] &= \arg\min_{\Delta U, \varepsilon} \frac{1}{2} \Delta U^T H \Delta U + F^T \Delta U \\ &\text{subject to} \quad G_u \Delta U + G_\varepsilon \varepsilon \le W \end{aligned} \tag{2.8}$$

Where $H, F, G_u, G_\varepsilon$ and $W$ are constant matrices and functions of reference, measured input, input target, the last control input, and the measured (or estimated) states at current sampling time instant [72]. Once the QP problem (2.8) is solved, the first element of optimal control sequence $\Delta U^*$ is applied to the plant, while others are discarded. Therefore, the control input at the $k^{th}$ sampling time instant is calculated by:

$$u(k) = u(k-1) + \Delta u^*(k|k) \tag{2.9}$$

### 2.3.3. Challenges for MPC-based EMS in vehicular applications

According to the discussions in subsection 2.3, one of the essential factors that would affect the control performance of MPC is the quality of plant modelling. In fact, a high-quality plant modelling can shrink the discrepancy between the actual system outputs and the one provided by the prediction model. To mitigate the control performance losses imposed by model distortion, the characteristics for powertrain components (e.g. the open-circuit voltage and internal resistance for battery, the efficiency curve of fuel cell system, the efficiency map of DC/DC converter and electric motor, etc.) should be iteratively calibrated through the experimentally-validated data covering a variety of working conditions [94]. In addition, advanced system modeling techniques (e.g. fuzzy modeling approach [61], [95]) and state estimation methods (e.g. battery SoC [96] and state-of-health (SOH) [97] estimation approaches) are also of great help to improve the MPC control accuracy. However, for real-time EMS problems, an over complicated or nonlinear plant model should be avoided since it would cause the exponentially increased computational or memory burden for onboard applications. Furthermore, except for properly simplifying the plant model, developing fast optimization solvers becomes another solution towards better real-time suitability of MPC-based EMSs [98], [99].

Another essential factor that would affect the MPC control performance is the disturbances, since the future plant outputs can be largely affected by the uncertainties in driving environment. Specifically, in vehicular EMS field, developing advanced driving prediction techniques is favorable for enhancing the forecast quality of future driving conditions and thus also the control accuracy of MPC, which is an important research focus of this thesis. It should be mentioned that a high-quality modeling of future driving uncertainties requires an in-depth understanding on the mutual interaction mechanism among drivers, vehicles and driving environment. In conclusion, as indicated in [77], [98], the prediction aspect of vehicular energy management problem is still a very open issue. Therefore, to improve the MPC performance, it is necessary to precisely model the future driving uncertainties as well as to find the proper way of integrating the predictive information into the EMS framework. To bridge these research gaps, this thesis especially concentrates on the development of advanced driving prediction techniques, and the related contents will be presented in detail in **Chapter 3**.

## 2.4. Conclusion

This chapter presents a comprehensive comparative study on the state-of-the-art energy management strategies (EMSs) for fuel cell-based hybrid electric vehicles (FCHEVs), which includes following major works:

- The working principle and the related literatures regarding the rule-based, global and real-time optimization-based strategies for fuel cell based HEVs/PHEVs are reviewed and analyzed. This allows the readers to have a clear clue regarding the discrepancy among different EMSs;

- Based on the comparison of various strategies, their benefits and drawbacks are carefully summarized in TABLE 2.1. Overall, rule-based strategies are easy to implement with high online computation efficiency since the power-allocating decisions are made without any optimization. Nevertheless, their performance optimality cannot be fully ensured especially when the driving conditions change dramatically. In contrast, global optimization-based strategies can offer the evaluation benchmark to other EMSs due to the performance optimality, but they cannot be directly applied to real-time control due to the requirement on complete driving cycle beforehand. In contrast, model predictive control (MPC) derives the control decisions by iteratively optimizing the performance index over receding horizons, which outperforms other approaches in terms of (i) the balanced performance between the optimal control and the real-time suitability, and (ii) the convenience of predictive information integration. Thus, MPC is eventually selected for real-time decision-making within the proposed EMS framework;
- After MPC is selected, its basic concepts, working principle and mathematical formulation are illustrated in detail, which thus establishes a solid basis and guideline for the development of MPC-based EMS in following chapters;
- Several challenging issues for MPC-based EMSs in vehicular applications are analyzed and summarized, which helps the readers to be aware of the potential research directions regarding the MPC energy management techniques. Finally, it is indicated that the major research focus of this thesis is to develop the advanced driving prediction techniques, so as to enhance the MPC performance by precisely modelling the future driving uncertainties.

The development of driving prediction techniques as well as the corresponding integrated predictive energy management strategies will be presented in the following chapters.

## References


[1]. D. Tran, M. Vafaeipour, M.E. Baghdadi, R. Barrero, J. V. Mierlo, O. Hegazy, Thorough state-of-the-art analysis of electric and hybrid vehicle powertrains: Topologies and integrated energy management strategies, ***Renewable and Sustainable Energy Reviews***, Volume 119, 2020, 109596, https://doi.org/10.1016/j.rser.2019.109596.

[2]. A. Ravey, B. Blunier, A. Miraoui, "Control Strategies for Fuel-Cell-Based Hybrid Electric Vehicles: From Offline to Online and Experimental Results," in ***IEEE Transactions on Vehicular Technology***, vol. 61, no. 6, pp. 2452-2457, July 2012. doi: 10.1109/TVT.2012.2198680.

[3]. D. Zhou, A. Al-Durra, F. Gao, A. Ravey, I. Matraji, M.G. Simões, Online energy management strategy of fuel cell hybrid electric vehicles based on data fusion approach, ***Journal of Power Sources***, Volume 366, 2017, Pages 278-291, https://doi.org/10.1016/j.jpowsour.2017.08.107.

[4]. K. Song, F. Li, X. Hu, L. He, W. Niu, S. Lu, T. Zhang, Multi-mode energy management strategy for fuel cell electric vehicles based on driving pattern identification using learning vector quantization neural network algorithm, ***Journal of Power Sources***, Volume 389, 2018, Pages 230-239, https://doi.org/10.1016/j.jpowsour.2018.04.024.

[5]. M.A. Hannan, F.A. Azidin, A. Mohamed, Multi-sources model and control algorithm of an energy management system for light electric vehicles, ***Energy Conversion and Management***, Volume 62, 2012, Pages 123-130, https://doi.org/10.1016/j.enconman.2012.04.001.

[6]. H. Zhang, X. Li, X. Liu, J. Yan, Enhancing fuel cell durability for fuel cell plug-in hybrid electric vehicles through strategic power management, ***Applied Energy***, Volume 241, 2019, Pages 483-490, https://doi.org/10.1016/j.apenergy.2019.02.040.

[7]. T. Fletcher, R. Thring, M. Watkinson, An Energy Management Strategy to concurrently optimize fuel consumption & PEM fuel cell lifetime in a hybrid vehicle, ***International Journal of Hydrogen Energy***, Volume 41, Issue 46, 2016, Pages 21503-21515, https://doi.org/10.1016/j.ijhydene.2016.08.157.

[8]. W. Shabbir and S. A. Evangelou, "Exclusive Operation Strategy for the Supervisory Control of Series Hybrid Electric Vehicles," in ***IEEE Transactions on Control Systems Technology***, vol. 24, no. 6, pp. 2190-2198, Nov. 2016. doi: 10.1109/TCST.2016.2520904.

[9]. C.H. Zheng, C.E. Oh, Y.I. Park, S.W. Cha, Fuel economy evaluation of fuel cell hybrid vehicles based on equivalent fuel consumption, ***International Journal of Hydrogen Energy***, Volume 37, Issue 2, 2012, Pages 1790-1796, https://doi.org/10.1016/j.ijhydene.2011.09.147.

[10]. L. Xu, J. Li, M. Ouyang, J. Hua, G. Yang, Multi-mode control strategy for fuel cell electric vehicles regarding fuel economy and durability, ***International Journal of Hydrogen Energy***, Volume 39, Issue 5, 2014, Pages 2374-2389, https://doi.org/10.1016/j.ijhydene.2013.11.133.

[11]. Q. Li, H. Yang, Y. Han, M. Li, W. Chen, A state machine strategy based on droop control for an energy management system of PEMFC-battery-supercapacitor hybrid tramway, ***International Journal of Hydrogen Energy***, Volume 41, Issue 36, 2016, Pages 16148-16159, https://doi.org/10.1016/j.ijhydene.2016.04.254.

[12]. H. Alloui, M. Becherif, K. Marouani, "Modelling and frequency separation energy management of fuel Cell-Battery Hybrid sources system for Hybrid Electric Vehicle," ***21st Mediterranean Conference on Control and Automation***, Chania, 2013, pp. 646-651. doi: 10.1109/MED.2013.6608791.

[13]. H. Alloui, K. Marouani, M. Becherif, M. N. Sid, M. E. H. Benbouzid, "A control strategy scheme for fuel cell-vehicle based on frequency separation," ***2014 First International Conference on Green Energy ICGE 2014***, Sfax, 2014, pp. 170-175. doi: 10.1109/ICGE.2014.6835417.

[14]. P. J. Tritschler, S. Bacha, E. Rullière, G. Husson, "Energy management strategies for an embedded fuel cell system on agricultural vehicles," ***The XIX International Conference on Electrical Machines - ICEM 2010***, Rome, 2010, pp. 1-6. doi: 10.1109/ICELMACH.2010.5608314.

[15]. M. Ibrahim, S. Jemei, G. Wimmer, N.Y. Steiner, C.C. Kokonendji, D. Hissel, Selection of mother wavelet and decomposition level for energy management in electrical vehicles including a fuel cell, ***International Journal of Hydrogen Energy***, Volume 40, Issue 45, 2015, Pages 15823-15833, https://doi.org/10.1016/j.ijhydene.2015.06.055.

[16]. X. Zhang, C. C. Mi, A. Masrur, D. Daniszewski, Wavelet-transform-based power management of hybrid vehicles with multiple on-board energy sources including fuel cell, battery and ultracapacitor, ***Journal of Power Sources***, Volume 185, Issue 2, 2008, Pages 1533-1543, https://doi.org/10.1016/j.jpowsour.2008.08.046.

[17]. Y. Ates, O. Erdinc, M. Uzunoglu, B. Vural, Energy management of an FC/UC hybrid vehicular power system using a combined neural network-wavelet transform based strategy, ***International Journal of Hydrogen Energy***, Volume 35, Issue 2, 2010, Pages 774-783, https://doi.org/10.1016/j.ijhydene.2009.11.021.

[18]. B. Blunier, M. G. Simões, A. Miraoui, "Fuzzy logic controller development of a hybrid fuel cell-battery auxiliary power unit for remote applications," ***2010 9th IEEE/IAS International Conference on Industry Applications - INDUSCON 2010***, Sao Paulo, 2010, pp. 1-6. doi: 10.1109/INDUSCON.2010.5739890.

[19]. J. Hwang, J. Hu, C. Lin, Design of a range extension strategy for power decentralized fuel cell/battery electric vehicles, ***International Journal of Hydrogen Energy***, Volume 40, Issue 35, 2015, Pages 11704-11712, https://doi.org/10.1016/j.ijhydene.2015.04.026.

[20]. S. Faivre, A. Ravey, A. Djerdir, D. Bouquain, "Degraded control strategy using state-of-health in fuel cell hybrid electric vehicles," ***2013 IEEE Transportation Electrification Conference and Expo (ITEC)***, Detroit, MI, 2013, pp. 1-5. doi: 10.1109/ITEC.2013.6573498.

[21]. S. Ahmadi, S.M.T. Bathaee, Multi-objective genetic optimization of the fuel cell hybrid vehicle supervisory system: Fuzzy logic and operating mode control strategies, ***International Journal of Hydrogen Energy***, Volume 40, Issue 36, 2015, Pages 12512-12521, https://doi.org/10.1016/j.ijhydene.2015.06.160.

[22]. X. Lü, Y. Wu, J. Lian, Y. Zhang, C. Chen, P. Wang, L. Meng, Energy management of hybrid electric vehicles: A review of energy optimization of fuel cell hybrid power system based on genetic algorithm, ***Energy Conversion and Management***, Volume 205, 2020, 112474, https://doi.org/10.1016/j.enconman.2020.112474.

[23]. R. Zhang, J. Tao, "GA-Based Fuzzy Energy Management System for FC/SC-Powered HEV Considering H2 Consumption and Load Variation," in ***IEEE Transactions on Fuzzy Systems***, vol. 26, no. 4, pp. 1833-1843, Aug. 2018. doi: 10.1109/TFUZZ.2017.2779424.

[24]. S. Caux, W. Hankache, M. Fadel, D. Hissel, On-line fuzzy energy management for hybrid fuel cell systems, ***International Journal of Hydrogen Energy***, Volume 35, Issue 5, 2010, Pages 2134-2143, https://doi.org/10.1016/j.ijhydene.2009.11.108.

[25]. H. Liu, J. Chen, C. Wu, H. Chen, "Multi-objective optimization for energy management of fuel cell hybrid electric vehicles," ***2018 Annual American Control Conference (ACC)***, Milwaukee, WI, 2018, pp. 6303-6308. doi: 10.23919/ACC.2018.8430898.

[26]. C. Li, G. Liu, Optimal fuzzy power control and management of fuel cell/battery hybrid vehicles, ***Journal of Power Sources***, Volume 192, Issue 2, 2009, Pages 525-533, https://doi.org/10.1016/j.jpowsour.2009.03.007.

[27]. R. Zhang, J. Tao, H. Zhou, "Fuzzy Optimal Energy Management for Fuel Cell and Supercapacitor Systems Using Neural Network Based Driving Pattern Recognition," in ***IEEE Transactions on Fuzzy Systems***, vol. 27, no. 1, pp. 45-57, Jan. 2019. doi: 10.1109/TFUZZ.2018.2856086.

[28]. M. Yue, S. Jemei, N. Zerhouni, "Health-Conscious Energy Management for Fuel Cell Hybrid Electric Vehicles Based on Prognostics-Enabled Decision-Making," in ***IEEE Transactions on Vehicular Technology***, vol. 68, no. 12, pp. 11483-11491, Dec. 2019. doi: 10.1109/TVT.2019.2937130.

[29]. O. Sundstrom, L. Guzzella, "A generic dynamic programming Matlab function," ***2009 IEEE Control Applications, (CCA) & Intelligent Control, (ISIC)***, St. Petersburg, 2009, pp. 1625-1630. doi: 10.1109/CCA.2009.5281131.

[30]. L. Xu, M. Ouyang, J. Li, F. Yang, L. Lu, J. Hua, Application of Pontryagin's Minimal Principle to the energy management strategy of plugin fuel cell electric vehicles, ***International Journal of Hydrogen Energy***, Volume 38, Issue 24, 2013, Pages 10104-10115, https://doi.org/10.1016/j.ijhydene.2013.05.125.

[31]. A. Biswas, A. Emadi, "Energy Management Systems for Electrified Powertrains: State-of-the-Art Review and Future Trends," in ***IEEE Transactions on Vehicular Technology***, vol. 68, no. 7, pp. 6453-6467, July 2019. doi: 10.1109/TVT.2019.2914457.

[32]. J. Bernard, S. Delprat, F. Buechi, T. M. Guerra, "Global Optimisation in the power management of a Fuel Cell Hybrid Vehicle (FCHV)," ***2006 IEEE Vehicle Power and Propulsion Conference***, Windsor, 2006, pp. 1-6. doi: 10.1109/VPPC.2006.364289.

[33]. D. Fares, R. Chedid, S. Karaki, R. Jabr, F. Panik, H. Gabele, Y. Huang, Optimal power allocation for a FCHV based on linear programming and PID controller, ***International Journal of Hydrogen Energy***, Volume 39, Issue 36, 2014, Pages 21724-21738, https://doi.org/10.1016/j.ijhydene.2014.09.020.

[34]. R. Dinnawi, D. Fares, R. Chedid, S. Karaki, R. A. Jabr, "Optimized energy management system for fuel cell hybrid vehicles," MELECON 2014 - ***2014 17th IEEE Mediterranean Electrotechnical Conference***, Beirut, 2014, pp. 97-102. doi: 10.1109/MELCON.2014.6820514.

[35]. S. Caux, Y. Gaoua, P. Lopez, A combinatorial optimisation approach to energy management strategy for a hybrid fuel cell vehicle, ***Energy***, Volume 133, 2017, Pages 219-230, https://doi.org/10.1016/j.energy.2017.05.109.

[36]. Z. Chen, C. C. Mi, R. Xiong, J. Xu, C. You, Energy management of a power-split plug-in hybrid electric vehicle based on genetic algorithm and quadratic programming, ***Journal of Power Sources***, Volume 248, 2014, Pages 416-426, https://doi.org/10.1016/j.jpowsour.2013.09.085.

[37]. X. Hu, C. Zou, X. Tang, T. Liu, L. Hu, "Cost-Optimal Energy Management of Hybrid Electric Vehicles Using Fuel Cell/Battery Health-Aware Predictive Control," in ***IEEE Transactions on Power Electronics***, vol. 35, no. 1, pp. 382-392, Jan. 2020. doi: 10.1109/TPEL.2019.2915675.

[38]. H. Li, A. Ravey, A. N'Diaye, A. Djerdir, A novel equivalent consumption minimization strategy for hybrid electric vehicle powered by fuel cell, battery and supercapacitor, ***Journal of Power Sources***, Volume 395, 2018, Pages 262-270, https://doi.org/10.1016/j.jpowsour.2018.05.078.

[39]. X. Wu, X. Hu, X. Yin, L. Li, Z. Zeng, V. Pickert, Convex programming energy management and components sizing of a plug-in fuel cell urban logistics vehicle, ***Journal of Power Sources***, Volume 423, 2019, Pages 358-366, https://doi.org/10.1016/j.jpowsour.2019.03.044.

[40]. X. Hu, N. Murgovski, L. M. Johannesson, B. Egardt, "Optimal Dimensioning and Power Management of a Fuel Cell/Battery Hybrid Bus via Convex Programming," in ***IEEE/ASME Transactions on Mechatronics***, vol. 20, no. 1, pp. 457-468, Feb. 2015. doi: 10.1109/TMECH.2014.2336264.

[41]. X. Hu, L. Johannesson, N. Murgovski, B. Egardt, Longevity-conscious dimensioning and power management of the hybrid energy storage system in a fuel cell hybrid electric bus, ***Applied Energy***, Volume 137, 2015, Pages 913-924, https://doi.org/10.1016/j.apenergy.2014.05.013.

[42]. Y. Huang, H. Wang, A. Khajepour, H. He, J. Ji, Model predictive control power management strategies for HEVs: A review, ***Journal of Power Sources***, Volume 341, 2017, Pages 91-106, https://doi.org/10.1016/j.jpowsour.2016.11.106.

[43]. J. P. F. Trovão, V. D. N. Santos, P. G. Pereirinha, H. M. Jorge, C. H. Antunes, "A Simulated Annealing Approach for Optimal Power Source Management in a Small EV," in ***IEEE Transactions on Sustainable Energy***, vol. 4, no. 4, pp. 867-876, Oct. 2013. doi: 10.1109/TSTE.2013.2253139.

[44]. R. Koubaa, L. krichen, Double layer meta heuristic based energy management strategy for a Fuel Cell/Ultra-Capacitor hybrid electric vehicle, ***Energy***, Volume 133, 2017, Pages 1079-1093, https://doi.org/10.1016/j.energy.2017.04.070.

[45]. H. Li. Energy consumption minimization strategy for fuel cell hybrid electric vehicles. ***PhD Thesis. Université Bourgogne Franche-Comté***, 2018. English. NNT: 2018UBFCA034. tel-02084175. https://tel.archives-ouvertes.fr/tel-02084175.

[46]. R. Eberhart, J. Kennedy, "A new optimizer using particle swarm theory," MHS'95. ***Proceedings of the Sixth International Symposium on Micro Machine and Human Science***, Nagoya, Japan, 1995, pp. 39-43. doi: 10.1109/MHS.1995.494215.

[47]. Q. Jiang, F. Ossart, C. Marchand, "Comparative Study of Real-Time HEV Energy Management Strategies," in ***IEEE Transactions on Vehicular Technology***, vol. 66, no. 12, pp. 10875-10888, Dec. 2017, doi: 10.1109/TVT.2017.2727069.

[48]. Q. Jiang, O. Béthoux, F. Ossart, E. Berthelot, C. Marchand, A comparison of real-time energy management strategies of FC/SC hybrid power source: Statistical analysis using random cycles, ***International Journal of Hydrogen Energy***, 2020, https://doi.org/10.1016/j.ijhydene.2020.06.003.

[49]. Lahlou A., Ossart F., Boudard E., Roy F. Bakhouya M. A Real-Time Approach for Thermal Comfort Management in Electric Vehicles. ***Energies*** 2020, 13, 4006. https://doi.org/10.3390/en13154006.

[50]. Paganelli G, Guerra TM, Delprat S, Santin J-J, Delhom M, Combes E. Simulation and assessment of power control strategies for a parallel hybrid car. ***Proc Inst Mech Eng - Part D J Automob Eng*** 2000;214:705–17. https://doi.org/10.1243/ 0954407001527583.

[51]. P. García, J.P. Torreglosa, L.M. Fernández, F. Jurado, Viability study of a FC-battery-SC tramway controlled by equivalent consumption minimization strategy, ***International Journal of Hydrogen Energy***, Volume 37, Issue 11, 2012, Pages 9368-9382, https://doi.org/10.1016/j.ijhydene.2012.02.184.

[52]. C. Sun, F. Sun, H. He, Investigating adaptive-ECMS with velocity forecast ability for hybrid electric vehicles, ***Applied Energy***, Volume 185, Part 2, 2017, Pages 1644-1653, https://doi.org/10.1016/j.apenergy.2016.02.026.

[53]. Sinoquet, D., Rousseau, G. & Milhau, Y. Design optimization and optimal control for hybrid vehicles. ***Optim Eng*** 12, 199–213 (2011). https://doi.org/10.1007/s11081-009-9100-8.

[54]. C.H. Zheng, G.Q. Xu, Y.I. Park, W.S. Lim, S.W. Cha, Prolonging fuel cell stack lifetime based on Pontryagin's Minimum Principle in fuel cell hybrid vehicles and its economic influence evaluation, ***Journal of Power Sources***, Volume 248, 2014, Pages 533-544, https://doi.org/10.1016/j.jpowsour.2013.09.110.

[55]. S. Xie, H. Li, Z. Xin, T. Liu, L. Wei, A Pontryagin minimum principle-based adaptive equivalent consumption minimum strategy for a plug-in hybrid electric bus on a fixed route, ***Energies***, 10 (9) (2017), pp. 1379-1399. https://doi.org/10.3390/en10091379.

[56]. S. Xie, X. Hu, S. Qi, K. Lang, An artificial neural network-enhanced energy management strategy for plug-in hybrid electric vehicles, ***Energy***, Volume 163, 2018, Pages 837-848, https://doi.org/10.1016/j.energy.2018.08.139.

[57]. S. Zhang, X. Hu, S. Xie, Z. Song, L. Hu, C. Hou, Adaptively coordinated optimization of battery aging and energy management in plug-in hybrid electric buses, ***Applied Energy***, Volume 256, 2019, 113891, https://doi.org/10.1016/j.apenergy.2019.113891.

[58]. Li L, Huang H, Lian J, Yao B, Zhou Y, Chang J, Ning'an Z, Research of ant colony optimized adaptive control strategy for hybrid electric vehicle. ***Mathematical Problems in Engineering.*** 2014;2014:1–10. https://doi.org/10.1155/2014/239130.

[59]. X. Li, Y. Wang, D. Yang, Z. Chen, Adaptive energy management strategy for fuel cell/battery hybrid vehicles using Pontryagin's Minimal Principle, ***Journal of Power Sources***, Volume 440, 2019, 227105, https://doi.org/10.1016/j.jpowsour.2019.227105.

[60]. J. Han, Y. Park, Y. Park, A novel updating method of equivalent factor in ECMS for prolonging the lifetime of battery in fuel cell hybrid electric vehicle, ***IFAC Proceedings Volumes***, Volume 45, Issue 30, 2012, Pages 227-232, https://doi.org/10.3182/20121023-3-FR-4025.00059.

[61]. D. Shen, C. Lim, P. Shi, Robust fuzzy model predictive control for energy management systems in fuel cell vehicles, ***Control Engineering Practice***, Volume 98, 2020, 104364,

https://doi.org/10.1016/j.conengprac.2020.104364.
[62]. C. Sun, S. J. Moura, X. Hu, J. K. Hedrick, F. Sun, "Dynamic Traffic Feedback Data Enabled Energy Management in Plug-in Hybrid Electric Vehicles," in ***IEEE Transactions on Control Systems Technology***, vol. 23, no. 3, pp. 1075-1086, May 2015. doi: 10.1109/TCST.2014.2361294.
[63]. Y. Zhou, A. Ravey, M.C. Péra, Multi-mode predictive energy management for fuel cell hybrid electric vehicles using Markov driving pattern recognizer, ***Applied Energy***, Volume 258, 2020, 114057, https://doi.org/10.1016/j.apenergy.2019.114057.
[64]. Y. Zhou, H. Li, A. Ravey, M.C. Péra, An integrated predictive energy management for light-duty range-extended plug-in fuel cell electric vehicle, ***Journal of Power Sources***, Volume 451, 2020, 227780, https://doi.org/10.1016/j.jpowsour.2020.227780.
[65]. T. Li, H. Liu, H. Wang, Y. Yao, Hierarchical predictive control-based economic energy management for fuel cell hybrid construction vehicles, ***Energy***, Volume 198, 2020, 117327, https://doi.org/10.1016/j.energy.2020.117327.
[66]. T. Li, H. Liu, D. Ding, Predictive energy management of fuel cell supercapacitor hybrid construction equipment, ***Energy***, Volume 149, 2018, Pages 718-729, https://doi.org/10.1016/j.energy.2018.02.101.
[67]. T. Li, L. Huang, H. Liu, Energy management and economic analysis for a fuel cell supercapacitor excavator, ***Energy***, Volume 172, 2019, Pages 840-851, https://doi.org/10.1016/j.energy.2019.02.016.
[68]. Yazdani, A., Bidarvatan, M., "Real-Time Optimal Control of Power Management in a Fuel Cell Hybrid Electric Vehicle: A Comparative Analysis," ***SAE International Journal of Alternative Powertrains***. 7(1):43-54, 2018, https://doi.org/10.4271/08-07-01-0003.
[69]. S. D. Cairano, D. Bernardini, A. Bemporad, I. V. Kolmanovsky, "Stochastic MPC With Learning for Driver-Predictive Vehicle Control and its Application to HEV Energy Management," in ***IEEE Transactions on Control Systems Technology***, vol. 22, no. 3, pp. 1018-1031, May 2014. doi: 10.1109/TCST.2013.2272179.
[70]. F. Payri, C. Guardiola, B. Pla, D. Blanco-Rodriguez, A stochastic method for the energy management in hybrid electric vehicles, ***Control Engineering Practice***, Volume 29, 2014, Pages 257-265, https://doi.org/10.1016/j.conengprac.2014.01.004.
[71]. X. Zeng, J. Wang, "A Parallel Hybrid Electric Vehicle Energy Management Strategy Using Stochastic Model Predictive Control With Road Grade Preview," in ***IEEE Transactions on Control Systems Technology***, vol. 23, no. 6, pp. 2416-2423, Nov. 2015. doi: 10.1109/TCST.2015.2409235.
[72]. H. Borhan, A. Vahidi, A. M. Phillips, M. L. Kuang, I. V. Kolmanovsky, S. Di Cairano, "MPC-Based Energy Management of a Power-Split Hybrid Electric Vehicle," in ***IEEE Transactions on Control Systems Technology***, vol. 20, no. 3, pp. 593-603, May 2012.doi: 10.1109/TCST.2011.2134852.
[73]. F. Ma, Y. Yang, J. Wang, Z. Liu, J. Li, J. Nie, Y. Shen, L. Wu, Predictive energy-saving optimization based on nonlinear model predictive control for cooperative connected vehicles platoon with V2V communication, ***Energy***, Volume 189, 2019, 116120, https://doi.org/10.1016/j.energy.2019.116120.
[74]. V. Ngo, T. Hofman, M. Steinbuch, A. Serrarens, "Predictive gear shift control for a parallel Hybrid Electric Vehicle," ***2011 IEEE Vehicle Power and Propulsion Conference***, Chicago, IL, 2011, pp. 1-6.doi: 10.1109/VPPC.2011.6043185.
[75]. D. Shen, C. Lim, P. Shi, P. Bujlo, "Energy Management of Fuel Cell Hybrid Vehicle Based on Partially Observable Markov Decision Process," in ***IEEE Transactions on Control Systems Technology***, vol. 28, no. 2, pp. 318-330, March 2020. doi: 10.1109/TCST.2018.2878173.
[76]. C. Sun, X. Hu, S. J. Moura, F. Sun, "Velocity Predictors for Predictive Energy Management in Hybrid Electric Vehicles," in ***IEEE Transactions on Control Systems Technology***, vol. 23, no. 3, pp. 1197-1204, May 2015. doi: 10.1109/TCST.2014.2359176.
[77]. Y. Zhou, A. Ravey, M.C. Péra, A survey on driving prediction techniques for predictive energy management of plug-in hybrid electric vehicles, ***Journal of Power Sources***, Volume 412, 2019, Pages 480-495, https://doi.org/10.1016/j.jpowsour.2018.11.085.
[78]. X. Li, L. Han, H. Liu, W. Wang, C. Xiang, Real-time optimal energy management strategy for a dual-mode power-split hybrid electric vehicle based on an explicit model predictive control algorithm, ***Energy***, Volume 172, 2019, Pages 1161-1178, https://doi.org/10.1016/j.energy.2019.01.052.
[79]. C. Xiang, F. Ding, W. Wang, W. He, Energy management of a dual-mode power-split hybrid electric vehicle based on velocity prediction and nonlinear model predictive control, ***Applied Energy***, Volume 189, 2017, Pages 640-653, https://doi.org/10.1016/j.apenergy.2016.12.056.
[80]. L. Nieto Degliuomini, D. Zumoffen, M. Basualdo, D. Feroldi, J. Riera, "Adaptive predictive robust control for fuel cells hybrid vehicles," ***2010 IEEE Vehicle Power and Propulsion Conference, Lille***, 2010, pp. 1-6. doi: 10.1109/VPPC.2010.5729254.

[81]. D. Zhou, A. Al-Durra, I. Matraji, A. Ravey, F. Gao, "Online Energy Management Strategy of Fuel Cell Hybrid Electric Vehicles: A Fractional-Order Extremum Seeking Method," in ***IEEE Transactions on Industrial Electronics***, vol. 65, no. 8, pp. 6787-6799, Aug. 2018. doi: 10.1109/TIE.2018.2803723.

[82]. D. Zhou, A. Ravey, A. Al-Durra, F. Gao, A comparative study of extremum seeking methods applied to online energy management strategy of fuel cell hybrid electric vehicles, ***Energy Conversion and Management***, Volume 151, 2017, Pages 778-790, https://doi.org/10.1016/j.enconman.2017.08.079.

[83]. N. Bizon, A. G. Mazare, L. M. Ionescu, F. M. Enescu, Optimization of the proton exchange membrane fuel cell hybrid power system for residential buildings, ***Energy Conversion and Management***, Volume 163, 2018, Pages 22-37, https://doi.org/10.1016/j.enconman.2018.02.025.

[84]. D. Di Domenico, G. Fiengo, "A decoupled controller for fuel cell hybrid electric power split," ***2008 American Control Conference***, Seattle, WA, 2008, pp. 597-604. doi: 10.1109/ACC.2008.4586557.

[85]. Moré, J.J., Puleston, P.F., Fossas, E. Cristian, K. Decoupled inputs sliding mode controllers for a fuel cell-supercapacitor module in hybrid generation applications. ***International Journal of Energy and Environment Engineering***. 10, 257–269 (2019). https://doi.org/10.1007/s40095-019-0307-y.

[86]. M.Y. Ayad, M. Becherif, A. Henni, Vehicle hybridization with fuel cell, supercapacitors and batteries by sliding mode control, ***Renewable Energy***, Volume 36, Issue 10, 2011, Pages 2627-2634, https://doi.org/10.1016/j.renene.2010.06.012.

[87]. Y. Liu, J. Liu, D. Qin, G. Li, Z. Chen, Y. Zhang, Online energy management strategy of fuel cell hybrid electric vehicles based on rule learning, ***Journal of Cleaner Production***, Volume 260, 2020, 121017, https://doi.org/10.1016/j.jclepro.2020.121017.

[88]. H. Sun, Z. Fu, F. Tao, L. Zhu, P. Si, Data-driven reinforcement-learning-based hierarchical energy management strategy for fuel cell/battery/ultracapacitor hybrid electric vehicles, ***Journal of Power Sources***, Volume 455, 2020, 227964, https://doi.org/10.1016/j.jpowsour.2020.227964.

[89]. J. Yuan, L. Yang, Q. Chen, Intelligent energy management strategy based on hierarchical approximate global optimization for plug-in fuel cell hybrid electric vehicles, ***International Journal of Hydrogen Energy***, Volume 43, Issue 16, 2018, Pages 8063-8078, https://doi.org/10.1016/j.ijhydene.2018.03.033.

[90]. M. M. Morato, J. E. Normey-Rico, O. Sename, Model predictive control design for linear parameter varying systems: A survey, ***Annual Reviews in Control***, Volume 49, 2020, Pages 64-80, https://doi.org/10.1016/j.arcontrol.2020.04.016.

[91]. M. M. Morato, M. Q. Nguyen, O. Sename, L. Dugard, Design of a fast real-time LPV model predictive control system for semi-active suspension control of a full vehicle, ***Journal of the Franklin Institute***, Volume 356, Issue 3, 2019, Pages 1196-1224, https://doi.org/10.1016/j.jfranklin.2018.11.016.

[92]. S. Olivier, P. Gaspar, J. Bokor, eds. Robust control and linear parameter varying approaches: application to vehicle dynamics. Vol. 437. ***Springer***, 2013. Doi: 10.1007/978-3-642-36110-4.

[93]. Matlab documentation: Time-varying MPC, https://www.mathworks.com/help/mpc/ug/time-varying-mpc.html.

[94]. S. Di Cairano, W. Liang, I. V. Kolmanovsky, M. L. Kuang, A. M. Phillips, "Power Smoothing Energy Management and Its Application to a Series Hybrid Powertrain," in ***IEEE Transactions on Control Systems Technology***, vol. 21, no. 6, pp. 2091-2103, Nov. 2013. doi: 10.1109/TCST.2012.2218656.

[95]. Tanaka K., Wang H.O. Fuzzy control systems design and analysis: a linear matrix inequality approach John ***Wiley & Sons*** (2004).

[96]. X. Chen, H. Lei, R. Xiong, W. Shen, R. Yang, A novel approach to reconstruct open circuit voltage for state of charge estimation of lithium ion batteries in electric vehicles, ***Applied Energy***, Volume 255, 2019, 113758, https://doi.org/10.1016/j.apenergy.2019.113758.

[97]. J. Tian, R. Xiong, W. Shen, "State of health estimation based on differential temperature for lithium ion batteries," in ***IEEE Transactions on Power Electronics***. doi: 10.1109/TPEL.2020.2978493.

[98]. S. East, M. Cannon, "Energy Management in Plug-In Hybrid Electric Vehicles: Convex Optimization Algorithms for Model Predictive Control," in ***IEEE Transactions on Control Systems Technology***. doi: 10.1109/TCST.2019.2933793.

[99]. S. East, M. Cannon, "An ADMM Algorithm for MPC-based Energy Management in Hybrid Electric Vehicles with Nonlinear Losses," ***2018 IEEE Conference on Decision and Control (CDC)***, Miami Beach, FL, 2018, pp. 2641-2646. doi: 10.1109/CDC.2018.8619731.

# Chapter 3. Development of driving prediction techniques

## 3.1. Introduction

As discussed in **Chapter 2**, we select model predictive control (MPC) as the real-time decision-making framework in the development of predictive energy management strategies. It should be mentioned that the power allocation decisions made by MPC is based on the anticipation of future system behaviors. In our case, the system's future behaviors are greatly affected by the upcoming power demands over each rolling optimization horizon. Considering the dependency between the propulsion power request and the velocity trajectory of vehicles, it is thus necessary to study how to precisely estimate the distribution of vehicle's future speed profiles. This yields the necessity of investigating the advanced driving prediction techniques, which is one of major research focuses of this thesis. Although numerous efforts have been made on this subject, further improvement of prediction quality (accuracy and robustness) can be made by bridging the following knowledge gaps: (i) how to enhance the prediction accuracy in face of the discrepancy between the offline training database and the online realistic driving conditions; (ii) how to improve the prediction reliability under vehicles' different driving stages; (iii) For plug-in hybrid electric vehicles, how to plan battery energy usage under changeable driving patterns in a time-efficient manner with the assistance of partially previewed route information; (iv) how to effectively identify the real-time driving patterns based on the recent measurements, so as to guarantee the adaptability of control strategies towards the changes of driving conditions.

To address the aforementioned issues, **Chapter 3** presents the development of driving prediction techniques, which is organized as follows:

In subsection 3.2, two widely used data-driven speed prediction methods are introduced at first, namely a back propagation neural network (BPNN) predictor and a multi-step Markov Chain (MSMC) predictor. Subsequently, an online-learning enhanced MC predictor is proposed, which can automatically adapt to the newly-encountered driving conditions via updating its transition probability matrices (TPM) using real-time measured driving data. Moreover, a cooperative Markov speed forecast approach assisted by fuzzy C-means clustering technique is presented, which contains multiple predictive sub-models for handling different vehicles' operation stages.

In subsection 3.3, with the help of the real-time updated speed forecasting results, an adaptive integrable battery SoC reference generator is devised for guiding the future battery energy usage under different driving conditions, whose performance is compared with the benchmark: a linear SoC reference model.

In subsection 3.4, a driving pattern recognition (DPR) approach based on Markov Chain and moving window technique is proposed, where the transition probability matrices of Markov Chain is used to characterize the velocity-acceleration transition behavior of each driving segment. Thereafter, the real-time pattern identification results are derived by quantifying the resemblance between the online-

estimated TPM and the offline-benchmark TPM.

A brief summary of the major works and the conclusions are presented in the subsection 3.5.

## 3.2. Speed forecasting techniques

Subsection 3.2 presents the development of speed forecasting methods to fulfil the MPC's rolling optimization framework. Firstly, two widely used prediction methods are introduced as the benchmarks, namely a back propagation neural network (BPNN)-based speed predictor and a multi-step Markov Chain (MSMC)-based speed predictor. Thereafter, several improved speed predictors based on layer recurrent neural network (LRNN), online-learning enhanced Markov Chain (OL-MC) and fuzzy C-means clustering enhanced Markov Chain (FCM-MC) are proposed to enhance the prediction quality of benchmark predictors.

### 3.2.1. Benchmark speed predictors

To establish a basis for forecast performance comparison, two commonly used speed predictors are introduced as the benchmark, namely a multi-step MC (MSMC) predictor and a BPNN predictor.

#### 3.2.1.1. Multi-step Markov Chain speed predictor

Considering the driving uncertainties in reality, vehicle's future acceleration can be deemed as a stochastic process, which can be modelled by the Markov Chain. In this thesis, taken vehicle's acceleration as the Markov state, under the interval-encoding framework [1], the continuous acceleration domain is discretized by several disjoint intervals $I_j, j \in \{1, \dots, s\}$, where every interval midpoint is tagged by a single Markov state, marked as $a_j \in I_j$ . Subsequently, a countable set $X_a = \{a_1, \dots, a_s\}$ containing all feasible acceleration states defines the state space of Markov Chain. For multi-step prediction purpose, a transition probability matrix (TPM) group $T_G = \left\{T_1, \dots, T_{H_p}\right\}$ should be established, where the $l^{th}$ element in $T_G$ is an s-order square matrix denoting the $l$-step ahead probability distribution ($l \in \{1, \dots, H_p\}$, $H_p$ is the prediction horizon). Its element in the $i^{th}$ row and $j^{th}$ column, denoted as $[T_l]_{ij}$, indicates the probability of state transition from $a_i$ to $a_j, i, j \in \{1, \dots, s\}$, where the value of $[T_l]_{ij}$ can be estimated by [1]:

$$[T_l]_{ij} = \Pr\{a(k+l) = a_j | a(k) = a_i\} \approx \frac{\mathbf{Num}_{ij}^l}{\mathbf{Num}_{oi}^l}, l \in \{1, \dots, H_p\}, i, j \in \{1, \dots, s\}. \quad (3.1)$$

Where $\mathbf{Num}_{ij}^l$ and $\mathbf{Num}_{oi}^l$ are the numbers of Markov state transition, with the superscript $l$ being the time step and the two subscripts being the indices of transition incidents (e.g. $ij$ for the transitions from $a_i$ to $a_j$, whereas $oi$ for the transitions originating from $a_i$). Based on the standard driving cycles with multiple driving patterns extracted from ADVISOR [2] (see figure 3.1), figure 3.2 gives a graphic representation of a one-step 50×50 TPM ($l = 1, s = 50$). Once the TPM group $T_G$ is established by Eq.

(3.1), given the $k^{th}$ acceleration state $a(k)$, the acceleration in future $l$-step ahead can be forecasted by the probability maximization [1]:

$$a^*(k+l) = a_j, if\ a(k) \in I_i, j \in \arg\max_k [T_l]_{ik} \tag{3.2}$$

or, alternatively, by the probability-weighted average (expected value) of each interval mid-point [1]:

$$a^*(k+l) = \sum_{j=1}^{s} [T_l]_{ij} \cdot a_j, if\ a(k) \in I_i \tag{3.3}$$

Correspondingly, the $l$-step ahead velocity $v^*(k+l)$ can be derived by:

$$v^*(k+l) = v(k) + \sum_{q=1}^{q=l} a^*(k+q) \cdot \Delta T \tag{3.4}$$

Where $v(k)$ is the $k^{th}$ speed sample and $\Delta T$ is the discrete sampling time interval.

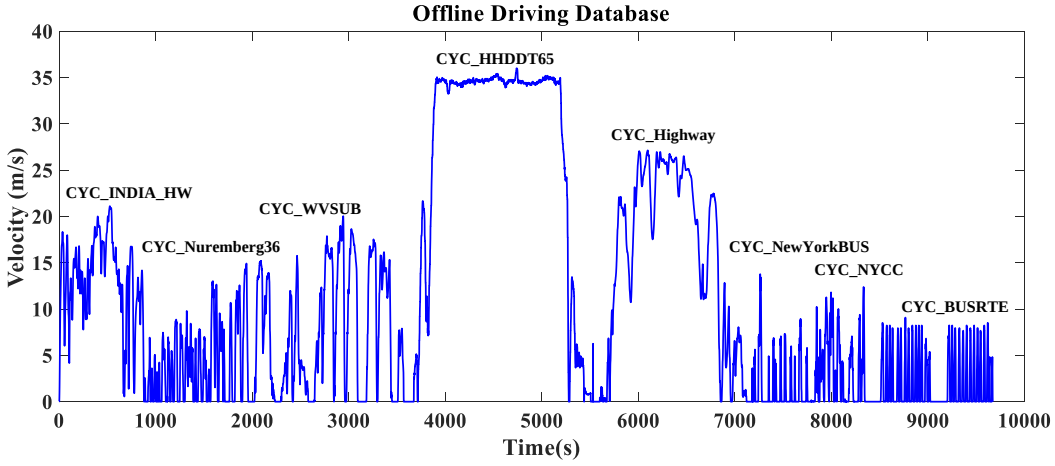


Figure 3.1. Multiple standard driving cycles extracted from ADVISOR simulator [2].

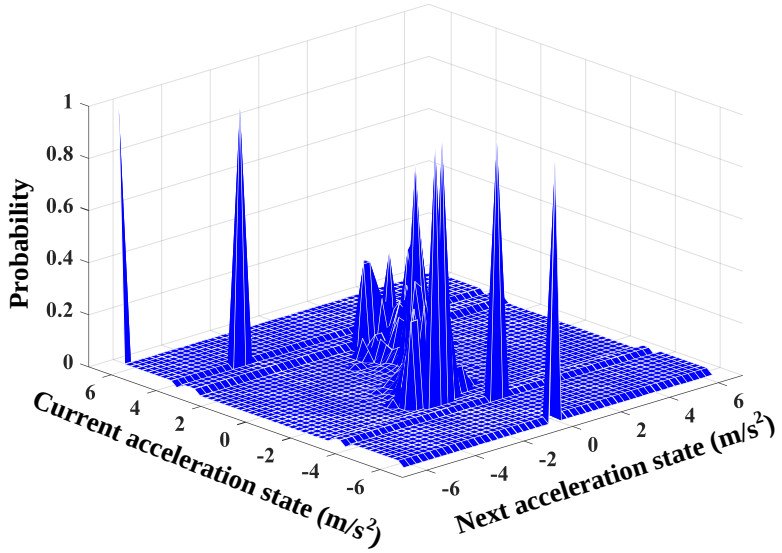


Figure 3.2. Example of one-step TPM with 50 Markov states ($l = 1, s = 50$).

To increase the speed prediction accuracy, single-order MC model can be extended to $q$-order ($q > 1$)

MC model by using the following definition of transition probability [3]:

$$\Pr\left[a(k+l)=a_j|a(k)=a_{i_0},a(k-1)=a_{i_1},\dots,a(k-q+1)=a_{i_q}\right],l\in\{1,\dots,H_p\} \quad (3.5)$$

Where $q$ is the order of Markov Chain. Obviously, with the growth of $q$, more historical driving samples are required to compute the transition probability, thus increasing the resolution of TPM and eventually the precision of speed prediction. In fact, at least $s\times s$ samples are required to cover all possible input states for single-order Markov Chain, where this number grows to $s\times s^q$ for a $q$-order Markov Chain. In this case, the increased size of high-order TPM needs huge amount of driving data, which leads to the difficulty in actual applications. Besides, the corresponding exponentially increased computational and memory burden would also hinder the real application of high-order MC in speed prediction field [3].

### 3.2.1.2. Back propagation neural network speed predictor

As indicated in **Chapter 1**, another commonly used predictor in vehicular EMS field is based on neural networks (NN), due to their proven capacity in learning predictive knowledge from available dataset and then reproducing the similar behaviors in future tasks [4]. Compared to single-order Markov Chain-based prediction models, which are powerful in characterizing stochastic processes (e.g. acceleration), NN is an advanced tool in modeling nonlinear time-series by mapping multiple historical signal values into future ones, which has been intensively proven effective for speed-forecasting in previous researches [3]-[6]. Despite various NN variants (e.g. radial basis functional NN (RBF-NN) [5], nonlinear autoregressive NN (NARNN) [6], etc.) for speed forecasting, the most widely-used one is back propagation NN (BPNN). A three-layer BPNN has a hierarchical feed forward network structure, which is the basis of other network structures. Figure 3.3 depicts the structure of a three-layer BPNN predictor.

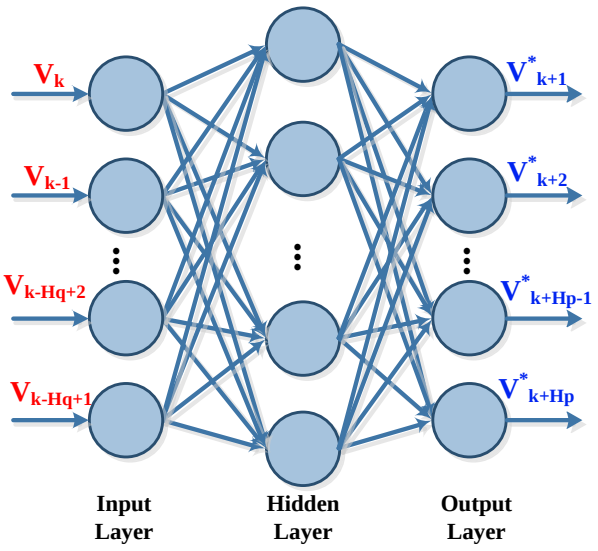


Figure 3.3. Graphic representation of a three-layer BPNN speed predictor.

As can be seen, the input layer of BPNN receives historical speed vector $V_k = \left[v_{k-H_q+1}, \dots, v_{k-1}, v_k\right]$, the hidden layer approximates the nonlinear relationship in time-series through the connections between input and hidden neurons with proper weights and bias vectors, and the output layer converts the hidden outputs into future speeds $V_k^* = \left[v_{k+1}^*, v_{k+2}^*, \dots, v_{k+H_p}^*\right]$. $H_q$ and $H_p$ respectively denote the input and output size of BPNN. Mathematically, BPNN predictor is a multi-input-multi-output function that maps the input speed sequence into future ones, as given below:

$$\left[v_{k+1}^*, v_{k+2}^*, \dots, v_{k+H_p}^*\right] = f_{\text{BPNN}}\left(v_{k-H_q+1}, \dots, v_{k-1}, v_k\right) \tag{3.6}$$

or, alternatively, as the following form:

$$V_k^* = \mathbf{purelin}(W_{HO} \cdot \mathbf{tansig}(W_{IH} \cdot V_k + b_H) + b_O) \tag{3.7}$$

Where **tansig** and **purelin** respectively represent the hyperbolic tangent-sigmoid and linear transfer function, $W_{IH}, W_{HO}$ respectively the weight vectors from input to hidden layer and from hidden to output layer, $b_H, b_O$ the bias vectors in hidden and output layer, respectively. To guarantee a satisfied prediction performance, the weights and bias of BPNN should be tuned to minimize the discrepancy between the NN outputs and the target output on the available dataset, with such process termed as NN training. However, BPNN suffers from two major drawbacks: (i) the slow convergence rate, and (ii) the risk of being trapped into the local optima in training phase.

Although MSMC and BPNN predictors have been widely applied in previous studies, their limitations are also obvious. In order to improve the prediction quality of the benchmark predictors, several speed-forecast approaches are put forwarded in the following parts of subsection 3.2.

### 3.2.2. Layer recurrent neural network speed predictor

To overcome the deficiency of BPNN, we propose the use of layer recurrent neural network (LRNN) for speed prediction. LRNN is one type of recurrent neural network (RNN), which is a connectionist model including a self-connected hidden layer. The biggest advantage of the recurrent connection is that a "memory" of previous inputs remains in the network's internal state [7]. The structure of the proposed LRNN speed predictor is depicted in figure 3.4. As can be seen, the LRNN consists of an input layer, multiple middle layers and an output layer. Please note the output of each middle layer is feedback to itself with a time delay. Such recurrent network structure helps the LRNN to store historical temporal information, thus better capturing the dynamics in a time-series in contrast to a basic BPNN.

Likewise, the function of LRNN predictor can be written as follows:

$$\left[v_{k+1}^*, v_{k+2}^*, \dots, v_{k+H_p}^*\right] = f_{\text{LRNN}}\left(v_{k-H_q+1}, \dots, v_{k-1}, v_k\right) \tag{3.8}$$

To tradeoff between the performance optimality and NN complexity, the parameter configuration of

middle layers should be carefully determined, including the number of middle layer and the number of neurons in each middle layer. As reported in [8], a multi-layer NN structure may result in higher prediction precision. Therefore, by numerous trial and errors, the number of LRNN middle layer is set to three and the number of nodes in each middle layer are respectively {3, 4, 6}. To give the reason of using such middle layer node configuration, a sensitivity analysis will be conducted afterwards to detail the related determination process. Finally, the hyperbolic tangent-sigmoid transfer function (**tansig**) is picked as the activation function.

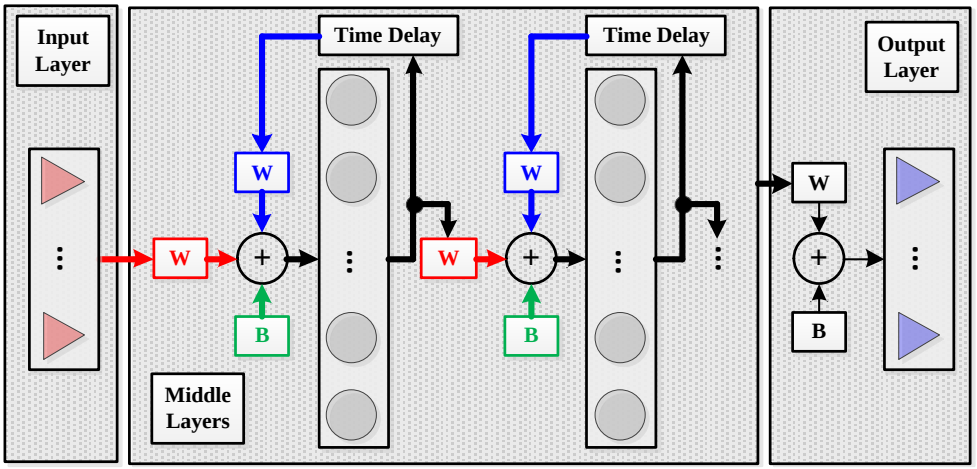


Figure 3.4. Schematic diagram of the LRNN predictor.

In addition, based on the literature survey and the results presented in [3],[8], it is suggested to set the length of speed forecast horizon to 1-10 seconds (with sampling time period being 1 second) in vehicular energy management problems. The reasons for such settings are given as follows: (i) high precision of speed forecast in a longer time horizon is hard to achieve due to a variety of unpredictable traffic factors; (ii) the heavy computation burden for online optimization over a longer prediction horizon may degrade the real-time practicality of corresponding control strategies. Therefore, in this study, the upper limit for velocity prediction horizon is set to 10s, while the length of input speed sequence for NN-based predictors is set the same as the prediction horizon.

Due to the data-driven characteristics of the aforementioned speed predictors, the estimation of Markov TPM and the training of NN should be accomplished based on a comprehensive driving database. To guarantee a satisfied prediction accuracy, this driving database should contain abundant driving cycles representing different driving scenarios. To this end, eight standard driving cycles, namely INDIA_HW, Nuremberg36, WVSUB, HHDDT65, Highway, NewYorkBUS, NYCC and BUSRTE, are concatenated to form the offline driving database, as shown in figure 3.1. It should be noted that the Nuremberg36, NewYorkBUS, NYCC and BUSRTE represent the typical city driving scenarios, where the average speed is low and frequent vehicle starts-stops can be observed. In contrast, INDIA_HW and WVSUB denote the suburban driving scenarios, where the average speed is increased and the vehicle stop per

kilometer is decreased compared to city driving scenarios. In addition, HHDDT65 and Highway represent the highway driving scenarios, which have much higher average speed compared to urban/suburban scenarios and no vehicle stop can be observed within the entire cycle. Please note these standard driving cycles with multiple driving patterns (urban/suburban/highway) are extracted from the advanced vehicular simulator ADVISOR [2].

Thereafter, another standard driving cycle, Urban Dynamometer Driving Schedule (UDDS), is picked from ADVISOR to validate the performance of three speed predictors. The root-mean-square-error (RMSE) over the k-th prediction horizon and over the entire driving cycle are used as the evaluation metric for forecast precision, as calculated by Eq.(3.9a) and Eq.(3.9b), respectively:

$$\begin{cases} \mathrm{RMSE}(k) = \sqrt{\frac{1}{H_p}\sum_{q=1}^{q=H_p}\left(v^*(k+q) - v(k+q)\right)^2} & (a) \\ \overline{\mathrm{RMSE}} = \frac{1}{N_{cycle}}\sum_{k=1}^{k=N_{cycle}} \mathrm{RMSE}(k) & (b) \end{cases} \tag{3.9}$$

- **Impact of percentage of training sample and middle layer configuration**

Before online implementation, a sensitivity analysis is conducted to explore the impacts on prediction accuracy of LRNN predictor caused by different percentage of network training samples and different node combinations in LRNN middle layer, so as to find the most appropriate parameter settings of LRNN to further improve the quality of speed prediction.

Firstly, to study the impact on prediction accuracy by different ratios of network training sample (note the training sample ratio is defaulted at 70% in MATLAB Neural Fitting toolbox), the LRNN is trained with seven different percentage of driving data, and then the performance is tested under the UDDS driving cycle. Please note that the middle layer configuration of LRNN is {3,4,6}. TABLE 3.1 details the prediction results under different training percentage. As can be seen, with the increment of training ratio from 35% to 85%, the forecast accuracy of LRNN is improved when $H_p$ = 3, 5 and 10s. This is mainly because, with a higher ratio of training sample, LRNN can learn predictive knowledge from a wider range of driving scenarios, thereby increasing its forecast precision in face of the newly-encountered driving conditions. Nevertheless, too much training sample (e.g. 95%) would degrade the prediction accuracy to some extent, since an over high ratio of training sample would compromise the generalization capacity of LRNN, thus reducing the prediction accuracy. As a result, the ratio of training sample is set to 85% since it can improve the prediction accuracy without over degrading the network generalization capacity.

Moreover, we keep using 85% of driving data (8227 out of 9479 speed samples) presented in figure 3.1 as the training sample for LRNN. Thereafter, by maintaining the three-middle-layer structure unchanged, the total number of middle nodes as a constant (e.g. in our case, 13), and altering the node numbers in the first two middle layers, LRNN predictor is tested under UDDS driving cycle, with the average

prediction error (RMSE) under different node combinations listed in TABLE 3.2. As can be observed, when $H_p$ = 3, 5 and 10s, the highest prediction accuracy is achieved under the middle layer configuration III, namely {3,4,6}.

TABLE 3.1. Average RMSE (km/h) under different training data percentage.

| | **35%** | **45%** | **55%** | **65%** | **75%** | **85%** | **95%** |
|---|---|---|---|---|---|---|---|
| **$H_p$ = 3s** | 1.75 | 1.78 | 1.82 | 1.74 | 1.72 | 1.67 | 1.70 |
| **$H_p$ = 5s** | 3.00 | 2.98 | 3.06 | 2.96 | 2.91 | 2.85 | 2.97 |
| **$H_p$ =10s** | 6.31 | 6.31 | 6.43 | 6.29 | 6.20 | 6.09 | 6.28 |

TABLE 3.2. Average RMSE (km/h) under different node combinations of LRNN middle layer.

| **$H_p$** | **Config. I {1,6,6}** | **Config. II {2,5,6}** | **Config. III {3,4,6}** | **Config. IV {4,3,6}** | **Config. V {5,2,6}** | **Config. VI {6,1,6}** |
|---|---|---|---|---|---|---|
| **3s** | 2.66 | 1.81 | 1.67 | 2.08 | 3.04 | 2.89 |
| **5s** | 3.46 | 2.92 | 2.85 | 3.12 | 3.76 | 3.59 |
| **10s** | 6.72 | 6.21 | 6.09 | 6.22 | 6.75 | 6.70 |

To sum up, based on the results of sensitivity analysis, for LRNN predictor, 85% of data in offline driving database is used for network training while the remaining 15% is for performance validation, and the hidden layer node configuration is set to {3,4,6} for online implementation.

- **Performance comparison with benchmark predictors**

In this part, the prediction performance of LRNN approach and two benchmark methods are compared under UDDS testing cycle. Figure 3.5 depicts their performance discrepancy (global view), where the blue and red curves respectively denote the real speed and the forecasted speed over each prediction horizon. The length of prediction $H_p$ = 10s with the sampling time interval $\Delta T = 1s$. The number of MC state is set to 50 and the MC order is set to one.

As shown in figure 3.5, due to the stochastic nature of Markov Chain, the speed prediction results of multi-step Markov Chain (MSMC) tend to diverge significantly from the actual speed traces, thus leading to the largest prediction error among three approaches. Besides, since the order of MC is set to one, the MSMC predictor forecasts the future velocity distributions only based on the current driving state, making it hard to describe the blended and changeable driving behaviors.

In contrast, when using more historical speed samples for prediction, the back propagation neural network (BPNN) predictor characterizes the future velocity distributions in a more convincing manner, leading to the quality enhancement of prediction. Benefiting from the additional "memory" effect imposed by the recurrent network structure, the forecasted speed profiles of LRNN approach distribute closer to the actual speed trajectories, compared to BPNN predictor, implying the improved forecast accuracy.

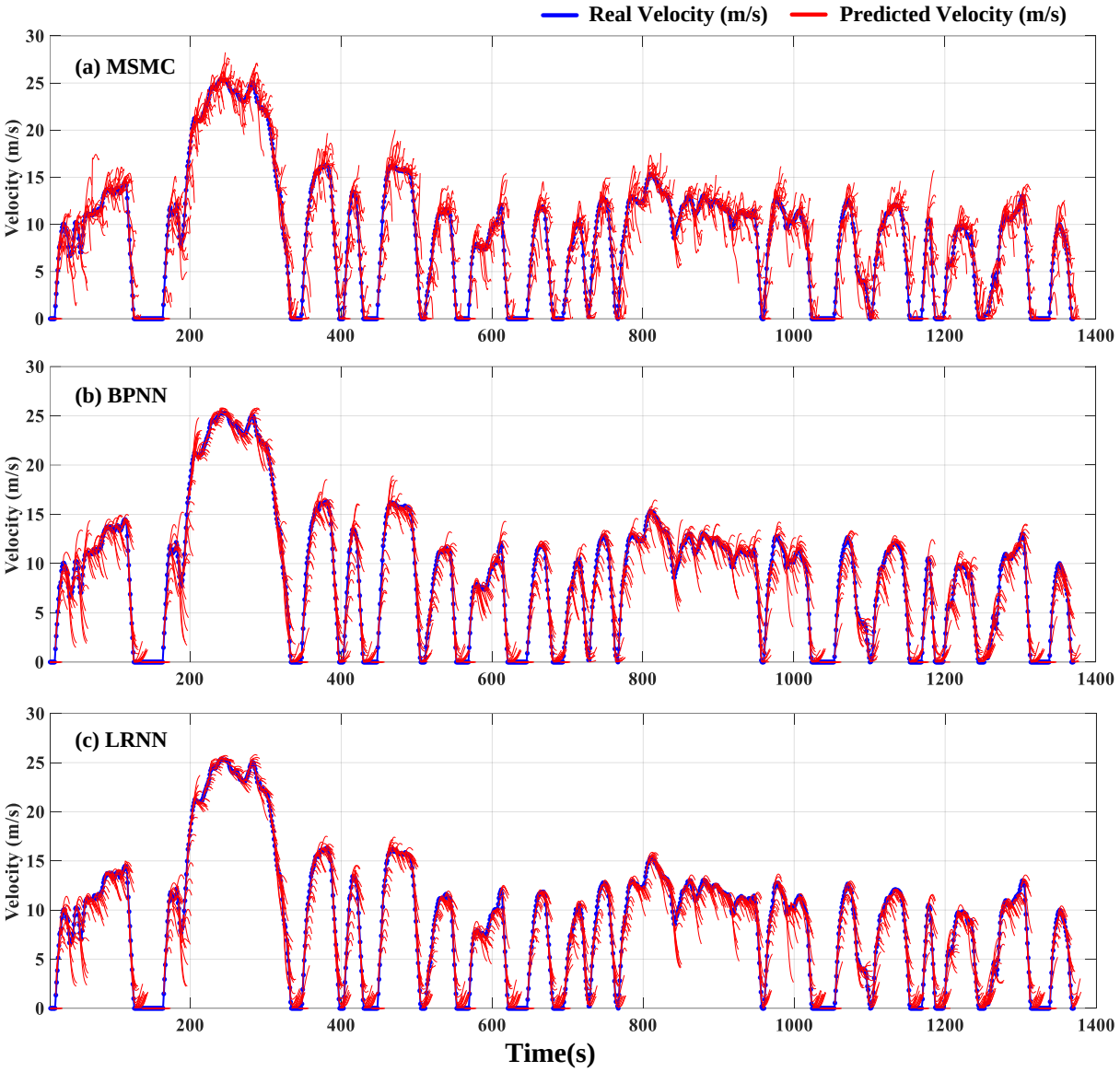


Figure 3.5. Global view of speed prediction results over UDDS driving cycle ($H_p$ = 10s, $\Delta T$ = 1s): (a) Multiple-step Markov Chain approach, (b) Back propagation neural network approach, and (c) Layer recurrent neural network approach.

In addition, as highlighted in the dashed regions in figure 3.6, compared to benchmark predictors, the proposed LRNN predictor exhibits an overall higher re-convergence rate after the speed inflection points, indicating that it can more promptly adapt to recent driving changes.

TABLE 3.3 lists the average RMSE of three speed predictors with different $H_p$ (3s, 5s and 10s) on UDDS testing cycle, where the percentage denotes the $\overline{\text{RMSE}}$ decrement by LRNN predictor. Specifically, in contrast to benchmark predictors (MSMC and BPNN), the proposed LRNN approach can respectively reduce the average forecast error by at least 16.23% and 6.16%, indicating the enhanced prediction precision.

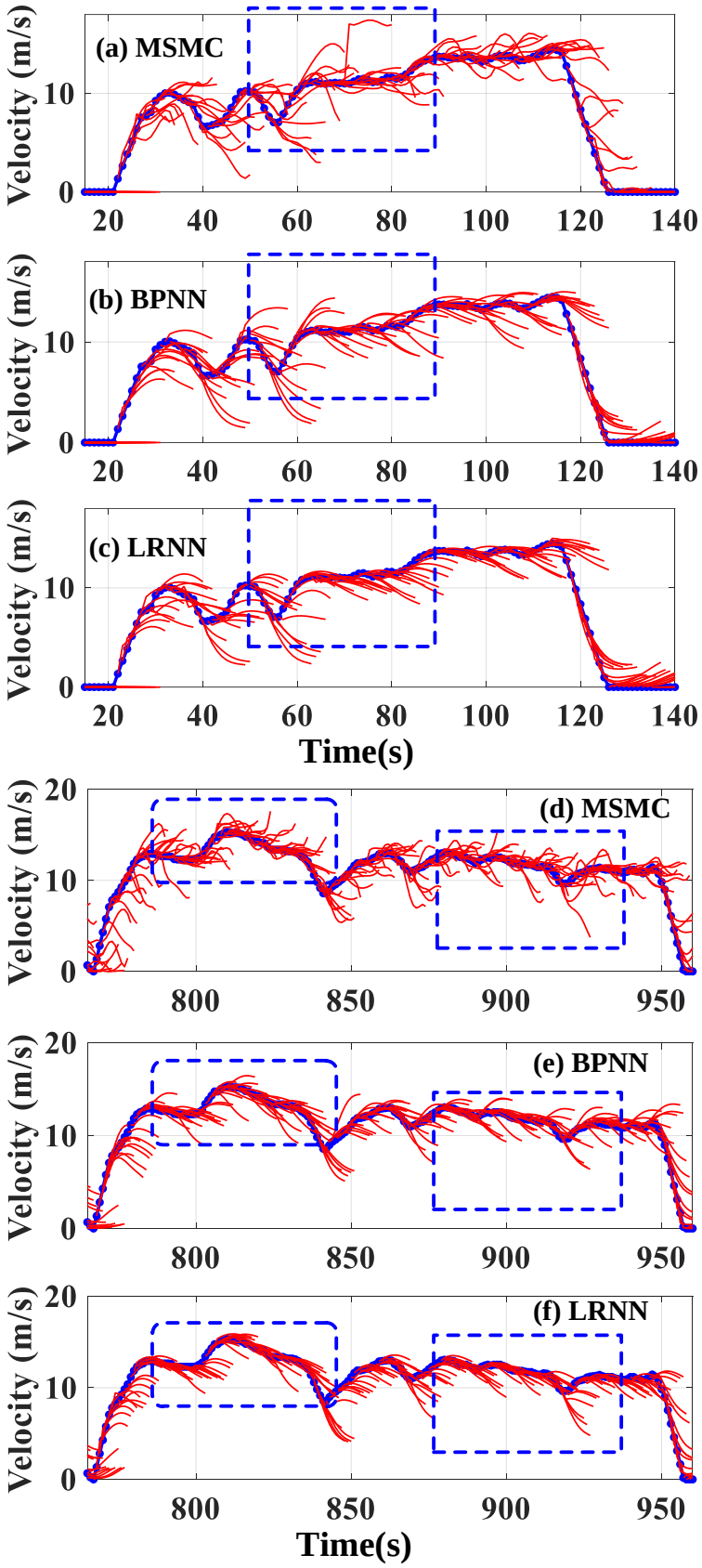


Figure 3.6. Local view of speed prediction results over UDDS driving cycle ($H_p$ = 10s, $\Delta T$ = 1s): (a)-(c) performance from 10s to 140s; and (d)-(f) 760s to 950s.

TABLE 3.3. Average RMSE and prediction accuracy improvement on UDDS driving cycle

| Hp | | MSMC | BPNN | LRNN |
|---|---|---|---|---|
| **3s** | $\overline{\text{RMSE}}$ (km/h) | 2.34 | 1.97 | 1.67 |
| | Improvement | **28.63%** | **15.23%** | N/A |
| **5s** | $\overline{\text{RMSE}}$ (km/h) | 3.98 | 3.18 | 2.85 |
| | Improvement | **28.39%** | **10.38%** | N/A |
| **10s** | $\overline{\text{RMSE}}$ (km/h) | 7.27 | 6.49 | 6.09 |
| | Improvement | **16.23%** | **6.16%** | N/A |

From the aforementioned analyses, following conclusions can be drawn:

- MSMC predictor leads to the largest forecast error among three methods due to its stochastic nature and the difficulty of expanding single-order MC to high-order MC;
- BPNN predictor results in higher precision compared to MSMC predictor due to the utilization of more historical speed samples for prediction;
- LRNN predictor outperforms the benchmark methods, indicating the effectiveness of enhancing the prediction quality via using an improved type of network structure.

It can be seen that all of three predictors follow the same establishment procedure: offline-training + online-application. Nevertheless, the vehicle's speed in realistic driving conditions would be greatly affected by the unpredictable traffic factors, like the stochastic distribution of traffic lights and the unexpected pedestrian movements. If the realistic driving cycles were highly divergent from the historical ones, the forecast precision of these offline-trained prediction models would be dramatically compromised [4].

Therefore, how to enhance the adaptability of the conventional speed predictors towards the newly-encountered driving scenarios should be further investigated. In the next subsection, we develop an adaptive speed predictor with the help of self-learning technique to tackle this issue.

### 3.2.3. Online-learning enhanced Markov speed predictor

To overcome the deficiency of traditional offline-trained speed predictors, subsection 3.2.3 presents a novel multi-step Markov speed predictor enhanced by online transition probability updating technique, whose development procedure is detailed as follows.

#### 3.2.3.1. Online transition probability updating technique

To estimate the TPM group through the online measurements, the state transition number **Num** in Eq. (3.1) should be substituted to the state transition frequency **Fre** . Consequently, the transition probability estimation model can be reformulated as follows [1]:

$$[T_l(L)]_{ij} \approx \frac{\mathbf{Num}_{ij}^{l}(L)/L}{\mathbf{Num}_{oi}^{l}(L)/L} = \frac{\mathbf{Fre}_{ij}^{l}(L)}{\mathbf{Fre}_{oi}^{l}(L)} \tag{3.10}$$

$$\mathbf{Fre}_{ij}^{l}(L) = \mathbf{Num}_{ij}^{l}(L)/L = \frac{1}{L}\sum_{t=1}^{L}\mathbf{flag}_{ij}^{l}(t) \tag{3.11}$$

$$\mathbf{Fre}_{oi}^{l}(L) = \mathbf{Num}_{oi}^{l}(L)/L = \frac{1}{L}\sum_{t=1}^{L}\mathbf{flag}_{oi}^{l}(t) \tag{3.12}$$

$$\mathbf{flag}_{oi}^{l}(t) = \sum_{j=1}^{s}\mathbf{flag}_{ij}^{l}(t) \tag{3.13}$$

Where $L$ denotes the observation length. Moreover, **flag** indicates the occurrence of related transition incidents, $i, j \in \{1, \dots, s\}$ and $l \in \{1, \dots, H_p\}$. For instance, $\mathbf{flag}_{ij}^{l}(t) = 1$ only when the state transition incident $a_i \to a_j$ occurs at time step $t$ ($t \in [1, L]$), while $\mathbf{flag}_{oi}^{l}(t) = 1$ only when the state transition incident originates from state $a_i$ at time step $t$. If the related transition incidents do not happen, they both take zero values. Moreover, the transition frequency $\mathbf{Fre}_{ij}^{l}$ and $\mathbf{Fre}_{oi}^{l}$ can be expanded into the following recursive form [1]:

$$\begin{aligned}\mathbf{Fre}_{ij}^{l}(L) &= \frac{1}{L}\sum_{t=1}^{L}\mathbf{flag}_{ij}^{l}(t) = \frac{1}{L}\cdot\left[(L-1)\mathbf{Fre}_{ij}^{l}(L-1) + \mathbf{flag}_{ij}^{l}(L)\right] \\ &= \mathbf{Fre}_{ij}^{l}(L-1) + \frac{1}{L}\cdot\left[\mathbf{flag}_{ij}^{l}(L) - \mathbf{Fre}_{ij}^{l}(L-1)\right] \\ &\approx \mathbf{Fre}_{ij}^{l}(L-1) + \boldsymbol{\varphi}\cdot\left[\mathbf{flag}_{ij}^{l}(L) - \mathbf{Fre}_{ij}^{l}(L-1)\right]\end{aligned} \tag{3.14}$$

$$\begin{aligned}\mathbf{Fre}_{oi}^{l}(L) &= \frac{1}{L}\sum_{t=1}^{L}\mathbf{flag}_{oi}^{l}(t) = \frac{1}{L}\cdot\left[(L-1)\mathbf{Fre}_{oi}^{l}(L-1) + \mathbf{flag}_{oi}^{l}(L)\right] \\ &= \mathbf{Fre}_{oi}^{l}(L-1) + \frac{1}{L}\cdot\left[\mathbf{flag}_{oi}^{l}(L) - \mathbf{Fre}_{oi}^{l}(L-1)\right] \\ &\approx \mathbf{Fre}_{oi}^{l}(L-1) + \boldsymbol{\varphi}\cdot\left[\mathbf{flag}_{oi}^{l}(L) - \mathbf{Fre}_{oi}^{l}(L-1)\right]\end{aligned} \tag{3.15}$$

To help TPM group adapt to recent driving changes, the varying decay factor $1/L$ is replaced by a constant forgetting factor $\boldsymbol{\varphi}$ ($0 < \boldsymbol{\varphi} < 1$) in Eq. (3.14) and Eq. (3.15), which is equivalent to stepwise erasing the impact on transition probabilities imposed by older measurements. A larger $\varphi$ implies a higher TPM updating rate, while a smaller one means the opposite. Specifically, all the measurements $\left[\mathbf{flag}_{ij}^{l}(1), \dots, \mathbf{flag}_{ij}^{l}(L)\right]$ and $\left[\mathbf{flag}_{oi}^{l}(1), \dots, \mathbf{flag}_{oi}^{l}(L)\right]$ are assigned with a set of exponentially decreasing weights $[\boldsymbol{\varphi}(1-\boldsymbol{\varphi})^{L-1}, \dots, \boldsymbol{\varphi}(1-\boldsymbol{\varphi}), \boldsymbol{\varphi}]$, wherein all weight elements add up to one. Hence, the probability $[T_l(L)]_{ij}$ can be renewed online by [1]:

$$[T_l(L)]_{ij} \approx \frac{\mathbf{Fre}_{ij}^{l}(L-1) + \boldsymbol{\varphi}\cdot\left[\mathbf{flag}_{ij}^{l}(L) - \mathbf{Fre}_{ij}^{l}(L-1)\right]}{\mathbf{Fre}_{oi}^{l}(L-1) + \boldsymbol{\varphi}\cdot\left[\mathbf{flag}_{oi}^{l}(L) - \mathbf{Fre}_{oi}^{l}(L-1)\right]}, i, j \in \{1, \dots, s\}, l \in \{1, \dots, H_p\}. \tag{3.16}$$

Through Eq. (3.16), the MC predictor can converge to the recent driving changes by stepwise updating its transition probabilities using the incrementally obtained driving information.

#### 3.2.3.2. Speed forecasting using self-learning enhanced Markov Chain

Benefiting from the online TPM updating technique, a novel speed forecasting method is proposed, whose three working phases are detailed as below.

- **Parameter initializing phase**. Before online TPM estimation, the size of Markov state $s$, the

forgetting factor $\boldsymbol{\varphi}$ and the initial TPM group $\mathrm{T_{ini}} = \left\{\mathrm{T_1}(0), \ldots, \mathrm{T_{H_p}}(0)\right\}$ are built. Note the $l^{th}$ element in $\mathrm{T_{ini}}$ is an $s$-order square matrix, with all elements being $1/\boldsymbol{s}$. As mentioned previously, $\boldsymbol{s}$ is set to 50 for the OL-MC speed predictor.

- **TPM updating phase**. Sample the most recent acceleration states: $a(L) = a_j$ and $a(L-l) = a_{i_l}$, where $a_j, a_{i_l} \in X_a, l \in \{1, \ldots, H_p\}$. Calculate $\mathbf{flag}_{ij}^{l}(L)$ and $\mathbf{flag}_{oi}^{l}(L)$ based on the state transition incidents from $a_{i_l}$ to $a_j$. Then, the $L^{th}$ transition frequency $\mathbf{Fre}_{ij}^{l}(L)$ and $\mathbf{Fre}_{oi}^{l}(L)$ can be derived based on the $(L-1)^{th}$ transition frequency $\mathbf{Fre}_{ij}^{l}(L-1)$ and $\mathbf{Fre}_{oi}^{l}(L-1)$ as indicated by Eq. (3.14) and Eq. (3.15). Afterwards, each element within the $i_l^{th}$ row of the $l$-step TPM $T_l(L)$ is renewed by Eq. (3.16), thus leading to the evolution of $T_G(L) = \left\{T_1(L), \ldots, T_{H_p}(L)\right\}$. Specially, if there is not enough data for TPM estimation ($L \leq H_p$), initial TPM group is adopted for velocity prediction.
- **Prediction and post-processing phase.** Given the updated TPM group $T_G(L)$ and the $L^{th}$ acceleration state $a(L) = a_j$, the acceleration in next $l$-step is obtained by the probability-weighted average (expected value) of each interval middle point through Eq. (3.3). Therefore, the $l$-step ahead velocity can be predicted by Eq. (3.4). Finally, to guarantee the smoothness of the forecasted speed profiles, the polynomial fitting algorithm is adopted for post-processing the velocity-forecast profiles. The degree N of polynomial depends on the length of prediction horizon ($\mathrm{H_p}$). Specifically, N = 2 when $\mathrm{H_p} \in \{3,4,5\}$; N = 3, when $\mathrm{H_p} \in \{6,7,8\}$; N = 4 when $\mathrm{H_p} \in \{9,10\}$. When $\mathrm{H_p} \in \{1,2\}$, no fitting algorithm is used and the predicted velocity is used as the final output.

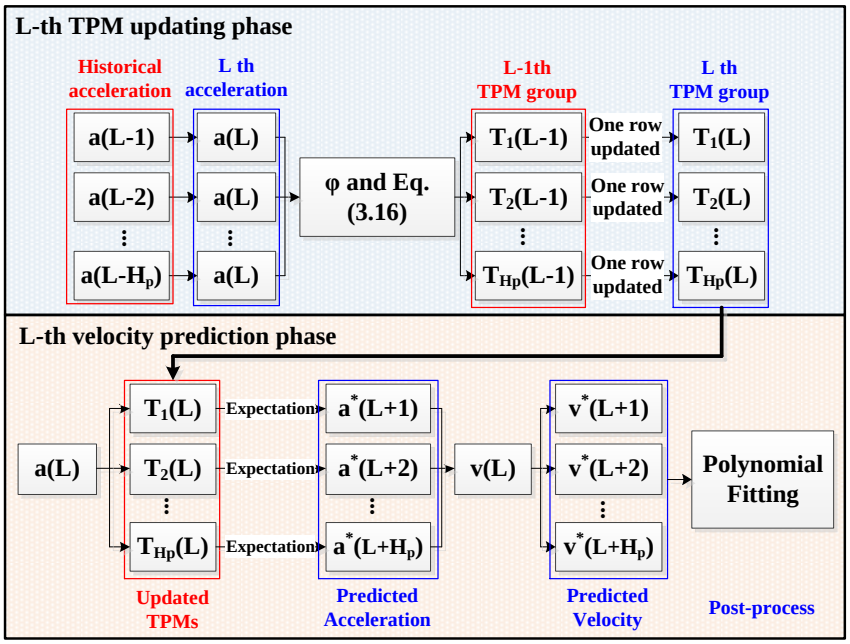


Figure 3.7. Flowchart of the $L^{th}$ updating and prediction phase of the online-learning enhanced Markov predictor.

To sum up, without using the offline driving database, the TPM of the OL-MC speed predictor is estimated based on the real-time measured driving data, whose working principle at $L^{th}$ time step is depicted in figure 3.7. Although the dependency on the offline driving database is removed during the establishment of the proposed method, its prediction performance may be greatly affected by the forgetting factor $\boldsymbol{\varphi}$, which thus should be carefully tuned before online applications. Please note the tuning process of forgetting factor will be presented in the next subsection.

#### 3.2.3.3. Influence on prediction performance imposed by forgetting factor $\varphi$

This subsection presents an example of the determination of forgetting factor $\varphi$ for the online-learning enhanced Markov Chain (OL-MC) speed predictor, so as to tradeoff between the sensitivity towards the new driving changes and the overall prediction reliability.

As mentioned before, a small $\varphi$ would reduce the updating rate of TPM group, which would degrade the adaptability of the prediction model in face of driving changes. In contrast, a large $\varphi$ would shorten the effective memory length $D_\varphi = 1/\varphi$, which would reduce the completeness and reliability of the MC model. In fact, the optimal settings of $\varphi$ (that bring the highest prediction accuracy) may vary under different driving patterns. For example, a larger $\varphi$ is suitable for city driving scenarios with rapid-changing driving conditions, since it can help OL-MC predictor promptly learn from recent driving changes. In contrast, a smaller $\varphi$ would be sufficient for highway driving conditions, where the external driving environment is more stable than in urban scenarios. This implies the fact that if we focus on one specific type of driving cycle for the determination of $\varphi$, the prediction performance may degrade on the other types of driving pattern. Therefore, to obtain a convincing tuning result of $\varphi$, this subsection adopts a combined testing cycle INRETS, which covers multiple driving patterns and thus can roughly represent the daily driving conditions [2], where the prediction performance of OL-MC with multiple forgetting factor candidates is detailed in figure 3.8-3.10.

Figure 3.9 and 3.10 demonstrate the forecast results when $H_p$ = 5s in detail, where the $\overline{\mathrm{RMSE}}$ under different $\varphi$ are respectively 1.1946 m/s ($\varphi = 0.1$), 0.9766 m/s ($\varphi = 0.01$) and 0.9594 m/s ($\varphi = 0.002$). Specifically, when $\varphi = 0.1$, the forecasted speed profiles tend to diverge significantly from the actual one. When $\varphi$ reduces from 0.1 to 0.002, the quality of prediction improves greatly, especially in the dashed regions, since the corresponding enlarged $D_\varphi$ (from 10 to 500) enables adequate measurements for TPM estimation, thus improving the forecast precision. Nevertheless, if $\varphi$ continues to decrease, the forecast precision would decrease to some extent, as shown in TABLE 3.4. This is because the enlarged $D_\varphi$ (from 500 to 10000) would include superfluous information that cannot represent recent driving conditions, thus reducing the forecast reliability. Meanwhile, when $H_p$ = 10s, similar tendency would also be detected. As summarized in figure 3.11, to tradeoff between the forecast precision and the online memory burden, $\varphi$ is set as 0.002 ($D_\varphi = 500$) to handle the changeable driving conditions.

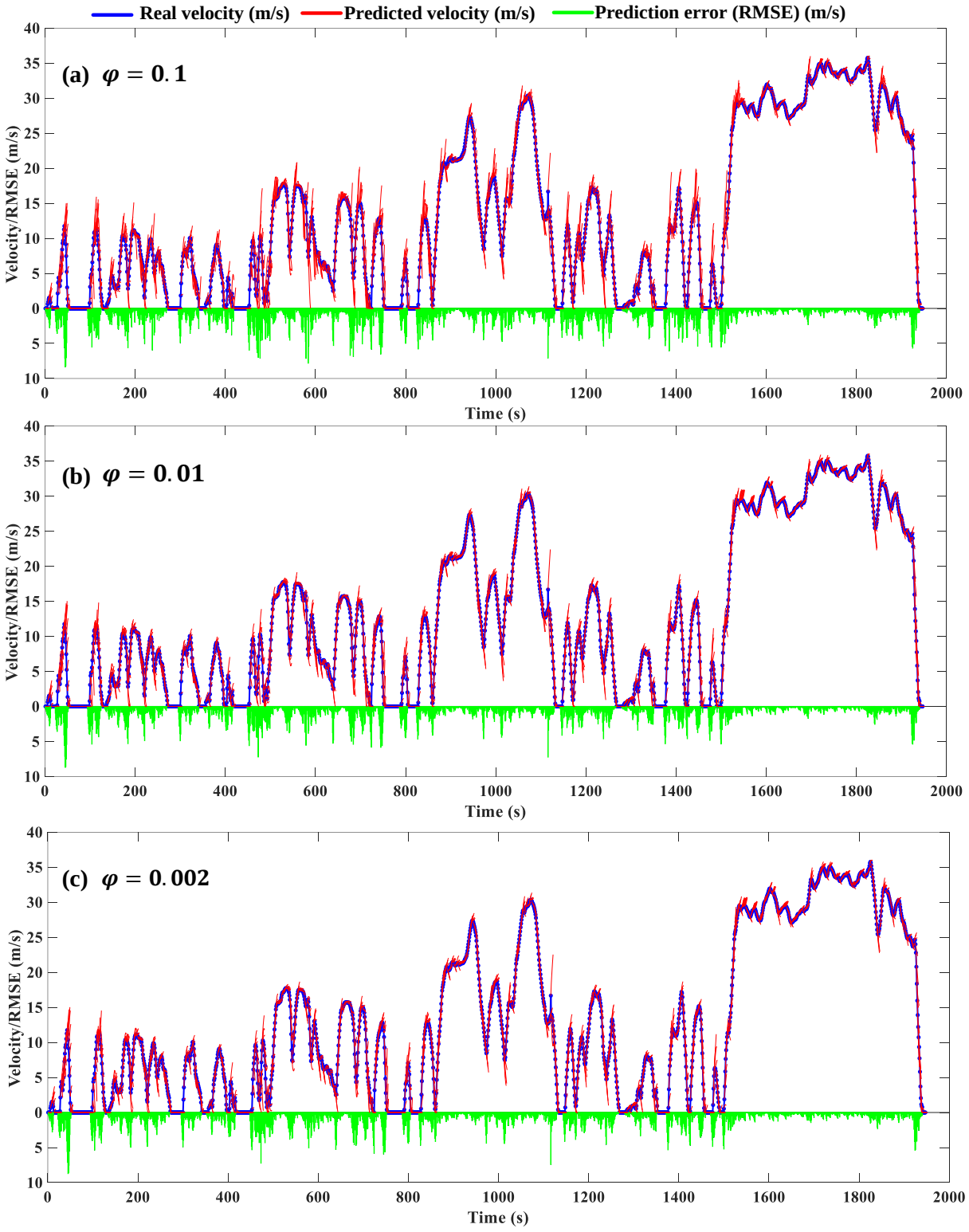


Figure 3.8. Global view of prediction performance ($H_p$ = 5s) with different $\varphi$: (a) $\varphi = 0.1$. (b) $\varphi = 0.01$ (c) $\varphi = 0.002$.

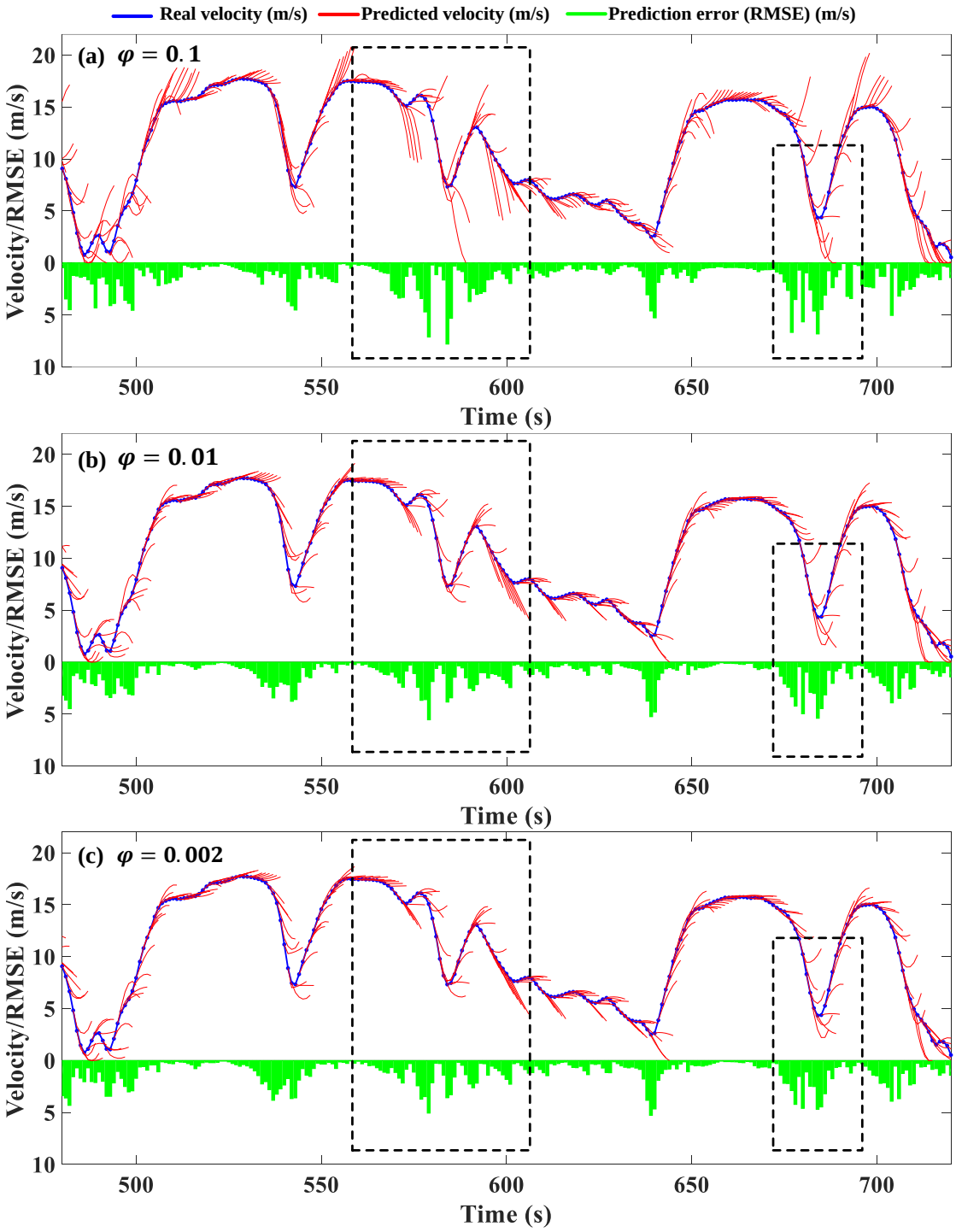


Figure 3.9. Local view (480s to 720s) of prediction performance ($H_p$ = 5s) with different $\varphi$: (a) $\varphi = 0.1$. (b) $\varphi = 0.01$ (c) $\varphi = 0.002$.

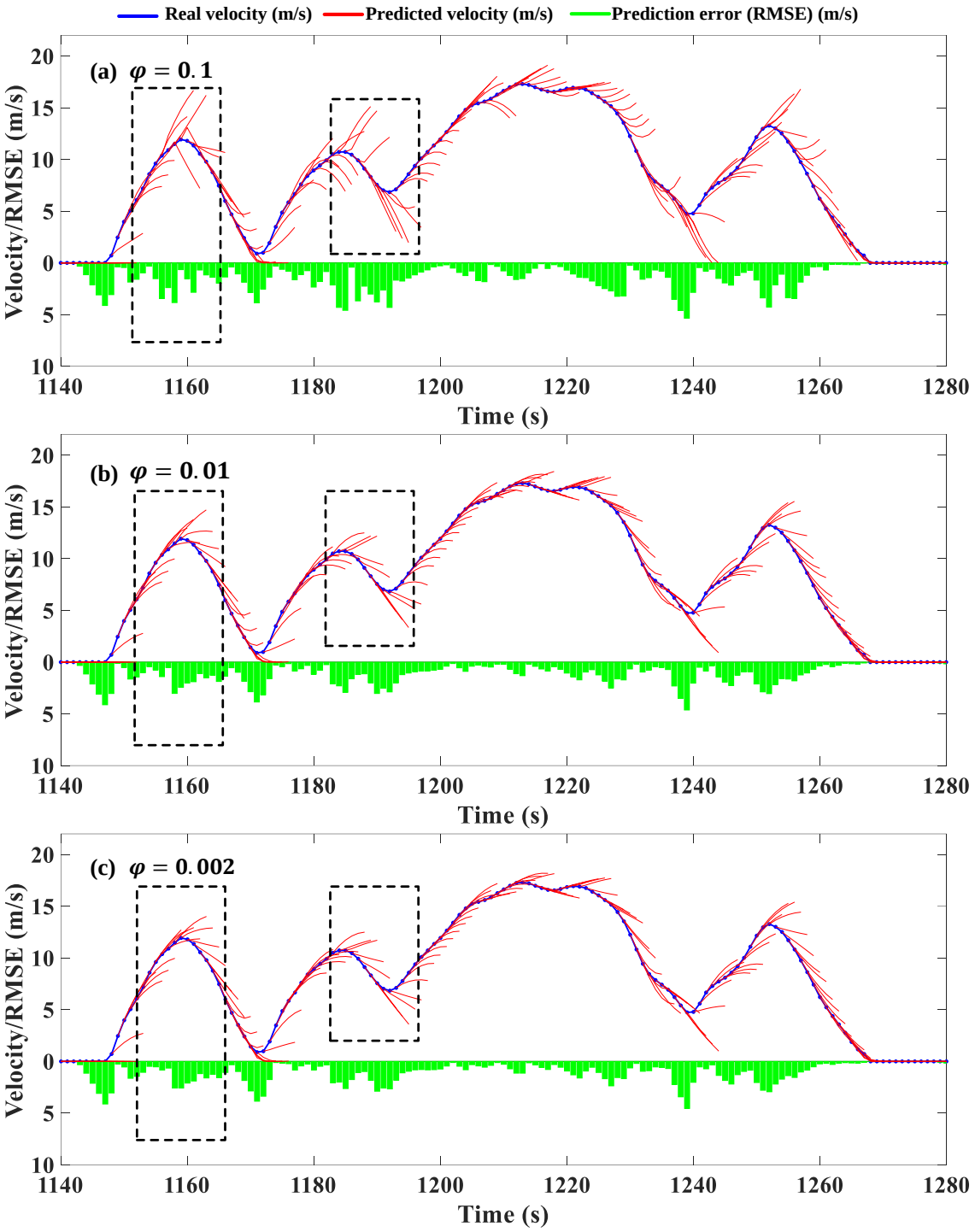


Figure 3.10. Local view (1140s to 1280s) of prediction performance ($H_p$ = 5s) with different $\varphi$: (a) $\varphi = 0.1$. (b) $\varphi = 0.01$ (c) $\varphi = 0.002$.

TABLE 3.4. $\overline{\text{RMSE}}$ (m/s) with respect to different $D_\varphi = 1/\varphi$ under INRETS cycle

| $D_\varphi$ | 5 | 10 | 50 | 100 | 200 | 500 | 1000 | 2000 | 5000 | 10000 |
|---|---|---|---|---|---|---|---|---|---|---|
| **$H_p$ = 5s** | 1.1946 | 1.1336 | 1.0102 | 0.9766 | 0.9624 | 0.9594 | 0.9713 | 0.9782 | 0.9828 | 0.9844 |
| **$H_p$ = 10s** | 2.5048 | 2.3823 | 2.1211 | 2.0513 | 2.0275 | 2.0198 | 2.0433 | 2.0550 | 2.0643 | 2.0661 |

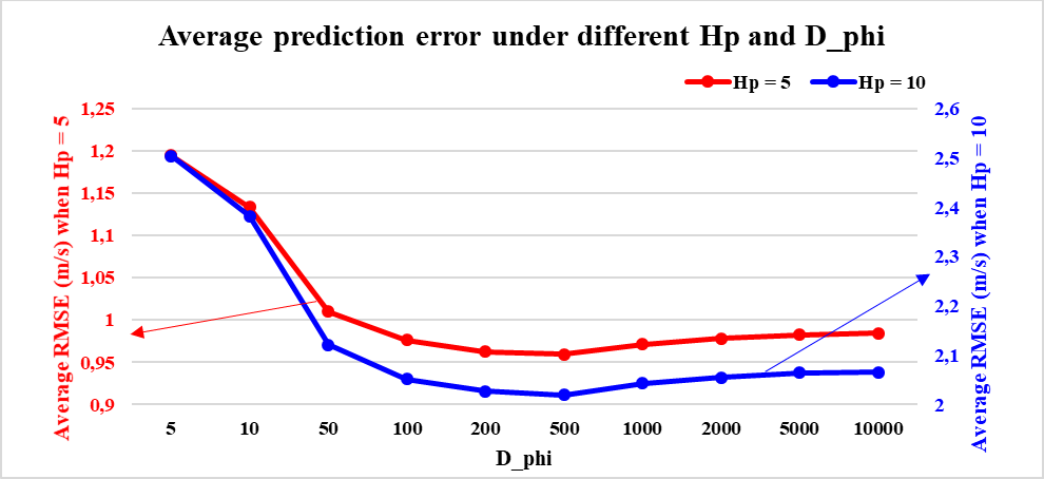


Figure 3.11. Average RMSE under different prediction horizon $H_p$ and effective memory depth ($D_\varphi$).

### 3.2.3.4. Performance comparison with benchmark predictors

To verify the effectiveness of the OL-MC speed predictor, a comparative study against benchmark methods (multi-step Markov Chain (MSMC) and back propagation neural network (BPNN)) is conducted in this subsection, so as to fully display their performances under different driving scenarios. Please note the training of BPNN and the TPM estimation of MSMC are accomplished offline based on the combined driving cycle shown in figure 3.1.

- **Performance comparison under repetitive driving conditions**

Firstly, the performance of three predictors is compared under the Manhattan driving cycle, which represents the typical urban driving scenarios with very low average speed, frequent start-and-stops, and repetitive driving patterns.

Taken $H_p$ = 5s as an example, the prediction performance discrepancy is detailed in figure 3.12-3.14. Specifically, both MSMC and BPNN predictors perform stably over the entire cycle. In comparison, due to the use of initial TPM groups, the online-learning enhanced Markov (OL-MC) predictor results in the largest error in the first 200 seconds (figure 3.13). As the updating of TPM group, its forecast errors gradually decrease to a lower level. Especially, as shown in the circled regions in figure 3.14, it even slightly performs better compared to benchmark predictors.

Moreover, figure 3.15 exhibits the error evolution processes (per 100s) of three predictors. Within the first 200s, the OL-MC predictor leads to the significantly larger error compared to benchmark predictors. Thereafter, due to the online updating of transition probability matrices (TPM), its performance discrepancy against other predictors is shrinking. Specifically, it outperforms the MSMC predictor after 200s. After 500s, it even slightly outperforms the BPNN predictor until the trip end. Besides, the average RMSE along the trip is summarized in TABLE 3.5. Unlike benchmark predictors, under two identical drive blocks, the average RMSE for the proposed method is reduced by 20.4% (from 1.0247 m/s to

0.8156 m/s). This indicates the proposed method can acquire predictive knowledge from the online measured driving data and thus its dependency on offline driving database is reduced compared to benchmark predictors. Moreover, the effectiveness in enhancing the forecast precision by the online-learning technique is also verified.

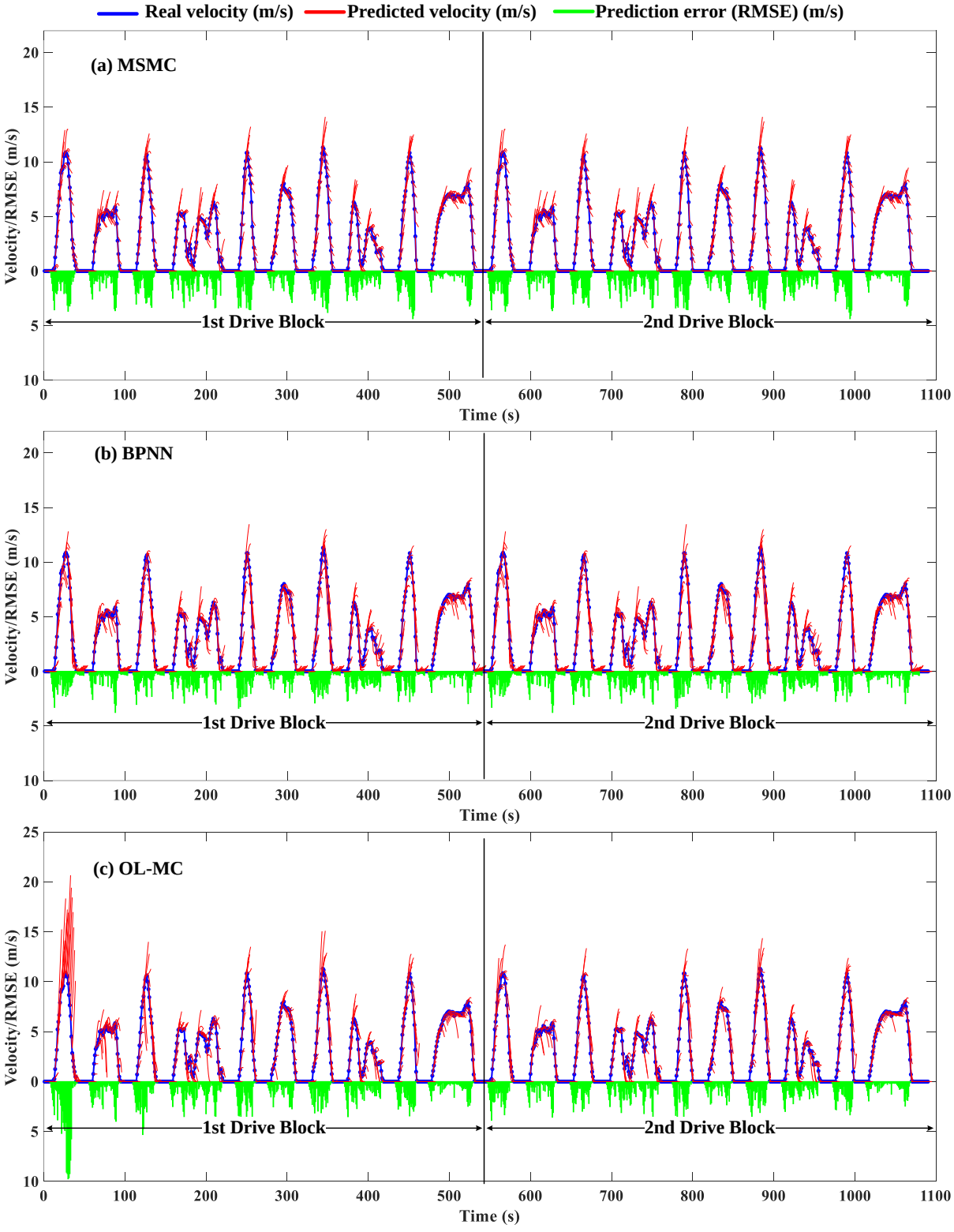


Figure 3.12. Global view of speed forecasting performance under Manhattan driving cycle ($H_p$ = 5s).

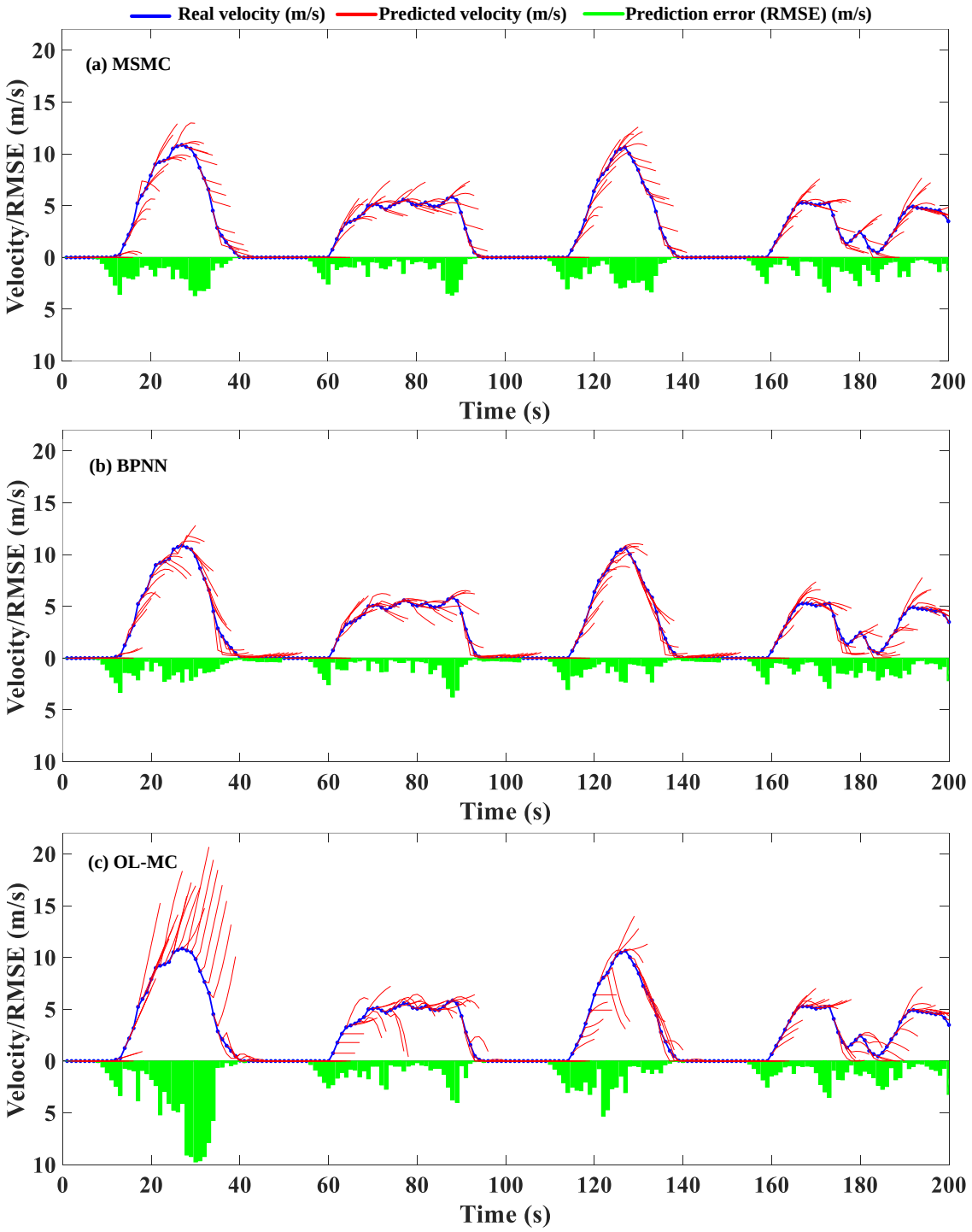


Figure 3.13. Local view (0-200s) of speed forecasting performance under Manhattan driving cycle ($H_p$ = 5s).

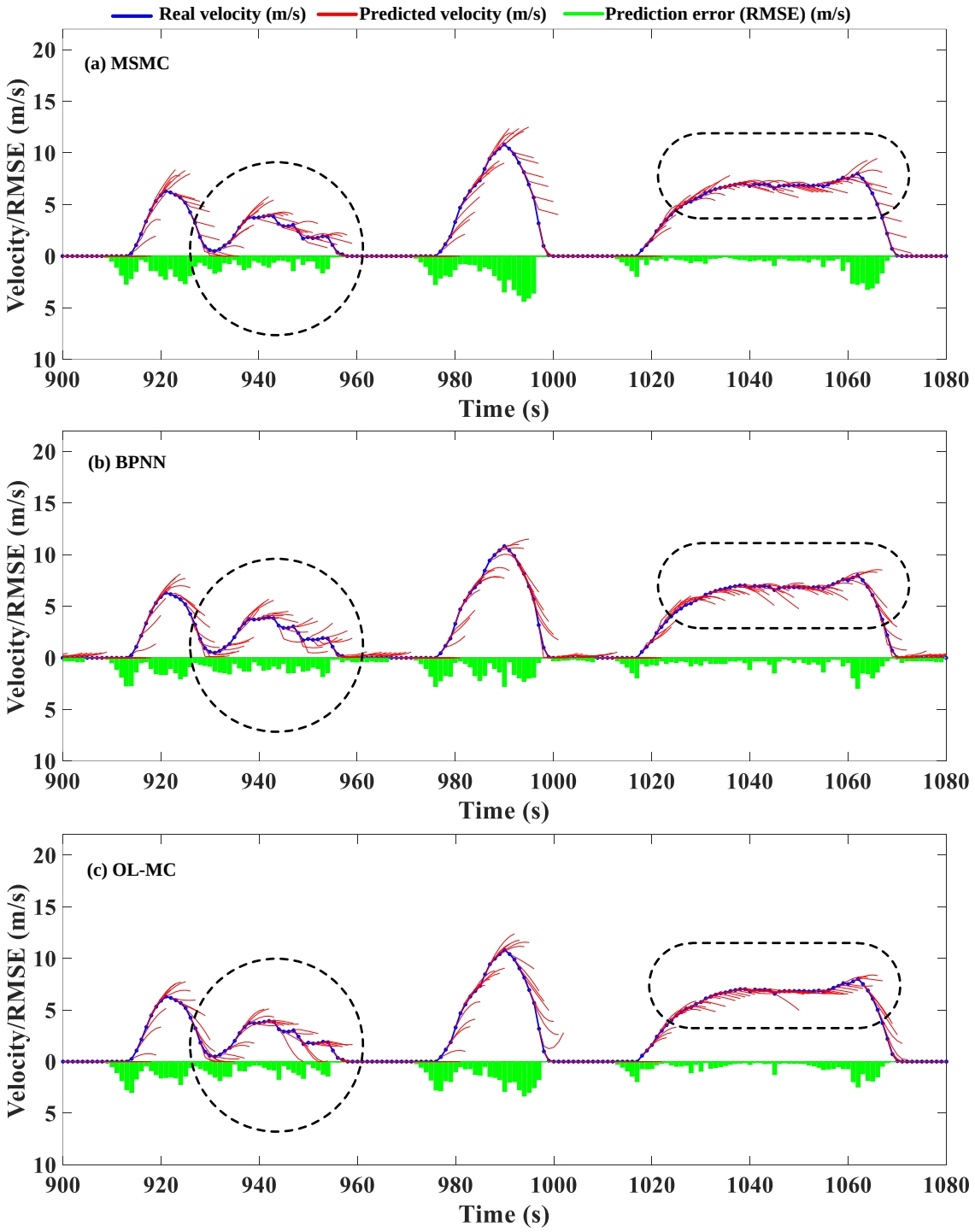


Figure 3.14. Local view (900-1080s) of speed forecasting performance under Manhattan driving cycle ($H_p$ = 5s).

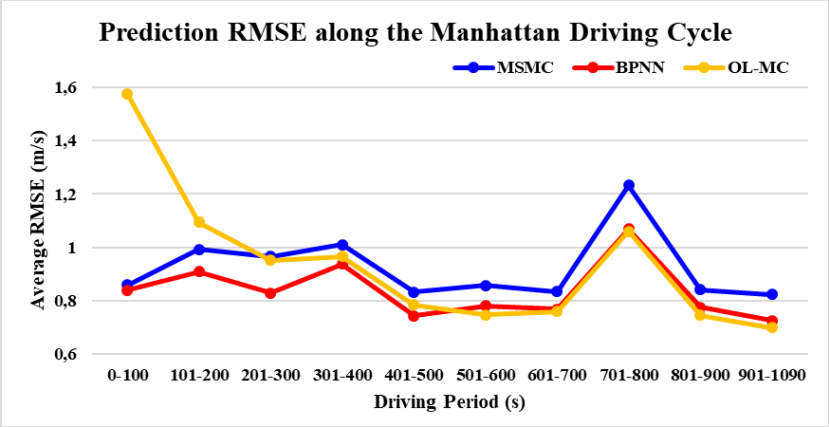


Figure 3.15. Average RMSE comparison (per 100s) under Manhattan driving cycle.

TABLE 3.5. Average RMSE (m/s) under Manhattan driving cycle.

| | 1st Drive Block | 2nd Drive Block | Total |
|---|---|---|---|
| **MSMC** | 0.9124 | 0.9208 | 0.9166 |
| **BPNN** | 0.8279 | 0.8279 | 0.8279 |
| **OL-MC** | 1.0247 | 0.8156 | 0.9206 |

- **Performance comparison under combined driving conditions**

To further evaluate the prediction performance under complex driving conditions, three standard cycles are concatenated to form a multi-pattern testing cycle, as shown in figure 3.16-3.18. Note $H_p$ is set as 10s to clearly show their performance discrepancies. Please note the training of back propagation neural network (BPNN) predictor and the transition probability matrix (TPM) estimation of multi-step Markov Chain (MSMC) predictor are accomplished offline based on the driving database shown in figure 3.1.

As can be seen from figure 3.16, three predictors tend to generate smaller errors over the CRUISE3 and HWFET cycles, whereas larger errors appear over the INDIA_URBAN cycle. This is because the actual speed profile changes more sharply under city driving conditions, making higher forecast accuracy hard to achieve. Moreover, as depicted in the circled region I of figure 3.17, the forecasted speed profiles by MSMC predictor tend to remain the same tendency (rising or falling) as the input driving states, while other predictors can more precisely describe the future velocity dynamics. In comparison with BPNN benchmark, the OL-MC predictor can more promptly re-converge to the real speed trace after each inflection point, thus increasing the prediction accuracy during this period. Similarly, as shown in the zoomed regions II (in figure 3.17) and III, IV (in figure 3.18), the proposed method shows the higher forecast precision and robustness compared to benchmark predictors.

The reason for such performance discrepancies is given as follows. Benchmark predictors learn future velocity dynamics from the offline stationary database and thus their predictive behaviors toward each driving pattern is pre-determined. Nevertheless, owing to the absence of online-update mechanism, it is hard for them to fully adapt to the novel driving characteristics, thus compromising the forecast

performance. In contrast, the proposed method can adjust its predictive behaviors by using the real-time updated TPMs, thus leading to the improved performance.

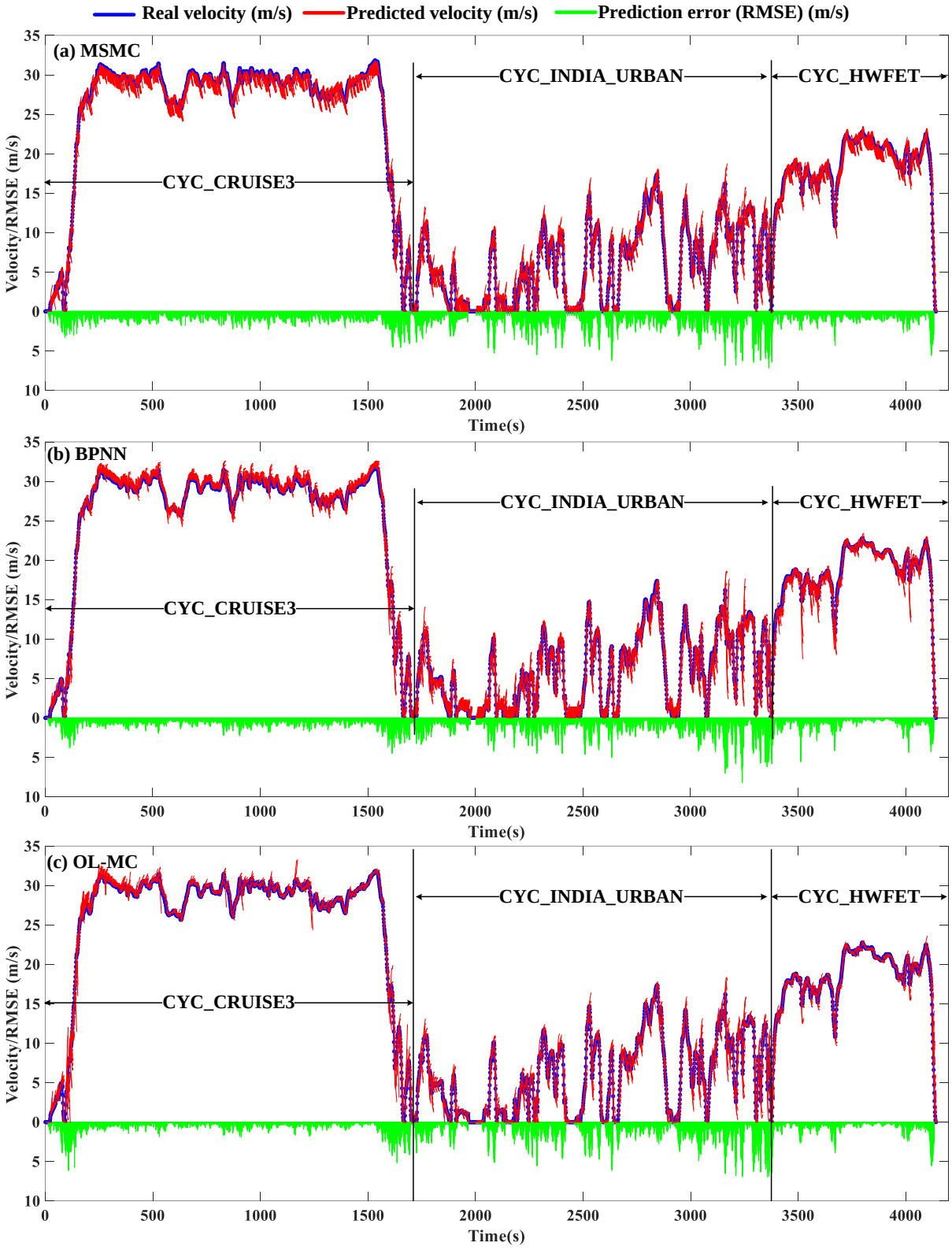


Figure 3.16. Global view of speed forecasting performance under combined driving cycle ($H_p$ = 10s).

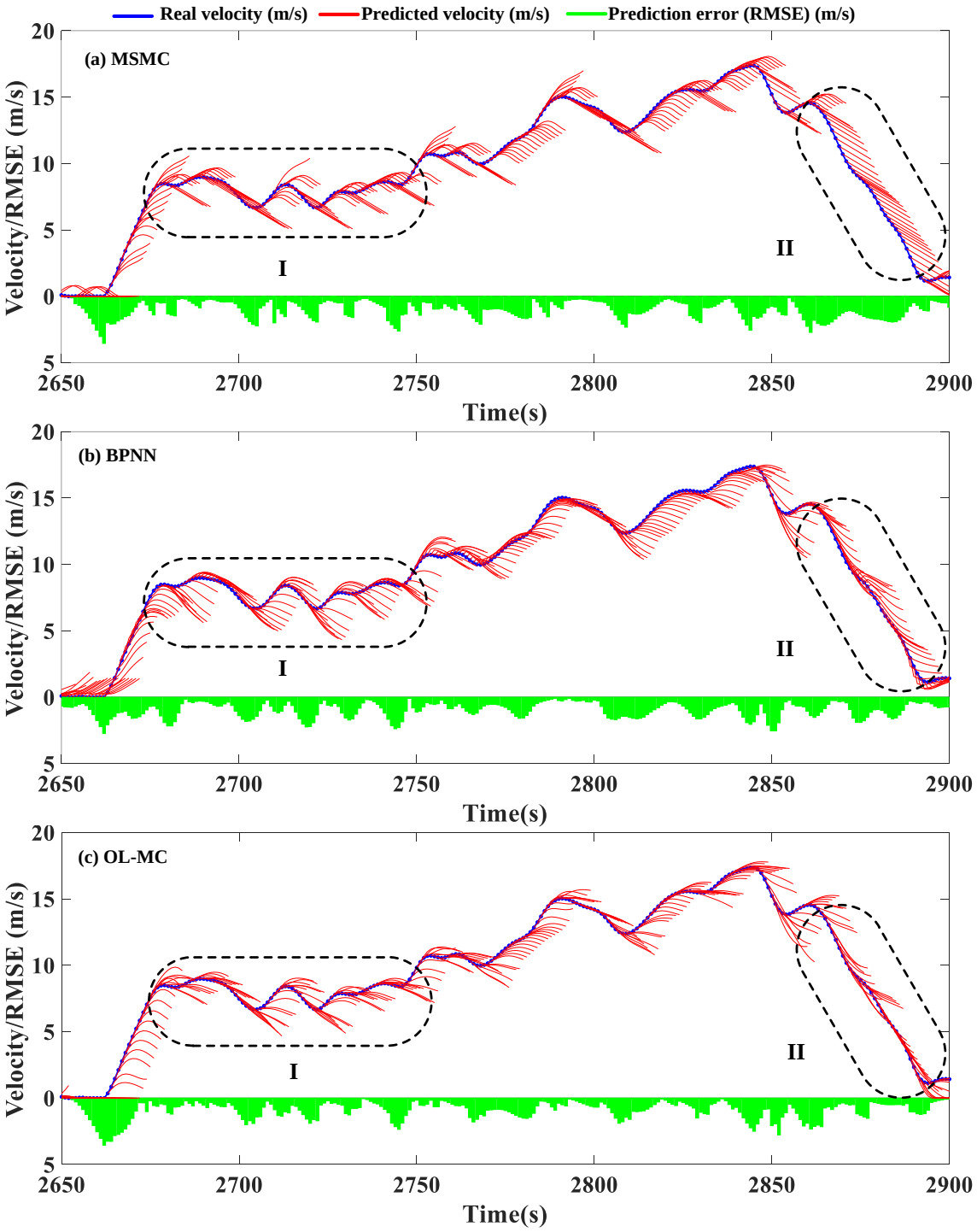


Figure 3.17. Local view (2650s-2900s) of speed forecasting performance under combined driving cycle ($H_p$ = 10s).

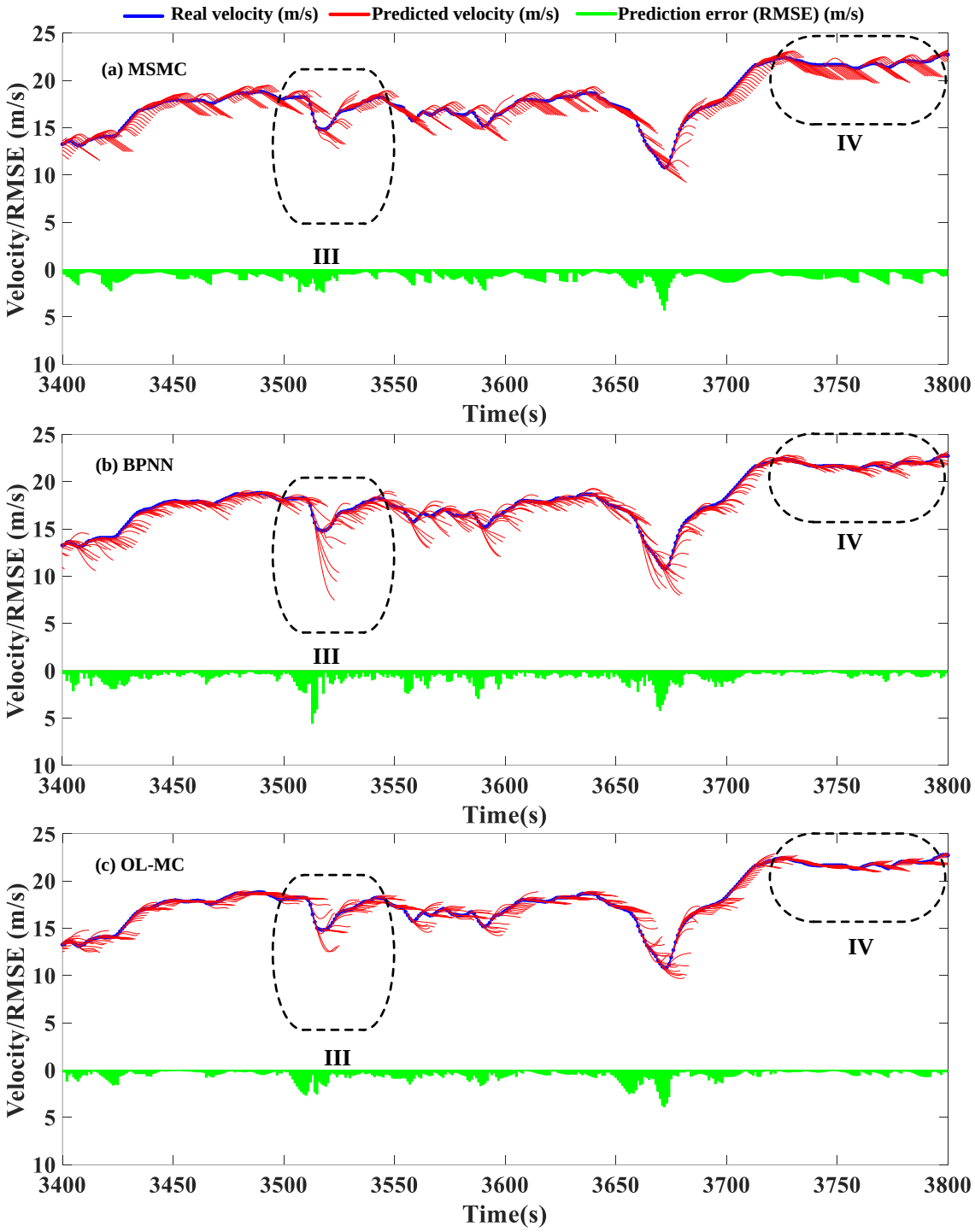


Figure 3.18. Local view (3400s-3800s) of speed forecasting performance under combined driving cycle ($H_p$ = 10s).

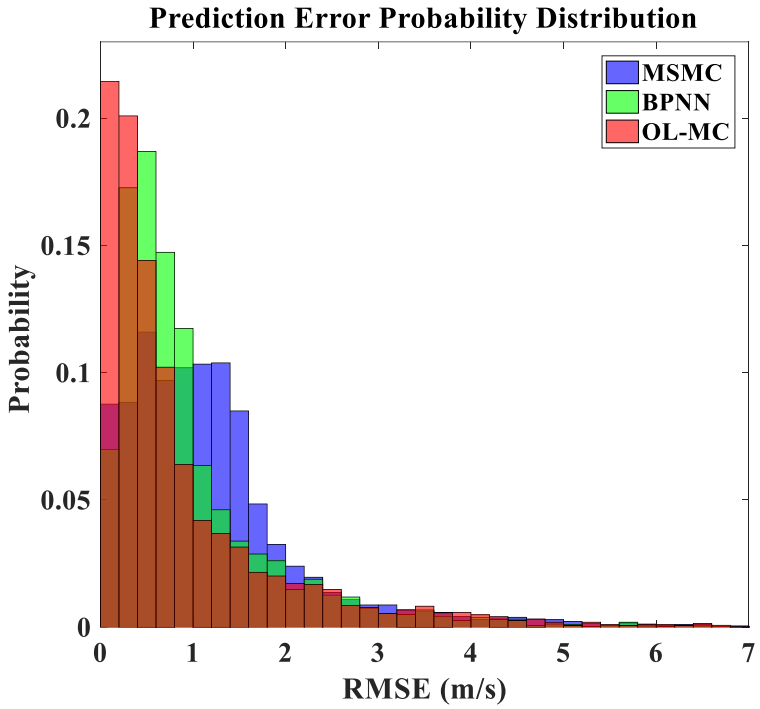


Figure 3.19. Average RMSE probability distribution under multi-pattern testing cycle ($H_p$ = 10s).

In addition, as displayed in figure 3.19, the proposed method tends to generate smaller errors among three approaches. Moreover, as summarized in TABLE 3.6, the proposed method can bring down the average RMSE by 25.73% (MSMC) and 7.90% (BPNN) under the multi-pattern testing cycle. Therefore, it can be confirmed that the proposed OL-MC speed predictor can effectively characterize the future speed dynamics under changeable driving conditions with the reasonable forecast precision.

TABLE 3.6. Average RMSE (m/s) under multi-pattern driving cycle.

| | CYCLE_Cruise3 | CYCLE_INDIA_URBAN | CYCLE_HWFET | Total |
|---|---|---|---|---|
| **MSMC** | 1.0365 | 1.4422 | 1.0540 | 1.2032 |
| **BPNN** | 0.7577 | 1.3204 | 0.6839 | 0.9703 |
| **OL-MC** | 0.6434 | 1.2662 | 0.6387 | 0.8936 |

To sum up, the major advances of the OL-MC speed predictor over the conventional predictors are summarized as follows:

- With the help of the online-learning technique, the OL-MC speed predictor can acquire the predictive knowledge from the real-time measured data, thus reducing the dependency on offline driving database in contrast to conventional speed predictors.
- Moreover, under the repetitive driving scenarios, the effectiveness in forecast precision enhancement by online-learning technique is verified.
- With the real-time updated TPM, the predictive behaviors of the proposed method can be adjusted accordingly with the changes of driving patterns, thus leading to the improved prediction performance under complicated driving scenarios compared to the benchmark predictors.

### 3.2.4. Fuzzy C-means clustering enhanced Markov speed predictor

A common drawback of the aforementioned speed predictors is that they are established and validated based on the standard driving cycles, wherein the speed profiles are obtained by processing (e.g. normalization, filtering, etc.) the raw driving data, which cannot fully reflect the real driving conditions. Hence, a higher prediction accuracy on these standard driving cycles does not necessarily mean a reliable forecast performance in realistic driving conditions [9]. To overcome this deficiency, real GPS-collected speed profiles for postal-delivery FCHEVs [10] are utilized for the development of prediction model in this subsection, so as to further improve the credibility of velocity prediction in real urban driving scenarios.

Under realistic driving conditions, driver's intentions would vary from vehicle's operation stages. For instance, aggressive driving behaviors with large acceleration would be detected in the vehicle's start-up phases, while mild driving behaviors tend to appear during the vehicle's cruising phases. Obviously, various driving intentions would lead to different future velocity distributions. Hence, if a single-mode speed predictor were used to cope with multiple types of input driving states, the overall forecast credibility would be compromised [11]. To address this issue, subsection 3.2.4 proposes a cooperative speed forecast approach based on fuzzy C-means clustering and multi-step Markov Chain (FCM-MC), which contains multiple predictive sub-models for dealing with different input driving stages. The prediction robustness is enhanced by a fusion strategy, which aggregates the predicted speed profiles from all sub-models with the real-time quantified fuzzy membership degrees. The detail design process is presented as follows.

#### 3.2.4.1. Fuzzy classification and Markov predictive model estimation

As depicted in figure 3.20, the proposed FCM-MC speed forecast approach comprises two working phases. Subsection 3.2.4.1 presents the principal of offline working phase.

To establish multiple predictive sub-models, the original driving database should be classified into several groups based on the feature of driving samples. Specifically, the GPS-collected driving database contains speed and acceleration sequences, namely $[v_1, \dots, v_N]$ and $[a_1, \dots, a_N]$. Afterwards, the original driving database is partitioned into numerous $\mathrm{H_m}$- dimensional driving vectors, where the $k^{th}$ sample can be expressed as $\left[v_k, \dots, v_{k+H_m-1}\right]$ and $\left[a_k, \dots, a_{k+H_m-1}\right]$. Furthermore, three parameters are selected to characterize each driving sample, namely the average speed $v_{k\_ave}$, the speed standard deviation $v_{k\_std}$ and the average acceleration $a_{k\_ave}$. To eliminate the negative impacts on classification results by different data scales, the k-th feature vector $x_k = \left[\mathrm{V_{k\_ave}}, \mathrm{V_{k\_std}}, \mathrm{A_{k\_ave}}\right]$ consists of the related normalized terms, where $\mathrm{V_{k\_ave}} = \frac{v_{k\_ave}}{v_{ave}^{max}} \in [0,1], \mathrm{V_{k\_std}} = \frac{v_{k\_std}}{v_{std}^{max}} \in [0,1], \mathrm{A_{k\_ave}} = \frac{a_{k\_ave} - a_{ave}^{min}}{a_{ave}^{max} - a_{ave}^{min}} \in [0,1]$. Besides, the superscripts "max" and "min" specify the extremum of corresponding physical quantities. As a result, each driving sample is denoted by a three-dimensional feature vector $x$.

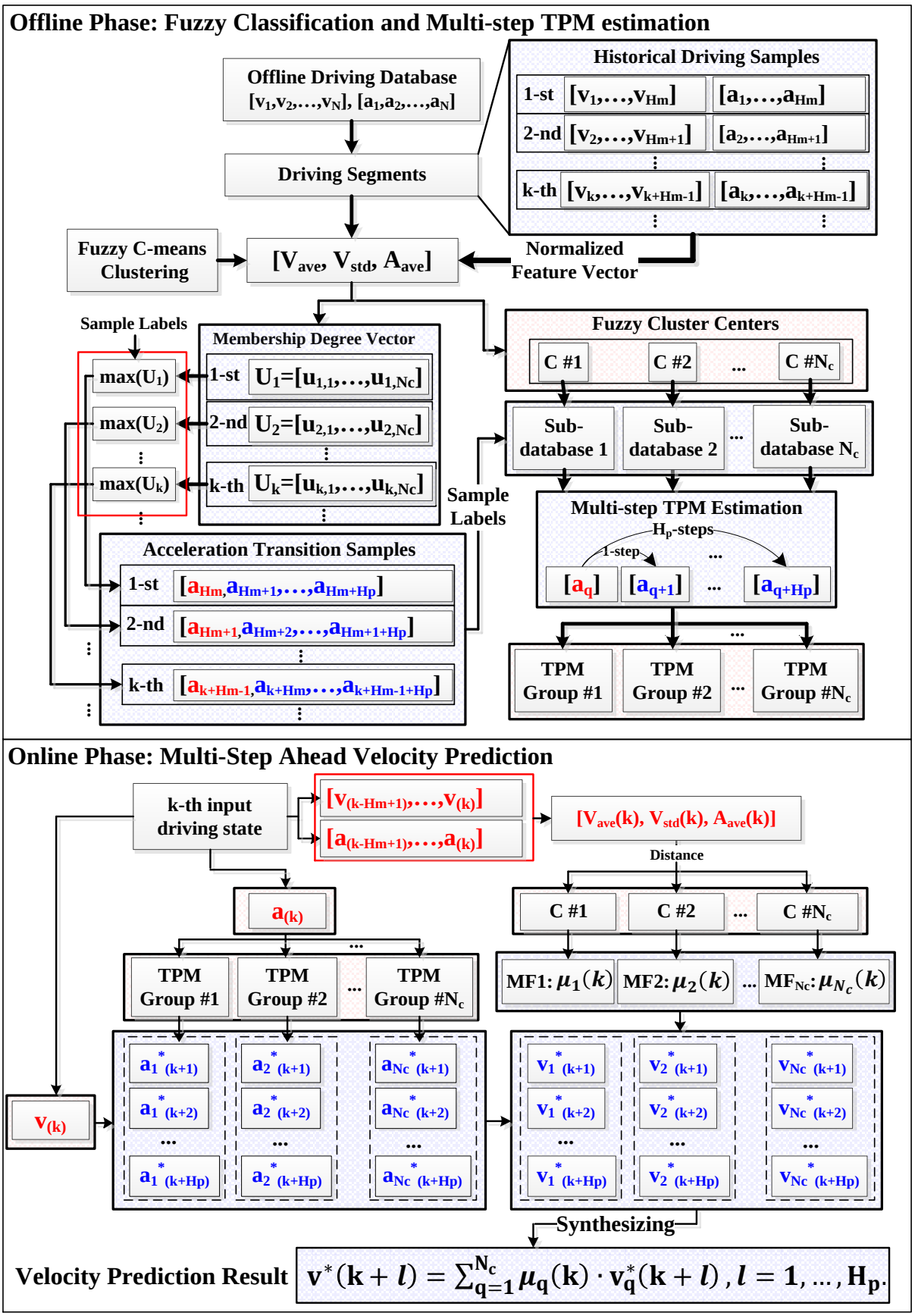


Figure 3.20. Working flowchart of fuzzy C-means enhanced Markov speed predictor.

As there is no uniform definition on the pattern of driving state x, the classification process should be unsupervised. To perform the unsupervised classification, the FCM technique is introduced. Given the number of clusters $N_c$ and a finite dataset $X = \{x_1, \dots, x_n\}$, the FCM returns a list of cluster centers $C = \{c_1, \dots, c_{Nc}\}$ and a fuzzy partition matrix $U \in R^{n \times N_c}$, wherein its $(i,j)$-th element $\mu_{ij} \in [0,1]$ $(i = 1,2, \dots, n, j = 1,2, \dots, N_c)$ indicates the membership degree of the data point $x_i$ in the $j^{th}$ cluster. The sum of membership value in all clusters equals to one, namely $\sum_{j=1}^{N_c} \mu_{ij} = 1$. The FCM working process is summarized in figure 3.21 [12]. Please note that the parameter m (in step 2) is fuzzy partition matrix exponent, which is used to control the degree of fuzzy cluster overlap. A larger m means a higher degree of fuzziness in neighboring clusters. In this study, the Matlab-embedded fuzzy C-means clustering function (*fcm*) is used for data pre-processing, where the parameter m is set as its default value two. The operator $\|\cdot\|$ (in step 3) means the Euclidean Distance from the data point $x_i$ to centroid $c_j$.

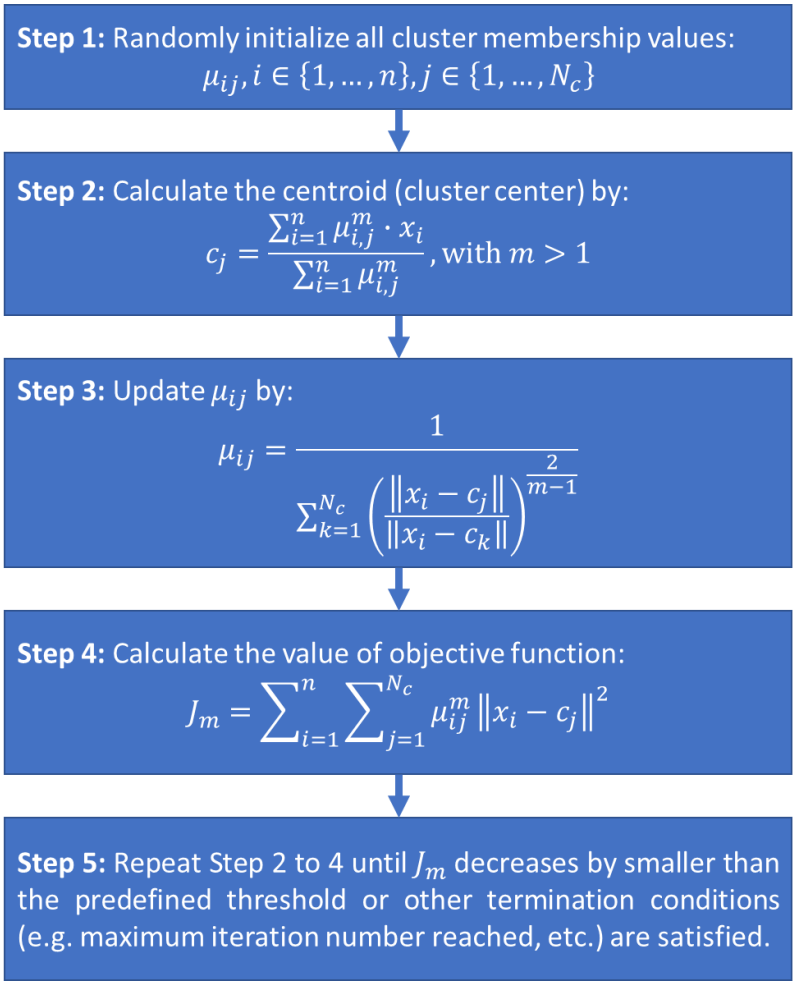


Figure 3.21. Flowchart of fuzzy C-means clustering algorithm.

To obtain the deterministic classification results, the largest membership degree $\mu_{i\_max}$, where $\mu_{i\_max} = \max[\mu_{i1}, \dots, \mu_{iN_c}]$, labels the feature vector $x_i$ to one of $N_c$ clusters. Based on the labels, corresponding acceleration transition database (wherein the $k^{th}$ sample is marked as $\left[a_{k+H_m-1}, \dots, a_{k+H_m-1+H_p}\right]$) is

divided into $N_c$ sub-databases, where $H_p$ is prediction horizon. The acceleration samples within each sub-database are then used to estimate the multi-step TPM (by Eq. (3.1)) for the corresponding Markov predictive sub-model.

#### 3.2.4.2. Real-time fuzzy membership degree quantification and multi-step velocity prediction

Once the cluster centers $\{c_1, \dots, c_{N_c}\}$ and $N_c$ TPM groups $\{T_{G\_1}, \dots, T_{G\_N_c}\}$ are established, they can be used for multi-step speed forecasting. Three working steps of velocity prediction are given as follows:

- At $t = k$, sample the $k^{th}$ driving states, namely $[v(k + H_m - 1), \dots, v(k)]$ and $[a(k + H_m - 1), \dots, a(k)]$, and calculate the corresponding normalized feature vector, namely $x(k) = [\mathrm{V_{ave}}(k), \mathrm{V_{std}}(k), \mathrm{A_{ave}}(k)]$. Afterwards, quantify the membership degree of $x(k)$ in $N_c$ clusters, with the quantification result expressed by $[\mu_1(k), \dots, \mu_{N_c}(k)]$.
- Encode the acceleration $a(k)$ into the Markov state $a_i$. Then, the *l*-step ahead acceleration is computed by probability-weighted average of each interval mid-point:$a_q^*(k + l) = \sum_{j=1}^{s} [T_l^q]_{ij} \cdot a_j, if\ a(k) \in I_i$, where $T_l^q \in T_{G\_q}, q = 1, \dots, N_c, l = 1, \dots, H_p$. Thereafter, the velocity prediction result from the $q^{th}$ MC sub-model is expressed by: $v_q^*(k + l) = v(k) + \sum_{r=1}^{r=l} a_q^*(k + r) \cdot \Delta T$.
- By synthesizing the quantified membership degree with the velocity prediction results from all MC sub-models, the final speed forecasting result is: $v^*(k + l) = \sum_{q=1}^{N_c} \mu_q(k) \cdot v_q^*(k + l), l = 1, \dots, H_p$. Finally, the polynomial fitting algorithm is employed to smooth the forecasted speed profiles.

It should be mentioned that, by using the weighted velocity prediction results from all MC sub-models, it is beneficial for reducing the negative impacts on prediction reliability imposed by the identification uncertainty of the input driving states.

#### 3.2.4.3. Mobypost vehicle driving database pre-processing

In this subsection, an example of fuzzy C-means clustering technique applied to the real mail-delivery mission profiles of a light-duty FCHEV, termed as “Mobypost” [10], is given. Thereafter, based on the analyses of the clustering results, the determination processes of parameter $H_m$ (the length of input driving sample) and $N_c$ (the number of clusters) are given in detail.

As depicted in figure 3.22, the speed profiles of 12 mail-delivery tasks collected on the fixed routes (data sampled at 1Hz) are regarded as the original driving database for building the velocity predictor. The mileage of each single delivery task is around 25 km, which is equivalent to 4 to 4.5 hours’ trip duration and the peak speed is below 60 km/h [10]. Moreover, two typical driving scenarios (flowing and congested) of the Mobypost vehicle on speed profile No.1 are given in the bottom subfigures to display the feature of mail-delivery mission profiles.

Before TPM estimation, this database should be divided into $N_c$ sub-databases according to the feature

of driving samples. Taken $H_m$ = 5s as an example, the FCM is performed on all $H_m$ –dimensional driving samples (speed vector) extracted from the original database. The deterministic clustering results are derived by the largest element within the quantified membership degree vector, as shown in figure 3.23(a)-(c).

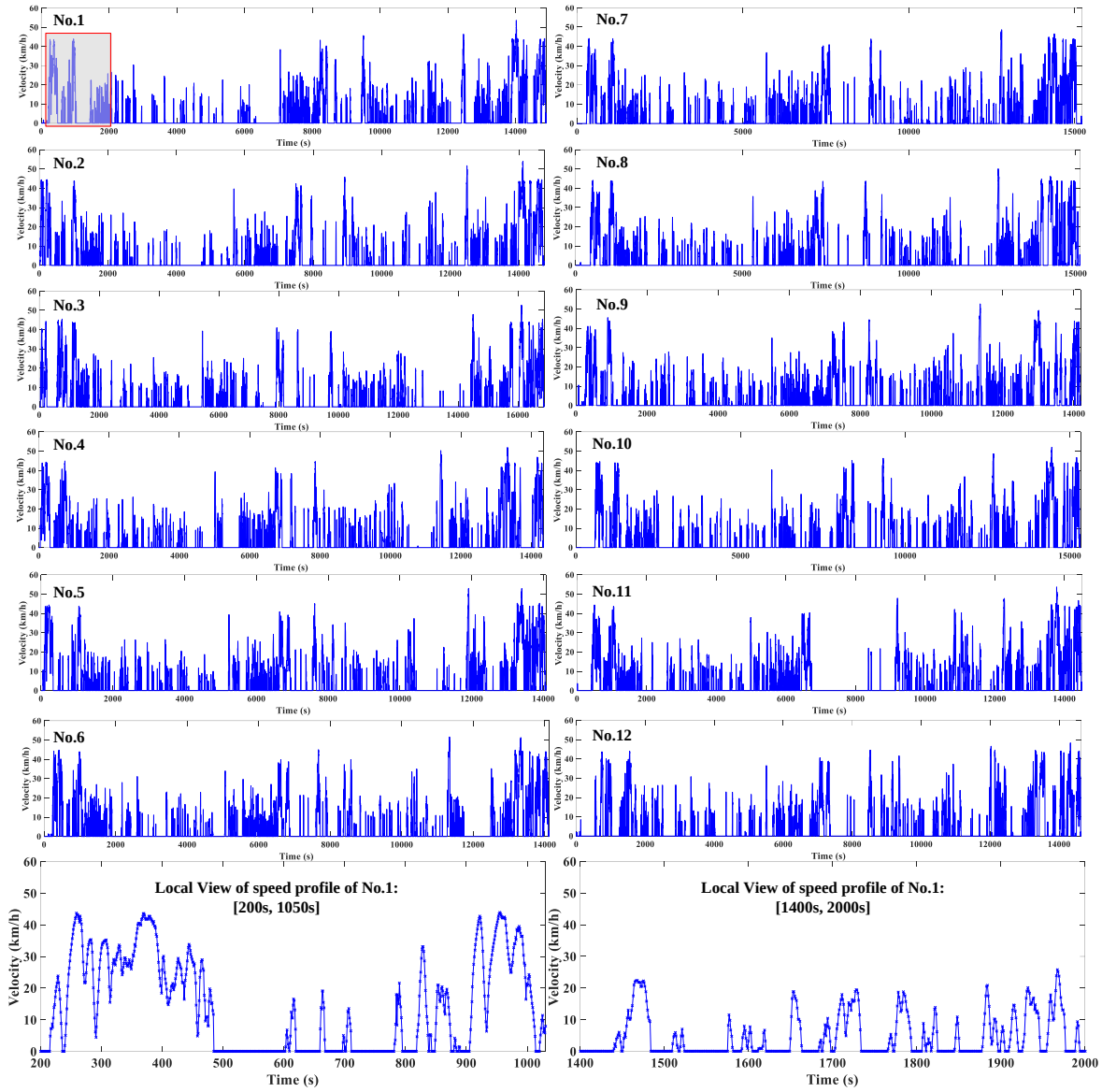


Figure 3.22. Actual speed profiles collected by GPS on the mail-delivery routes.

As can be seen, by labeling the original driving samples with the feature vector $[V_{ave}, V_{std}, A_{ave}]$, the driving database are categorized into $N_c$ groups, where the speed samples in each group are associated with similar changing tendencies (e.g. upwards, downwards, cruising etc.). In addition, using a larger $N_c$ makes the samples within each cluster distributed closer to each other, meaning a stronger correlation. However, the sample discrepancies among different sub-groups are insignificant if an overlarge $N_c$ is picked (e.g. samples in cluster 7 and 8 of figure 3.23(c)), implying the risk of over-classification.

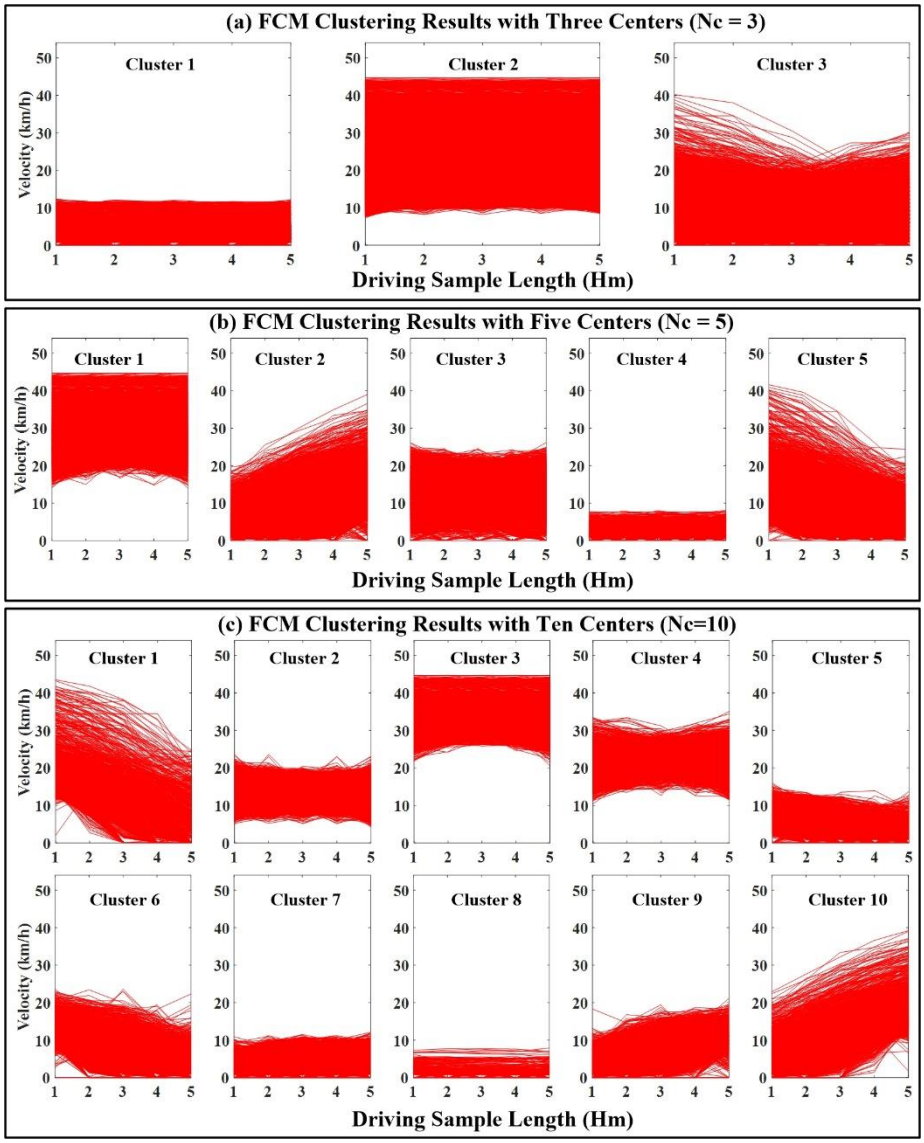


Figure 3.23. FCM clustering results (driving sample length: $H_m$ = 5s) with different $N_c$.

Furthermore, the length of driving samples $H_m$ would also affect the quality of classification. For instance, if $H_m$ is set too small, it is hard to comprehensively describe the recent driving intentions via the insufficient information. In contrast, an overlarge $H_m$ may contain the redundant information that is irrelevant to recent driving changes, increasing the risk of mis-classifications. Hence, the settings on $N_c$ and $H_m$ would affect the quality of driving sample clustering, thus further influencing the velocity prediction performance. Thus, they should be carefully tuned before online applications.

To find the proper settings on $N_c$ and $H_m$, the MC predictor with different $(N_c, H_m)$ candidates is tested on the combined testing cycle (including all speed profiles in figure 3.22)). Figure 3.24(a) presents the average RMSE results ($H_p$ = 5). As can be seen, the highest prediction accuracy is achieved when $N_c = 4$ and $H_m = 5$. Moreover, figure 3.24(b) presents an example of classification results using such parameter setting. For better graph readability, each class of speed samples in moving horizons is marked with a specific color and the samples in different moving horizons are separated with offset. As

can be seen, speed samples are correctly classified into four states, indicating the vehicles' related operation stages. Hence, it can be confirmed that when $N_c = 4$ and $H_m = 5$, the original database can be properly separated into multiple sub-databases via the proposed data structure $[V_{ave}, V_{std}, A_{ave}]$. Note such parameter setting is adopted for the FCM-MC predictor.

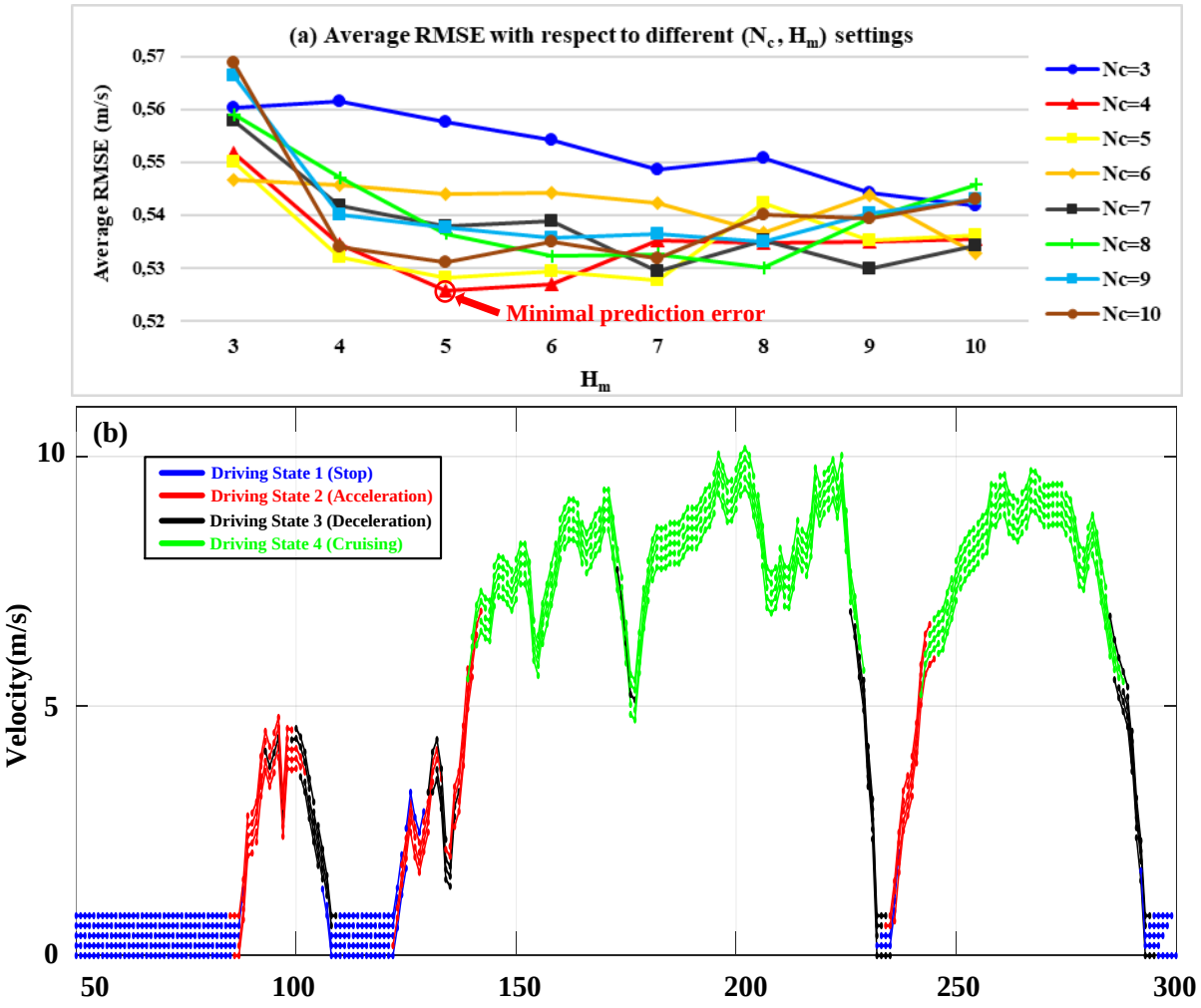


Figure 3.24. (a) Average RMSE ($H_p$ = 5) on the testing cycle under different ($N_c, H_m$) settings. (b). Example of classification results when $N_c = 4$ and $H_m = 5$.

### 3.2.4.4. Performance comparison against benchmark predictors

After the parameters of the FCM-MC predictor is well-tuned offline, this subsection presents a comparative study on prediction performance among the FCM-MC and two benchmark predictors, namely Multi-step Markov Chain (MSMC) and back propagation neural network (BPNN).

Compared to the FCM-MC predictor, the TPM group of MSMC predictor is estimated based on the original driving database (figure 3.22) without preprocessing by the FCM technique. Please note the number of MC state is set to 50. Additionally, the training of BPNN is also accomplished based on the driving data in figure 3.22, where 85% of data is used for network training while the remaining 15% is for performance validation.

Another speed profile for mail delivery (marked as CYCLE_I) is used as the testing cycle, as depicted in figure 3.25(a). Specifically, figure 3.25(b)-(d) detail the prediction results of three methods ($H_p$ = 5), where the prediction results of MSMC approach tend to diverge dramatically from the actual speed profile, leading to the worst performance among all predictors. This is because the MSMC predictor characterizes the future velocity distributions only based on the current driving state, making it hard to describe the blended and changeable driving behaviors. In contrast, when using more historical driving data for prediction, the BPNN predictor characterizes the future velocity distributions in a more convincing manner, leading to the quality enhancement of prediction.

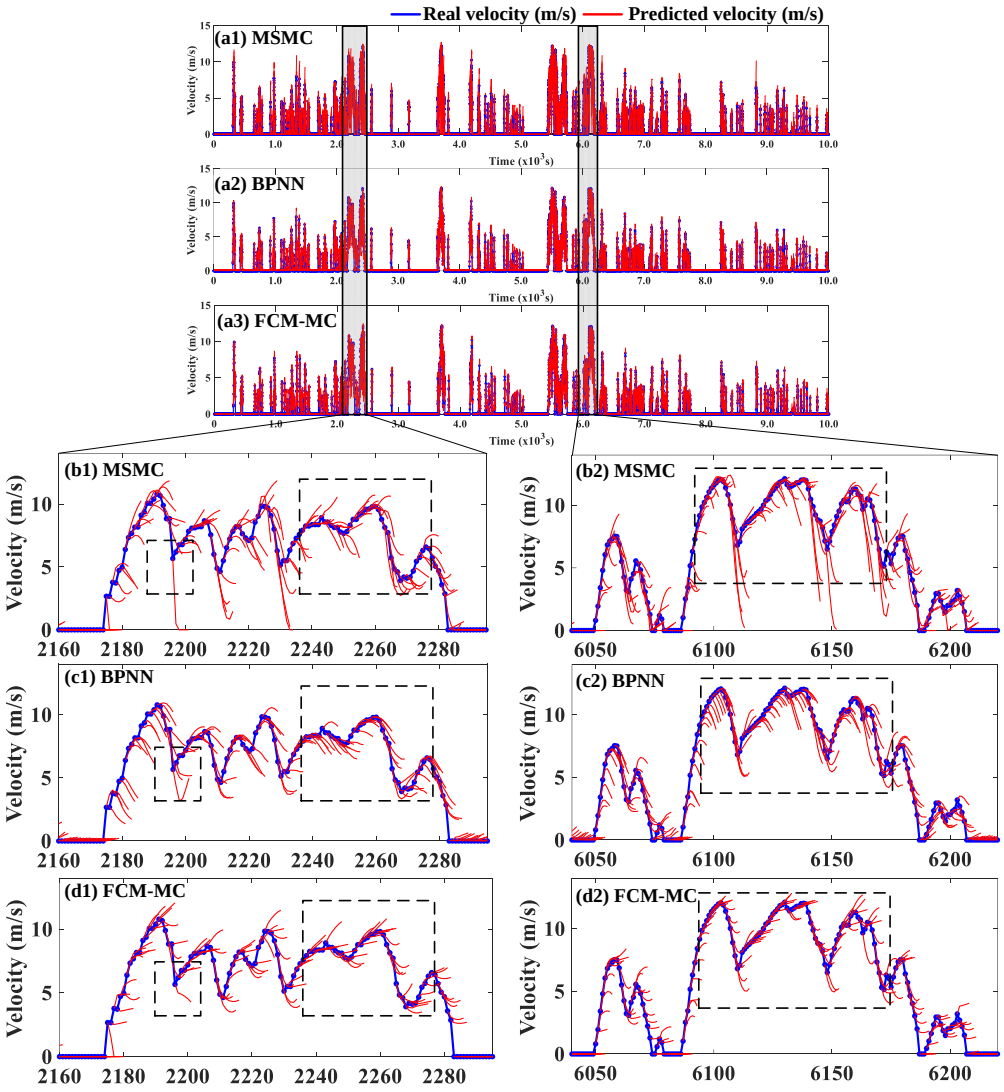


Figure 3.25. Speed forecasting performance evaluation on CYCLE_I ($H_p$ = 5): (a) global view of prediction results, (b) performance of conventional multi-step Markov predictor (MSMC), (c) performance of back propagation neural network (BPNN) predictor and (d) performance of fuzzy C-means based Markov predictor (FCM-MC).

Additionally, as depicted in figure 3.25(d), the FCM-MC predictor outperforms the benchmark predictors in terms of the overall prediction accuracy. Besides, it exhibits a quicker re-convergence rate after the speed inflection points, as highlighted in the dashed rectangle regions within each subfigure.

The reason for such performance improvement is: (1) based on the identification results of recent driving states, proper predictive sub-models are adopted for online speed forecasting; (2) by aggregating the forecasted speed profiles from all sub-models with the quantified fuzzy membership degrees, the proposed method has a certain level of robustness towards the mis-identification of input driving states.

Similarly, the comparative studies are also conducted under other four testing cycles, namely CYCLE_II to CYCLE_V. TABLE 3.7 lists the average RMSE of all predictors, where the FCM-MC predictor results in the highest prediction accuracy among three approaches under five testing cycles. Specifically, compared to MSMC, the average forecast precision improvement by the FCM-MC predictor are respectively 9.31% ($H_p$ = 5) and 14.57% ($H_p$ = 10). Besides, compared with the BPNN predictor, the FCM-MC can reduce the average prediction error by 10.24% ($H_p$ = 5) and 9.87% ($H_p$ = 10), respectively. Therefore, it can be confirmed that the FCM-MC predictor can improve the quality of speed prediction compared to benchmark approaches.

TABLE 3.7. Average RMSE (m/s) of three predictors under five testing cycles.

| **Items** | **CYCLE_I** | | **CYCLE_II** | | **CYCLE_III** | | **CYCLE_IV** | | **CYCLE_V** | |
|---|---|---|---|---|---|---|---|---|---|---|
| **$H_p$** | 5s | 10s | 5s | 10s | 5s | 10s | 5s | 10s | 5s | 10s |
| **MSMC** | 0.5100 | 0.8289 | 0.5750 | 0.9224 | 0.6193 | 0.9896 | 0.5710 | 0.9240 | 0.5518 | 0.8876 |
| **BPNN** | 0.5263 | 0.8072 | 0.5860 | 0.8920 | 0.6192 | 0.9481 | 0.5801 | 0.8940 | 0.5533 | 0.8232 |
| **FCM-MC** | **0.4569** | **0.6937** | **0.5272** | **0.7985** | **0.5685** | **0.8558** | **0.5236** | **0.7972** | **0.4976** | **0.7472** |

To sum up, the major advance of FCM-MC predictor against the benchmark predictors are summarized as follows:

- In offline stage, the fuzzy C-means clustering technique is adopted to preprocess the original driving database, leading to the generation of multiple Markov predictive sub-models, where each sub-model characterizes the future velocity distribution of specific type of input driving states.
- At the online application stage, to reduce the negative impacts caused by the uncertainty of driving state identification, the final prediction results are obtained by synthesizing the forecasted speed profiles from all sub-models with the real-time quantified fuzzy membership degrees.
- Validation results have demonstrated that, under realistic mail-delivery mission profiles, (i) the FCM can correctly capture the input driving states via the proposed data structure; (ii) the FCM-MC predictor outperforms the benchmark approaches regarding prediction accuracy and robustness, leading to at least 9.31% error reduction.

## 3.3. Battery energy depletion planning approaches

For PHEV applications, the plug-in property permits the onboard battery to be recharged via the external grid power, which, hence, enables a way towards better fuel economy by consuming the low-cost electricity energy for vehicle propulsion. Moreover, fuel economy performance of PHEVs is closely related to the way of battery energy depletion. Therefore, an explicit SoC reference profile is necessary

to realize the efficient utilization of battery energy under sophisticated traffic conditions.

To address this issue, in this subsection, an integrable battery SoC reference estimation method is proposed to regulate the SoC declining rates, so as to better guide the allocation of battery energy under different driving patterns. Besides, a commonly-used battery SoC reference planning approach is introduced as the evaluation benchmark.

### 3.3.1. Benchmark SoC reference estimation approach

This subsection introduces the linear SoC reference model as the benchmark, whose working principle is given as follows:

**Linear SoC reference model** [13]: as mentioned in **Chapter 1**, with the assistance of the modern telematics systems, the duration of a trip $T_{trip}$ can be estimated in advance. Given the previewed trip duration, the reference SoC is designed to linearly decline from initial (maximum) value to the terminal (minimum) one, implying a single SoC depleting rate over the trip. The working principle of the linear SoC reference model is given as:

$$SoC_{ref}^{*}(k) = SoC_{ini} - \frac{k}{T_{trip}}\left(SoC_{ini} - SoC_{final}\right) \tag{3.17}$$

Where $SoC_{ref}^{*}$ is the reference SoC value, $SoC_{ini}$ and $SoC_{final}$ respectively the target SoC value at the beginning and end of the trip, and $k$ the current time step.

The advantage of this model lies in its real-time practicality, since it has a simple mathematical principle and the only required route knowledge is the estimated trip duration, which can be easily obtained from the contemporary telematics systems. Nevertheless, its drawback is also obvious: the inherent single SoC depleting rate over the trip may be improper for realistic cycles with multiple different driving patterns [14]. To overcome this limitation, an adaptive SoC reference generator will be introduced in the next subsection, which can effectively regulate the declining rate of battery SoC in face of different driving patterns, so as to more reasonably allocate battery energy compared to the traditional linear SoC reference model.

### 3.3.2. Integrable adaptive SoC reference estimation approach

In fact, each driving pattern has its own characteristics. For instance, high average speed and low speed changing rate usually occur in highway cruising driving scenarios, which indicates the high-average power requests. In this case, the cost-effective electricity should be primarily utilized to save the hydrogen consumption, which leads to a high declining rate of SoC. In contrast, low average speed and high velocity changing rate tend to appear in urban driving scenarios, where the corresponding low-average power requests would contribute to a relatively low SoC declining rate.

Based on the aforementioned analyses, it can be found that depleting battery energy at various rates to

cope with multiple driving patterns may enhance the overall fuel economy performance. Thus, this subsection presents an adaptive SoC reference generator, which can be easily integrated into the EMS framework to guide the allocation of battery energy for fuel cell/battery-based PHEVs. Figure 3.26(a) details the SoC declining rate regulation mechanism of the proposed method.

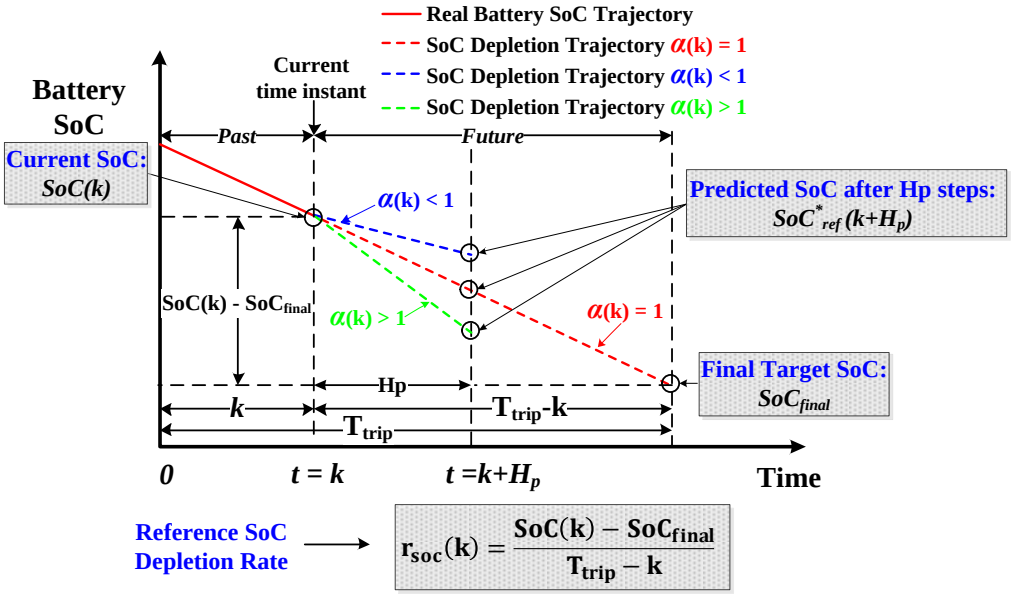


Figure 3.26(a). Schematic diagram of the adaptive SoC reference generator.

The maturation of modern telematics techniques makes it possible to acquire the estimated trip duration information $T_{trip}$ in advance. At $t = k$, let SoC(k) denotes the actual SoC, $SoC_{final}$ the terminal SoC target and $V_k^* = [v^*(k+1), \ldots, v^*(k+H_p)]$ the forecasted speed profile, the predicted reference SoC at $t = k + H_p$ can be calculated by Eq. (3.18a).

$$SoC_{ref}^*(k+H_p) = SoC(k) - r'_{soc}(k) \cdot H_p \tag{3.18a}$$

$$r'_{soc}(k) = \alpha(k) \cdot r_{soc}(k) \tag{3.18b}$$

$$r_{soc}(k) = \frac{SoC(k) - SoC_{final}}{T_{trip} - k} \tag{3.18c}$$

$$\alpha(k) = \frac{k_\alpha}{1 + \frac{v_{std}(k)}{v_{ave}(k)}} \tag{3.18d}$$

Where, as shown in Eq. (3.18b), the modified SoC declining rate $r'_{soc}(k)$ is derived by the production of adjusting factor $\alpha(k)$ and the $k^{th}$ reference SoC declining rate $r_{soc}(k)$. Moreover, as indicated by Eq. (3.18c), $r_{soc}(k)$ is obtained through dividing the permissible SoC variation $(SoC(k) - SoC_{final})$ by the remaining trip time $(T_{trip} - k)$. Besides, Eq. (3.18d) gives the expression of the adjusting factor $\alpha(k) \in (0, k_\alpha]$, where the constant parameter $k_\alpha > 0$ specifies the upper boundary of $\alpha$. Specifically, reducing $k_\alpha$ would slow down the overall SoC declining rate and thus may fail to entirely exploit the battery

energy, whereas an exceeding large $k_\alpha$ would extremely accelerate the battery energy depletion, thus prolonging the vehicle's charge-sustaining (CS) working period. Hence, a trade-off decision on the EMS performance against the battery energy utilization ratio should be made by using an appropriate $k_\alpha$.

Additionally, $v_{std}(k)$ and $v_{ave}(k)$ represent the standard deviation and mean value of the predicted velocity $V_k^*$, respectively. Note the forecasted speed trace $V_k^*$ with higher $v_{ave}$ and lower $v_{std}$ implies the highway scenario, leading to a larger $\alpha$. In contrast, a speed profile with lower $v_{ave}$ and higher $v_{std}$ indicates the urban scenario, meaning a smaller $\alpha$. Consequently, via the obtained $\alpha$ in different driving scenarios, the actual SoC declining rate $r'_{soc}$ is tuned by the following mechanism. If $\alpha > 1$, $r'_{soc}$ is larger than the reference declining rate ($r_{soc}$). If $\alpha < 1$, $r'_{soc}$ is smaller than $r_{soc}$. Besides, $\alpha = 0$ if and only if $v_{ave} = 0$. Finally, to ensure battery operation safety, the obtained SoC reference values should be bounded within $[\mathrm{SoC}_{\min}, \mathrm{SoC}_{\max}]$, so as to prevent battery over-charge or over-discharge.

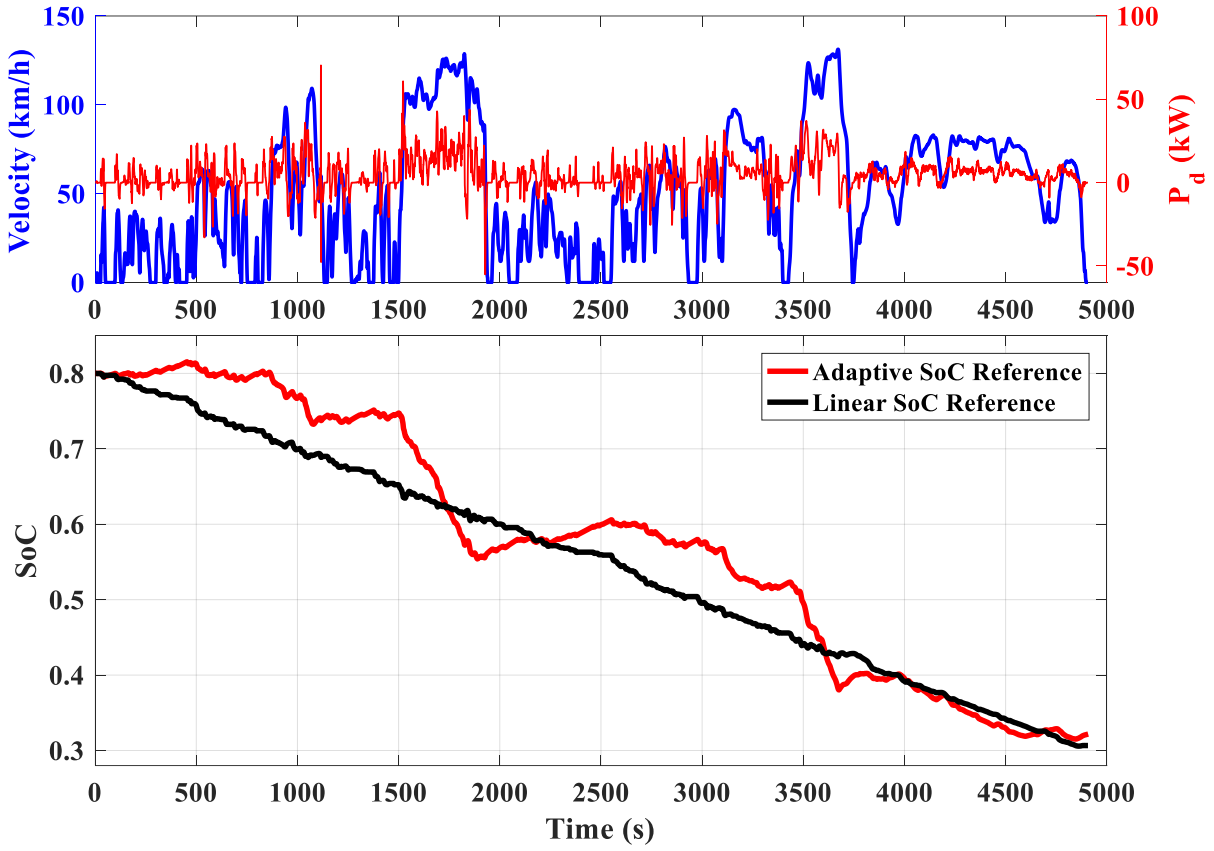


Figure 3.26(b). An example of the SoC regulation performance comparison of the linear SoC reference Eq. (3.17) and the adaptive SoC reference Eq. (3.18).

Furthermore, an example of SoC regulation performance comparison between the linear SoC reference Eq. (3.17) and the proposed adaptive SoC reference Eq. (3.18) (e.g. $k_\alpha = 2$) is given here. In figure 3.26(b), the upper frame gives the speed and the power demand profiles of the combined testing cycle, while the bottom frame shows the battery SoC profiles under the guidance of two different reference generators. As can be observed, the linear SoC reference leads to the single depleting rate over the entire

testing cycle, regardless of the changes in external driving patterns. In contrast, the proposed adaptive SoC reference can help adjust SoC depleting rates to cope with different driving patterns. For example, in urban driving conditions (e.g. 0-500s and 1000-1500s), battery SoC is kept varying around the fixed value since the average power demand is relatively low. While in highway driving conditions (e.g. 1500-1800s), battery SoC is rapidly depleted to handle the high average power demand. To sum up, it can be concluded that, compared to the linear SoC reference, the proposed adaptive SoC reference can more flexibly use electricity to handle changeable driving patterns, which would lead to a more reasonable power-allocating effect, thus further enhancing vehicle's fuel economy.

More detailed performance validation of the proposed adaptive SoC reference would be conducted together with the evaluation of EMS in **Chapter 4**.

## 3.4. Driving pattern recognition techniques

A common drawback in previous studies is that the EMS parameters are optimized for specific driving cycles (e.g. [15]), which, however, did not fully consider the impacts of various driving patterns. In light of the changeable driving conditions in reality, adaptive EMSs for FCHEVs should be able to effectively distribute power demands under multiple driving patterns. In parallel, this yields a challenging task: driving pattern recognition (DPR). To address this issue, this subsection develops a DPR approach based on Markov Chain (MC) and moving window approach, which can differentiate the real-time driving segment into one of three predefined modes. The design process will be detailed in the following parts.

### 3.4.1. Working principle of the Markov Chain based DPR approach

To discriminate various driving patterns, proper feature parameters that can describe each type of driving condition should be predetermined. In this study, the velocity-acceleration (v-a) transition behavior is picked as the feature of each driving pattern, which is quantified by the TPM of Markov Chain.

The principle of the proposed DPR approach is illustrated in figure 3.27, including four working phases: (a) benchmark scenario-based TPMs estimation phase, (b) real-time multi-step TPMs identification phase, (c) similarity quantification phase and (d) DPR accuracy compensating phase, where phase (a) is finished offline whereas others are accomplished online. Detail information about each working phase is introduced in the following parts.

### 3.4.2. Conventional and self-learning Markov model

As indicated by figure 3.27, conventional MC model is used to estimate offline benchmark TPMs for three typical driving patterns, namely urban, suburban and highway. In contrast, the TPMs reflecting the recent driving changes can be identified based on the self-learning MC model. By quantifying the similarity degree between the online estimated TPMs and the offline benchmark TPMs, the real-time driving pattern can be determined.

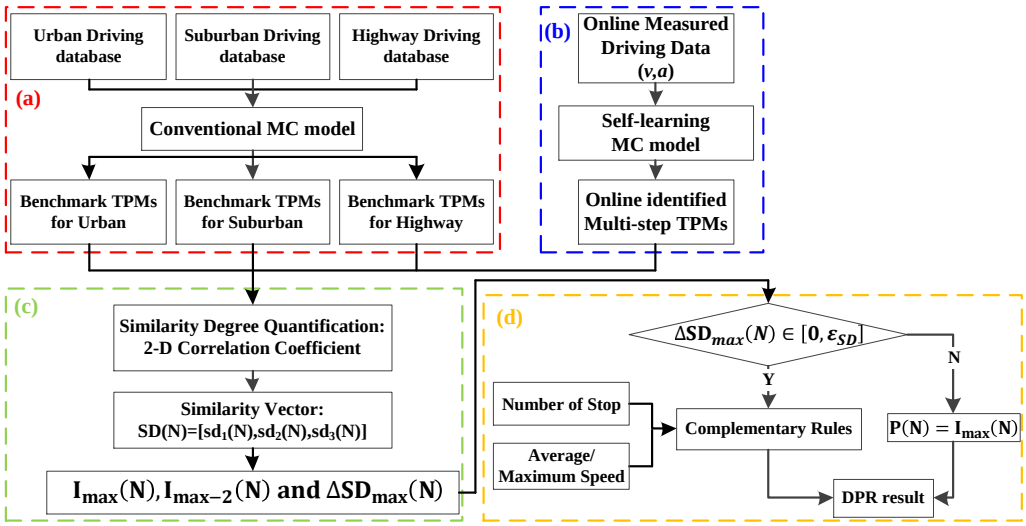


Figure 3.27. Working flowchart of the Markov-based DPR approach: (a) subsection 3.4.2.1: benchmark scenario-based TPMs estimation phase, (b) subsection 3.4.2.2: real-time multi-step TPMs identification phase, (c) subsection 3.4.2.3: similarity quantification phase and (d) subsection 3.4.2.4: DPR accuracy compensating phase

For DPR purpose, the MC state is specified as the (v-a) pair in discrete-value domain, marked as $x(k) = \big(v(k), a(k)\big)$. Therefore, the $(i,j)^{th}$ element in the $l$-step $s$-order TPM can be estimated by:

$$\begin{aligned} &[T_l]_{ij} = \Pr\{x(k+l) = x_j | x(k) = x_i\} \approx \mathbf{Num}_{ij}^{l} / \mathbf{Num}_{oi}^{l} \quad (a) \\ &\mathbf{Num}_{oi}^{l} = \textstyle\sum_{j=1}^{s} \mathbf{Num}_{ij}^{l}, i,j \in \{1,2,\dots,s\}, l \in \{1,\dots,N_T\} \quad (b) \end{aligned} \tag{3.19}$$

where $\mathbf{Num}_{ij}^{l}$ is the number of transitions from $x_i$ to $x_j$ after $l$ time steps, $\mathbf{Num}_{oi}^{l}$ the number of transitions starting from $x_i$ , and $N_T$ denotes the time scale range of the conventional MC.

Here, the formulation of self-learning MC model is omitted to avoid repetitive illustration. More details regarding its formulation is given by Eq. (3.10)-Eq. (3.16), as presented in subsection 3.2.3.1.

### 3.4.2.1. Offline benchmark transition probability matrices estimation phase

Overall, figure 3.28 depicts the working flow of offline benchmark TPM estimation phase. Specifically, three major working steps of this phase are given as follows:

- **Step 1:** As shown in figure 3.28(a), numerous standard driving cycles are extracted from ADVISOR [2], namely HWFET, Cruise3, HHDDT65, ARTEMIS_HW, US06_HW, ARTEMIS_UB, Manhattan, BUSRTE, NurembergR36, AQMDRTC2, WVUINTER, ARTEMIS_SUB, UNIF01, IM240 and WVUSUB. Note the driving cycles with the same pattern are aggregated to form the corresponding sub-database.
- **Step 2**: As shown in figure 3.28(b), combined driving cycle within each sub-database is discretized into numerous (v-a) pairs. These time-labelled data are then projected into the V-A plane, wherein the samples falling into the same rectangle zone are assigned with the identical MC state index.

- **Step 3**: Based on the measurements on the V-A plane, the multi-step TPMs under each driving scenario can be estimated using Eq. (3.19). These established TPMs are stored as the offline basis for online similarity quantification. As a result, it can be observed from the 3-D bar diagrams in figure 3.28(c) that each driving pattern is associated with its own (v-a) transition characteristic. In other words, the established multi-timescale TPM groups can be used to characterize corresponding driving patterns.

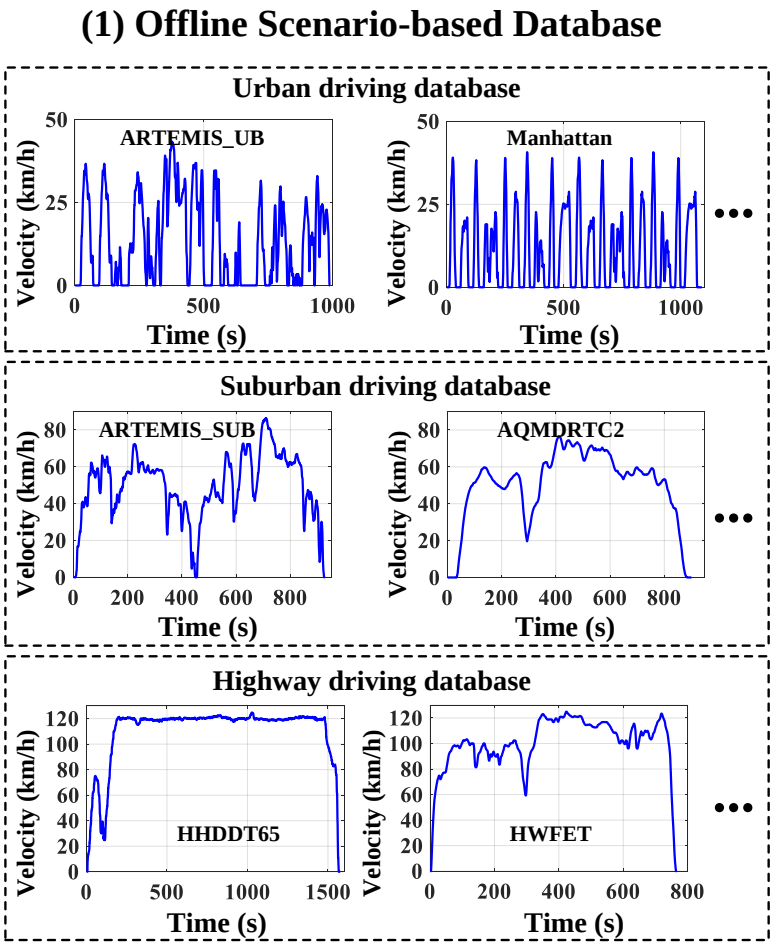


Figure 3.28(a). Flowchart of offline scenario-based benchmark TPMs estimation phase (e.g. $s = 36$ and $N_T = 3$): Step 1. Establishment of the offline scenario-based driving database.

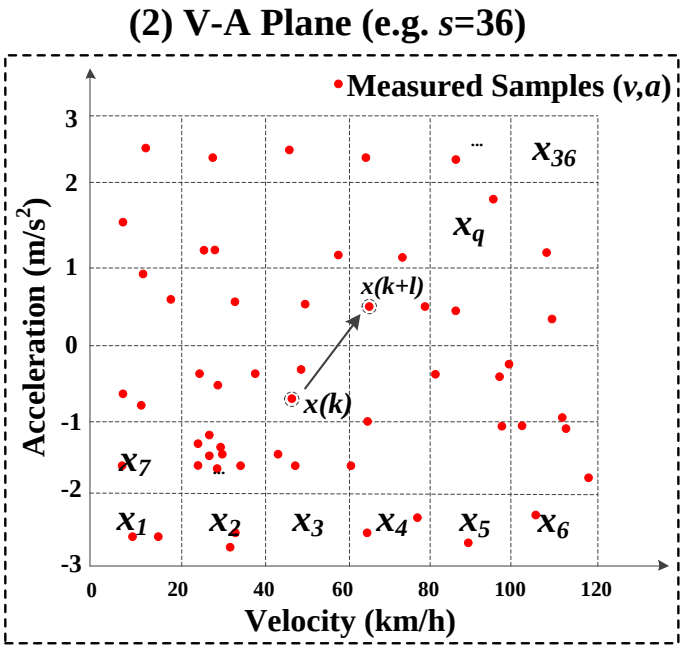


Figure 3.28(b). Flowchart of offline scenario-based benchmark TPMs estimation phase (e.g. $s = 36$ and $N_T = 3$): Step 2. Discretion & projection speed samples into the V-A plane.

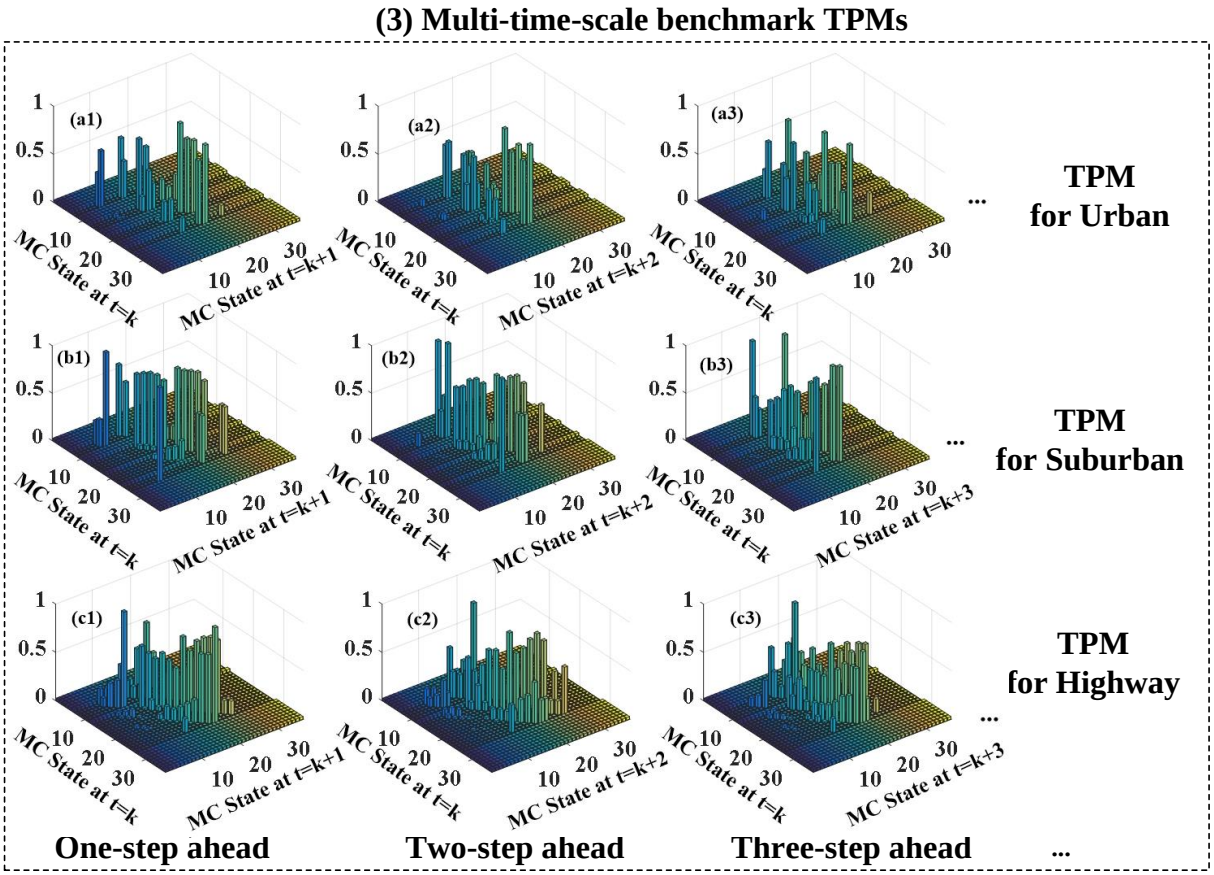


Figure 3.28(c). Flowchart of offline scenario-based benchmark TPMs estimation phase (e.g. $s = 36$ and $N_T = 3$): Step 3. Estimation of offline benchmark TPM groups in different driving patterns.

### 3.4.2.2. Online transition probability matrices identification phase

Figure 3.29 presents the working flow of online TPM identification phase. As can be seen, the self-learning MC model is implemented on each driving segment within the moving window horizon, where $L_s$ and $L_u$ respectively denote the length of sampling and updating window. Based on the sampled (v-a) data, the transition probabilities can be updated at each sampling time step, thus leading to the evolution of online TPM groups from the initial ones to the terminal ones.

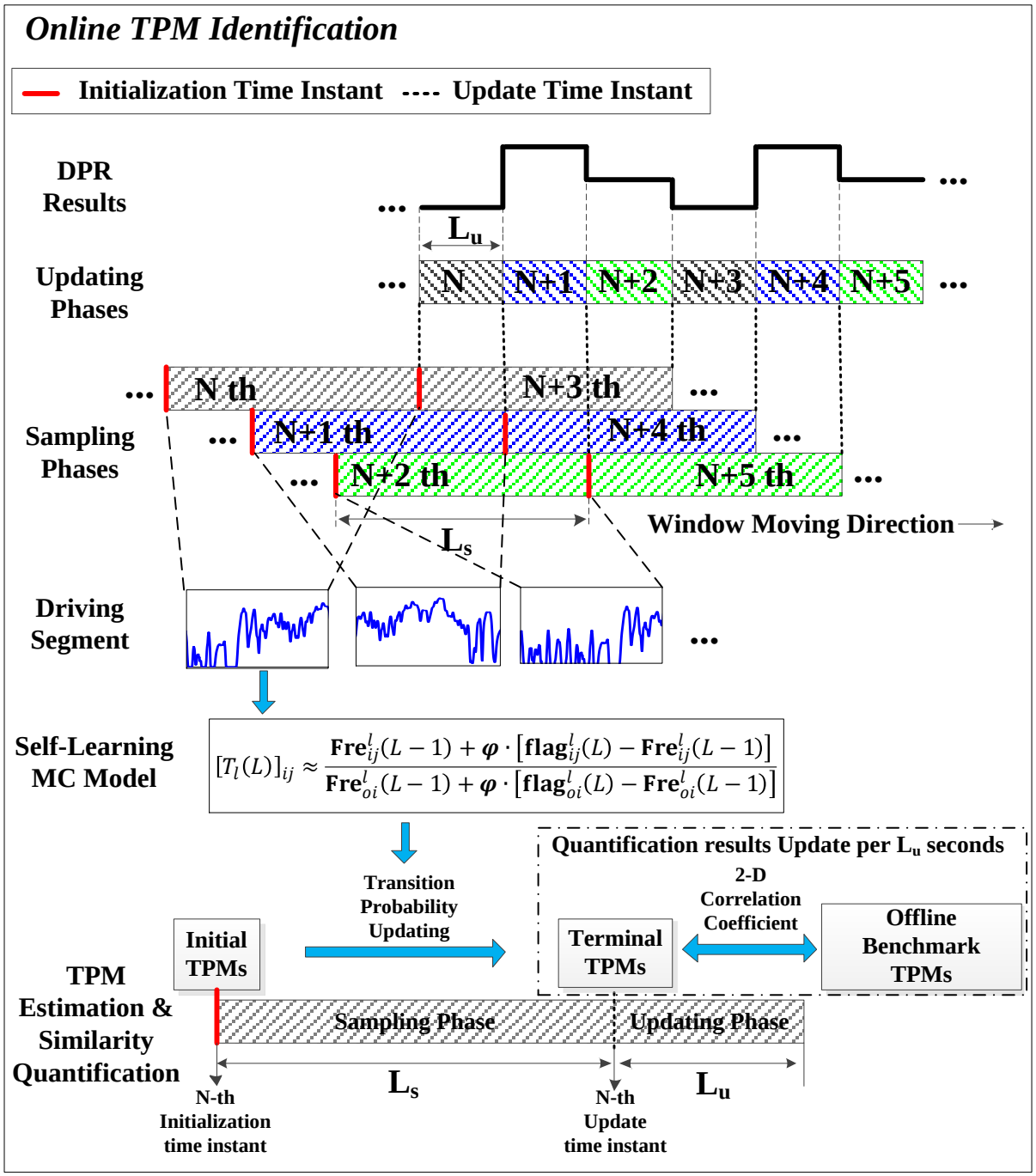


Figure 3.29. Flowchart of online multi-scale TPM identification phase.

Therefore, the resemblance between the real-time identified TPMs and the benchmark TPMs is

quantified at the end of each sampling phase. Note the quantification results remain unchanged within the entire updating phase ($L_u$ seconds). Afterwards, to quickly eliminate the negative impacts by the old observations, all the elements within the online TPMs are re-initialized to $1/s$ at each initialization time instant (marked as red solid line in figure 3.29). Hence, the quantification results are updated per $L_u$ seconds, which are then used to finalize the pattern identification of current driving segment. Note the detail information about the TPM similarity quantification process will be introduced afterwards.

To ensure the online identified TPMs fully representing the driving behaviors of current segment, the MC effective memory depth $D_\varphi$ is set the same as the sampling window length $L_s$. Obviously, a larger $L_s$ enables a wider coverage of historical driving conditions. However, an overlarge $L_s$ may contain superfluous information and increase the computational burden as well. As reported in [16], the typical driving period of HEVs is around 180 seconds. In other words, as a reasonable compromise, $L_s$ should be specified as an approximate value to this threshold. Besides, the updating window length $L_u$ should be given a proper value to ensure the updating rate of the real-time DPR results without frequent pattern switching. Considering these issues, $L_s$ and $L_u$ are respectively set as 150s and 50s. Note these values are obtained through a large amount of cross-validation test.

#### 3.4.2.3. Similarity degree quantification

To quantify the similarity of the real-time identified TPMs towards the offline benchmark TPMs, the 2-D correlation coefficient $r \in [0,1]$ is introduced. Note $r(A,B)$ is to evaluate the similarity degree between two matrices $A, B \in R^{m\times n}$, which can be computed by:

$$r(A,B) = \frac{\sum_{i=1}^{m}\sum_{j=1}^{n}([A]_{i,j}-\bar{A})([B]_{i,j}-\bar{B})}{\sqrt{(\sum_{i=1}^{m}\sum_{j=1}^{n}([A]_{i,j}-\bar{A})^2)(\sum_{i=1}^{m}\sum_{j=1}^{n}([B]_{i,j}-\bar{B})^2)}} \tag{3.20}$$

where $[A]_{i,j}$ and $[B]_{i,j}$ respectively denote the $(i,j)^{th}$ element of $A$ and $B$. $\bar{A}$ and $\bar{B}$ denote the average of matrix elements. A larger $r(A,B)$ indicates a higher degree of similarity between the examined matrix pairs. Besides, let $N$ denotes the index of the updating window. Therefore, at time step $t = k, N = fix(k/L_u)$, where $L_u = 50$s and the $fix$ function returns the integer portion of $k/L_u$.

At the $N^{th}$ updating time instant, the real-time identified TPMs, marked as $T_l(N)$, are compared with the benchmark TPMs, marked as $T_l^i$, $l = 1,2,\dots,N_T$. Note $i$ is the index of the pre-defined driving patterns (1: urban, 2: suburban, 3: highway). Hence, the quantification results are denoted by a similarity vector $SD(N) = [sd_1(N), sd_2(N), sd_3(N)]$. Note $sd_i(N) \in [0,1], i = 1,2,3$ quantifies the average similarity of the online estimated TPMs against each type of benchmark TPMs, which can be computed by:

$$sd_i(N) = \frac{1}{N_T}\sum_{l=1}^{N_T} r\left(T_l(N), T_l^i\right), i = 1,2,3. \tag{3.21}$$

Furthermore, let $\Delta SD_{max}(N) \in [0,1]$ denotes the difference between the largest and the second largest element in $SD(N)$, $\varepsilon_{SD} \in (0,1)$ the confidence threshold and $I_{max}(N), I_{max-2}(N) \in \{1,2,3\}$ respectively the index of the largest and the second largest element in $SD(N)$. Note the setting of $\varepsilon_{SD}$ would affect the pattern identification accuracy. After trials and errors, $\varepsilon_{SD}$ is set to 0.05 in this work. The effect of $\varepsilon_{SD}$ will be discussed in detail in subsection 3.4.3. Based on these definitions, there are two possible cases at the end of the $N^{th}$ sampling horizon:

- **Case I**: If $\Delta SD_{max}(N) > \varepsilon_{SD}$, such similarity discrepancy is deemed adequate to separate different driving patterns. Hence, the real-time driving pattern can be confidently categorized into the one of three modes by $P(N) = I_{max}(N)$. This case tends to occur if the (v-a) transitions come from single driving pattern, as shown in the $k^{th}$ and the $r^{th}$ phases in figure 3.30(a).
- **Case II**: If $\Delta SD_{max}(N) \leq \varepsilon_{SD}$, it is not convincing to discriminate driving patterns based on such insignificant similarity discrepancies. This case tends to happen during either the driving pattern shifting phases (e.g. $q^{th}$ phase of 3.30(a)) or the confusion phases (e.g. $s^{th}$ phase of figure 3.30(a)).

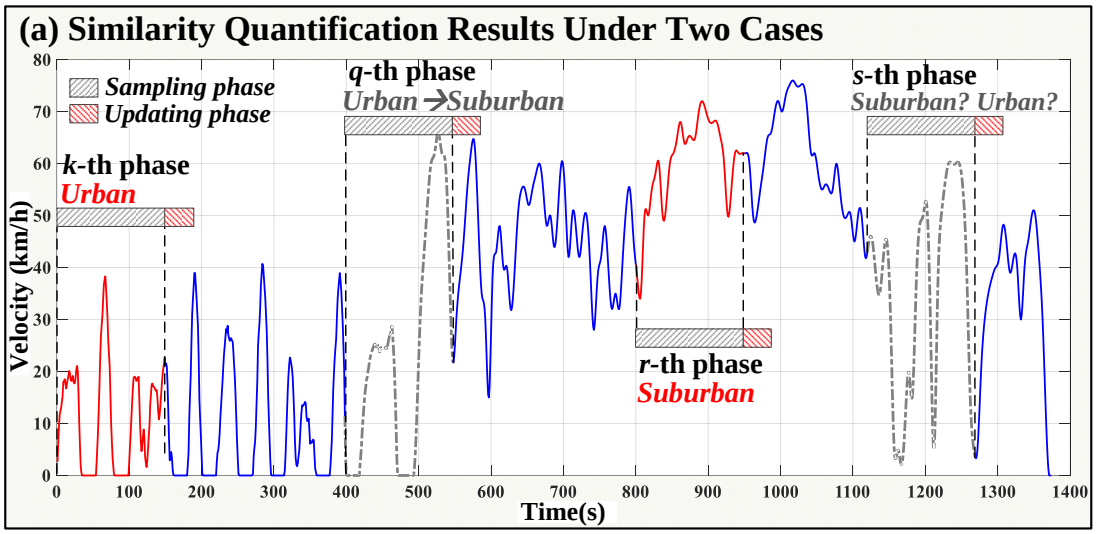


Figure 3.30(a). Flowchart of similarity quantification and DPR accuracy compensate phases: similarity degree quantification results.

In **case II**, TPM similarity quantification results cannot bring a reasonable separation of two conflict patterns (determined by $I_{max}$ and $I_{max-2}$), which requires additional rules to improve the DPR accuracy. In fact, different DPR decisions should be made under two possible driving scenarios. Specifically, although $\Delta SD_{max}(N) \leq \varepsilon_{SD}$ during pattern shifting phases (e.g. figure 3.30(b1), where larger portion of measurements is from "urban" pattern, and figure 3.30(b2), where larger portion of measurements is from "suburban" pattern), it is reasonable to set the DPR result as the upcoming "suburban", since the pattern switching moment (marked with the purple dashed curve) exists in the current sampling horizon. However, to avoid the mis-recognition in confusion phases (figure 3.30(c1) and (c2)), it is better to keep the current DPR result as the "urban" since the actual driving pattern does not change.

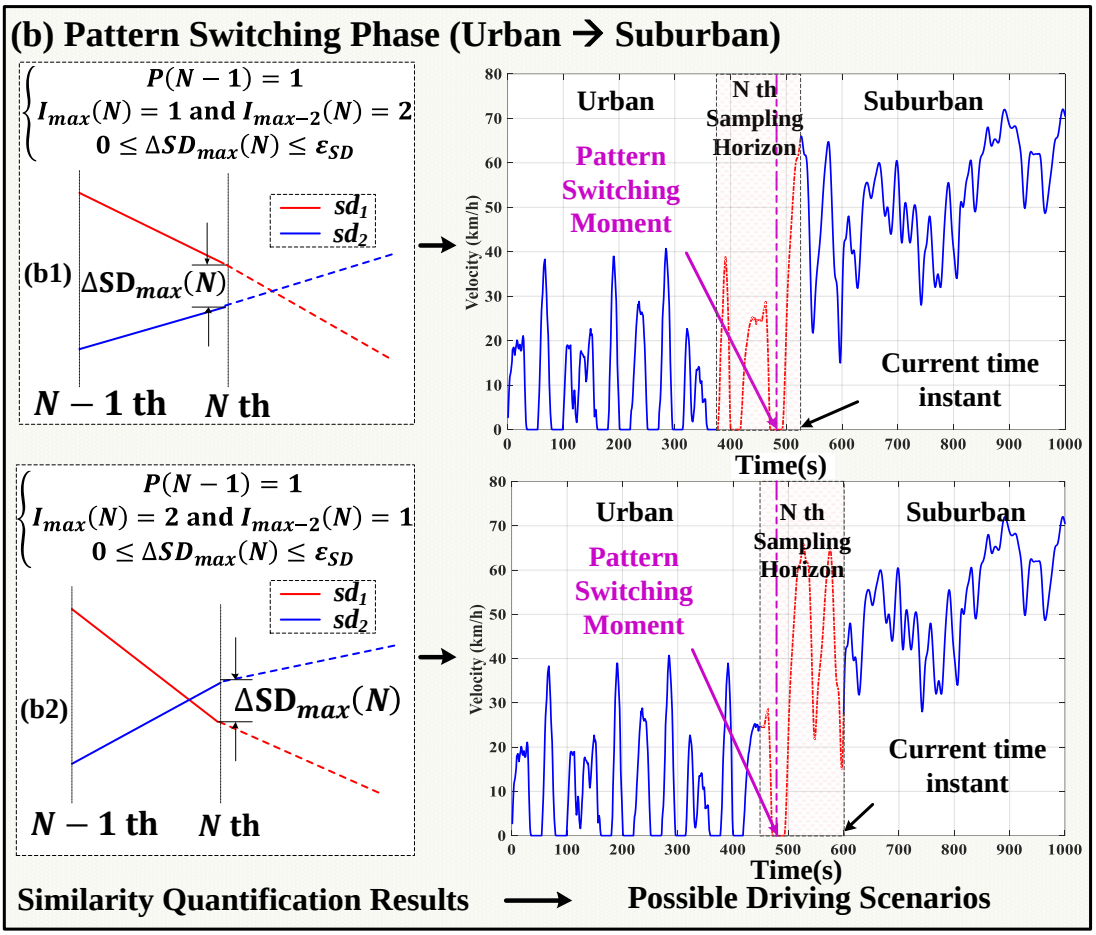


Figure 3.30(c). Flowchart of similarity quantification and DPR accuracy compensate phases: real driving pattern-switching phases (e.g. urban to suburban).

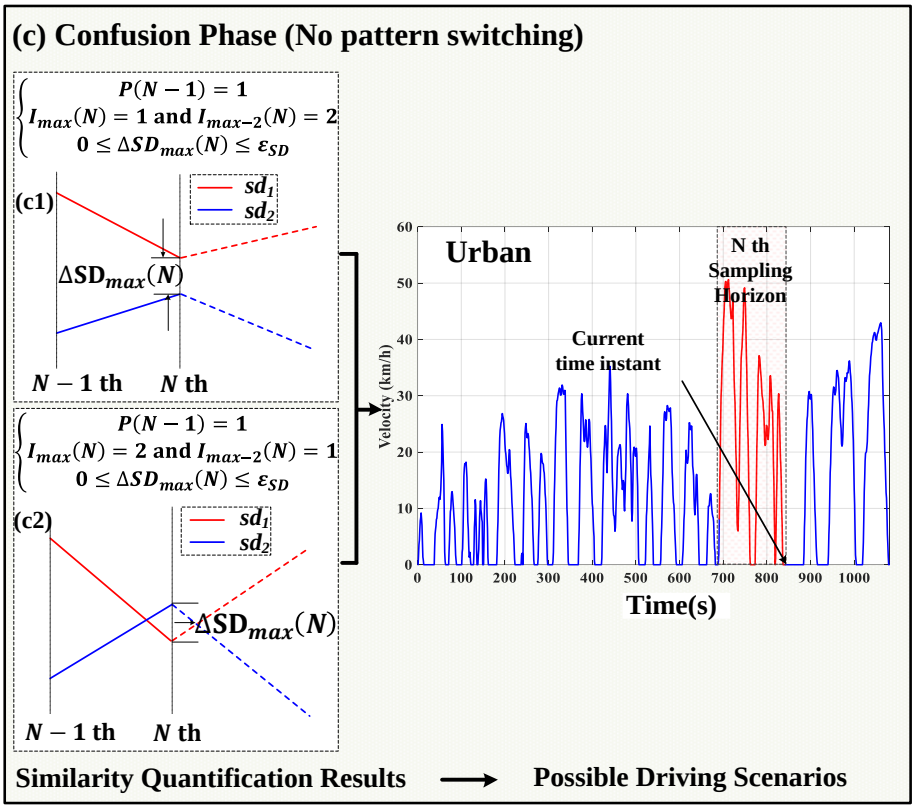


Figure 3.30(d). Flowchart of similarity quantification and DPR accuracy compensate phases: confusion phases (e.g. urban vs. suburban).

### 3.4.2.4. Complementary rules

To differentiate the pattern switching phases from corresponding confusion phases, the basic principle of the proposed solution (as shown in figure 3.30(d)) can be stated as follows:

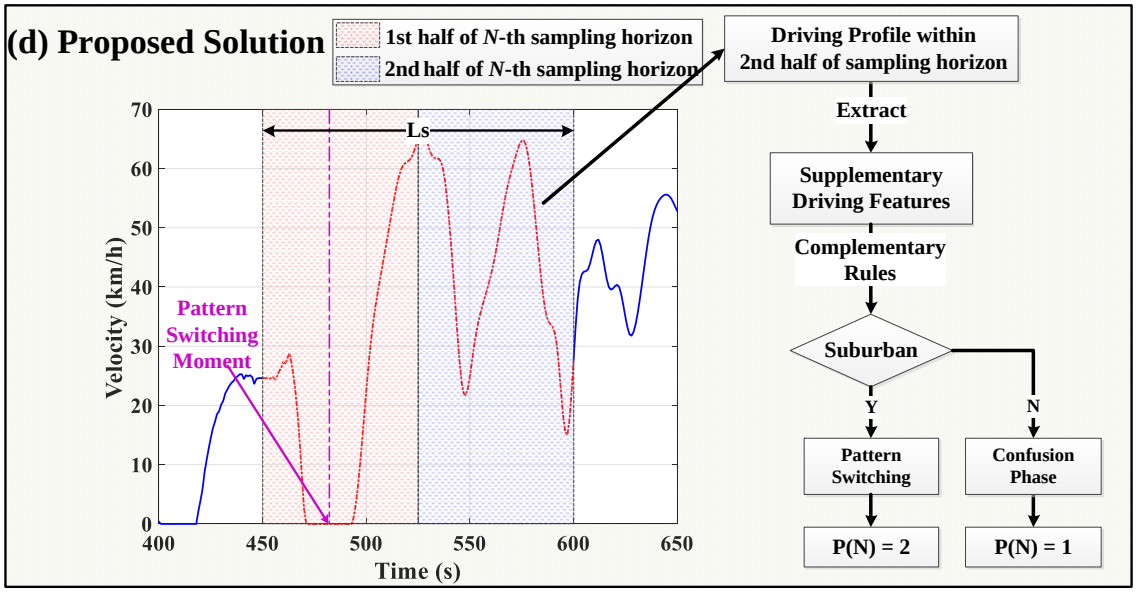


Figure 3.30(e). Flowchart of similarity quantification and DPR accuracy compensate phases: proposed solution to separate pattern switching phases from corresponding confusion phases (e.g. urban vs suburban).

Given (i) $P(N-1)=1$, (ii) $I_{max}(N), I_{max-2}(N) \in \{1,2\}$ and (iii) $\Delta SD_{max}(N) \leq \varepsilon_{SD}$, the $N^{th}$ DPR result $P(N)$ should be selected from $I_{max}(N)$ and $I_{max-2}(N)$. Thus, we divide the $N^{th}$ sampling window into two identical parts. If the driving segment within the second half of sampling horizon has enough supplementary driving features belonging to "suburban" pattern then $P(N)=2$. Otherwise, $P(N)=1$. Similarly, if "urban" and "highway" or "suburban" and "highway" become the conflict pattern pairs, the same strategy can be used to finalize the current DPR results.

To achieve such objective, supplementary driving features should be extracted from the second half of the sampling horizon if $\Delta SD_{max}(N) \leq \varepsilon_{SD}$. Based on the extracted features, the related complementary rules come into effect to judge whether the measured driving fragment can be classified into the upcoming pattern or not. In the following part, a brief introduction of the supplementary driving feature selection under urban/suburban patterns as well as the establishment of complementary rules are provided to explain the separation criterion of such conflict pattern pairs.

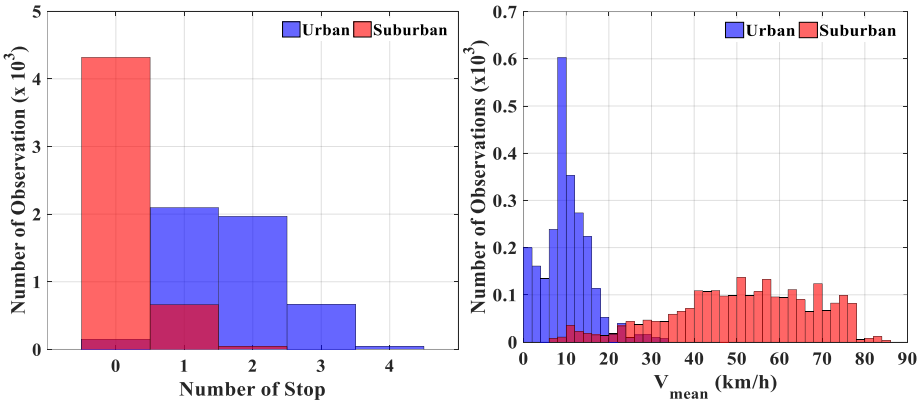


Figure 3.31. Histogram on NoS and $v_{mean}$ of driving samples (per 75s) under urban and suburban patterns.

The number of stop event (zero-speed) (NoS) and the average speed ($v_{mean}$) are selected as the supplementary driving features when "urban" and "suburban" become the conflict pattern pairs. To analyze the statistical distributions on the selected features, large amount of driving samples with fixed length ($0.5L_s = 75\ s$) are extracted from the offline database (as shown in figure 3.28(a)). Based on these samples, the histograms of the selected features are given in figure 3.31. Moreover, some key figures are listed in TABLE 3.8, where $Pr(\cdot)$ is the probability of the studied event. Based on the statistics in TABLE 3.8, the complementary rule to separate urban/suburban scenarios is given in figure 3.32(a). Moreover, the complementary rules for other situations can be established in the similar way. To avoid repetitive illustration, here we only give the related separation rules (figure 3.32(b) and (c)), rather than detailing the establishment processes.

TABLE 3.8. Statistical distributions (per 75s) for the supplementary driving features

| | $\mathbf{Pr}(NoS=0)$ | $\mathbf{Pr}(NoS=1)$ | $\mathbf{Pr}(NoS>1)$ | $\mathbf{Pr}(v_{mean}>20km/h)$ |
|---|---|---|---|---|
| **Urban** | 3.07% | 42.55% | 54.38% | 4.57% |
| **Suburban** | 86.01% | 13.15% | 0.84% | 95.10% |

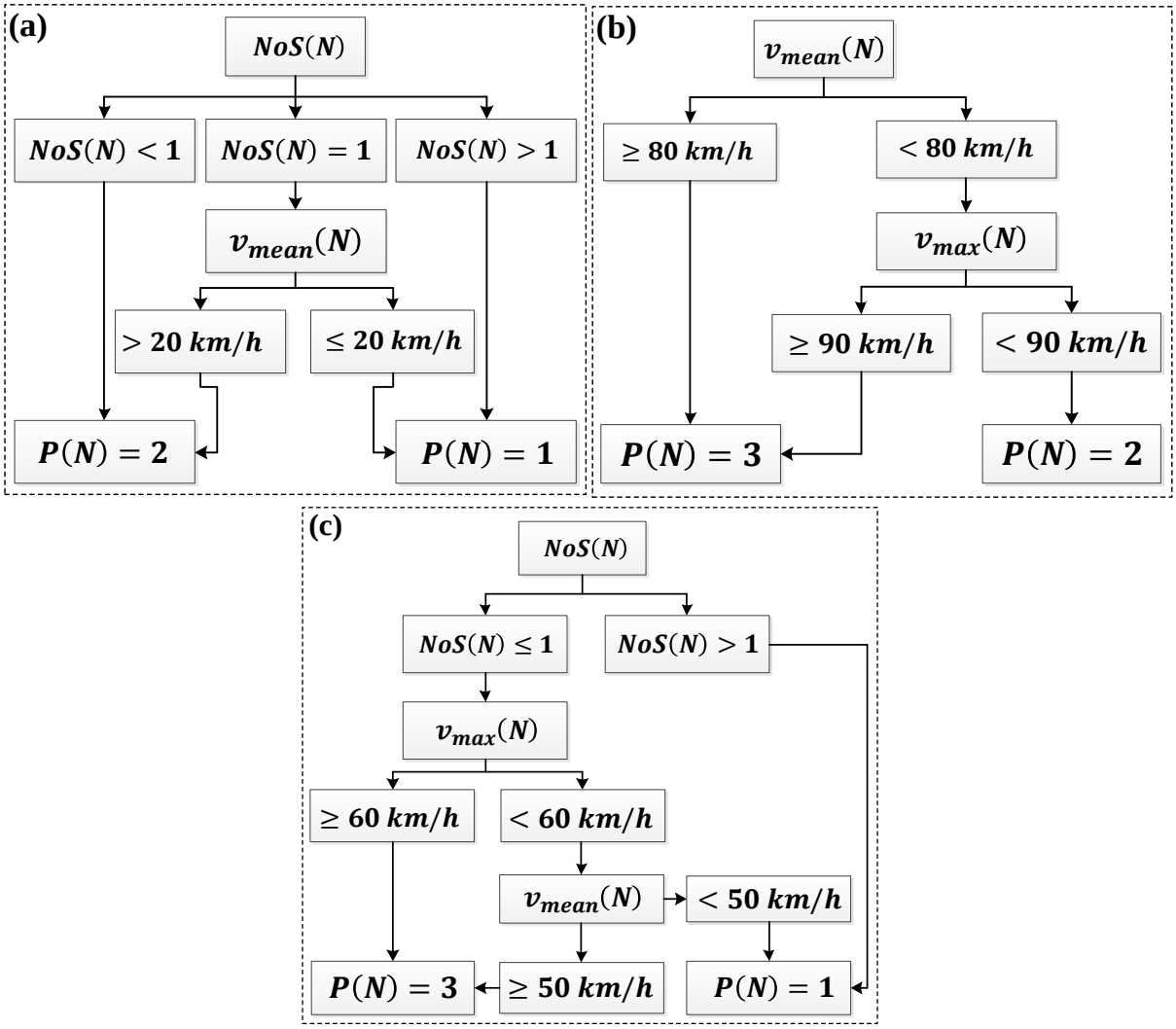


Figure 3.32. Complementary rules for (a) urban/suburban, (b) highway/suburban and (c) urban/highway.

### 3.4.3. Driving pattern recognition performance validation

The effectiveness of the proposed MC-based DPR approach is validated under multi-pattern test cycles, where the number of MC state $s$ and the MC time scale $N_T$ are respectively set as 16 and 5 in these tests.

- **Impacts on pattern identification accuracy imposed by confidence threshold $\varepsilon_{SD}$**

The confidence threshold $\varepsilon_{SD}$ determines the intervention frequency of the complementary rules, where a larger $\varepsilon_{SD}$ would lead to a higher frequency, while a smaller $\varepsilon_{SD}$ would lead to a lower frequency. Hereafter, an example is given in figure 3.33 to illustrate the effect on pattern identification results brought by different $\varepsilon_{SD}$ settings.

Figure 3.33(a) gives the speed profile of the testing cycle, and figure 3.33(b)-(d) show the pattern identification results under different $\varepsilon_{SD}$ settings. Taken the performance of $\varepsilon_{SD} = 0.05$ as basis, if we increase the $\varepsilon_{SD}$ (e.g. to 0.5), the frequent intervention of complementary rules would interfere the normal operation of TPM similarity quantification. Yet, only when the quantified similarity discrepancy

is insignificant, the complementary rules should become effective. This is the reason there are many frequent pattern-switching in figure 3.33(b) compared to the outcome in figure 3.33(c), indicating a compromised DPR reliability. In contrary, if we reduce the $\varepsilon_{SD}$ (e.g. to 0.005), the intervention frequency of complementary rules would be too low to help separate the conflict patterns. This would also lead to the drop of DPR accuracy when $\Delta SD_{max}(N) \leq \varepsilon_{SD}$, as underlined by grey shadows in figure 3.33(c) and (d). As a tradeoff, this work sets the confidence threshold $\varepsilon_{SD} = 0.05$.

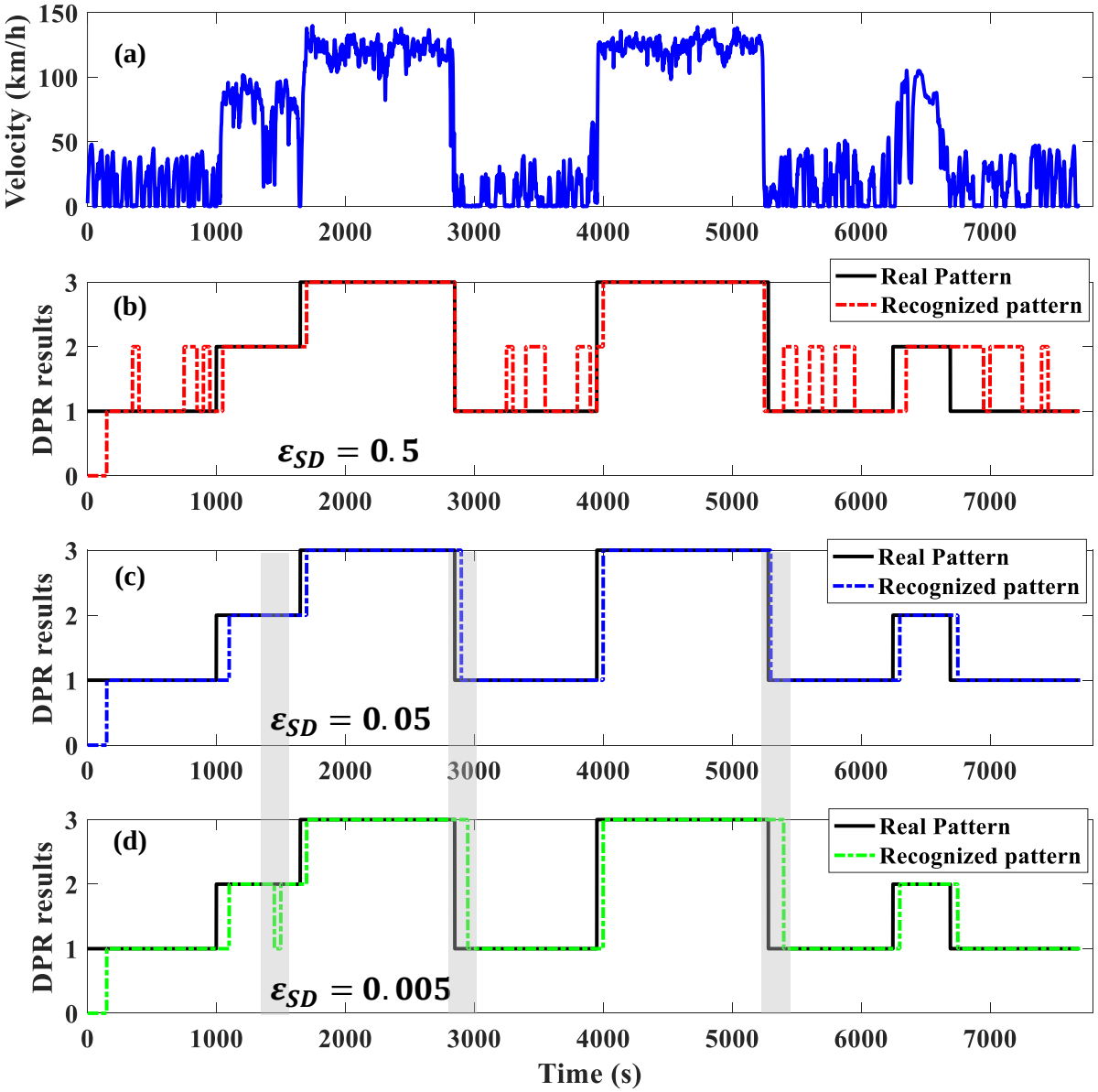


Figure 3.33. Impacts on pattern identification accuracy by different settings on confidence threshold $\varepsilon_{SD}$.

- **Evaluation results on test cycle I and II**

Firstly, its performance is evaluated under test cycle I and II. As depicted in figure 3.34(a) and (e), two combined cycles comprise eight identical standard driving cycles with different concatenating sequences. These standard cycles are extracted from the offline database for benchmark TPMs estimation.

Moreover, as shown in figure 3.34(b) and (f), the red, blue, and green curves respectively denote the obtained similarity degrees $(sd_1, sd_2, sd_3)$ towards three pre-defined patterns, and the black curve is the index of the largest element within the similarity vector. Furthermore, the DPR results are given in figure 3.34(c), (d) and (g), (h). Overall, based on $I_{max}$, the proposed approach can properly identify driving pattern when external driving condition is stable. Yet, as shown in figure 3.34(c) and (g), recognition errors tend to occur when $\Delta SD_{max} \leq \varepsilon_{SD}$. In contrast, after using the complementary rules, the risk of frequent pattern switching can be greatly reduced, thus improving the accuracy and the reliability of pattern identification, as shown in figure 3.34(d) and (h). Besides, the DPR result is set as "unrecognized (0)" during the first 150s since there are not enough historical data for pattern recognition during the start-up phase. By comparing the pattern identification results under two test cycles, it can be confirmed that the connecting sequence of standard cycles will not bring significant DPR performance discrepancy.

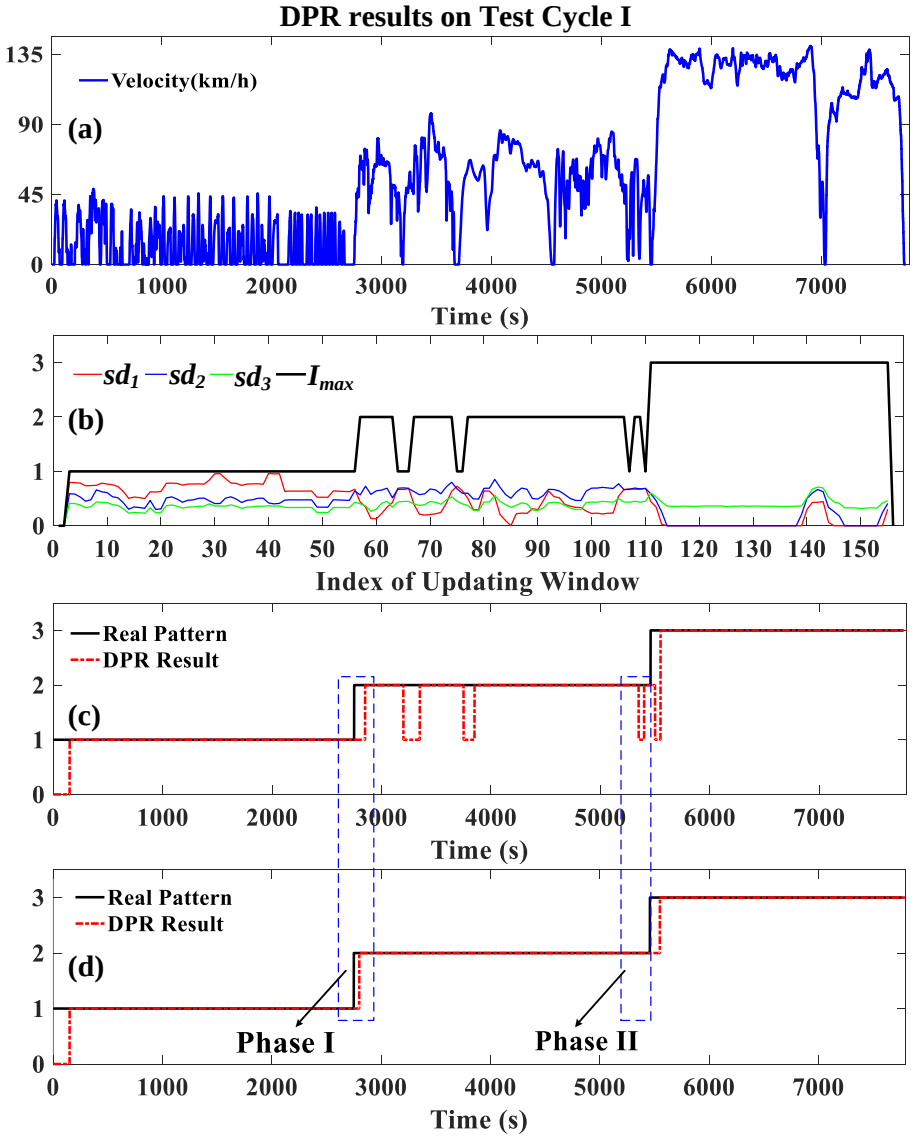


Figure 3.34(a)-(d). DPR results on test cycle I. Fig. (a): speed profile of driving cycle I, Fig. (b): similarity quantification results, Fig. (c) and (d): DPR results without and with complementary, respectively.

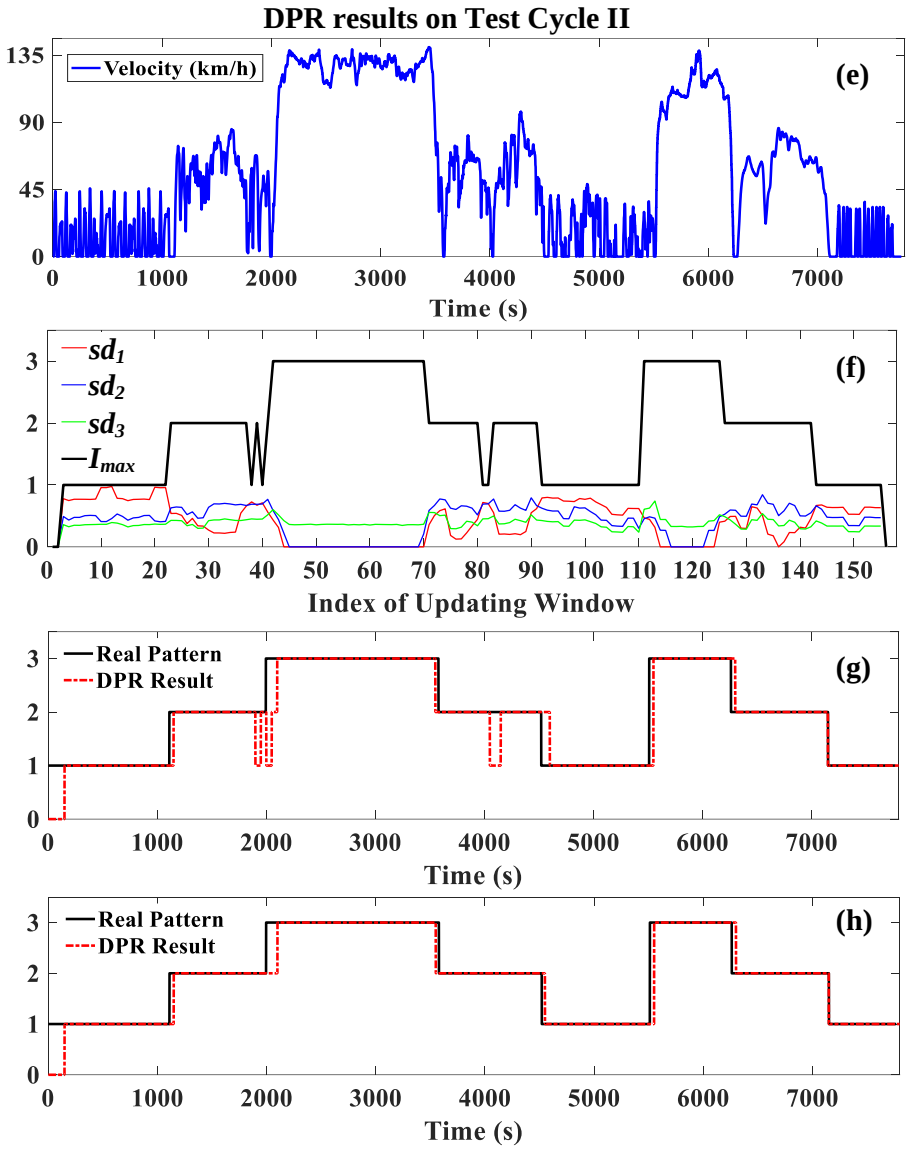


Figure 3.34(e)-(h). DPR results on test cycle II. Fig. (e): speed profile of driving cycle II, Fig. (f): similarity quantification results, Fig. (g) and (h): DPR results without and with complementary, respectively.

- **Evaluation results on test cycle III**

To further verify the DPR performance, eight driving cycles, which are not used for the benchmark TPMs estimation, are concatenated to form test cycle III, as shown in figure 3.35(a). Overall, as depicted in figure 3.35(b)-(d), the proposed method can generate the reasonable pattern separation results, indicating its effectiveness in coping with new driving conditions.

Specifically, after using the complementary rules, the DPR performance enhanced from two aspects: 1) the risks of the mis-recognition are reduced; 2) the latency before correctly recognizing the upcoming pattern is decreased. For example, as shown in figure 3.35(e), the obtained similarity degree $\mathrm{sd}_1(29)$ is larger than $\mathrm{sd}_2(29)$ but their discrepancy (0.0052) is smaller than the threshold $\varepsilon_{\mathrm{SD}} = 0.05$. Consequently, if without the complementary rules, the DPR result is set to "urban" since $\mathrm{I}_{\max}(29) = 1$,

which causes the mis-recognition of driving pattern, as shown in phase III of figure 3.35(c). In contrast, as shown in figure 3.35(f), there is no vehicle stop (zero-speed) event within the second half of 29th sampling horizon. According to the complementary rules shown in figure 3.32(a), current DPR result is set to "suburban" so that the pattern mis-recognition can be avoided, as shown in phase III of figure 3.35(d). Similarly, as shown in figure 3.35(g), due to $I_{max}(58) = 3$, the 58th DPR result is set to "highway" if without the complementary rules, leading to the pattern identification delay, as shown in phase IV of figure 3.35(c). In contrast, within the second half of 58th sampling horizon (figure 3.35(h)), three times of vehicle stop event are detected ($NoS > 1$). According to the complementary rules given in figure 3.32(c), the 58th DPR result is set to "urban", leading to the acceleration of pattern identification, as shown in phase IV of figure 3.35(d).

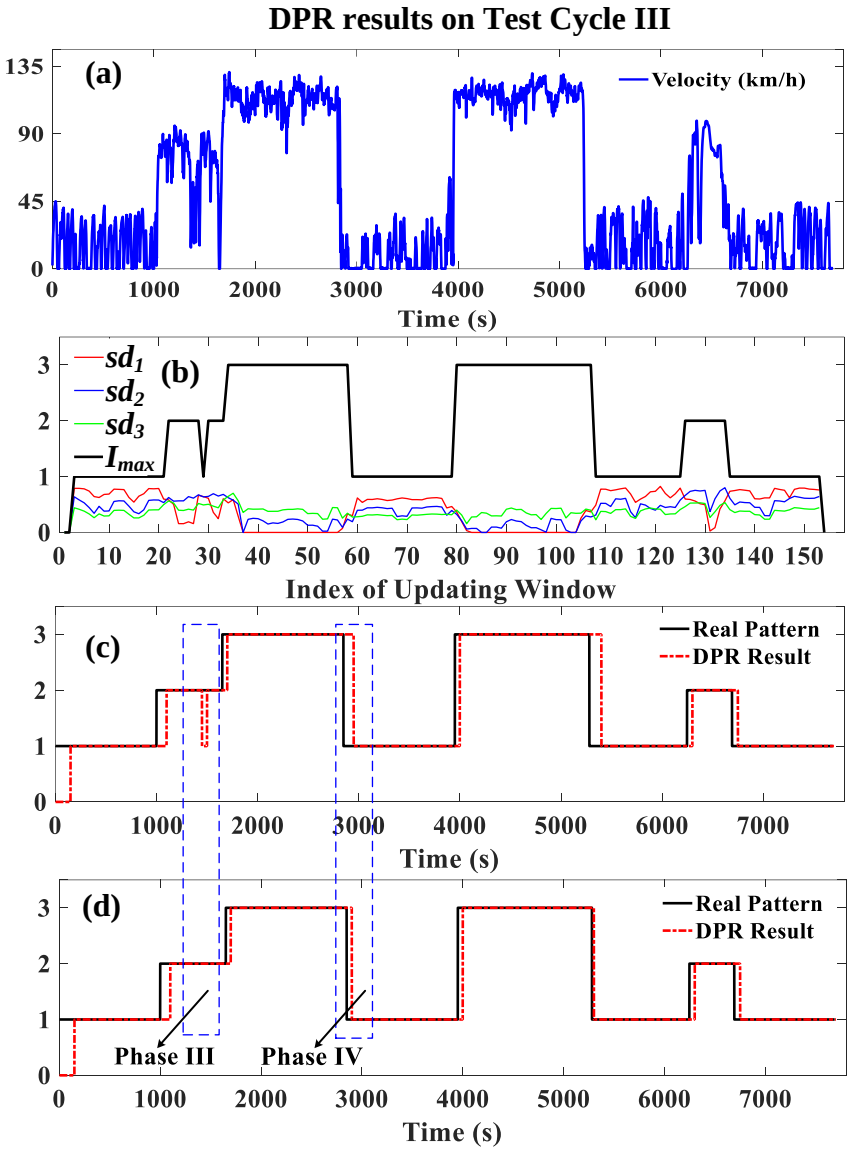


Figure 3.35(a)-(d). DPR results on test cycle III. Fig. (a): speed profile of driving cycle III, Fig. (b): similarity quantification results, Fig. (c) and (d): DPR results without and with complementary, respectively.

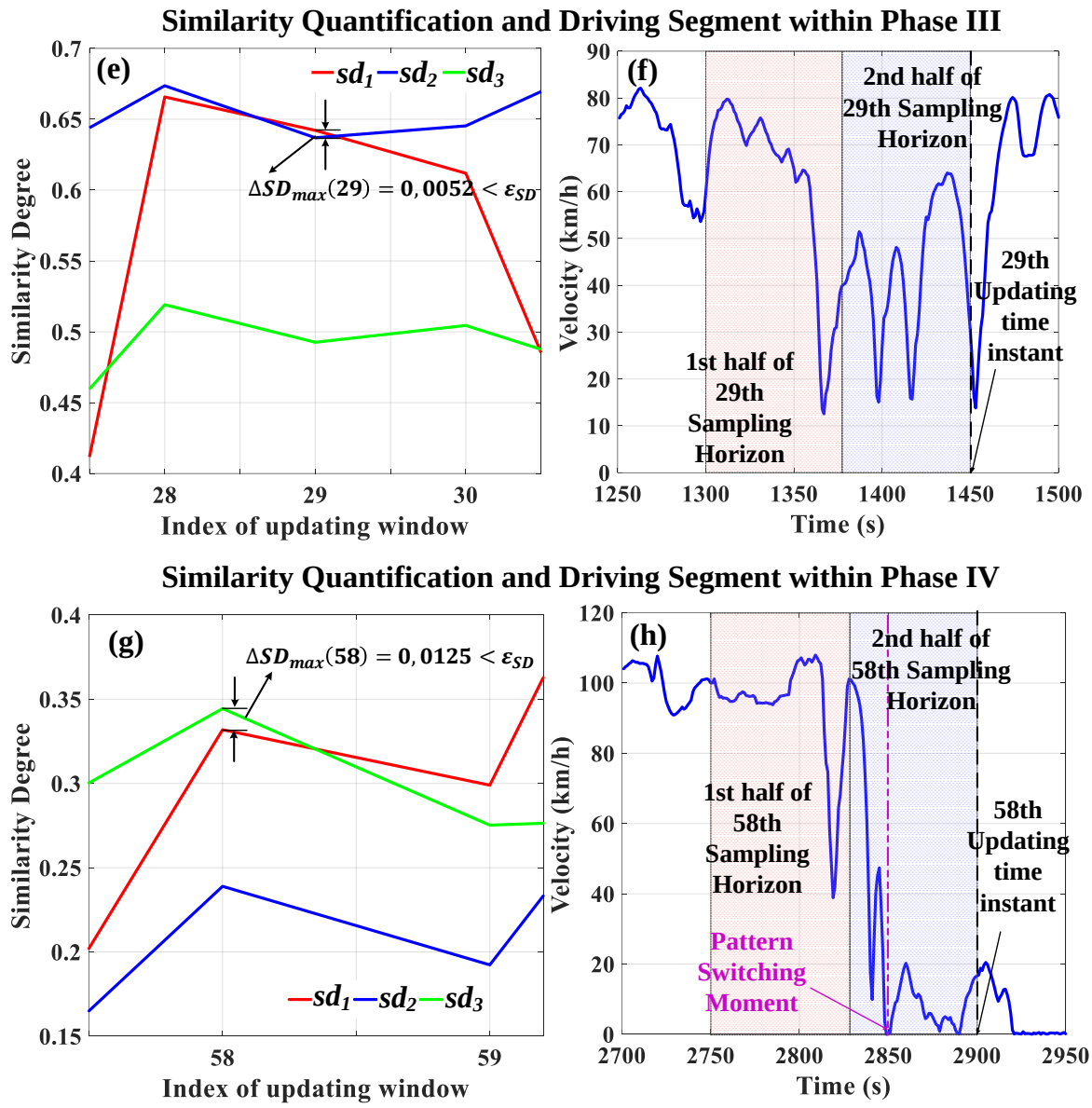


Figure 3.35(e)-(h). DPR results on test cycle III: driving segments and similarity quantification results within phase III and IV.

TABLE 3.9. DPR Accuracy Comparison with/without Complementary Rules ($s = 16$ and $N_T = 5$)

| | Test cycle I | Test cycle II | Test cycle III |
|---|---|---|---|
| **Without complementary rules** | 93.55% | 92.89% | 92.32% |
| **With complementary rules** | 98.16% | 95.55% | 94.97% |
| **Accuracy Improvement** | **+4.61%** | **+2.66%** | **+2.65%** |

TABLE 3.9 lists the DPR accuracy under three test cycles. As can be seen, without complementary rules, the MC recognizer can achieve over 92.00% DPR accuracy on three test cycles. In comparison, the complementary rules can bring additional 2.65% to 4.61% accuracy improvement, due to the reduced risk of frequent pattern switching. Moreover, since the role of Markov-based DPR method is the upper-level controller, the prevention of frequent pattern switching would also strengthen the reliability of lower-level EMS controller, thus reducing the potential damages to powertrain components by improper

power-allocating commands. From this aspect, the improved DPR accuracy could further enhance the vehicle's operation safety, which should be deemed as the meaning of using complementary rules. Overall, 94.97% to 98.16% DPR accuracy indicates the proposed MC pattern recognizer can effectively separate the real-time driving patterns.

- **Impacts on pattern identification accuracy imposed by $s$ and $N_T$**

Note the setting of $s$ and $N_T$ would affect the performance of the proposed DPR approach. Therefore, a sensitivity analysis is presented to reveal the impacts on DPR accuracy brought by different $s$ and $N_T$. Corresponding numerical results are given in TABLE 3.10.

TABLE 3.10. DPR Accuracy Comparison with Different Parameter Configurations

| Parameter Settings | | Test cycle I | Test cycle II | Test cycle III |
|---|---|---|---|---|
| $\mathbf{s = 16}$ | $\mathbf{N_T = 1}$ | 88.19% | 86.98% | 91.64% |
| | $\mathbf{N_T = 2}$ | 92.90% | 92.89% | 92.31% |
| | $\mathbf{N_T = 3}$ | 94.87% | 94.87% | 92.32% |
| | $\mathbf{N_T = 4}$ | 97.49% | 95.52% | 92.98% |
| | $\mathbf{N_T = 5}$ | 98.16% | 95.55% | 94.97% |
| $\mathbf{s = 36}$ | $\mathbf{N_T = 1}$ | 86.87% | 85.88% | 91.66% |
| | $\mathbf{N_T = 2}$ | 89.50% | 89.81% | 91.66% |
| | $\mathbf{N_T = 3}$ | 93.44% | 92.23% | 90.99% |
| | $\mathbf{N_T = 4}$ | 93.44% | 92.23% | 90.99% |
| | $\mathbf{N_T = 5}$ | 94.09% | 93.54% | 90.99% |

Under three test cycles, the highest DPR accuracy is attained when $s = 16$ and $N_T = 5$. If the size of MC continues to grow, more observations are required to ensure the completeness of the online-estimated TPMs. In other words, the limited amount of driving data within the fixed sampling horizon ($\mathrm{L_s} = 150\mathrm{s}$) makes the enlarged TPMs fail to fully characterize the (v-a) transition behaviors of recent driving segments, thus reducing the DPR accuracy. Furthermore, a larger $N_T$ can contribute to the higher DPR accuracy in most cases. This is because, a larger $N_T$ enables more real-time identified TPMs for similarity quantification (Eq. (3.21)). In this case, the sensitivity towards the abnormal quantification results would be reduced by using the average filtering, thus leading to the overall enhanced DPR accuracy. However, when $N_T$ exceeds 5 seconds, such accuracy increment effect can be neglected.

- **Performance comparison with existing DPR approaches**

In pattern identification tasks, the recognition accuracy and the computation burden are two concerning issues for real applications. In this subsection, the proposed Markov-based DPR approach is compared to existing DPR approaches on these two issues, with the comparison results listed in TABLE 3.11, where SVM refers to support vector machine, MLPNN means multilayer perceptron neural network and LVQNN stands for learning vector quantization neural network. Regarding the proposed method, the average DPR accuracy on three test cycles ($s = 16$ and $N_T = 5$) is adopted for comparison. The proposed method adopts five feature parameters for pattern identification, namely the velocity sequence,

the acceleration sequence, the number of stops, the average and maximum speed.

Overall, the pattern identification accuracy of the proposed method is comparable to those in existing studies [16]- [19]. Although the DPR method in [19] results in slightly higher accuracy compared to this work, it adopts 19 feature parameters for pattern identification, which is nearly four times amount of feature parameters used in this study. It should be noted that using exceeding large amount of feature parameters would increase the complexity of NN structure, thus contributing to the enlarged offline training time, the slow convergence rate and the increased risk of overfitting. To sum up, compared to existing DPR approaches, the proposed method can achieve the well balance between the identification accuracy and the online computation burden.

TABLE 3.11. DPR Performance Comparison Results

| DPR methods | Number of Feature Parameters | Average DPR Accuracy |
|---|---|---|
| Proposed | 5 | 96.22% |
| SVM-based [16] | 4 | 95.20% |
| MLPNN-based [17] | 6 | 95.82% |
| Clustering +SVM [18] | 6 | 95.00% |
| LVQNN-based [19] | 19 | 98.00% |

In conclusion, the major advances of the proposed method against existing DPR methods are summarized as follows:

- As far as known, the velocity-acceleration (v-a) transition behaviors, for the first time, are used as the driving feature parameters for DPR problems in contrast to the stationary feature parameters (e.g. average speed, maximum acceleration, etc.) used by traditional DPR approaches. This measure permits a more accurate description of each type of driving pattern;
- Transition probability matrices (TPM) of Markov Chain are used to characterize the (v-a) transition behavior of each driving pattern. The pattern recognition results are obtained by quantifying the similarity between the online estimated TPM and the offline benchmark TPM;
- The proposed complementary rules can effectively compensate for DPR accuracy losses during the pattern-shifting phases, thus improving the reliability of pattern identification versus traditional DPR approaches.

Simulation results demonstrate the proposed method can identify the real-time driving pattern with an average of 96.22% precision, where the periodically updated DPR results can greatly facilitate the realization of multi-mode EMS framework under changeable driving scenarios.

## 3.5. Conclusion

**Chapter 3** presents the development of the advanced driving prediction techniques applied to EMSs for FCHEVs, which contains the following major contributions:

- To fulfil the MPC optimization framework, three novel velocity-forecast approaches are proposed, namely a layer recurrent neural network (LRNN)-based, an online-learning enhanced MC-based

(OL-MC) and a fuzzy C-means clustering enhanced MC-based (FCM-MC) methods. In contrast to benchmark predictors, the LRNN-based predictor is more capable of capturing the dynamics in a time-series by using the recurrent network structure; the OL-MC predictor can adjust its predictive behaviors under different driving conditions through the real-time updated TPM group; the FCM-MC predictor can identify the input driving states and aggregate the speed-forecast results from all predictive sub-models with the real-time quantified fuzzy membership degrees. Validation results show that the proposed methods outperform the benchmark approaches in terms of prediction precision and robustness. Please note the proposed OL-MC and FCM-MC approaches are adaptive speed-forecast methods. Nevertheless, the benchmark predictors used in this chapter (multi-step Markov chain (MSMC) and back propagation neural network (BPNN)) are non-adaptive ones. To further enhance the fairness of comparison, adaptive NN-based benchmark predictors, which are equipped with online-learning ability or driving-style conscious, would be introduced in future works, so as to better justify the advantage of the proposed methods.

- With the help of the estimated trip duration information and the real-time updated speed forecast results, an integrable adaptive battery SoC reference planning method is proposed, aiming at guiding the depletion of battery energy under different driving patterns. The performance would be compared against two benchmark strategies in the next chapter.
- As the basis of the multi-mode EMS framework, a DPR approach based on Markov Chain and moving window technique is proposed, which uses the TPM of Markov Chain to characterize the velocity-acceleration transition behavior of each driving fragment. Afterwards, based on the similarity quantification results between online-estimated TPM and offline-benchmark TPM, the real-time driving pattern recognition results can be derived. Moreover, three sets of complementary rules are also devised to enhance the identification credibility over pattern shifting phases. Validation results indicate that, under multi-pattern driving cycles, an average of 96.22% DPR accuracy can be achieved by the proposed method.

With the help of the advanced driving prediction techniques developed in **Chapter 3**, **Chapter 4** will focus on integrating the predicted results into the EMS control framework, so as to investigate the potential EMS performance improvement brought by predictive knowledge integration.

## References


[1]. D. P. Filev, I. Kolmanovsky, "Generalized Markov Models for Real-Time Modeling of Continuous Systems," in ***IEEE Transactions on Fuzzy Systems***, vol. 22, no. 4, pp. 983-998, Aug. 2014. doi: 10.1109/TFUZZ.2013.2279535.

[2]. ADVISOR Advanced Vehicle Simulator. http://adv-vehicle-sim.sourceforge.net/.

[3]. C. Sun, X. Hu, S. J. Moura, F. Sun, "Velocity Predictors for Predictive Energy Management in Hybrid Electric Vehicles," in ***IEEE Transactions on Control Systems Technology***, vol. 23, no. 3, pp. 1197-1204, May 2015. DOI: 10.1109/TCST.2014.2359176.

[4]. Y. Zhou, A. Ravey, M.C. Péra, A survey on driving prediction techniques for predictive energy management of plug-in hybrid electric vehicles, ***Journal of Power Sources***, Volume 412, 2019, Pages 480-495,

https://doi.org/10.1016/j.jpowsour.2018.11.085.
[5]. Z. Chen, N. Guo, J. Shen, R. Xiao, P. Dong, "A Hierarchical Energy Management Strategy for Power-Split Plug-in Hybrid Electric Vehicles Considering Velocity Prediction," in ***IEEE Access***, vol. 6, pp. 33261-33274, 2018. DOI: 10.1109/ACCESS.2018.2848464.
[6]. D. Zhou, F. Gao, A. Ravey, A. Al-Durra, M. G. Simões, "Online energy management strategy of fuel cell hybrid electric vehicles based on time series prediction," ***2017 IEEE Transportation Electrification Conference and Expo (ITEC)***, Chicago, IL, 2017, pp. 113-118. doi: 10.1109/ITEC.2017.7993256.
[7]. A. Graves, M. Liwicki, S. Fernández, R. Bertolami, H. Bunke, J. Schmidhuber, "A Novel Connectionist System for Unconstrained Handwriting Recognition," in ***IEEE Transactions on Pattern Analysis and Machine Intelligence***, vol. 31, no. 5, pp. 855-868, May 2009. doi: 10.1109/TPAMI.2008.137.
[8]. Liu, K., Asher, Z., Gong, X., Huang, M., Kolmanovsky, I. "Vehicle Velocity Prediction and Energy Management Strategy Part 1: Deterministic and Stochastic Vehicle Velocity Prediction Using Machine Learning," ***SAE Technical Paper*** 2019-01-1051, 2019, https://doi.org/10.4271/2019-01-1051.
[9]. S. Xie, X. Hu, Z. Xin, L. Li, "Time-Efficient Stochastic Model Predictive Energy Management for a Plug-In Hybrid Electric Bus With an Adaptive Reference State-of-Charge Advisory," in ***IEEE Transactions on Vehicular Technology***, vol. 67, no. 7, pp. 5671-5682, July 2018. doi: 10.1109/TVT.2018.2798662.
[10]. C. Higel, F. Harel, D. Candusso, S. Faivre, A. Ravey, D. Guilbert, A. N' diaye, D. Bouquain, A. Djerdir, A. Gaillard. Part 1: Mobypost vehicle's powertrain modeling, simulation and sizing. ***Conference on Fundamentals and Development of Fuel Cells (FDFC 2013)***, Apr. 2013, Germany.
[11]. Y. Zhou, H. Li, A. Ravey, M.C. Péra, An integrated predictive energy management for light-duty range-extended plug-in fuel cell electric vehicle, ***Journal of Power Sources***, Volume 451, 2020, 227780, https://doi.org/10.1016/j.jpowsour.2020.227780.
[12]. J. C. Bezedek. Pattern recognition with fuzzy objective function algorithms. ***Springer Science & Business Media***. 2013.
[13]. G. Li, J. Zhang, H. He, Battery SOC constraint comparison for predictive energy management of plug-in hybrid electric bus, ***Applied Energy***, Volume 194, 2017, Pages 578-587, https://doi.org/10.1016/j.apenergy.2016.09.071.
[14]. S. Xie, H. He, J. Peng, An energy management strategy based on stochastic model predictive control for plug-in hybrid electric buses, ***Applied Energy***, Volume 196, 2017, Pages 279-288, https://doi.org/10.1016/j.apenergy.2016.12.112.
[15]. A. Ravey, B. Blunier, A. Miraoui, "Control Strategies for Fuel-Cell-Based Hybrid Electric Vehicles: From Offline to Online and Experimental Results," in ***IEEE Transactions on Vehicular Technology***, vol. 61, no. 6, pp. 2452-2457, July 2012. doi: 10.1109/TVT.2012.2198680.
[16]. X. Huang, Y. Tan, X. He, "An Intelligent Multifeature Statistical Approach for the Discrimination of Driving Conditions of a Hybrid Electric Vehicle," in ***IEEE Transactions on Intelligent Transportation Systems***, vol. 12, no. 2, pp. 453-465, June 2011. doi: 10.1109/TITS.2010.2093129.
[17]. R. Zhang, J. Tao, H. Zhou, "Fuzzy Optimal Energy Management for Fuel Cell and Supercapacitor Systems Using Neural Network Based Driving Pattern Recognition," in ***IEEE Transactions on Fuzzy Systems***, vol. 27, no. 1, pp. 45-57, Jan. 2019. doi: 10.1109/TFUZZ.2018.2856086.
[18]. Z. Chen, L. Li, B. Yan, C. Yang, C. Marina Martínez, D. Cao, "Multimode Energy Management for Plug-In Hybrid Electric Buses Based on Driving Cycles Prediction," in ***IEEE Transactions on Intelligent Transportation Systems***, vol. 17, no. 10, pp. 2811-2821, Oct. 2016. doi: 10.1109/TITS.2016.2527244.
[19]. Q. Zhang, W. Deng, G. Li, "Stochastic Control of Predictive Power Management for Battery/Supercapacitor Hybrid Energy Storage Systems of Electric Vehicles," in ***IEEE Transactions on Industrial Informatics***, vol. 14, no. 7, pp. 3023-3030, July 2018. doi: 10.1109/TII.2017.2766095.

# Chapter 4. Integrated predictive energy management strategies for fuel cell hybrid electric vehicles

## 4.1. Introduction

**Chapter 3** focuses on the design and implementation of driving prediction techniques, with the purpose of forecasting the vehicle's speed profile, planning the battery energy depletion and identifying the real-time driving patterns, so as to facilitate the development of predictive energy management strategies (PEMS) for fuel cell/battery-based hybrid electric vehicles. Nevertheless, based on the review of the state-of-the-art researches, it can be found that the following issues need to be further investigated to improve the performance of existing PEMSs: i) how to properly integrate the predictive information into the PEMS? ii) how to compensate for the performance losses brought by mis-predictions? iii) And how to enhance the overall calculation efficiency of the proposed PEMS? To address these issues, **Chapter 4** provides several solutions of embedding the predictive knowledge into the real-time optimization framework of model predictive control (MPC), leading to the birth of several integrated PEMSs for fuel cell/battery-based HEVs. The rest of this chapter is organized as follows:

Subsection 4.2 presents the vehicle's powertrain topology and the modelling of powertrain components, including fuel cell systems (FCS), battery, power converters and electric machine (EM). On this basis, several integrated PEMSs are going to be presented in the following subsections.

Subsection 4.3 combines the layer recurrent neural network (LRNN) speed predictor and the Markov driving pattern recognizer with the MPC framework, leading to the birth of a multi-mode PEMS, which can execute suitable power-allocating decisions in face of changeable driving patterns.

Subsection 4.4 takes advantage of the online-learning enhanced Markov (OL-MC) speed predictor and the adaptive battery SoC reference generator to form a multi-criteria PEMS for a midsize fuel cell electric vehicle under multiple driving patterns.

Subsection 4.5 develops an integrated PEMS for a light-duty range-extended fuel cell electric vehicle dedicated to postal delivery, with the help of the fuzzy C-means enhanced Markov speed predictor (FCM-MC) and the adaptive SoC reference planning approach.

In subsection 4.6, a numerical analysis of the impacts on EMS performance induced by different component-sizing configurations is presented, so as to explore the potential fuel economy and durability improvement of changing vehicle's configurations.

The major findings of this chapter are briefed in the subsection 4.7.

## 4.2. Powertrain architecture and system modelling

This subsection presents the modelling of the vehicle structure, the hybrid propulsion system and the powertrain components, so as to establish the basis for energy management strategy development. Please note that the research focus and the effective novelty of this thesis are not introduced by subsection 4.2. The adoption of these models is a tradeoff decision between precision and computing burden, so as to facilitate the validation of energy management strategies in both offline-simulation and Software-in-the-Loop (SIL) testing.

### 4.2.1. Vehicle model and powertrain architecture

A proper design of vehicular structure and powertrain topology is of great significance in terms of vehicle's operation safety and dynamic performance. This thesis focuses on two specific types of vehicle models, including a midsize sedan and a light-duty vehicle. As depicted in figure 4.1(a), the midsize sedan model is picked from the database of the advanced vehicular simulator ADVISOR [1]. Similarly, figure 4.1(b) depicts the outline of the light-duty vehicle, which is the prototype that has been developed in the "Mobypost" project [2]. This vehicle has a very light weight (579 kg), and it is designed for postal delivery in urban driving scenarios, with the maximal speed less than 60 km/h. The key specifications of the two studied vehicle models are listed in TABLE 4.1.

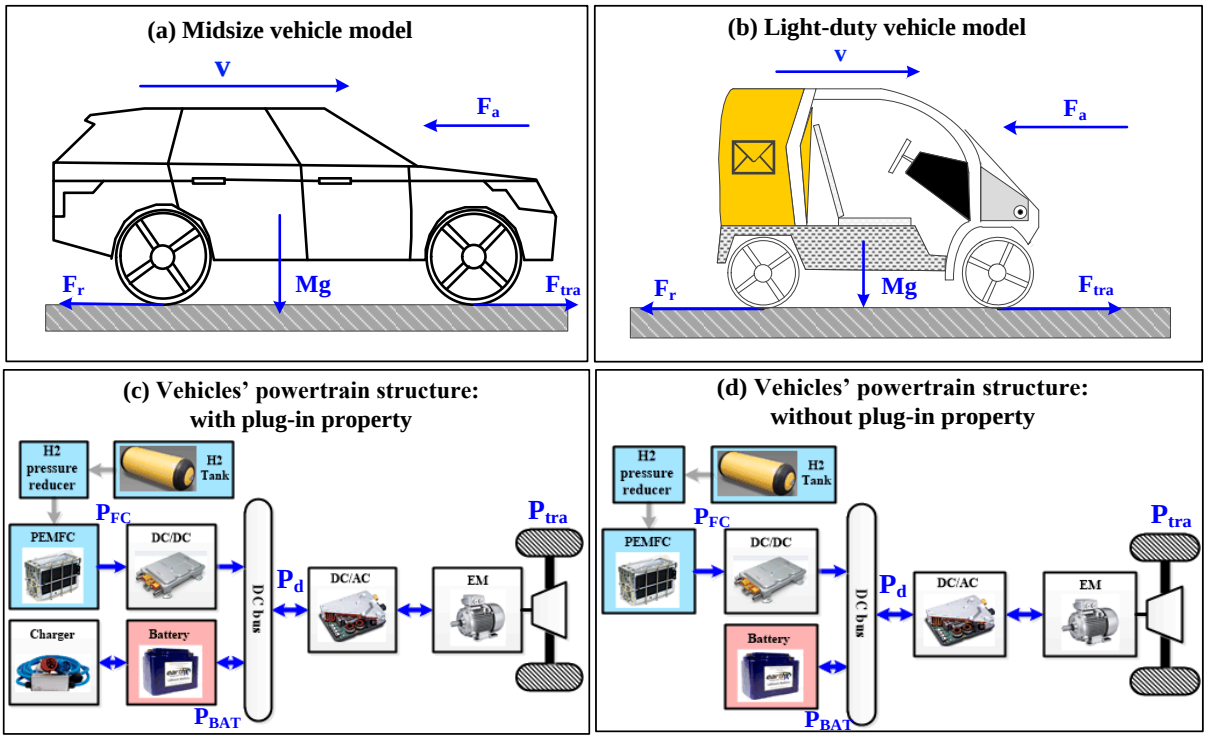


Figure 4.1. Vehicle's outline and dynamics in motion of (a) midsize sedan model and (b) light-duty vehicle model. (c) Powertrain topology with plug-in property. (d) Powertrain topology without plug-in property.

Figure 4.1(c) and (d) scheme the topology of the studied hybrid propulsion system, where the fuel cell

system (FCS), connected to the DC bus via a unidirectional DC/DC converter, and the battery, directly linked to the DC bus, work cooperatively to response the power request from the electric machine (EM). For Mobypost prototype, two in-wheel motors on the rear are actually used in the powertrain. To simplify the powertrain modeling, a single EM model, which can provide enough vehicular power and torque requests, is picked from ADVISOR database to replace the original dual-motor driving system. In addition, the driveline model is assumed to have a constant efficiency and a fixed final drive ratio.

Moreover, the propulsion power ($P_{tra}$) needed by vehicle in motion can be calculated as a function of its weight (M) and speed (v), as denoted by Eq. (4.1) [3]. Accordingly, the output power of FCS ($P_{FC}$) and battery ($P_{BAT}$) together satisfy the DC bus power demand ($P_d$), as denoted by Eq. (4.2).

$$P_{tra} = v \cdot F_{tra} = v \cdot \left[ \underbrace{c_r M g \cos(\theta)}_{F_r} + \underbrace{0.5 \rho_{air} S_f c_d v^2}_{F_a} + M\dot{v} \right] \tag{4.1}$$

$$P_d = \frac{P_{tra}}{\eta_{drive} \cdot \eta_{DC/AC} \cdot \eta_{EM}} = P_{BAT} + P_{FC} \cdot \eta_{DC/DC} \tag{4.2}$$

where $c_r$ is the rolling resistance coefficient, $\rho_{air}$ the air density (1.21 kg/m$^3$), $S_f$ the front surface area, $c_d$ the aerodynamic drag coefficient, g the gravitational acceleration, $\eta_{drive}$ the driveline efficiency, $\eta_{DC/DC}, \eta_{DC/AC}$ the power converters' efficiency and $\eta_{EM}$ the EM efficiency. Due to the lack of related road slope information of the testing cycles, a horizontal vehicle model is considered in this thesis, and thus the road slope $\theta$ takes zero. This hypothesis represents a limitation of the current work, since vehicular power demand would be affected by the inclination of road. Nevertheless, this issue can be addressed once the related road slope information is available or can be estimated.

TABLE 4.1. Powertrain specifications of the vehicle models used in this thesis

| Category | Item | Config. I: Midsize sedan without plug-in property | Config. II: Midsize sedan with plug-in property | Config. III: Light-duty vehicle |
|---|---|---|---|---|
| **Vehicle Structural Parameters** | Vehicle mass | 1360 kg | | 579 kg |
| | Vehicle front surface | 1.746 m$^2$ | | 2.48 m$^2$ |
| | Tire radius | 0.32 m | | 0.29 m |
| | Aerodynamic coefficient | 0.3 | | 0.7 |
| | Rolling coefficient | 0.0135 | | 0.015 |
| | Driveline efficiency | 0.91 | | 0.92 |
| | Gravitational acceleration | 9.81 m/s$^2$ | | |
| **PEMFC System** | Rated power | 30 kW | | 1200 W |
| | Maximum efficiency | 50.3 % | | 43.2% |
| **Battery Pack** | Type | Lithium-ion | | Lead-acid |
| | Nominal energy capacity | 6.4 kWh | 12.8 kWh | 5.5 kWh |
| **Electrical Machine** | Maximum power | 150 kW | 75 kW | 30 kW |
| | Maximum torque | 220 N·m | 271 N·m | 125 N·m |
| | Maximum rotation speed | 11000 rpm | 10000 rpm | 9000 rpm |
| **Others** | DC/DC converter Efficiency | 0.90 | | |
| | DC/AC converter Efficiency | 0.95 | | |

After the vehicle model and the powertrain topology have been specified, the sizes of powertrain

components should be carefully determined. As seen from TABLE 4.1, this thesis employs three different sizing configurations (**Config. I** to **III**) for EMS development. Since the major research focus is to devise control strategies for the given fuel cell hybrid electric vehicles (FCHEVs) instead of optimally sizing the components, we adopt the following criteria for the sizing determination:

**Configuration I** (30 kW FCS + 6.4 kWh Battery): this configuration is designed for a FC-battery-based hybrid sedan without plug-in property, which means the battery can only be charged via DC bus by FCS or the regenerative energy. The sizes of FCS and battery are determined using the sizing methodology proposed in [4], wherein the FCS is dedicated to providing the average power demand of driving cycles, while the battery is used to compensate for the remaining energy of driving cycles. The standard driving cycles (e.g. WLTP_Class3, INRETS, LA92 etc.) for component sizing are extracted from ADVISOR database, and these cycles represent the combined driving scenarios.

**Configuration II** (30 kW FCS + 12.8 kWh Battery): this configuration is designed for a FC-battery-based hybrid sedan with plug-in property, where the battery can be recharged either by DC bus or by external grid power via the onboard charger. The sizes of FCS and battery are adopted from the existing study in the literature [5].

**Configuration III** (1.2 kW FCS +5.5 kWh Battery): this configuration is designed for a light-duty mail-delivery vehicle with plug-in property. The sizes of FCS and battery are extracted from the parameters of the actual Mobypost prototype given in the related works [2], [6].

In configurations I to III, the nominal power of electric machine (EM) is determined with respect to the power demand required by their own mission profiles. On this basis, proper EM models are picked from ADVISOR [1], which are built by the experimentally validated data. In this case, the operating ranges for motor torque and rotation speed are thus pre-determined, once the specific EM model is selected.

### 4.2.2. Quasistatic fuel cell model

Proton exchange membrane fuel cells (PEMFC) convert hydrogen energy into electricity power via a series of electrochemical reactions with pure water as the only byproduct. Also, the efficiency of a fuel cell is not limited by the Carnot efficiency [3]. With these technical advantages, PEMFCs are gradually becoming the competitive substitution to traditional internal combustion engines (ICE) in automotive field. This subsection presents the modelling of the studied PEMFC systems.

- **Cell voltage**

To properly model a fuel cell system, it should be starting from understanding the behavior of a single fuel cell, which is featured by the static dependency between the cell voltage $U_{cell}$ (in V) and the current density $i_{FC}$ (in mA/cm$^2$), with $i_{FC}$ being the cell current per active area: $i_{FC} = I_{FC}/A_{FC}$ [3]. The shape of a typical polarization curve of a fuel cell under the given operating conditions (e.g. partial pressure,

humidity and temperature, etc.) is depicted in figure 4.2.

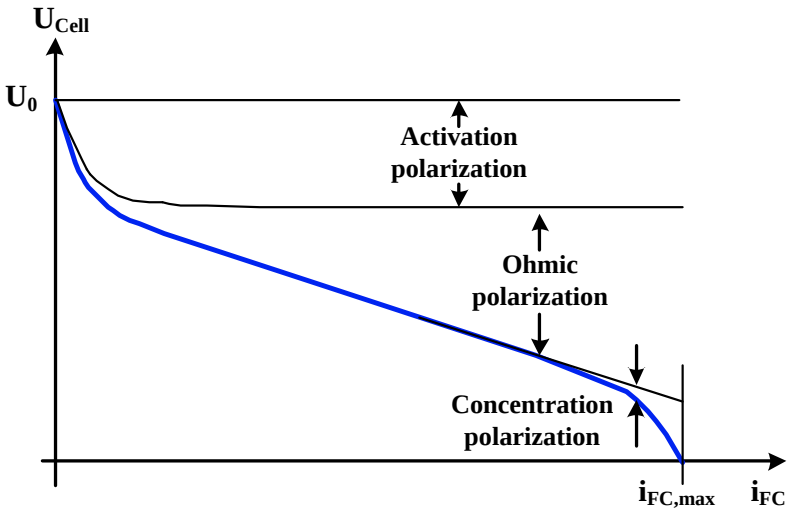


Figure 4.2. Typical polarization curve of a single fuel cell [3].

In this thesis, a simple model is adopted to describe the relationship of $U_{cell}$ and $i_{FC}$, which depends not on the activities of the species at the electrode/electrolyte interface, but rather on measurable values outside the cell. According to [3] and [7], the cell voltage $U_{cell}$ is derived by the difference between the equilibrium potential and the irreversible losses, where the losses can be attributed to three major factors: activation polarization, ohmic polarization and concentration polarization. In this work, a semi-empirical equation is adopted in order to represent the quasi-static behavior of the fuel cell, as denoted by:

$$U_{cell} = U_0 - U_{act} - U_{ohm} - U_{conc} \tag{4.3}$$

where $U_0$ is open-circuit voltage, and $U_{act}$, $U_{ohm}$, $U_{conc}$ represent different types of losses when a load drives current from fuel cell [8]. As reported in [8], the theoretical value of reversible cell voltage, obtained from the free energy of hydrogen combustion, can be 1.18 V, while, in practice, the value actually measured in open circuit would reduce to about 1.05 V mainly because of the formation of hydrogen peroxide as an intermediate stage of the cathode's oxygen reduction [9] and cross over currents.

The activation polarization is caused by the energy losses for initiating the reaction, relying on the type of catalyst [3]. This type of polarization is mainly due to the fact that the cathode reaction is inherently slower than the anode reaction, and it increases with the growth of the current density. A semi-empirical Tafel equation is used to characterize the relationship between $i_{FC}$ and $U_{act}$:

$$\begin{aligned} U_{act} &= c_0 \cdot ln(i_{FC}) \quad (a) \\ c_0 &= \frac{RT}{\alpha \cdot 2F} \quad (b) \end{aligned} \tag{4.4}$$

where R denotes the constant of ideal gas (8.3134 J/(mol·K)), T the stack temperature (in K), α the

exchange coefficient, and F the Faraday constant (96485 C/mol).

The ohmic polarization is attributed to the resistance to (i) the flow of ions in the membrane and in the catalyst layer, and (ii) the flow of electrons through the electrodes, with (i) being the dominant. Typically, it is assumed that both membrane and electrode behaviors can be described by Ohm's law, the ohmic losses can thus be expressed as:

$$U_{ohm} = \tilde{R}_{FC} \cdot i_{FC} \tag{4.5}$$

where $\widetilde{R}_{FC} = R_{FC} \cdot A_{FC}$ (in $k\Omega \cdot cm^2$) is the overall resistance, and the ohmic resistance $R_{FC}$ comprises the contributions owing to electronic, membrane (ionic), and contact resistance. Usually, only the dominant membrane resistance is considered in practical modelling [3].

The concentration polarization is because of the change in concentration of the reactants at the electrodes with their consumption during the reaction. Such losses become significant only at high current density, which can be calculated by [3]:

$$U_{conc} = c_1 \cdot \exp(c_2 \cdot i_{FC}) \tag{4.6}$$

where the coefficients $c_1, c_2$ are determined by the temperature and the partial pressure of the reactants. By substituting the related losses in Eq. (4.3) with the expressions in Eq. (4.4)-Eq. (4.6), the relationship between $U_{cell}$ and $i_{FC}$ can be detailed as:

$$U_{cell} = U_0 - c_0 \cdot ln(i_{FC}) - \tilde{R}_{FC} \cdot i_{FC} - c_1 \cdot \exp(c_2 \cdot i_{FC}) \tag{4.7}$$

It should be noted that this model is a very macroscopic approach to the phenomena internal to the cell, and thus its domain of validity around specific operating conditions is reduced. Nevertheless, Eq. (4.7) still presents a good indicator of fuel cell behavior under the constant operating conditions, e.g. pressure, temperature and humidity [8], which is sufficient for energy management development in this thesis.

TABLE 4.2. Ballard Mark V PEMFC coefficients (@ 55°C) [8]

| Coefficient | Value | Unit |
|---|---|---|
| $U_0$ | 1.033 | V |
| $c_0$ | 0.0315 | V |
| $\tilde{R}_{FC}$ | $2.93 \times 10^{-4}$ | $k\Omega \cdot cm^2$ |
| $c_1$ | $3.94 \times 10^{-5}$ | V |
| $c_2$ | $8.0 \times 10^{-3}$ | $cm^2/mA$ |

The model coefficients need to be identified from the stack polarization curve, so as to specify the relationship between $i_{FC}$ and $U_{cell}$. In this thesis, the specific values of these coefficients are listed in TABLE 4.2, which are obtained based on the experimentally validated data of the Ballard Mark V PEM fuel cell in previous publication [8]. Please note that the model coefficients change with the operating temperature of fuel cell stack. In this thesis, the adopted coefficients are derived by assuming the

operating temperature of fuel cell stack is fixed at 55 ℃ [8].

To increase the output power level, multiple fuel cells are concatenated together to form the fuel cell stack. Multiple auxiliaries (e.g. air compressor, etc.) are indispensable to ensure the normal operation of fuel cell stack. Thus, a fraction of generated current is delivered to auxiliary devices around the stack. When no external load drives current from fuel cell, the generated current is all used to satisfy the auxiliaries' power consumption, with this operating state termed as fuel cell "idling".

Due to the series arrangement, provided that all the cells in the stack is in the same electrochemical status, the stack voltage is derived by multiplying the cell voltage by the number of cells $N_{cell}$ in the stack,

$$U_{st} = N_{cell} \cdot U_{cell} \tag{4.8}$$

while the stack current equals to the cell current $I_{FC}$. Thus, the output power of a fuel-cell stack is:

$$P_{st} = U_{st} \cdot I_{st} = N_{cell} \cdot U_{cell} \cdot I_{FC} \tag{4.9}$$

The stack output power must cover the load demand $P_{FC}$ and the power requests from all auxiliaries $P_{AUX}$ (e.g. air compressor, hydrogen circulation pump, etc.), with such power balance denoted by:

$$P_{FC} = P_{st} - P_{AUX} \tag{4.10}$$

- **Fuel cell system**

A fuel cell system (FCS) is composed of the fuel cell stack and multiple auxiliary devices, where figure 4.3 gives the system-level block diagram of a fuel cell system [10]. The fuel-cell stack is the core of a PEMFC system, and each cell in the stack has the same geometric structure and material properties, with the structural diagram of PEMFC stack given in figure 4.4.

The FCS efficiency ($\eta_{FCS}$) is an essential performance indicator of energy conversion. In this thesis, we adopt the FCS efficiency definition provided in [10], wherein $\eta_{FCS}$ is defined as the ratio between the net power output form the system ($P_{net} = P_{FC}$) and the theoretical power supplied by hydrogen ($P_{H_2} = -\dot{n}_{H_2}\Delta h_f$):

$$\eta_{FCS} = \frac{P_{FC}}{P_{H_2}} = \frac{N_{cell} \cdot U_{cell} \cdot I_{FC} - P_{AUX}}{-\dot{n}_{H_2}\Delta h_f} \tag{4.11}$$

$$\dot{n}_{H_2} = F_{SA} \cdot \frac{N_{cell} \cdot I_{FC}}{2F} \tag{4.12}$$

where $\Delta h_f$ is the enthalpy of formation of a mole of water (-241.83 kJ/mol (steam), -285.84 kJ/mol (liquid)), which is also equivalent to the heat released by complete combustion of a mole of hydrogen. $\dot{n}_{H_2}$ is the molar flowrate of hydrogen consumed by the stack, and $F_{SA}$ is the ratio between the amount of hydrogen flowing into the cell and the amount of hydrogen consumed [10]. More details regarding

the modelling of power consumption from auxiliaries can be found in [3] and [12]. Also, an example of modeling the auxiliaries' power consumption of a 30-kW FCS is given in the annex.

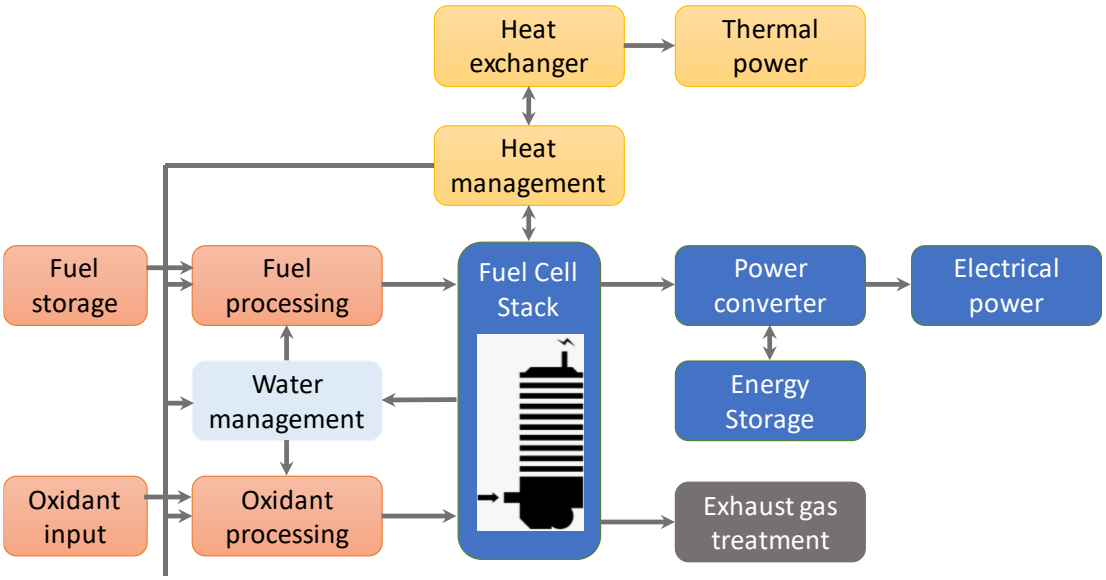


Figure 4.3. System-level block diagram of a fuel cell system [10].

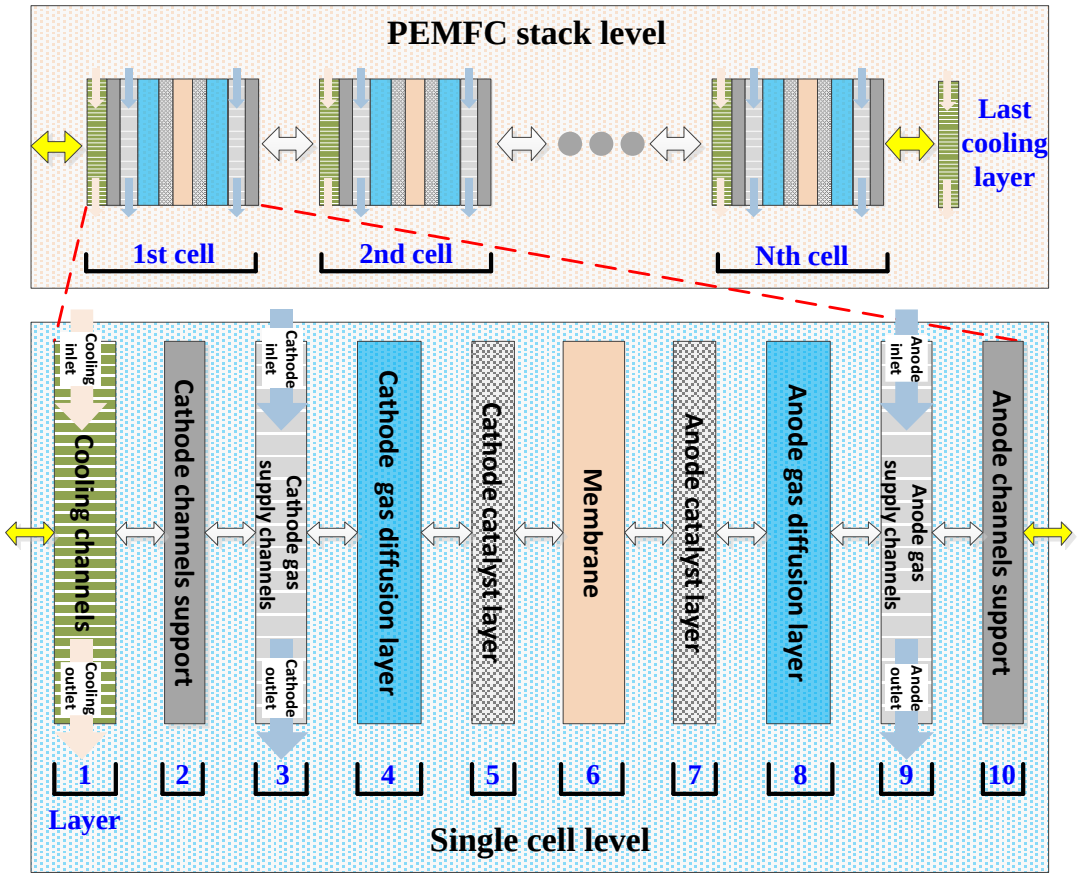


Figure 4.4. Structural representation of PEMFC stack level and single cell level [11].

As a result, the studied fuel cell efficiency curves are given in figure 4.5 and 4.6. To guarantee a high

operating efficiency of fuel cell system (FCS), the FCS net power with the highest system efficiency ($\eta_{max}$) is defined as the most efficient operating point, marked as $P_{\eta}^{max}$. In addition, the operating range $P_{FC} \in \left[P_{\eta}^{LOW}, P_{\eta}^{HIGH}\right]$, where the PEMFC system efficiency is higher than certain thresholds (e.g. $\eta_{FCS} \geq 47\%$ for 30-kW FCS and $\eta_{FCS} \geq 41\%$ for 1.2-kW FCS), is defined as the high efficiency area of the FCS.

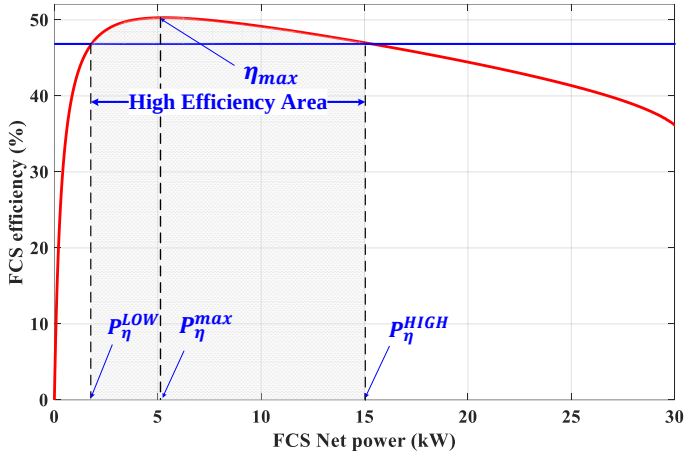


Figure 4.5. Efficiency curve of a 30kW fuel cell system [13].

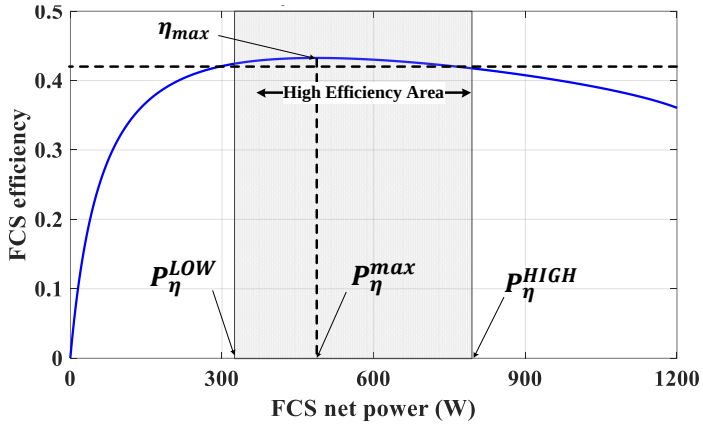


Figure 4.6. Efficiency curve of a 1.2 kW fuel cell system [14].

In addition, given the lower heating value of hydrogen ($LHV_{H_2}$, 120 MJ/kg), the hydrogen mass consumption ($M_{H_2}$) can be calculated by:

$$M_{H_2} = \int_0^t \frac{P_{FC}(\tau)}{\eta_{FCS}(P_{FC}) \cdot LHV_{H_2}} d\tau \tag{4.13}$$

### 4.2.3. Battery model

As the essential energy storage system in the studied hybrid propulsion system, batteries transform chemical energy into electrical energy and vice versa. Despite several types of traction batteries for EVs and HEVs, lithium-ion battery is the most competitive one due to its advantages in terms of specific power (W/kg), specific energy (Wh/kg) and reliability [3]. Figure 4.7 illustrates the basic structure of a

lithium-ion battery cell, which is composed of an anode, a cathode, a separator and the electrolyte. Specifically, the graphite (carbon) anode allows the lithium ions to intercalate in the interstitial spaces of the crystal. The cathode is lithium oxide and the electrolyte are made up of the lithiated liquid solution, while the function of separator (membrane) is to split the electrons from the lithium ions. Likewise, multiple battery cells are aggregated in series or parallel to form the battery pack, so as to meet the required power and energy capacity level for vehicular applications.

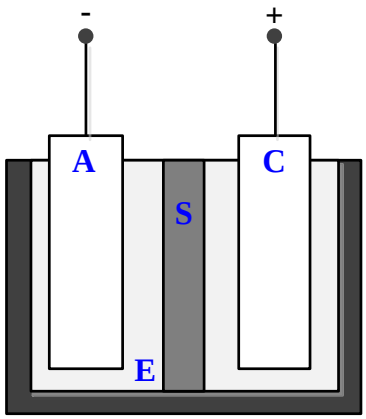


Figure 4.7. Graphic illustration of a lithium-ion battery cell. A: anode (carbon/current collector -), C: cathode (Lithium oxides/current collector +), E: electrolyte (lithiated solution), S: separator (membrane).

The battery model used in this thesis is described as follows. Firstly, the state-of-charge (SoC) is a percentage indicator of the remaining battery capacity (in Ah) in contrast to its nominal one, which can be calculated by:

$$\mathrm{SoC}(t) = \frac{Q_0 - Q(t)}{Q_{BAT}} = \mathrm{SoC}_0 - \int_0^t \frac{\eta_{BAT} \cdot I_{BAT}(\tau)}{Q_{BAT}} d\tau \tag{4.14}$$

where $Q_0$ is the initial electric charge, $Q(t)$ the consumed electric charge from 0 to $t$, $Q_{BAT}$ the nominal battery capacity, $\mathrm{SoC}_0$ the initial SoC, $I_{BAT}$ the battery current and $\eta_{BAT}$ the battery efficiency. In battery discharge phase, $\eta_{BAT}$ can be deemed as 1. In case of battery charge, a fraction of $I_{BAT}$ is not transformed into useful electric charge due to the irreversible, parasitic reactions in battery [3], making $\eta_{BAT} < 1$. Specifically, it is assumed the battery charge efficiency as a constant 0.95 [6].

In this thesis, a simple and effective internal resistance (R-int) model is used to represent the behavior of a battery, whose equivalent circuit is depicted in figure 4.8(a). The sampling period of the proposed energy management strategies is on the level of seconds (e.g. $\Delta T = 1s$). Hence, using a more complicated battery model, R-C model for instance, for precisely characterizing battery dynamic behavior does not make many senses in this thesis. According to Kirchhoff's voltage law, the DC bus voltage ($U_d$) can be calculated as:

$$U_d = U_{OC} - I_{BAT} \cdot R_{BAT} \tag{4.15}$$

where $R_{BAT}$ denotes the battery internal resistance and $U_{OC}$ the battery open-circuit voltage (OCV). Moreover, since the battery is directly connected to the DC bus, the output power from battery can be expressed as:

$$P_{BAT} = (U_{OC} - I_{BAT} \cdot R_{BAT}) \cdot I_{BAT} = U_d \cdot I_{BAT} \tag{4.16}$$

Combine Eq. (4.15) and Eq. (4.16), the expression of $I_{BAT}$ can be given as:

$$I_{BAT} = \frac{U_{OC}(SoC) - \sqrt{U_{OC}(SoC)^2 - 4 \cdot R_{BAT}(SoC) \cdot P_{BAT}}}{2 \cdot R_{BAT}(SoC)} \tag{4.17}$$

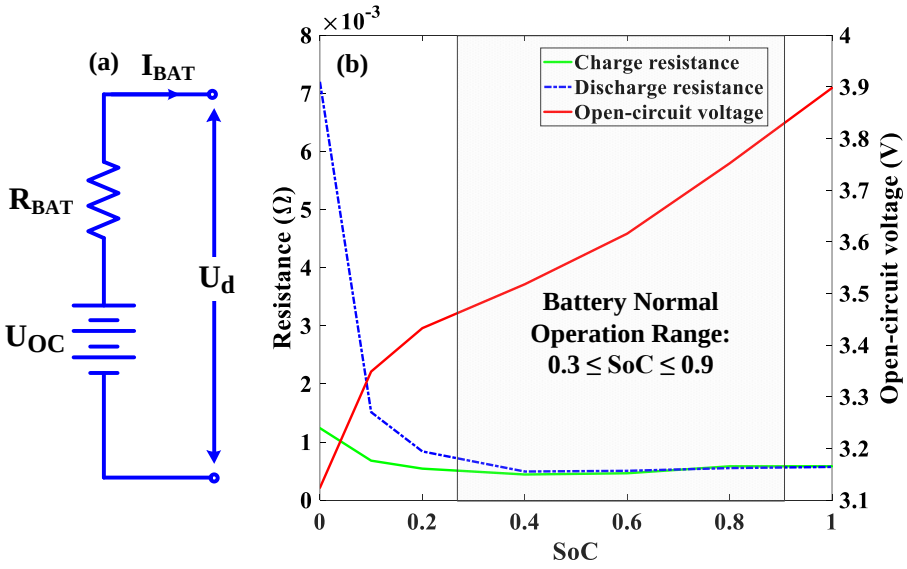


Figure 4.8. Modelling of battery: (a) equivalent circuit of the R-int model and (b) relationship of the internal resistance and OCV of a single cell with respect to its SoC.

Although multiple factors would affect the OCV and the internal resistance of a battery cell, related studies show that $U_{OC}$ and $R_{BAT}$ can be respectively casted into a function of SoC [3], which greatly facilitates the battery modelling. Figure 4.8(b) depicts how the OCV and internal resistance change with SoC. Please note the displayed battery characteristics are extracted from an experimentally validated lithium-ion battery model from ADVISOR [1]. In practical, battery over-discharge would compromise its working efficiency and increase the risk of failure of motor driving systems. Moreover, battery over-charge or over-discharge would also accelerate its performance degradation [15]. Thus, as shown in figure 4.8(b), it is recommended to restrict battery SoC within [0.3, 0.9] for ensuring its normal operation.

### 4.2.4. Electric machine model

Electric machine (EM) is the provider of vehicle's propulsion power. According to the different vehicle models and maximum power/torque demands by the mission profiles, a 150-kW, a 75-kW and a 30-kW EM models are selected from the database of ADVISOR [1], with the rotation speed and torque operating ranges listed in TABLE 4.1. Moreover, as depicted in figure 4.9, the corresponding EM

efficiency maps (extracted from ADVISOR) are used to calculate $\eta_{EM}$ when the torque and speed requests from wheel side are specified. In this case, as indicated by Eq. (4.2), the DC bus power demand ($P_d$) can thus be specified.

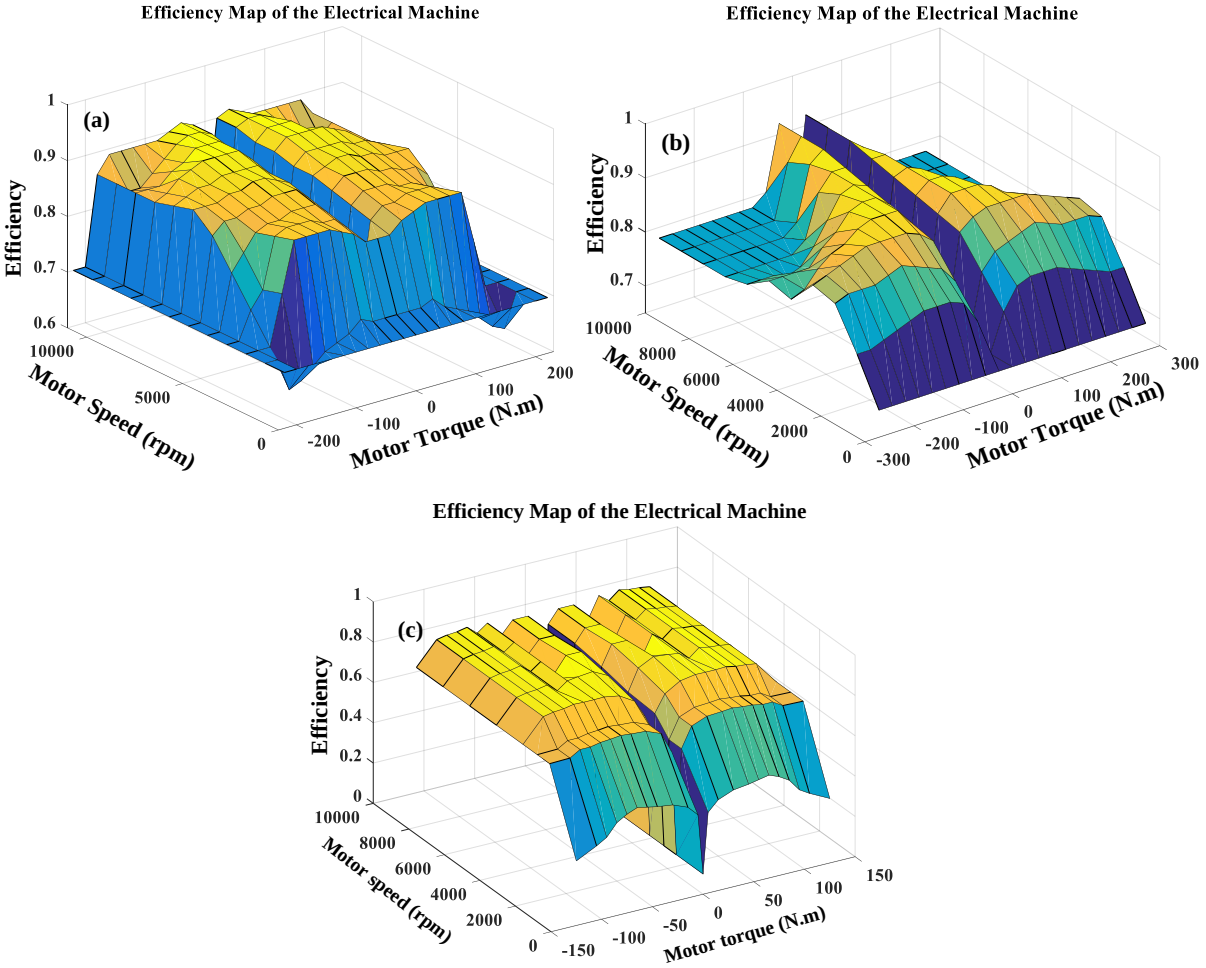


Figure 4.9. Efficiency maps of (a) 150-kW EM, (b) 75-kW EM and (c) 30-kW EM.

## 4.3. Multi-mode predictive energy management strategy

In face of changeable driving conditions in practice, energy management strategies (EMS) should be able to effectively distribute power demands under multiple driving patterns. To this end, subsection 4.3 presents a predictive EMS (PEMS) for fuel cell hybrid electric vehicles (FCHEV), which can work under multiple modes to adapt to different types of driving scenarios. Specifically, based on the Markov driving pattern recognizer (DPR) and the layer recurrent neural network (LRNN) speed predictor proposed in **Chapter 3,** model predictive control is leveraged to derive the optimal power-allocating decisions at each sampling period.

In this subsection, the major research intention is to investigate EMS performance improvement brought by the adaptability to different driving patterns, so the planning of battery energy depletion is not considered for simplification purpose. To this end, this subsection focuses on the midsize sedan **without**

**plug-in property**, with the specifications given in TABLE 4.1 (**configuration I**).

Figure 4.10 depicts the control framework of the proposed multi-mode EMS, which consists of a Markov driving pattern recognizer and a multi-mode model predictive controller (MPC). In the upper level, the Markov recognizer can periodically update the pattern identification results, where each driving pattern is related to one set of pre-optimized MPC control parameters. In the lower level, according to the selected control parameters and velocity prediction results by LRNN speed predictor, MPC can generate the desirable control sequences by solving the constrained optimization problem over each prediction horizon $H_p$. The sampling period $\Delta T$ is specified as one second in this thesis, which is identical to the data sampling rate of the standard driving cycles from ADVISOR [1]. Following parts would detail the design process of MPC.

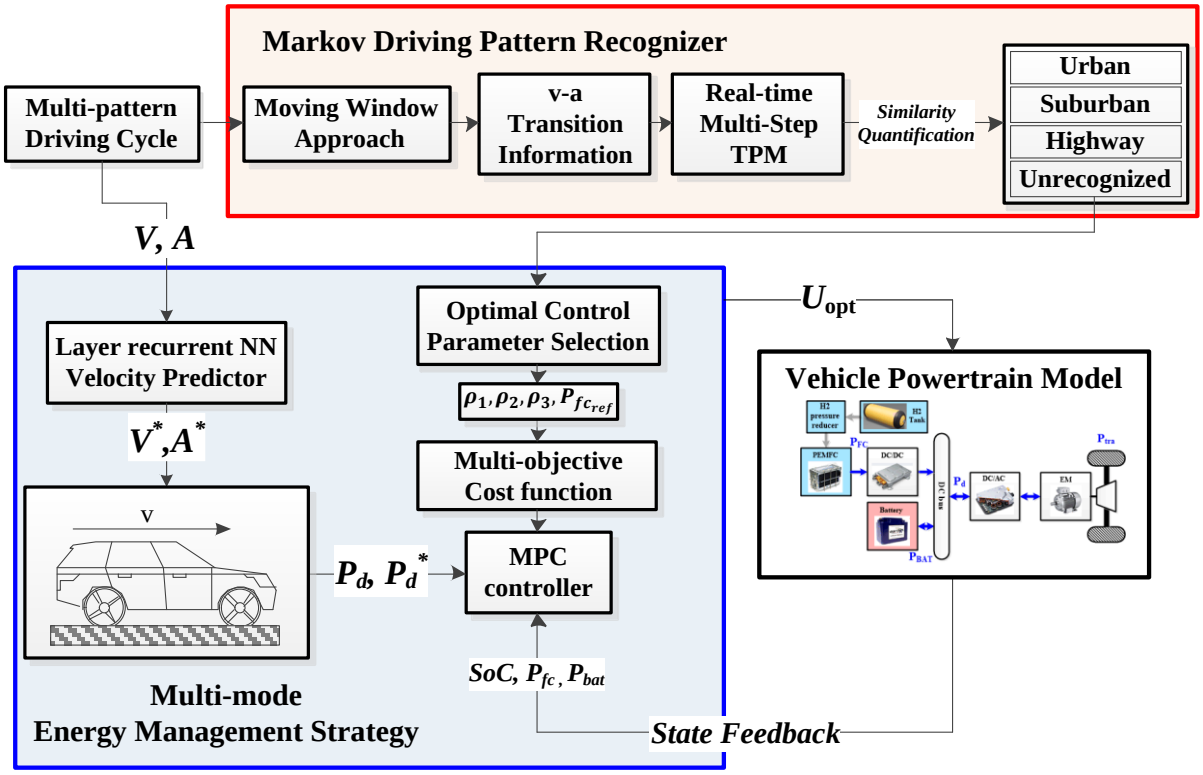


Figure 4.10. Control framework of the multi-mode energy management strategy.

### 4.3.1. Multi-mode model predictive controller

Subsection 4.3.1 presents the development of the multi-mode model predictive control framework.

#### 4.3.1.1. Control oriented model

Let $\mathbf{x}, \mathbf{u}, \mathbf{y}, \mathbf{w}$ respectively denote the state, control (input), output, and disturbance vector, a linear discrete-time control-oriented model is considered in this study, where its state-space representation and the definitions of system variables are given as follows:

$$\begin{aligned} &x(k+1) = A(k)x(k) + B_u(k)u(k) + B_w w(k) \quad (a) \\ &y(k) = Cx(k) \quad (b) \end{aligned} \tag{4.18}$$

$$\text{with} \begin{cases} x(k) &= [SoC(k)\ P_{FC}(k-1)]^T \\ u(k) &= \Delta P_{FC}(k) = \frac{P_{FC}(k)-P_{FC}(k-1)}{\Delta T} \\ y(k) &= [SoC(k)\ P_{FC}(k-1)]^T \\ w(k) &= P_d(k) \end{cases} \tag{4.19}$$

Besides, the reference vector $r(k) = \left[SoC_{ref}\ P_{fc_{ref}}(k)\right]^T$ includes the reference values for SoC and fuel cell power. Moreover, a first-order differential approximation of battery SoC dynamics [6] and the discrete form of DC bus power balance can be denoted by Eq. (4.20) and Eq. (4.21), respectively.

$$SoC(k+1) = SoC(k) - \frac{\Delta T \cdot \eta_{BAT}}{U_d(k) \cdot Q_{BAT}} \cdot P_{BAT}(k) \tag{4.20}$$

$$P_d(k) = P_{FC}(k) \cdot \eta_{DC/DC} + P_{BAT}(k) \tag{4.21}$$

Combine Eq. (4.18)-Eq. (4.21), the system matrices $A(k), B_u(k), B_w(k), C$ can be specified as:

$$\begin{aligned} &A(k) = \begin{bmatrix} 1 & \frac{\Delta T \cdot \eta_{DC/DC} \cdot \eta_{BAT}}{U_d(k) \cdot Q_{BAT}} \\ 0 & 1 \end{bmatrix} \qquad B_u(k) = \begin{bmatrix} \frac{\Delta T \cdot \eta_{DC/DC} \cdot \eta_{BAT}}{U_d(k) \cdot Q_{BAT}} & 1 \end{bmatrix}^T \\ &B_w(k) = \begin{bmatrix} -\frac{\Delta T \cdot \eta_{DC/DC} \cdot \eta_{BAT}}{U_d(k) \cdot Q_{BAT}} & 0 \end{bmatrix}^T \quad C = \begin{bmatrix} 1 & 0 \\ 0 & 1 \end{bmatrix} \end{aligned} \tag{4.22}$$

#### 4.3.1.2. Cost function and constraints

In this study, three EMS objectives are considered: 1) hydrogen consumption saving, 2) FCS lifespan prolongation and 3) battery SoC regulation. Please note the second objective is transformed into restricting the power transients of FCS, since the steadier the fuel cell power is, the friendlier the operating conditions are (e.g. limitation of the temperature variations, of the starvation risks, of the water management issues), which will mitigate the degradation of FCS and thus contribute to a longer service time. Therefore, at $t = k$, the multi-objective cost function $J(k)$ is formulated as follows:

$$J(k) = \sum_{i=1}^{H_p} [\boldsymbol{\rho}_1(k) \cdot \mathbf{C}_1(k+i) + \boldsymbol{\rho}_2(k) \cdot \mathbf{C}_2(k+i-1) + \boldsymbol{\rho}_3(k) \cdot \mathbf{C}_3(k+i)]$$

$$\text{with} \begin{cases} \mathbf{C}_1(k+i) &= \left(\frac{P_{FC}(k+i-1)-P_{ref}(k)}{P_{FC}^{max}}\right)^2 \\ \mathbf{C}_2(k+i-1) &= \left(\frac{\Delta P_{FC}(k+i-1)}{\Delta P_{FC}^{max}}\right)^2 \\ \mathbf{C}_3(k+i) &= \left(\frac{SoC(k+i)-SoC_{ref}}{SoC_{max}-SoC_{min}}\right)^2 \end{cases} \tag{4.23}$$

where $\mathbf{C}_1$ to $\mathbf{C}_3$ are the cost terms with respect to three EMS objectives, and $P_{FC}^{max} = 30\ \text{kW}, \Delta P_{FC}^{max} = 1\ \text{kW/s}, SoC_{max} = 0.8$ and $SoC_{min} = 0.6$. The major functions of three cost terms are specified as follows:

- $\mathbf{C_1}$ is used to urge fuel cell working towards the set point $P_{ref}$, where the determination of fuel cell reference working points $P_{ref}$ under different driving patterns would be illustrated thereafter;
- $\mathbf{C_2}$ is leveraged to limit the harsh power transients to mitigate the FCS performance degradation imposed by overlarge load dynamics [16];
- $\mathbf{C_3}$ is adopted to ensure the battery SoC regulation performance. Since a non-plug-in vehicle configuration is considered, the reference SoC value $SoC_{ref}$ is set the same as the initial SoC value $SoC_0$, so as to prevent battery over-charge or over-discharge, namely $SoC_{ref} = SoC_0 = 0.7$.

Besides, $\boldsymbol{\rho_1, \rho_2, \rho_3}$ are three penalty coefficients, representing the weights on the corresponding cost terms. The determination of penalty coefficients under different driving patterns will be presented afterwards. Moreover, the length of MPC control horizon is set the same as its prediction horizon, where $H_p$ is set to five steps. Within each optimization horizon, following constraints have to be enforced:

$$\begin{cases} \underline{SoC} \le SoC(k+i) \le \overline{SoC} & (a) \\ \underline{P_{FC}} \le P_{FC}(k+i-1) \le \overline{P_{FC}} & (b) \\ \underline{\Delta P_{FC}} \le \Delta P_{FC}(k+i-1) \le \overline{\Delta P_{FC}} & (c) \\ \underline{P_{BAT}} \le P_{BAT}(k+i) \le \overline{P_{BAT}} & (d) \\ w(k+i) = P_d^*(k+i), i \ge 1 & (e) \end{cases} \tag{4.24}$$

where constraint (4.24a) ensures the battery operation safety, where $\underline{SoC} = 0.55, \overline{SoC} = 0.85$. If SoC emergency event ($SoC < 0.6$ or $SoC > 0.8$) occurs, the EMS emergency working mode will be activated to enforce SoC back to the desired operation range [0.6, 0.8] as soon as possible. Besides, the operating boundaries for $P_{FC}$, $\Delta P_{FC}$ and $P_{BAT}$ are specified by constraints (4.24b)-(4.24d), where $\underline{P_{FC}} = 0\text{W}$, $\overline{P_{FC}} = 30\text{ kW}$, $\overline{\Delta P_{FC}} = -\underline{\Delta P_{FC}} = 1\text{ kW}$, $\underline{P_{BAT}} = -50\text{ kW}$ and $\overline{P_{BAT}} = 100\text{ kW}$. Moreover, constraint (4.24e) specifies the $k^{th}$ disturbance as the forecasted DC bus power demand $\left[P_d^*(k+1), \dots, P_d^*(k+H_p)\right]$, which is calculated based on the predicted speed $V_k^* = \left[v_{k+1}^*, \dots, v_{k+H_p}^*\right]$ by LRNN and the vehicles' dynamics by Eq. (4.1) and Eq. (4.2).

Since a quadratic performance index J(k) is used as the MPC cost function, the $k^{th}$ control sequence $U^*(k) = \left[u_1^*(k), \dots, u_{H_p}^*(k)\right]$ can be derived by minimizing Eq. (4.23) while respecting linear constraints Eq. (4.24). The aforementioned problem can be converted into a standard quadratic programming (QP) problem, and thus can be solved via calling the MATLAB-embedded ***quadprog*** function. Thereafter, according to MPC rolling optimization framework, only the first element of $U^*(k)$ is implemented to vehicle model, while the others are discarded.

#### 4.3.1.3. Multi-mode strategy and the design of model predictive control parameters

The performance of MPC relies highly on its control parameter settings, namely $(\boldsymbol{\rho_1, \rho_2, \rho_3})$ and $\mathbf{P_{ref}}$. To adapt to changeable driving scenarios, the proposed multi-mode EMS framework is achieved via

using different sets of MPC control parameters. Specifically, following working modes are considered:

**Normal working mode**. Three sets of MPC control parameters are tuned based on the power requirement under urban/suburban/highway scenarios. Then, with the periodically renewed DPR results, one set of offline-tuned parameters is selected for real-time control to deal with corresponding driving condition. The offline MPC control parameters tuning process will be introduced afterwards.

**SoC emergency mode**. When SoC < 0.6 or SoC > 0.8, $\boldsymbol{\rho_3}$ is set to ten times of its normal value to enforce SoC back to $[0.6,0.8]$. When SoC emergency incident occurs, the control parameter setting is switched to the "SoC emergency" mode and remains unchanged until next driving pattern recognition (DPR) result updating time instant.

**Start-up mode**. Due to the lack of historical driving information, the DPR result is set as "unrecognized" in the first sampling phase (e.g. $t \in [1,150]$). During the start-up phase, the MPC control parameters are tuned in such way that the battery is used to supply the majority of external power demands while the FC only works when the SoC value is below 0.6.

- **Working flow of MPC control parameter tuning**

To find the suitable MPC control parameter setting (namely, the fuel cell reference power, $\mathbf{P_{ref}}$, and the weighting coefficients in MPC cost function, $(\boldsymbol{\rho_1}, \boldsymbol{\rho_2}, \boldsymbol{\rho_3})$) for each driving pattern, the flowchart of parameter tuning is given in figure 4.11.

It contains four major steps: (i) dynamic programming (DP) is implemented under each type of combined driving cycle to extract the global optimal results. (ii) Corresponding $P_{ref}$ is attained based on the statistical distributions of DP-optimized FC working points. (iii) Given the FC reference power and penalty factor candidates, several performance metrics (e.g. final SoC, H2 consumption, FC power dynamics etc.) of MPC-based EMS on the same driving cycles are compared with DP-based optimal results. (iv) Based on their performance discrepancies, three penalty coefficients are tuned through trials and errors.

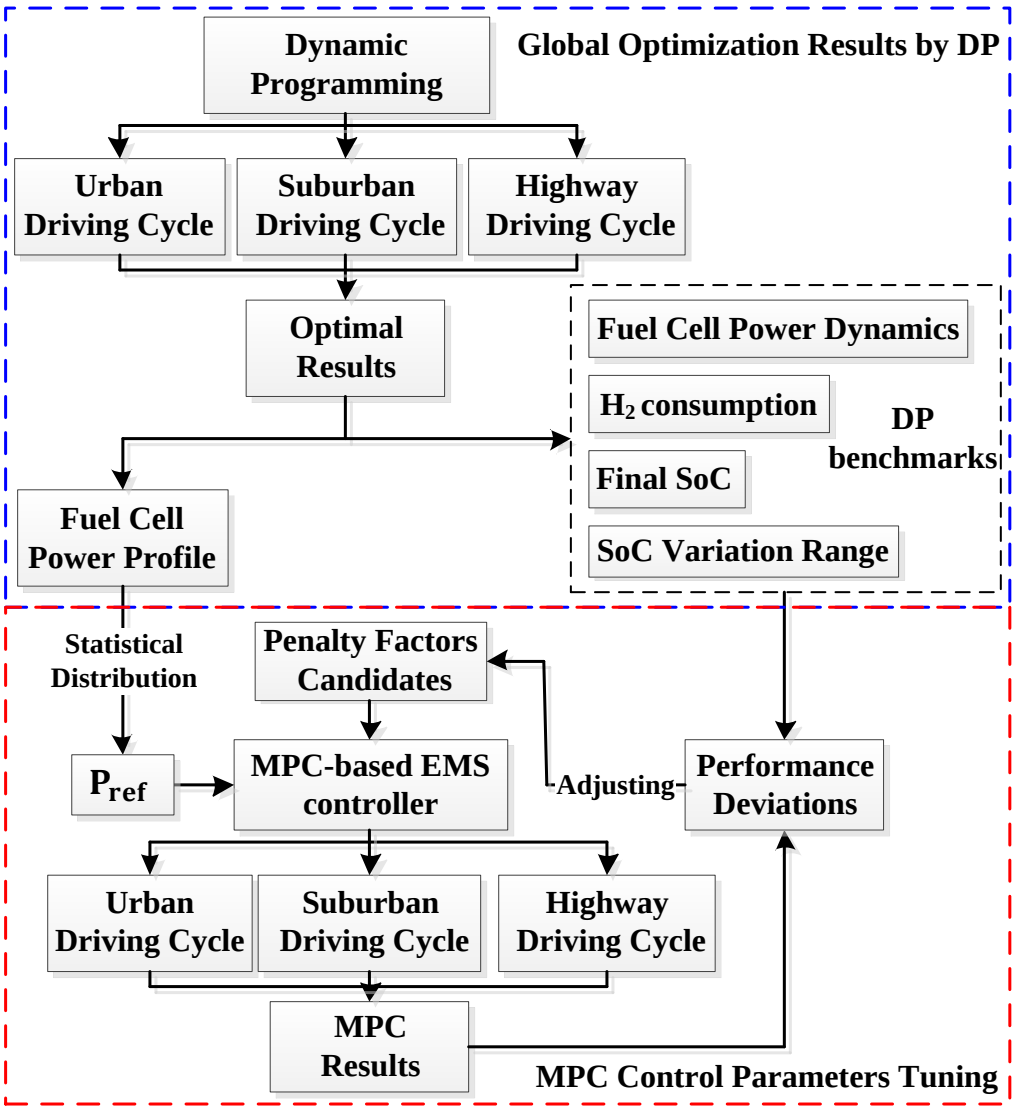


Figure 4.11. Flowchart of MPC control parameter tuning process.

- **Selection of fuel cell reference working points**

The optimization objective in urban regions is to restrict the FC power transients against the fast-dynamic power requests to extend the FCSs' lifespan. In contrast, in suburban and highway regions, the major objective is to urge FC working towards its high efficiency area to reduce the consumption of hydrogen fuel. Figure 4.12(a)-(c) depict the DP-optimized results under three driving patterns.

The corresponding FC power distributions are given in figure 4.12(d). In urban scenario, the optimal FC working points are distributed from 1.5 to 2.3 kW. In suburban regions, FC optimal working points are distributed within the range of 6.0 to 7.0 kW, while the optimal FC working range is 13.5 to 15.5 kW in highway regions. Thus, the reference FC power ($P_{ref}$) is set as their statistical average values, namely 1.78 kW (urban), 6.80 kW (suburban) and 14.40 kW (highway), respectively.

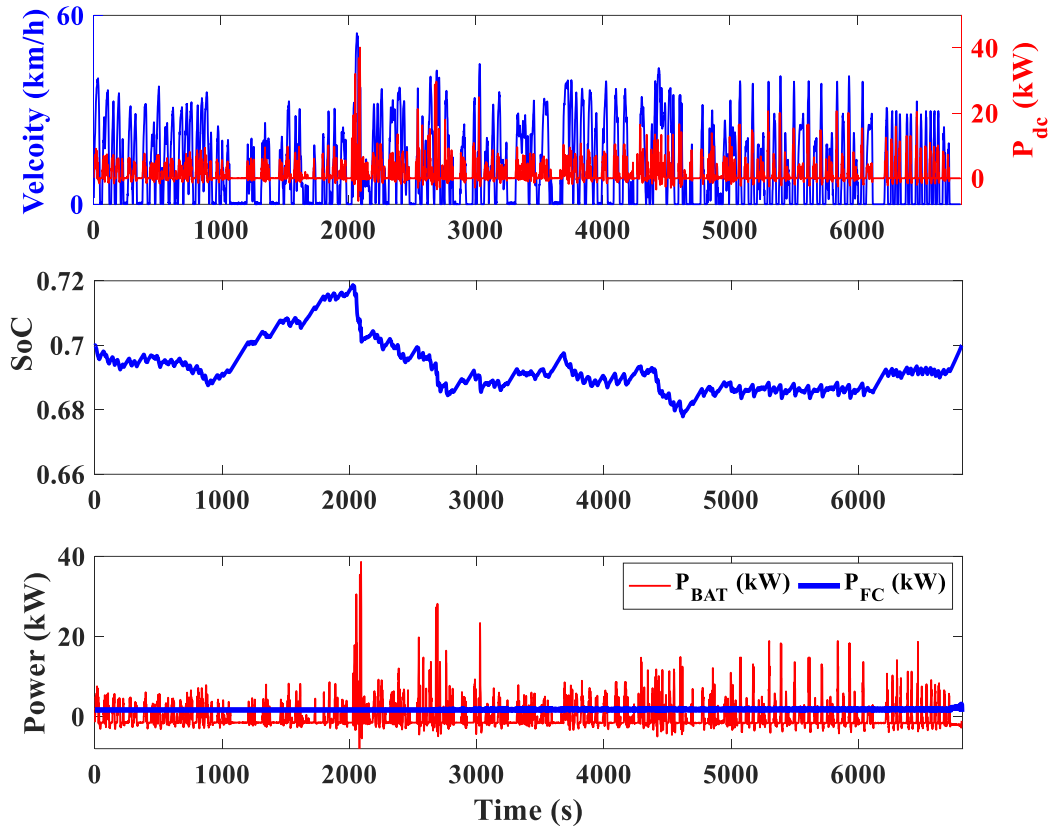


Figure 4.12(a). DP-based optimization results under urban driving pattern.

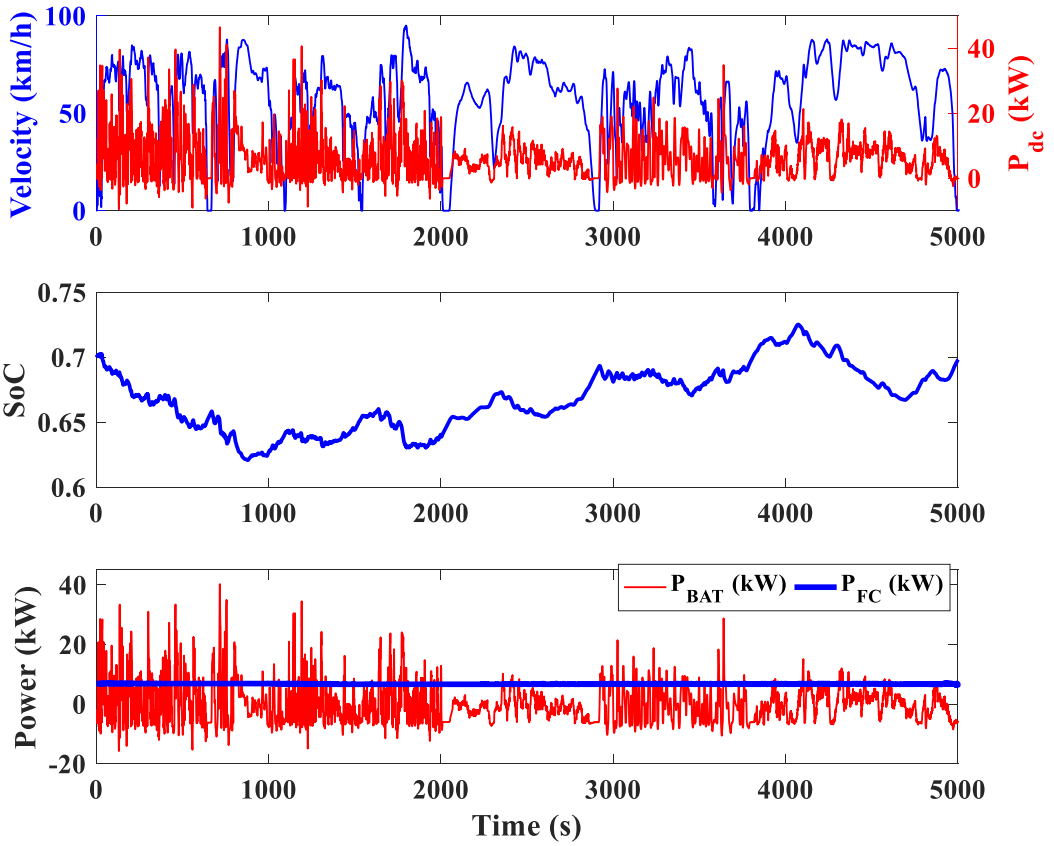


Figure 4.12(b). DP-based optimization results under suburban driving pattern.

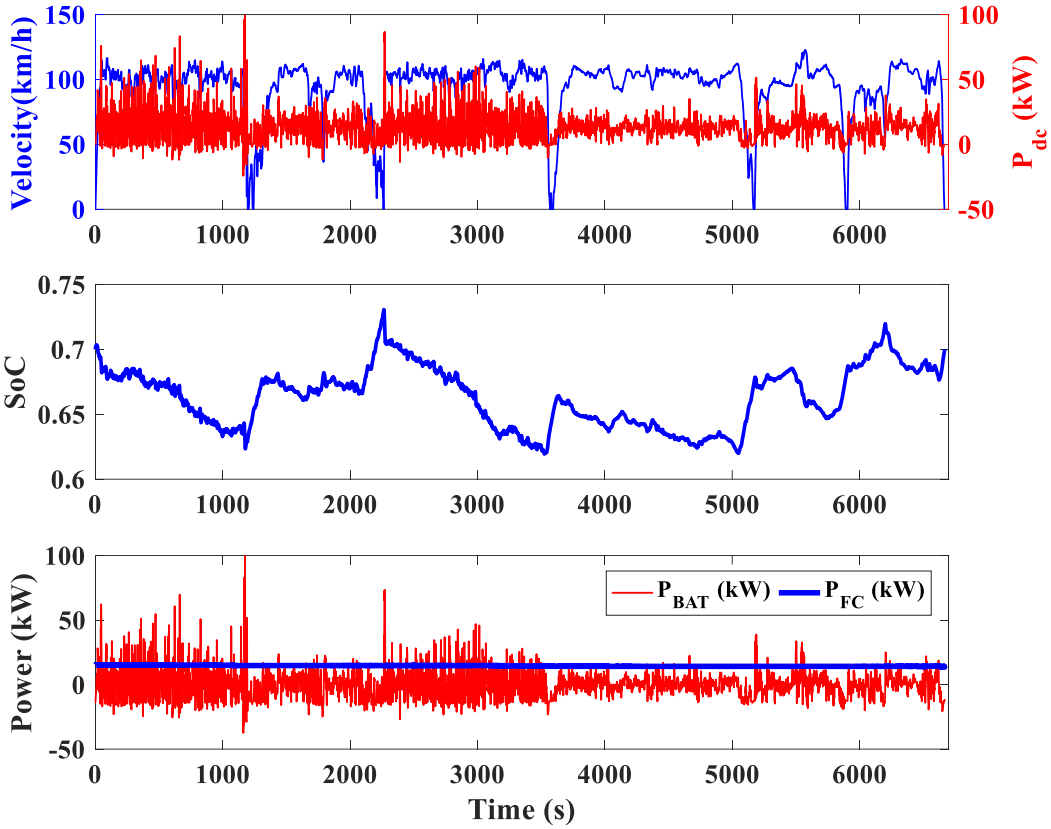


Figure 4.12(c). DP-based optimization results under highway driving pattern.

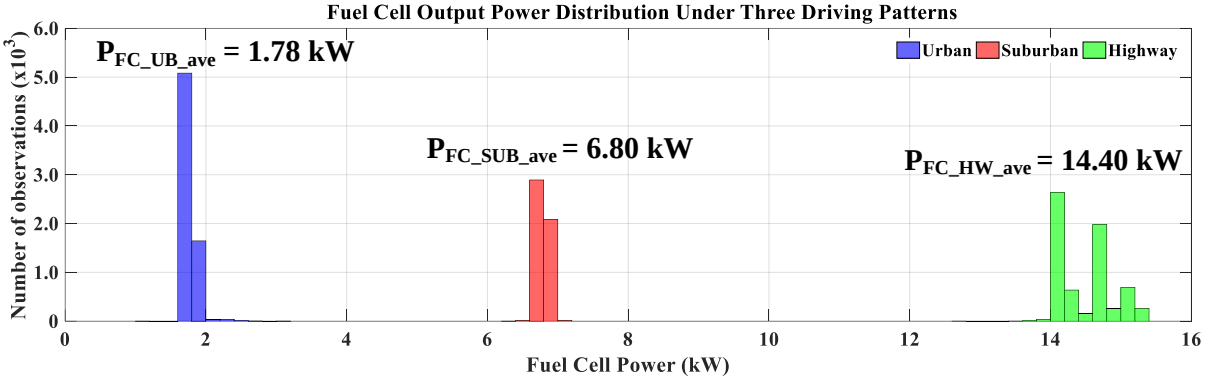


Figure 4.12(d). Distribution of fuel cell working points under three driving patterns.

- **Penalty coefficients tuning results**

Based on the selected $P_{ref}$, the MPC penalty factors tuning results are given in figure 4.13. Please note the non-tuned MPC uses the initial penalty coefficient setting (e.g. $\boldsymbol{\rho}_1 = \boldsymbol{\rho}_2 = 1,\ \boldsymbol{\rho}_3 = 1000$), which intends to keep battery working under charge sustaining mode. As seen from figure 4.13(a), after using the tuned penalty factors (red curve), the FC power transients under urban regions is greatly reduced compared to non-tuned MPC (green curve). Likewise, as shown in figure 4.13 (b) and (c), after penalty factor tuning, the variation of FC output power is restricted within a relatively narrow range and most of FC operating points are located in the high efficiency region.

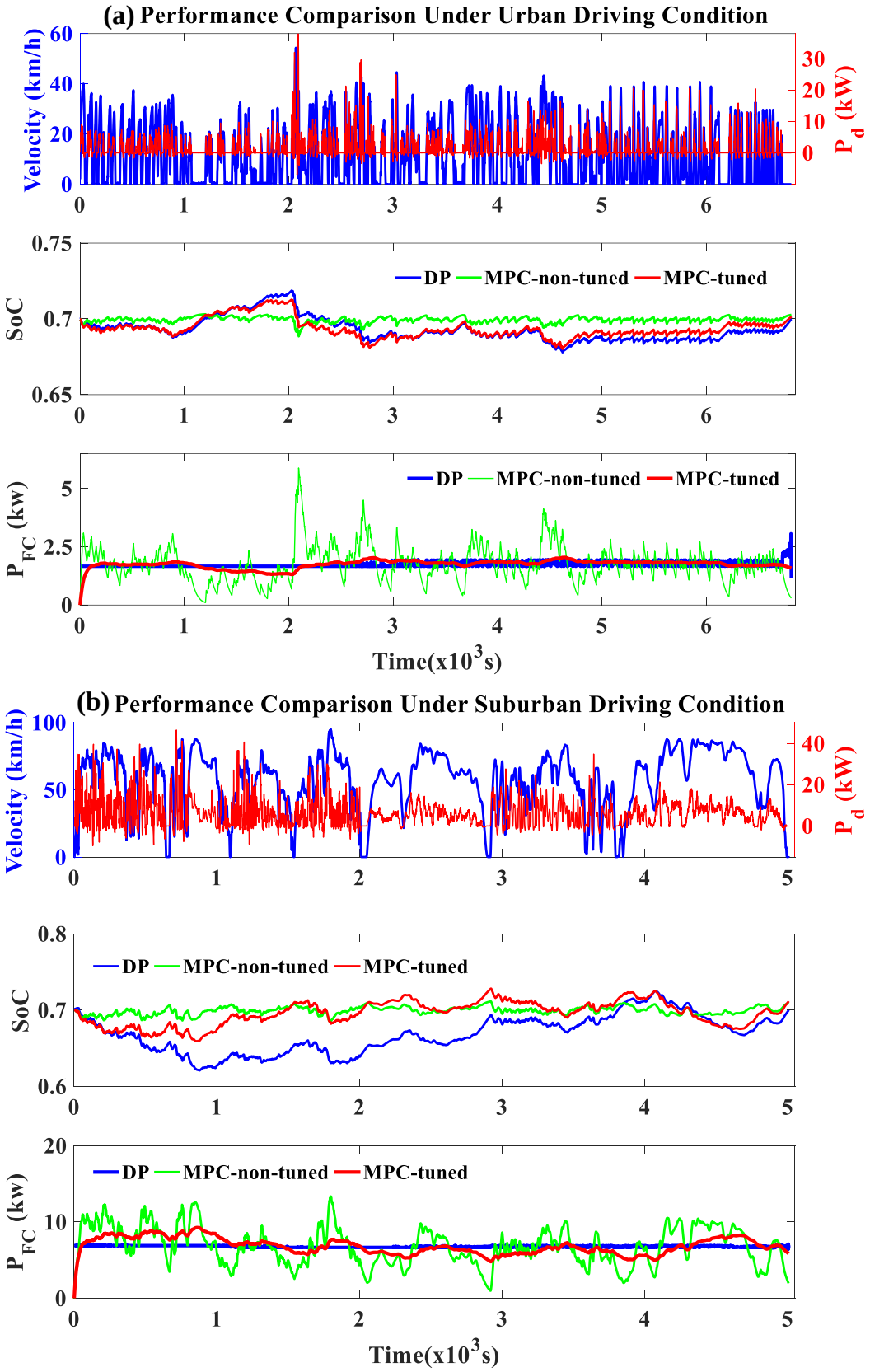


Figure 4.13. EMS performance comparison before/after MPC penalty factor tuning: (a) performance comparison under urban driving condition; (b) performance comparison under suburban driving condition.

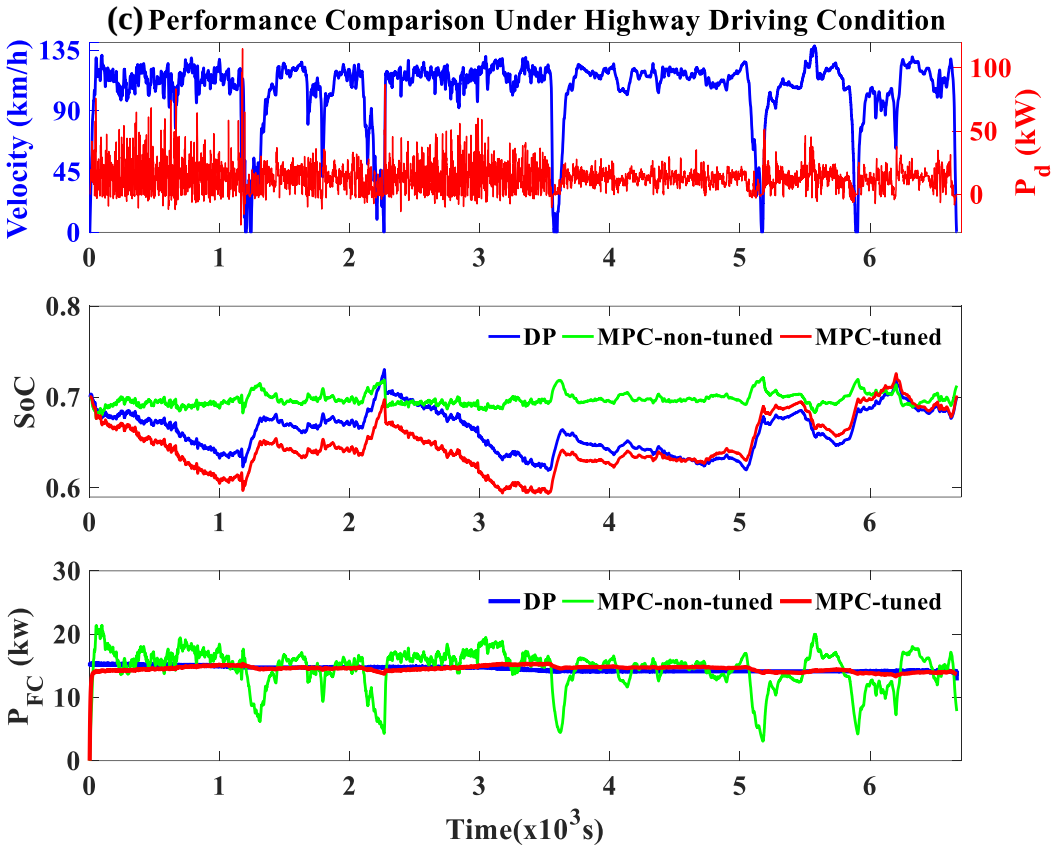


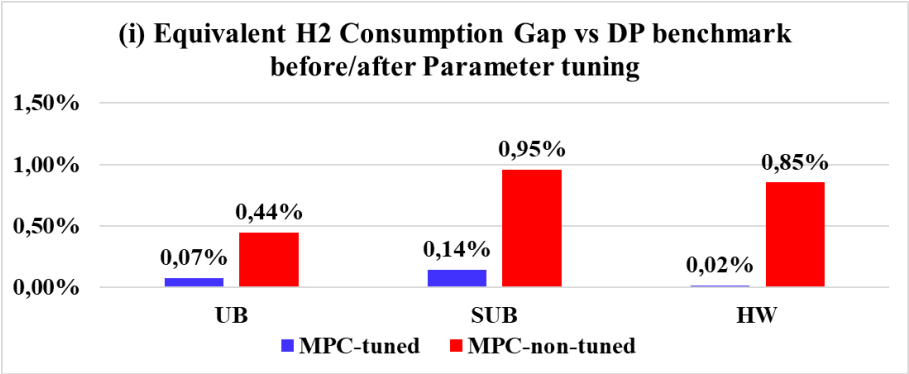


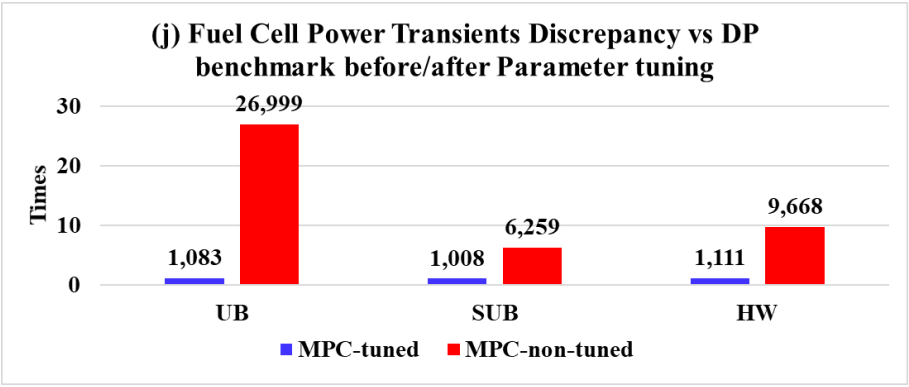


Figure 4.13(continued). (c) performance comparison under highway driving condition; (d) fuel economy discrepancy vs. DP benchmark; (e) fuel cell power dynamics discrepancy vs. DP benchmark (DP performance is deemed as "1").

Furthermore, the performance gaps among MPC-based strategies and DP benchmark are summarized

in TABLE 4.3. The terms "MPC-T" and "MPC-N" respectively denote the MPC with tuned and non-tuned penalty factors. Unlike the global optimization-based strategy (DP), the final battery SoC of MPC-based strategies may differ from its initial value (0.7). Such electricity energy gaps can only be compensated via DC bus by H2 consumption, since the battery pack, in this powertrain configuration, is not associated with plug-in property. This would increase or decrease the amount of H2 fuel actually consumed, with such corrected H2 consumption termed as equivalent H2 consumption ($m_{equ,H_2}$). More details regarding the calculation of equivalent H2 consumption can be found in [17]. As can be seen, after using the tuned penalty factors, the MPC-based EMS performs close to DP benchmark. In addition, as shown in figure 4.13(d), with tuned MPC parameters, the largest performance gap on $m_{equ,H_2}$ compared to the DP benchmark is only 0.14%. Moreover, as shown in figure 4.13(e), the average FC power transients obtained by non-tuned MPC is from 6.259 to 26.999 times of DP basis, whereas this value declined significantly (1.008 to 1.111 times) after using the tuned parameters. Hence, it can be confirmed that the MPC penalty factors are well tuned, where the tuned MPC control parameters are given in TABLE 4.3.

TABLE 4.3. MPC Performance Gaps against DP benchmark before/after parameter tuning

| **Driving pattern** | | **Urban (UB)** | | |
|---|---|---|---|---|
| **Control Strategy** | | **DP** | **MPC-T** | **MPC-N** |
| $\mathbf{SoC_N}$ | | 0.7000 | 0.7021 | 0.7032 |
| $\mathbf{m_{equ,H_2}(g)}$ | | 135.10 | 135.20 | 135.71 |
| $\mathbf{\lvert\Delta P_{fc}\rvert}$ **(w/s)** | | 1.41 | 1.42 | 35.29 |
| **Tuned MPC parameters** | $(\rho_1, \rho_2, \rho_3)$ | **(1,2,100)** | | |
| | $\mathbf{P_{ref}}$ | **1.78 kW** | | |
| **Driving pattern** | | **Suburban (SUB)** | | |
| **Control Strategy** | | **DP** | **MPC-T** | **MPC-N** |
| $\mathbf{SoC_N}$ | | 0.7000 | 0.7123 | 0.7102 |
| $\mathbf{m_{equ,H_2}(g)}$ | | 418.30 | 418.90 | 422.29 |
| $\mathbf{\lvert\Delta P_{fc}\rvert}$ **(w/s)** | | 13.32 | 13.43 | 83.39 |
| **Tuned MPC parameters** | $(\rho_1, \rho_2, \rho_3)$ | **(1,1,60)** | | |
| | $\mathbf{P_{ref}}$ | **6.80 kW** | | |
| **Driving pattern** | | **Highway (HW)** | | |
| **Control Strategy** | | **DP** | **MPC-T** | **MPC-N** |
| $\mathbf{SoC_N}$ | | 0.7000 | 0.7021 | 0.7131 |
| $\mathbf{m_{equ,H_2}(g)}$ | | 1302.50 | 1302.71 | 1313.62 |
| $\mathbf{\lvert\Delta P_{fc}\rvert}$ **(w/s)** | | 11.01 | 12.23 | 106.42 |
| **Tuned MPC parameters** | $(\rho_1, \rho_2, \rho_3)$ | **(1,0.2,54)** | | |
| | $\mathbf{P_{ref}}$ | **14.40 kW** | | |

## 4.3.2. Energy management strategy performance evaluation

A simulation study is conducted in this subsection to verify the performance of the proposed multi-mode MPC-based EMS against benchmark strategies.

### 4.3.2.1. Benchmark energy management strategy description

Dynamic programming is regarded as the upper benchmark strategy, with the global optimality defined as minimizing the hydrogen consumption over a known driving cycle:

$$\min_{\Delta P_{FC} \in \mu_{FC}} \sum_{k=0}^{N-1} \left[ \frac{P_{FC}(k)}{\eta_{FCS}(P_{FC}) \cdot LHV_{H_2}} \right] \cdot \Delta T$$

Subject to

$$\begin{cases} 0.6 \leq SoC(k) \leq 0.8 & (a) \\ 0 \leq P_{FC}(k) \leq 30\ kW & (b) \\ -1\ kW/s \leq \Delta P_{FC}(k) \leq 1\ kW/s & (c) \\ -50\ kW \leq P_{BAT}(k) \leq 100\ kW & (d) \\ SoC_0 = 0.7, P_{FC_0} = 0\ W & (e) \\ SoC_N = 0.7 & (f) \end{cases} \quad (4.25)$$

Where $\Delta P_{FC}$ is selected as the manipulated variable. $\mu_{FC}$ is the discretized feasible region for $\Delta P_{FC}$, with the grid resolution of 1 W/s. Constraints (4.25a) -(4.25d) respectively specify the operation boundaries for SoC, $P_{FC}$, $\Delta P_{FC}$ and $P_{BAT}$. Besides, (4.25e) indicates the initial status of SoC and FC power. Constraint (4.25f) ensures the final SoC reaching the initial value (since battery is not equipped with plug-in property in this case study).

Additionally, a single-mode MPC-based strategy is introduced as the lower benchmark, where its fuel cell power reference value is set as the most efficient FCS working point (see figure 4.5), namely $P_{ref} = P_{\eta}^{max}$. Besides, to cope with the unknown driving conditions, its penalty factors are tuned based on trials and errors with the purpose of keeping battery working in charge sustaining mode to the utmost extent.

#### 4.3.2.2. Evaluation results on multi-pattern driving cycles

Five multi-pattern driving cycles are used for performance evaluation, with the comparative results under combined cycle I and II detailed in figure 4.14.

As displayed in figure 4.14(a), the combined cycle I is a 6489s-long multi-pattern driving cycle, which comprises urban, suburban and highway driving scenarios. The real driving pattern is plotted in black solid curve and the pattern identification result (provided by Markov DPR approach) is given in red dashed curve. Overall, the MC pattern recognizer can achieve 97.05% DPR accuracy, with the errors mainly imposed by the identification delays during pattern switching phases. Please note in all case studies, the largest DPR delay is less than 100s, meaning the recognition latency would be compensated within two consecutive updating phases. Besides, figure 4.14(b) depicts the SoC traces of three EMSs, where DP charges battery in urban regions to prepare for the peaking power demands in the following suburban and highway regions. Regarding the multi-mode EMS, the battery SoC is strictly limited around 0.7 in urban regions, while the battery energy is used in a relatively flexible manner in other regions. In addition, the single-mode EMS keeps SoC strictly around 0.7 during the entire trip.

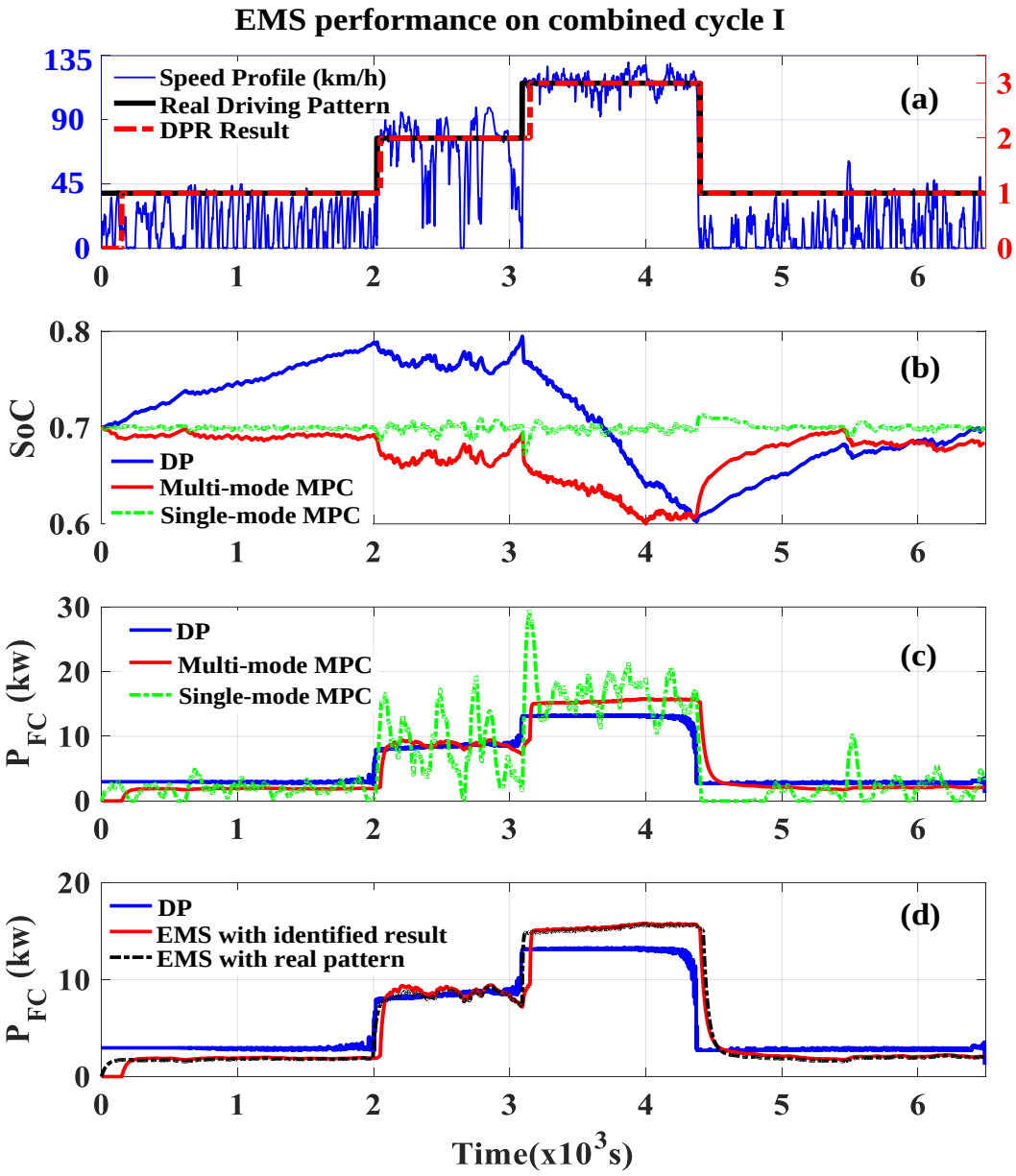


Figure 4.14. Evaluation results on testing cycle I: (a) speed profile and the related driving pattern (1: urban, 2: suburban, 3: highway); (b) battery SoC trajectory comparison; (c) fuel cell output power comparison; (d) impacts on fuel cell power profiles brought by driving pattern identification errors.

Moreover, in figure 4.14(c), DP urges FC working at different power levels under each driving pattern with few transients. Likewise, the multi-mode EMS urges FC working towards different set points in a relatively stable manner. In contrast, the single-mode EMS results in much more FC power transients and on-off cycles. Furthermore, figure 4.14(d) depicts the impacts on FC power caused by DPR errors, where the FC power profile of a multi-mode MPC with real driving pattern information (100% accuracy) is marked with black dashed format. Regarding the multi-mode EMS with pattern identification results, the FC power switching delay can be observed at each real pattern switching moment. When the external driving conditions become stable, their performance discrepancies are insignificant. Besides, as shown

in figure 4.14(e)-(h), similar evaluation results can be found under the combined cycle II.

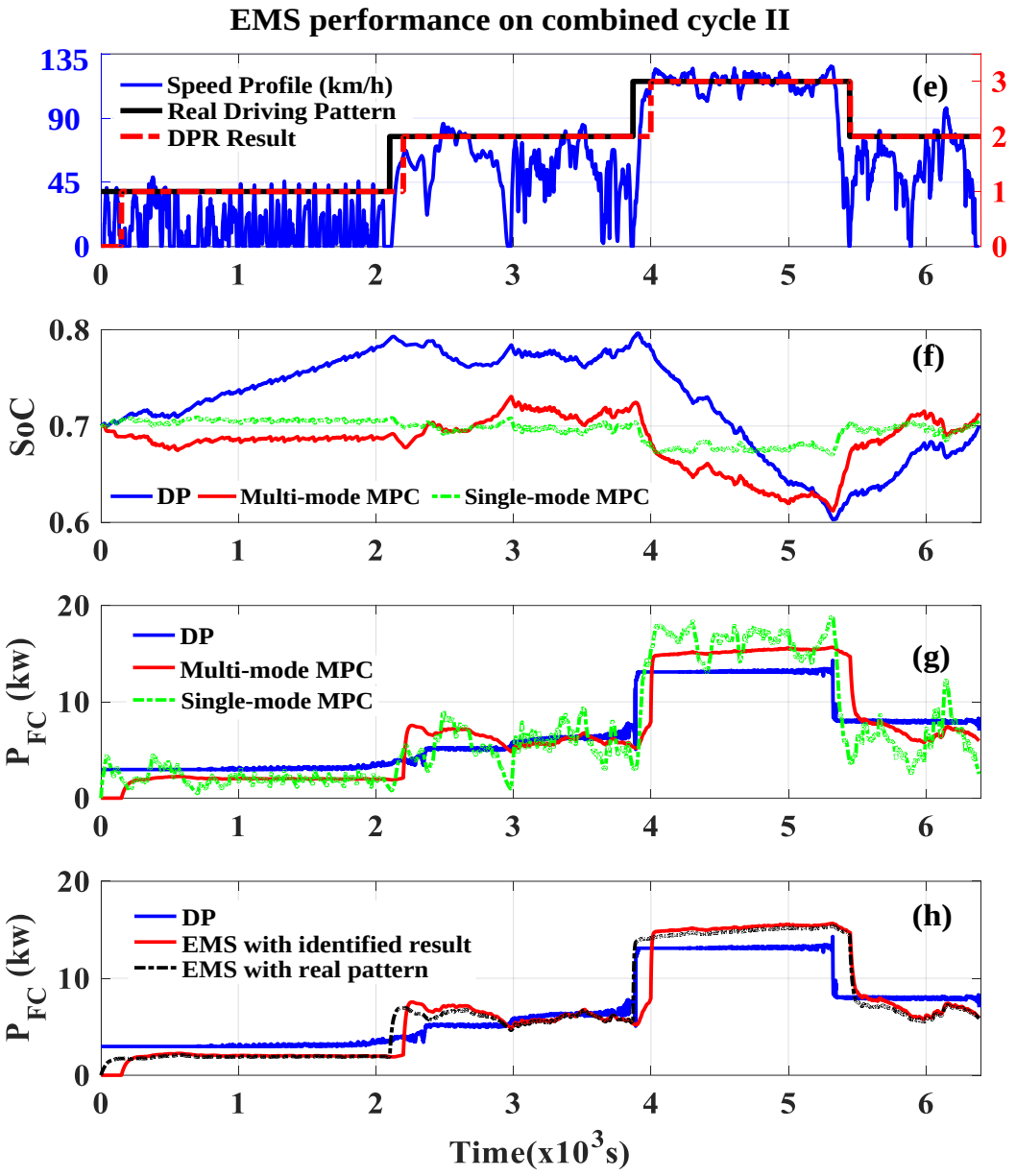


Figure 4.14 (continued). Evaluation results on testing cycle II: (e) speed profile and the related driving pattern; (f) battery SoC trajectory comparison; (g) fuel cell output power comparison; (h) impacts on fuel cell power profiles brought by driving pattern identification errors.

TABLE 4.4 summarizes the numerical evaluation results on five driving cycles. The abbreviation "MPC-S" represents the single-mode EMS, "MPC-R" and "MPC-M" refer to the multi-mode MPC equipped with real driving pattern and the online DPR results, respectively. By comparing the outcome of MPC-R and MPC-M strategies, the impacts on EMS performance by pattern identification errors can be revealed. $SoC_N$ is the SoC value at trip end, $m_{H_2}$ the actual hydrogen mass consumption, $m_{H_2,equ}$ the equivalent hydrogen mass consumption, and $|\overline{\Delta P_{FC}}|$ the average fuel cell power transients, which can be calculated by:

$$|\overline{\Delta P_{FC}}| = \frac{\sum_{i=1}^{N_{cycle}} |\Delta P_{FC}(i)|}{N_{cycle}}, with\ \Delta P_{FC}(i) = \frac{P_{FC}(i) - P_{FC}(i-1)}{\Delta T} \quad (4.26)$$

Where $N_{cycle}$ is the length of the driving cycle and $\Delta P_{FC}(i)$ is the changing rate of fuel cell power at the i-th discrete time step. As a global optimization strategy, DP consumes the least amount of $m_{equ,H_2}$ and leads to the smallest FC power transients $|\overline{\Delta P_{FC}}|$ on all test cycles. In contrast to the MPC-S strategy, the MPC-M strategy can reduce (1) $m_{equ,H_2}$ by 2.07% to 3.26% and (2) $|\overline{\Delta P_{FC}}|$ by 87.75% to 88.98% under five cycles, implying the improved fuel economy and the reduced risk of FCS degradations caused by frequent load changing. Furthermore, by comparing the results of MPC-R and MPC-M, it can be seen that the DPR errors could increase $m_{equ,H_2}$ by 0.06% to 1.30%.

TABLE 4.4. Numerical EMS evaluation results on five testing cycles.

| Type | Road information | Metrics | DP | MPC-R | MPC-M | MPC-S |
|---|---|---|---|---|---|---|
| **Combined Cycle I (CYC_I)** | **Type: "UB + SUB +HW +UB"** | **$SoC_N$** | 0.7000 | 0.6998 | 0.6844 | 0.7010 |
| | | **$m_{H_2}$ (g)** | **474.30** | 479.21 | 480.50 | 502.10 |
| | **DPR accuracy = 97.05%** | **$m_{equ,H_2}$ (g)** | | **479.50** | **486.02** | **501.72** |
| | | **$\overline{\lvert\Delta P_{fc}\rvert}$(w/s)** | **9.07** | **9.87** | **9.99** | **89.71** |
| **Combined Cycle II (CYC_II)** | **Type: "UB + SUB +HW +SUB"** | **$SoC_N$** | 0.7000 | 0.7149 | 0.7133 | 0.7030 |
| | | **$m_{H_2}$ (g)** | **552.10** | 566.10 | 566.51 | 576.1 |
| | **DPR accuracy = 96.26%** | **$m_{equ,H_2}$ (g)** | | **560.84** | **561.85** | **575.03** |
| | | **$\overline{\lvert\Delta P_{fc}\rvert}$(w/s)** | **8.89** | **9.58** | **9.63** | **87.40** |
| **Combined Cycle III (CYC_III)** | **Type: "UB + SUB +HW +SUB+UB"** | **$SoC_N$** | 0.7000 | 0.7067 | 0.7086 | 0.7012 |
| | | **$m_{H_2}$ (g)** | **488.90** | 503.7 | 504.60 | 512.70 |
| | **DPR accuracy = 96.24%** | **$m_{equ,H_2}$ (g)** | | **501.34** | **501.63** | **512.25** |
| | | **$\overline{\lvert\Delta P_{fc}\rvert}$(w/s)** | **9.85** | **10.03** | **10.59** | **86.48** |
| **Combined Cycle IV (CYC_IV)** | **Type: "UB + SUB +HW +UB"** | **$SoC_N$** | 0.7000 | 0.7055 | 0.7066 | 0.7012 |
| | | **$m_{H_2}$ (g)** | **527.02** | 541.10 | 542.05 | 553.62 |
| | **DPR accuracy = 94.95%** | **$m_{equ,H_2}$ (g)** | | **539.14** | **539.66** | **553.18** |
| | | **$\overline{\lvert\Delta P_{fc}\rvert}$(w/s)** | **8.27** | **8.83** | **8.95** | **79.27** |
| **Combined Cycle V (CYC_V)** | **Type: "UB + SUB +HW +UB"** | **$SoC_N$** | 0.7000 | 0.6956 | 0.6966 | 0.7011 |
| | | **$m_{H_2}$ (g)** | **450.40** | 458.50 | 459.50 | 476.60 |
| | **DPR accuracy = 96.61%** | **$m_{equ,H_2}$ (g)** | | **460.08** | **460.73** | **476.25** |
| | | **$\overline{\lvert\Delta P_{fc}\rvert}$(w/s)** | **9.89** | **10.41** | **10.53** | **93.09** |

To further evaluate the proposed EMS, an analysis on battery lifespan is conducted. To simplify the evaluation process, it is assumed that the battery pack is brand new, the operation temperature is fixed at 25℃ and the initial SoC is 0.7. Two evaluation criteria for battery lifetime are introduced, namely the battery current c-rate and the SoC range, where the first metric is to describe the battery charge/discharge rate while the second one indicates whether the battery is over-charge/discharge.

TABLE 4.5. Battery Current C-Rate (RMS value) and SoC range comparison under five testing cycles

| Metric | EMS | CYC_I | CYC_II | CYC_III | CYC_IV | CYC_V |
|---|---|---|---|---|---|---|
| **$I_{BAT}$ C-Rate** | **MPC-S** | 1.0860 | 0.8121 | 0.8379 | 0.7667 | 1.2030 |
| | **MPC-M** | 1.1438 (+5.32%) | 0.8446 (+4.00%) | 0.8586 (+2.47%) | 0.8064 (+5.18%) | 1.2605 (+5.04%) |
| **SoC Range** | **MPC-S** | [0.67,0.71] | [0.68,0.71] | [0.68,0.71] | [0.68,0.71] | [0.67,0.71] |
| | **MPC-M** | [0.60,0.70] | [0.61,0.73] | [0.62,0.72] | [0.61,0.72] | [0.61,0.73] |

TABLE 4.5 summarizes the comparative results of the root mean square (RMS) value of battery current c-rate and the SoC operation range under five testing cycles. Compared to MPC-S strategy, the MPC-M strategy enlarges the battery current C-rate by 2.47% to 5.32%, implying the slightly higher battery charge/discharge rate. Therefore, the power losses on battery internal resistance would increase and the rising temperature would intensify the side reactions within the battery cell and accelerate the fatigue of the active material crystal lattice, which would shorten the battery lifetime [15]. This is because that the control parameters for MPC-M strategy are optimized to limit the FC power transients for extending the FCSs' lifetime. Accordingly, battery is required to work more actively for handling the external power demand variations, thereby enlarging battery charge/discharge rate. Moreover, both strategies can maintain SoC within the predefined range [0.6, 0.8], implying a safe battery operation environment.

In summary, compared to single-mode strategy, the proposed multi-mode strategy can achieve (1) over 87.00% decrement on FC power transients and (2) at least 2.07% saving on hydrogen consumption. Although the battery durability could be slightly compromised, the significant performance improvement, especially on the FCS lifetime extension, brought by the multi-mode strategy is consistent with the initial EMS design objective. Furthermore, in face of the changeable driving conditions, the operation and maintenance cost of the FCS could be largely reduced by the proposed strategy, which should be regarded as the major advantage regarding the real implementation of the proposed EMS.

## 4.4. Online-learning enhanced predictive energy management strategy

Compared to hybrid electric vehicles (HEVs), plug-in hybrid electric vehicles (PHEVs) have larger battery capacity and plug-in property, which enables a way towards better fuel economy by using the onboard low-cost electricity power for vehicular propulsion.

Unlike the multi-mode EMS presented in subsection 4.3, which aims at keeping SoC within a predefined range (charge-sustaining mode), the energy management strategy (EMS) proposed in this subsection intends to optimally deplete battery energy with regard to different driving scenarios for better fuel economy. In addition, since the online learning enhanced Markov (OL-MC) predictor proposed in Chapter 3 can be renewed in real-time according to recent driving changes, the proposed EMS's adaptability towards driving discrepancy can be further improved. To this end, the subsection will focus on a midsize fuel cell hybrid electric vehicle (FCHEV) **with plug-in property**, where the vehicular specifications are given in TABLE 4.1 (**Config. II**).

Figure 4.15 presents the control framework of the devised predictive EMS (PEMS). In the supervisory level, the OL-MC speed predictor can forecast the speed profiles with the real-time updated transition probability matrices. Afterwards, the declining rate of battery SoC is regulated based on the partial trip information and speed-forecast results. In the rolling optimization level, combining the predicted velocity, the reference SoC traces and the current vehicle states, MPC derives the optimal control action

via minimizing the multi-objective cost function at each time step. Please note the development of the OL-MC speed predictor and the adaptive SoC reference generator are presented in **Chapter 3**.

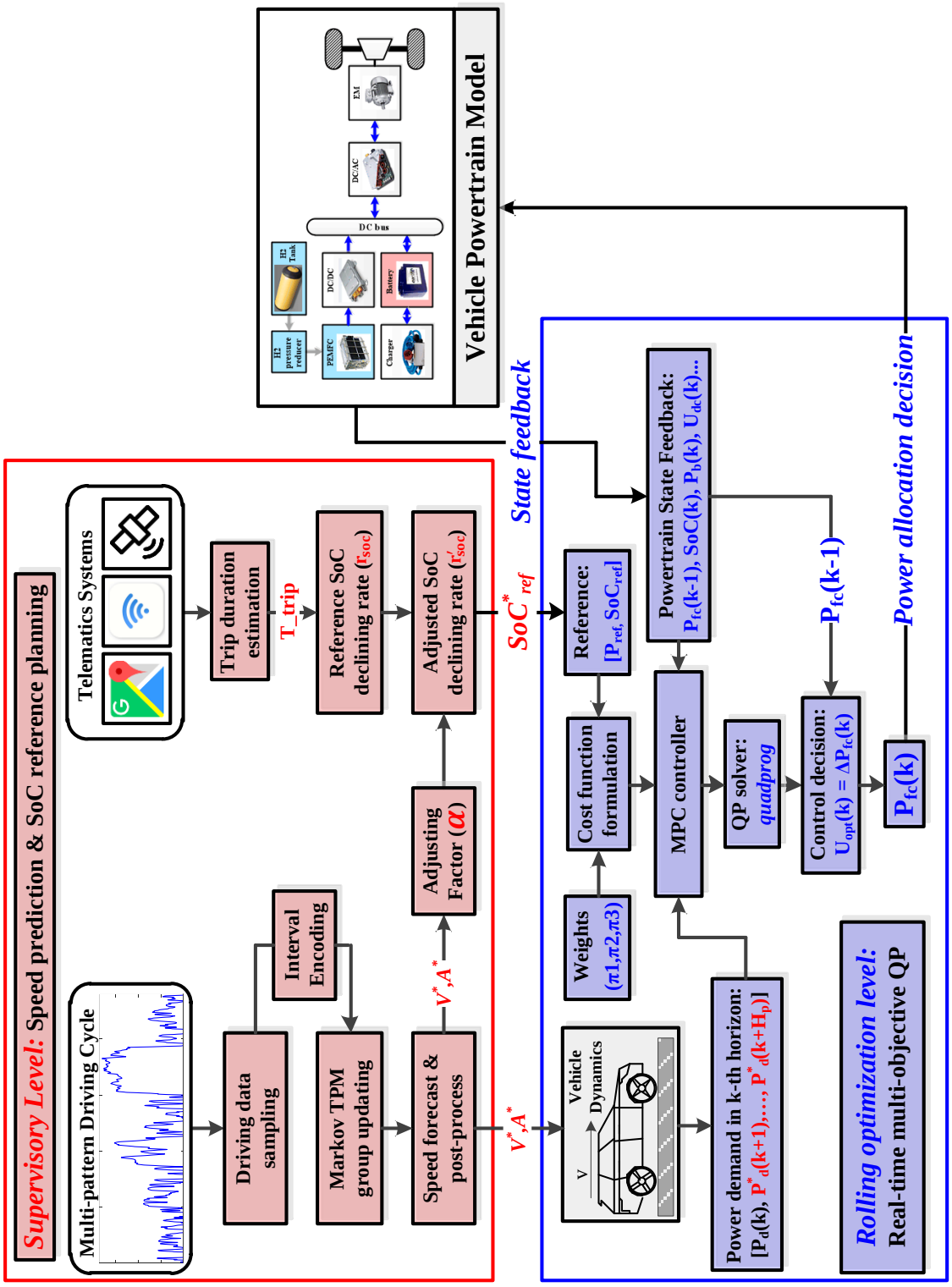


Figure 4.15. Control framework of the online-learning enhanced predictive energy management strategy.

### 4.4.1. Power allocation using model predictive control

This subsection presents the formulation of model predictive control for real-time decision-making.

#### 4.4.1.1. Control-oriented model

Let the symbol $\boldsymbol{x} \in R^{2\times1}$ being state variable, $\boldsymbol{u} \in R^{1\times1}$ the manipulated variable, $\boldsymbol{y} \in R^{1\times1}$ the system output, $\boldsymbol{w} \in R^{1\times1}$ the disturbance, the control-oriented model is formulated as a linear discrete-time system (with $\Delta T = 1s$) as denoted by Eq. (4.27), where the MPC control horizon is identical to its prediction horizon ($H_p$).

$$\begin{aligned} &x(k+1) = A(k)x(k) + B_u(k)u(k) + B_w w(k) \quad (a)\\ &y(k) = Cx(k) \quad (b)\\ &\text{with} \begin{cases} x(k) &= [SoC(k)\ P_{FC}(k-1)]^T \\ u(k) &= \Delta P_{FC}(k) = \frac{P_{FC}(k)-P_{FC}(k-1)}{\Delta T} \\ y(k) &= [SoC(k)\ P_{FC}(k-1)]^T \\ w(k) &= P_d(k) \end{cases} (c) \end{aligned} \tag{4.27}$$

Besides, the reference vector $r(k) = \left[SoC_{ref}\ P_{fc_{ref}}\right]^T$ includes the reference values for SoC and fuel cell power. Combine Eq. (4.27) with the first-order differential approximation of SoC dynamics (Eq. (4.20)) and the DC bus power balance relationship (Eq. (4.21)), the system matrices can be specified as:

$$\begin{aligned} &A(k) = \begin{bmatrix} 1 & \frac{\Delta T\cdot\eta_{DC/DC}\cdot\eta_{BAT}}{U_d(k)\cdot Q_{BAT}} \\ 0 & 1 \end{bmatrix} \qquad B_u(k) = \left[\frac{\Delta T\cdot\eta_{DC/DC}\cdot\eta_{BAT}}{U_d(k)\cdot Q_{BAT}} \quad 1\right]^T \\ &B_w(k) = \left[-\frac{\Delta T\cdot\eta_{DC/DC}\cdot\eta_{BAT}}{U_d(k)\cdot Q_{BAT}} \quad 0\right]^T \quad C = \begin{bmatrix} 1 & 0 \\ 0 & 1 \end{bmatrix} \end{aligned} \tag{4.28}$$

#### 4.4.1.2. Multi-criteria performance index formulation

Three metrics are included in the performance index, namely (i) FCS working efficiency, (ii) limiting the power transient of the FCS to enlarge its durability and (iii) SoC reference tracking ability. Accordingly, the $k^{th}$ control decision $U^*(k) = \left[u_1^*(k), \dots, u_{H_p}^*(k)\right]$ is obtained via minimizing the cost function Eq. (4.29) subject to constraints Eq. (4.30).

$$J(k) = \sum_{i=1}^{H_p} \left[ \pi_1 \cdot \underbrace{\left(\frac{P_{FC}(k+i-1)-P_{ref}}{P_{FC}^{max}}\right)^2}_{L_1} + \pi_2 \cdot \underbrace{\left(\frac{\Delta P_{FC}(k+i-1)}{\Delta P_{FC}^{max}}\right)^2}_{L_2} \right] + \pi_3 \cdot \underbrace{\left(\frac{SoC(k+H_p)-SoC_{ref}}{SoC_{max}-SoC_{min}}\right)^2}_{L_3} \tag{4.29}$$

$$\begin{cases} \underline{SoC} \le SoC(k+i) \le \overline{SoC} & (a)\\ \underline{P_{FC}} \le P_{FC}(k+i-1) \le \overline{P_{FC}} & (b)\\ \underline{\Delta P_{FC}} \le \Delta P_{FC}(k+i-1) \le \overline{\Delta P_{FC}} & (c)\\ \underline{P_{BAT}} \le P_{BAT}(k+i) \le \overline{P_{BAT}} & (d)\\ w(k+i) = P_d^*(k+i), i \ge 1 & (e) \end{cases} \tag{4.30}$$

Where $P_{FC}^{max} = 30$ kW, $\Delta P_{FC}^{max} = 1$ kW/s , $SoC_{min} = 0.3$ and $SoC_{max} = 0.9$. Moreover, to achieve a balanced EMS performance among three cost terms $(L_1, L_2, L_3)$, the penalty coefficients $(\pi_1, \pi_2, \pi_3)$ are tuned by trials and errors, based on the DP-optimized EMS performance. More details regarding the

parameter tuning process can be found in subsection 4.3.1.3. As a result, $\pi_1, \pi_2, \pi_3$ are set as 1, 8 and 80000, respectively. Besides, the major objectives of $L_1, L_2, L_3$ are attached as below:

- To guarantee the overall fuel cell operation efficiency, $L_1$ penalizes the FCS's operating points deviating from the reference one (the most efficient point, see figure 4.5), namely $P_{ref} = P_{\eta}^{max}$.
- $L_2$ lays a penalty on large $\Delta P_{FC}$ to retard the fuel cell degradation induced by dynamic loading conditions.
- The function of $L_3$ is to shrink the deviation between the real SoC and the reference one given by adaptive battery SoC reference generator (Eq. (3.18)). As mentioned in subsection 3.3.2, the SoC reference value is restricted in $[SoC_{min}, SoC_{max}]$ to prevent battery over-charge or over-discharge. However, the accuracy of SoC reference estimation tends to be affected by future driving uncertainties, and the improper reference values would degrade the EMS performance. Thus, we propose the following solution to compensate for the potential performance losses: by tracking the SoC reference value at the end of each optimization horizon, while ignoring the intermediate processes, there will be additional room for MPC to suppress the FCS power dynamics caused by improper SoC reference values. This is the major discrepancy between the cost function Eq. (4.29) and the cost function Eq. (4.23).

Furthermore, constraint (4.30a) enables a wider SoC variation range for real-time optimization, where $\underline{SoC} = 0.25$ and $\overline{SoC} = 0.95$. Similarly, if SoC emergency incident (SoC > 0.9 or SoC < 0.3) appears, $\pi_1$ and $\pi_2$ are set to zero to urge SoC back to [0.3, 0.9]. Constraints (4.30b)-(4.30d) denote the physical limitations on fuel cell and battery, where $\underline{P_{FC}} = 0\,\mathrm{W}$, $\overline{P_{FC}} = 30\,\mathrm{kW}$, $\overline{\Delta P_{FC}} = -\underline{\Delta P_{FC}} = 1\,\mathrm{kW/s}$, $\underline{P_{BAT}} = -25\,\mathrm{kW}$ and $\overline{P_{BAT}} = 50\,\mathrm{kW}$. Besides, (4.30e) sets the estimated DC power demands as the disturbance, where $P_d^*$ is derived based on the forecasted speed $V_k^*$ by OL-MC predictor and Eq. (4.1)-(4.2). Finally, the optimization problem, namely minimizing Eq. (4.29) subject to constraints Eq. (4.30), can be resolved by the ***quadprog*** function in the MATLAB optimization Toolbox.

### 4.4.2. Performance verification of predictive energy management strategy

The performance of the online-learning enhanced PEMS is validated in this subsection based on the simulation study. In all case studies, the initial and terminal SoC are set as 0.8 and 0.3, respectively.

#### 4.4.2.1. Impacts on EMS performance by $k_\alpha, H_p$ and different SoC references

Several parameters of the proposed PEMS would heavily affect its performance, which should be carefully tuned before online implementations. This subsection presents a detailed analysis regarding the determination criteria of EMS parameters and the battery energy allocation performance comparison with linear SoC reference Eq. (3.17).

- **Determination of SoC reference adjusting boundary $k_\alpha$**

As mentioned in subsection 3.3.2, $\alpha(k) = \frac{k_\alpha}{1+\frac{v_{std}(k)}{v_{ave}(k)}}$ is the adjusting factor of SoC depleting rate, which can help adjust battery energy depleting rates in different driving scenarios. The constant positive numerator $k_\alpha$ defines the upper boundary of $\alpha$. A proper setting on $k_\alpha$ could help fully utilize the onboard electricity, whereas an overlarge $k_\alpha$ would deplete battery energy too fast, leading to the extension of vehicle's charge-sustaining driving mileage. To find a proper $k_\alpha$ for online application, the MPC-based EMS with multiple $k_\alpha$ candidates (1 to 5) is tested under the multi-pattern driving cycle (figure 4.16(a)), where $H_p$ is set as 5 seconds.

Figure 4.16(b) displays the obtained SoC traces. Obviously, if $k_\alpha = 1$, larger final SoC value is detected compared to other $k_\alpha$ settings, meaning the overall SoC declining rate is insufficient to ensure the full utilization of battery energy. In contrast, although using larger $k_\alpha$ can ensure a deeper battery discharge, if $k_\alpha > 2$, the overlarge SoC declining rates would contribute to the SoC emergency events (SoC < 0.3, as shown in the zoomed area). Hence, set $k_\alpha$ as two is a reasonable trade-off decision between the battery working safety and the exploitation rate of electricity energy.

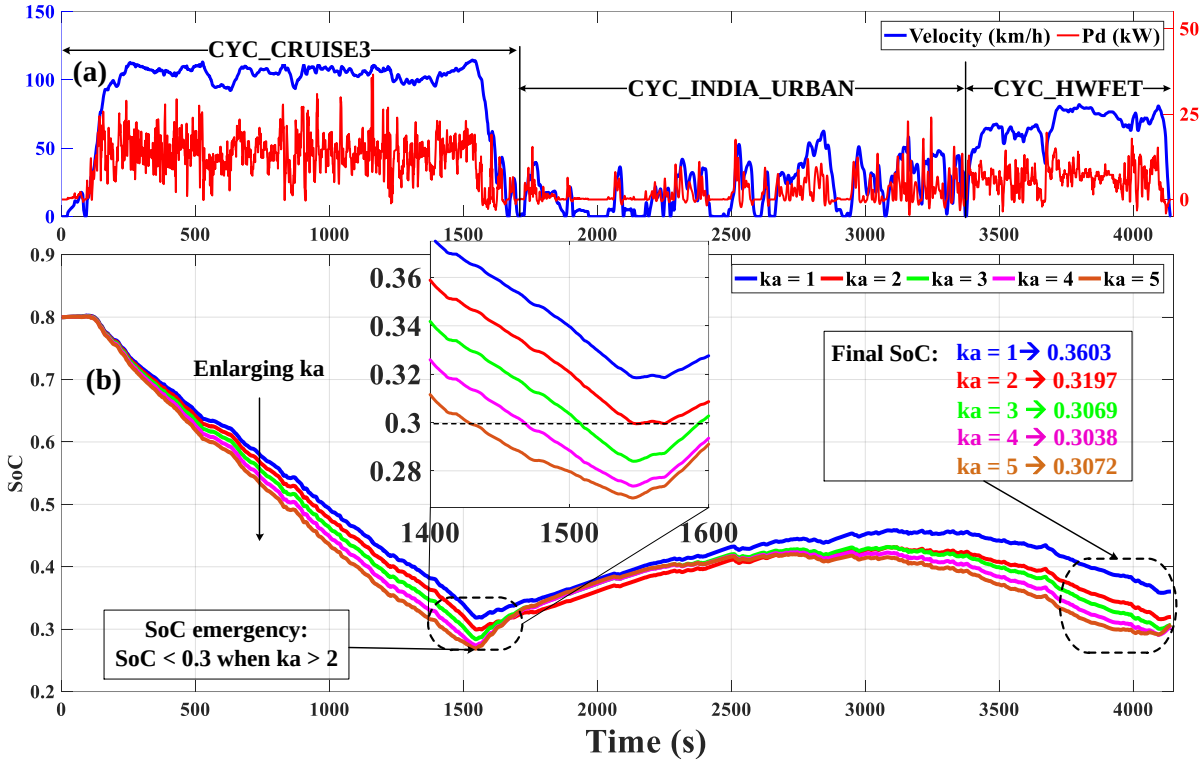


Figure 4.16. EMS performance comparison under different parameter settings. (a) Velocity and power request profiles of the testing cycle. (b) SoC profiles under multiple $k_\alpha$ ($H_p$ = 5s).

- **EMS performance discrepancy using different SoC reference generators**

Given $k_\alpha = 2$, the performances of MPC-based EMS with different SoC references are compared in figure 4.16(c)-(e). As for the linear SoC reference-based EMS, figure 4.16(c) and (d) only depict its

performance when $H_p$ = 5s, while the performance under other $H_p$ settings is given in TABLE 4.6.

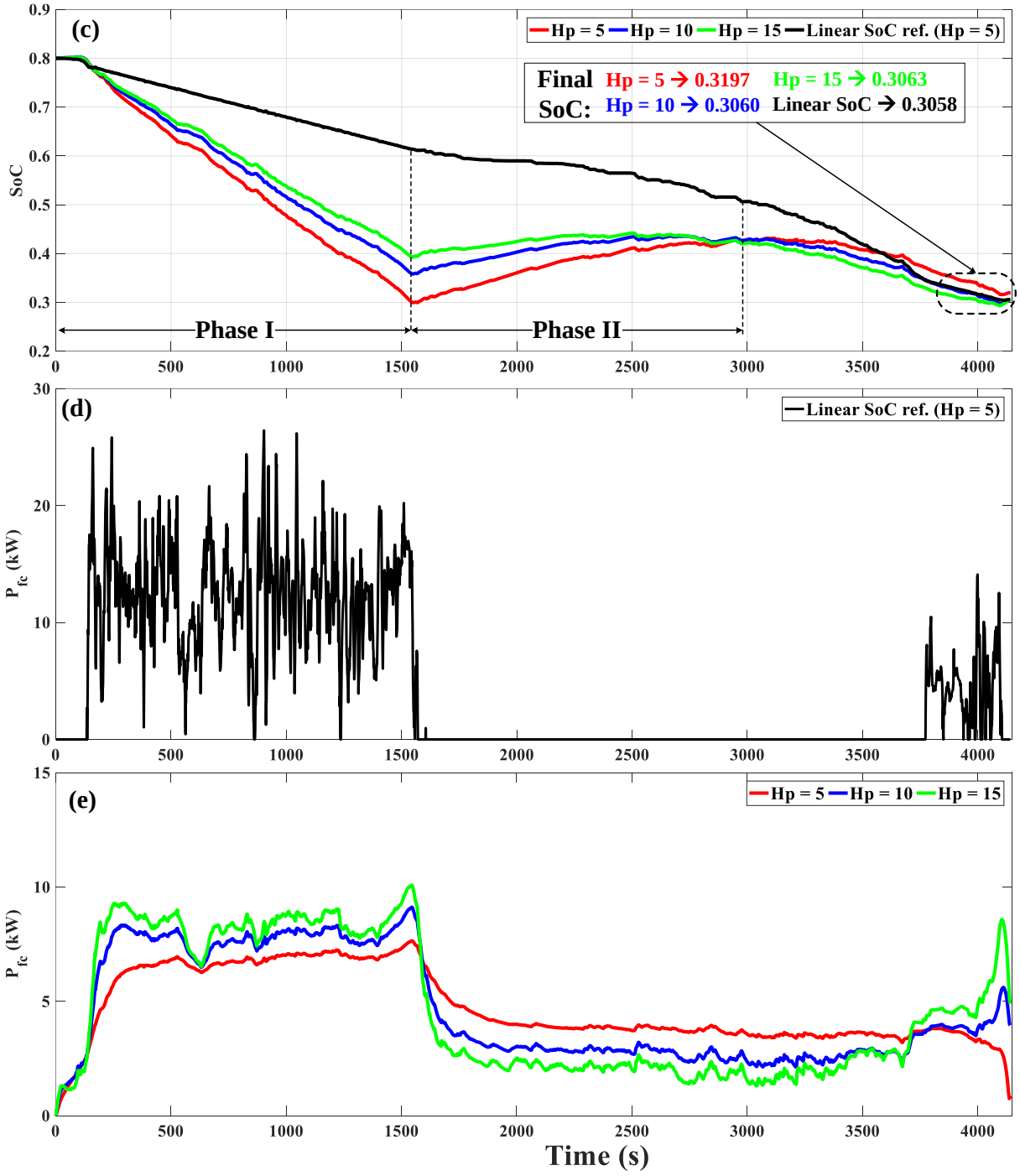


Figure 4.16(continued). EMS performance comparison under different parameter settings. (c) SoC regulation capacity comparison by different reference generators and different Hp ($k_\alpha = 2$). (d) Fuel cell power profile using linear SoC reference ($H_p$ = 5s). (e) Fuel cell power profiles using the proposed SoC reference and different $H_p$.

Figure 4.16(c) depicts the SoC regulation performance under two types of reference generators. The linear reference model (black curve) tends to evenly distribute battery energy over the entire trip. Due to the extremely low external power demand in phase II, despite the fuel cell has been turned off in this phase (figure 4.16(d)), the SoC declining rate is still slightly lower than that of phase I. In contrast, the

adaptive SoC reference generator ($H_p$ = 5s, red curve) can effectively adjust battery energy usage under different driving patterns. Specifically, the battery energy is largely used due to the high average power demand in highway scenario (phase I), whereas the battery tends to be recharged or less used in urban scenario (phase II).

Guided by the linear SoC reference, the EMS adjusts the fuel cell output power in an aggressive way, as displayed in figure 4.16(d). Large power transients and frequent start-stop cycles can be observed over the testing cycle, especially from 200s to 1500s and from 3700s to 4150s. Such loading conditions would accelerate the degradation of fuel cell system, leading to the compromised fuel cell durability. In contrast, as shown in figure 4.16(e), guided by the proposed SoC reference model, fuel cell works stably around the reference point, with few power transients. Besides, no fuel cell start-stop cycles can be observed within the entire testing cycle.

Moreover, TABLE 4.6 summarizes the EMS performance discrepancies under different SoC reference models, where $T_{step}$ is the online calculation time per step. It can be clearly seen that, after using the proposed SoC reference model Eq. (3.18), the equivalent H2 consumption $m_{H_2,equ}$ and the average fuel cell power transients $|\overline{\Delta P_{FC}}|$ are greatly reduced compared to the outcome of linear SoC reference-based EMS. Besides, both SoC reference-based EMSs perform similarly in terms of final SoC ($SoC_N$) and online computation efficiency.

TABLE 4.6. EMS Performance discrepancies under different $H_p$ and different types of SOC reference.

| SoC reference | $H_p$ | $m_{H_2}$ (g) | $m_{H_2,equ}$ (g) | $SoC_N$ | $\lvert\overline{\Delta P_{FC}}\rvert$ (W/s) | $T_{step}$ (ms) |
|---|---|---|---|---|---|---|
| **Linear Eq. (3.17)** | 5 | 256.0 | 253.9 | 0.3058 | 438.2 | 16.89 |
| **Linear Eq. (3.17)** | 10 | 254.4 | 252.4 | 0.3057 | 343.1 | 23.79 |
| **Linear Eq. (3.17)** | 15 | 253.8 | 251.8 | 0.3057 | 298.5 | 32.89 |
| **Adaptive Eq. (3.18)** | 5 | 236.7 | 229.8 | 0.3197 | 7.3 | 17.48 |
| **Adaptive Eq. (3.18)** | 10 | 234.0 | 231.8 | 0.3060 | 14.3 | 25.68 |
| **Adaptive Eq. (3.18)** | 15 | 235.8 | 233.6 | 0.3063 | 21.8 | 36.73 |

To sum up, the proposed SoC reference model Eq. (3.18) is capable of depleting battery energy in a flexible manner regarding different power requirements, thus enhancing the rationality of electricity energy allocation in contrast to linear reference model Eq. (3.17). Furthermore, benefiting from such proper battery energy distribution, the EMS can greatly suppress the fuel cell power spikes and effectively improve the fuel cell working efficiency.

- **Determination of prediction horizon $H_p$**

$H_p$ defines the length of speed prediction and the size of online optimization problem, which would have large impacts on both online computation efficiency and EMS performance. With different $H_p$ settings, the fuel cell power and SoC profiles of the adaptive SoC reference-based EMS are illustrated in figure 4.16(c) and (e), respectively, where the related quantitative results are listed in TABLE 4.6. It is clear

that increasing $H_p$ would enlarge $m_{H_2,equ}$ but guarantee a deeper battery discharge. Moreover, $|\overline{\Delta P_{FC}}|$ and $T_{step}$ increase with the growth of $H_p$. Therefore, set $H_p$ as five is a trade-off decision among the following metrics, namely the hydrogen consumption saving, the fuel cell power transients and the online calculation burden.

#### 4.4.2.2. Comparative study against benchmark control strategies

To thoroughly evaluate the proposed PEMS, two commonly-used control strategies are introduced as comparison basis, where the DP-based strategy is deemed as the upper benchmark and the Charge-depleting/Charge-sustaining (CD-CS) strategy is deemed as the lower benchmark.

- **Benchmark EMS description**

Similar as the way of DP formulation in subsection 4.3.2.1, the global optimality is to seek the minimization of hydrogen consumption over a trip while subject to following constraints:

$$\begin{cases} 0.3 \le SoC(k) \le 0.9 & (a) \\ 0 \le P_{FC}(k) \le 30\ kW & (b) \\ -1\ kW/s \le \Delta P_{FC}(k) \le 1\ kW/s & (c) \\ -25\ kW \le P_{BAT}(k) \le 50\ kW & (d) \\ SoC_0 = 0.8, P_{FC_0} = 0\ W & (e) \\ SoC_N = 0.3 & (f) \end{cases} \tag{4.31}$$

In contrast, CD-CS strategy controls the FC output power based on the SoC value. Specifically, when SoC is higher than the threshold 0.3, the FCS switches off. When SoC is lower than this threshold, FCS switches on and the reference working point is set as $P_{FC}^{max} = 30kW$. To guarantee the fairness for performance comparison, the permissible range on $\Delta P_{FC}$ for CD-CS strategy is bounded within $[-1, 1]$ kW/s, which is identical to DP-based and MPC-based EMSs.

- **Evaluation results against benchmarks**

Three EMSs are performed under two multi-pattern testing cycles (namely CYCLE1 and CYCLE2). Note $H_p$ is set to 5s and $k_\alpha$ is set to 2. The performance discrepancies among three EMSs are shown in figure 4.17(a)-(f).

As can be seen, under both testing cycles, the SoC profiles of the MPC-based EMS are close to the DP benchmarks, while the CD-CS strategy depletes the battery energy more quickly than other strategies. Specifically, due to the availability of entire trip information, DP strategy can urge the FCS working steadily along the trip with few power transients. MPC-based EMS can greatly restrict the FC power transients. In contrast, CD-CS strategy switches the FCS off when the SoC is higher than 0.3, and it frequently turns on and off when SoC is reaching the lower threshold (0.3). As a result, much more FC power transients can be observed within the entire CS phases.

TABLE 4.7 summaries the numerical results of three strategies. In contrast to CD-CS benchmark, MPC-based EMS can respectively reduce $m_{H_2,equ}$ by 15.30% and 12.05% under both testing cycles. Moreover, compared to DP benchmark, its performance gaps on $m_{H_2,equ}$ are respectively 3.74% (CYCLE1) and 4.88% (CYCLE2). In addition, MPC-based EMS can suppress the FC power transients under both testing cycles by 96.80% and 94.90% compared to CD-CS strategy, thus reducing the risk of fuel cell performance degradation imposed by dynamic loadings. Finally, it can be observed that as a global optima-searching approach, DP benchmark consumes the largest amount of computation time, while the online computation burden for MPC-based EMS is adequately smaller compared to the sampling period (1s) and thus is affordable for online implementations.

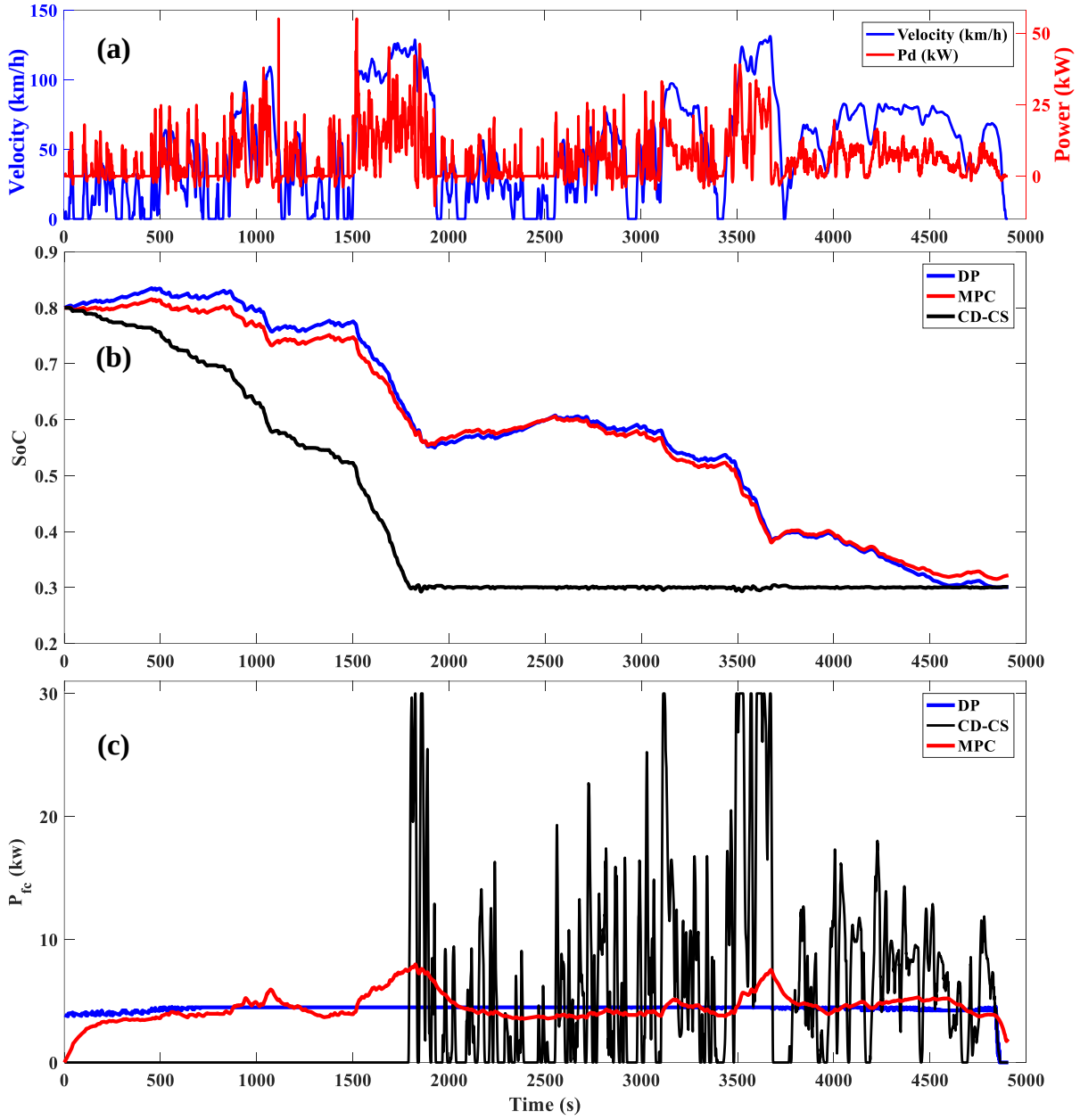


Figure 4.17. Performance discrepancy of three EMSs: (a) speed and power demand profiles of CYCLE I; (b) SoC profiles of three control strategies; (c) fuel cell power trajectories of thee control strategies.

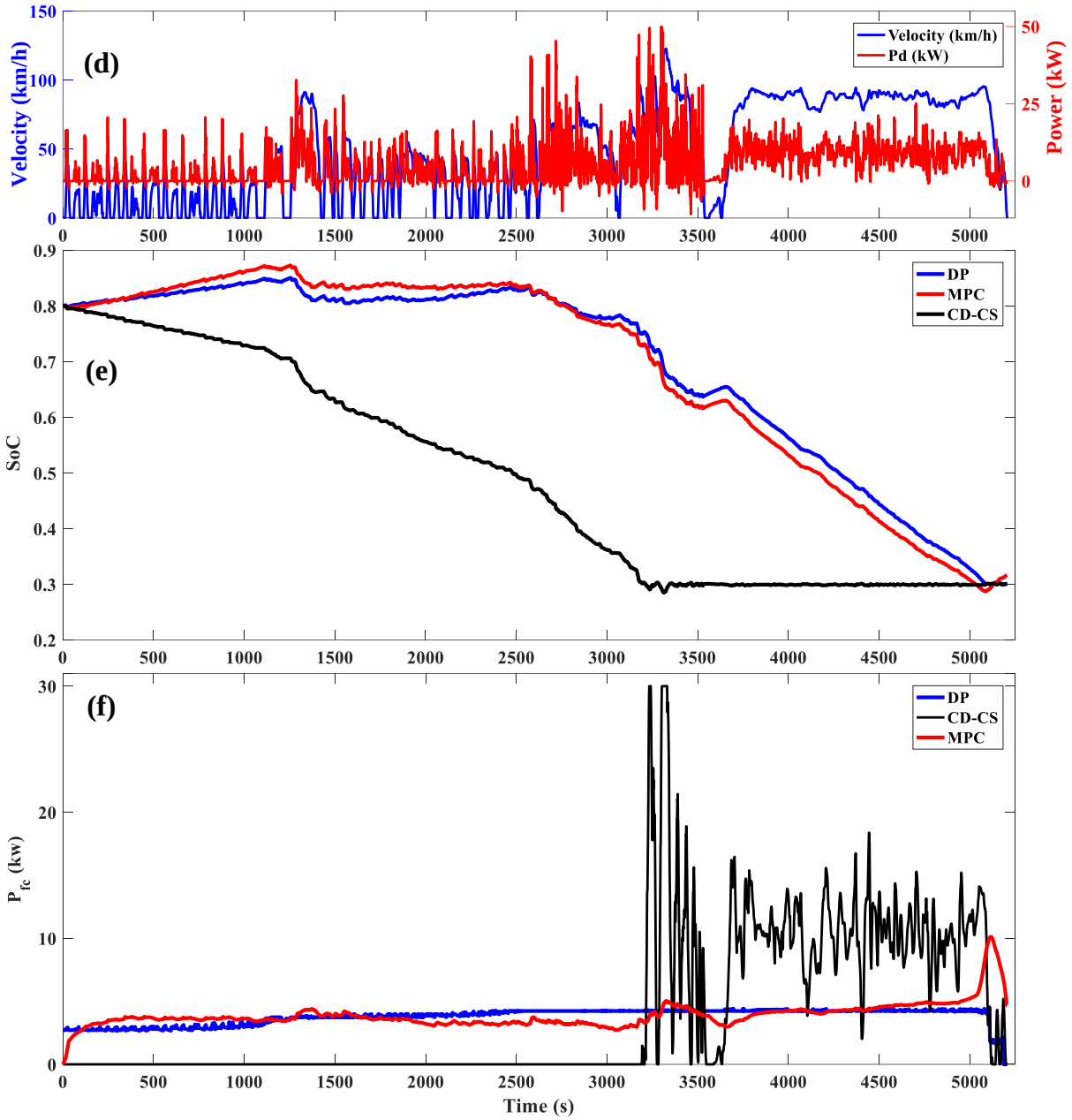


Figure 4.17 (continued). Performance discrepancy of three EMSs: (d) speed and power demand profiles of CYCLE II; (e) SoC profiles of three control strategies; (f) fuel cell power trajectories of thee control strategies.

TABLE 4.7. EMS results compared to benchmark strategies.

| EMS | | $m_{H_2}$ (g) | $m_{H_2,equ}$ (g) | $SoC_{end}$ | $\overline{\lvert\Delta P_{FC}\rvert}$ (W/s) | $T_{total}$ (s) | $T_{step}$ (ms) |
|---|---|---|---|---|---|---|---|
| **CYCLE1** | **DP** | 245.9 | 245.9 | 0.3000 | 5.6 | 412.36 | N/A |
| | **MPC** | 262.8 | 255.1 | 0.3218 | 11.8 | 81.13 | 16.39 |
| | **CD-CS** | 301.6 | 301.2 | 0.3011 | 375.1 | 11.48 | 2.32 |
| **CYCLE2** | **DP** | 223.5 | 223.5 | 0.3000 | 7.3 | 489.56 | N/A |
| | **MPC** | 240.3 | 234.4 | 0.3168 | 9.4 | 87.72 | 17.20 |
| | **CD-CS** | 266.8 | 266.5 | 0.3008 | 185.2 | 15.56 | 3.05 |

- **Influences on EMS performance imposed by trip duration estimation errors**

As mentioned in subsection 3.3.2, the reference SoC depleting rate $r_{soc}(k) = \frac{SoC(k)-SoC_{final}}{T_{trip}-k}$ is defined

by the ratio of the remaining useful SoC ($SoC(k) - SoC_{final}$) and the estimated remaining trip duration ($T_{trip} - k$). To calculate $r_{soc}(k)$, it is assumed that the trip duration $T_{trip}$ can be estimated before departure with the help of the modern telematics systems (e.g. GPS, ITS). Nevertheless, many uncertain events, like the traffic congestions or the driving routes adjustment, will eventually lead to the discrepancy between the estimated $T_{trip}$ and the actual one. To study the possible influences on EMS performance, different levels of trip duration errors (ranging from -50% to 50% of the real trip time) are applied to the proposed SoC reference generator Eq. (3.18). Positive errors mean the estimated trip duration $T_{trip}$ is larger compared to the real trip time, whereas negative ones mean the opposite.

Under -25% and -50% errors, the performance of MPC-based EMS under CYCLE1 and CYCLE2 is detailed in figure 4.18. Please note the terms "MPC-0", "MPC-25" and "MPC-50" respectively denote the MPC-based EMS with no trip errors, -25% and -50% trip duration estimation errors. As depicted in figure 4.18(b), when the negative errors are applied, the overall SoC declining rate is increased compared to the zero-error condition, making SoC reach the lower threshold (0.3) at around 3200s (MPC-50) and 3700s (MPC-25), as highlighted with dashed circles. Meanwhile, as shown in figure 4.18(c), the SoC emergency mode is activated when SoC < 0.3. For this reason, the FCS works no longer around its most efficient point (~5 kW) but towards higher power level. Besides, larger fuel cell power transients can be observed. As a consequence of that, SoC would not continue to drop but fluctuate around the lower threshold (0.3), meaning the proposed SoC emergency mode is able to prevent battery over-discharge, thus ensuring the operation safety of powertrain. Furthermore, similar EMS performance under negative trip duration estimation errors can also be observed under CYCLE2, as depicted in figure 4.18(e)-(h).

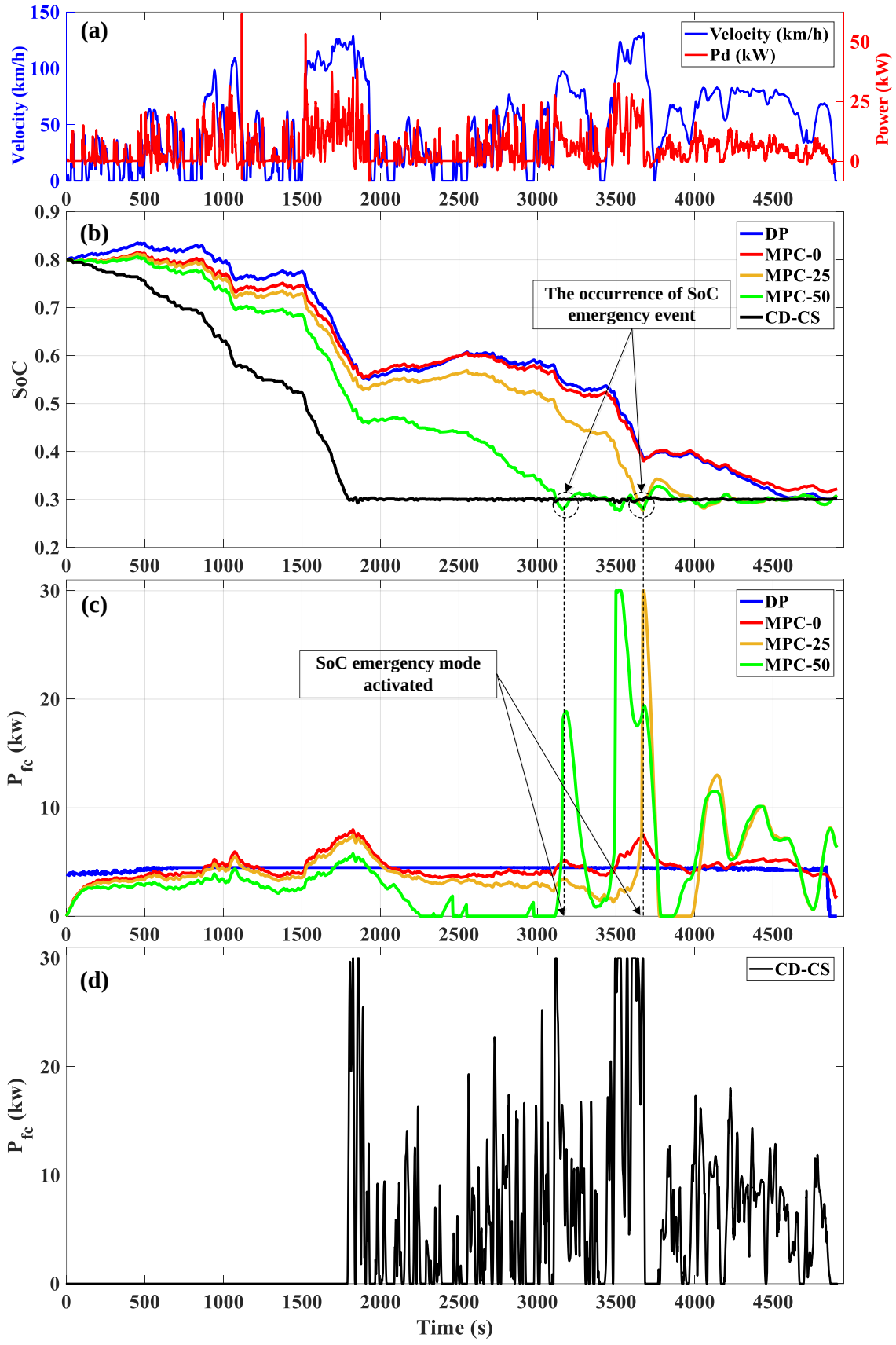


Figure 4.18(a)-(d). EMS performance comparison under CYCLE1 with negative $T_{trip}$ errors.

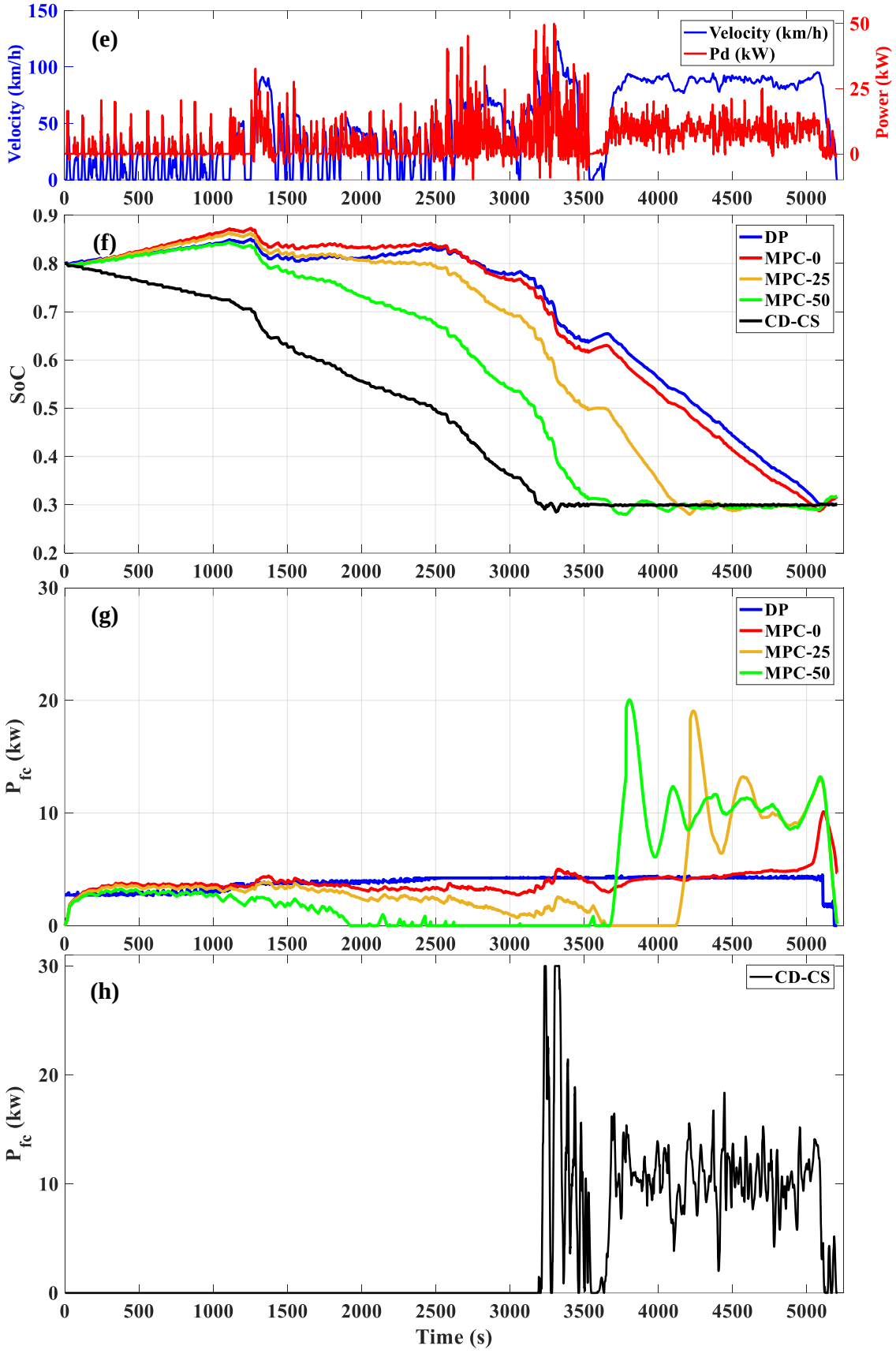


Figure 4.18(e)-(h). EMS performance comparison under CYCLE2 with negative $T_{trip}$ errors.

Moreover, under ± 50% $T_{trip}$ estimation errors, a numerical analysis of performance discrepancy between MPC-based EMS and CD-CS strategy is conducted, with the results given in figure 4.19.

As shown in figure 4.19(a), when positive errors (0 to 50%) appear, the performance gap on the actual H2 consumption against the CD-CS benchmark is shrinking on both testing cycles. This is because the enlarged $T_{trip}$ would slow down the SoC declining rate, resulting in the larger amount of remaining battery energy (see figure 4.19(b)). However, since the FCS's working efficiency can be maintained relatively stable, the performance on the equivalent H2 consumption remains almost the same as the "zero-error" conditions (figure 4.19(c)). In contrast, when negative errors occur (0% to -50%), the adaptive SoC reference generator would lead to a faster battery energy usage, thus extending the CS driving phases. Consequently, the FCS tends to work at higher power level for both supplying the external power demands and sustaining SoC level, thus compromising fuel efficiency performance.

Additionally, as depicted in figure 4.19(d), FC power transients would be enlarged if negative errors appear, whereas it would remain nearly unchanged when positive errors occur. This is because the prolonged CS phases imposed by the minus errors enforce fuel cell operating in a more active manner, thus increasing the power spikes. In contrast, the period of CS working stage would be reduced (or even eliminated) under positive errors and thus the FC power transients would remain almost the same level as "zero-error" conditions. Overall, despite ± 50% trip duration errors, the proposed EMS can effectively (1) improve the fuel efficiency by at least 4.68% (CYCLE1) and 6.14% (CYCLE2), and (2) reduce the FC power spikes by at least 83.90% (CYCLE1) and 79.81% (CYCLE2), compared to CD-CS strategy.

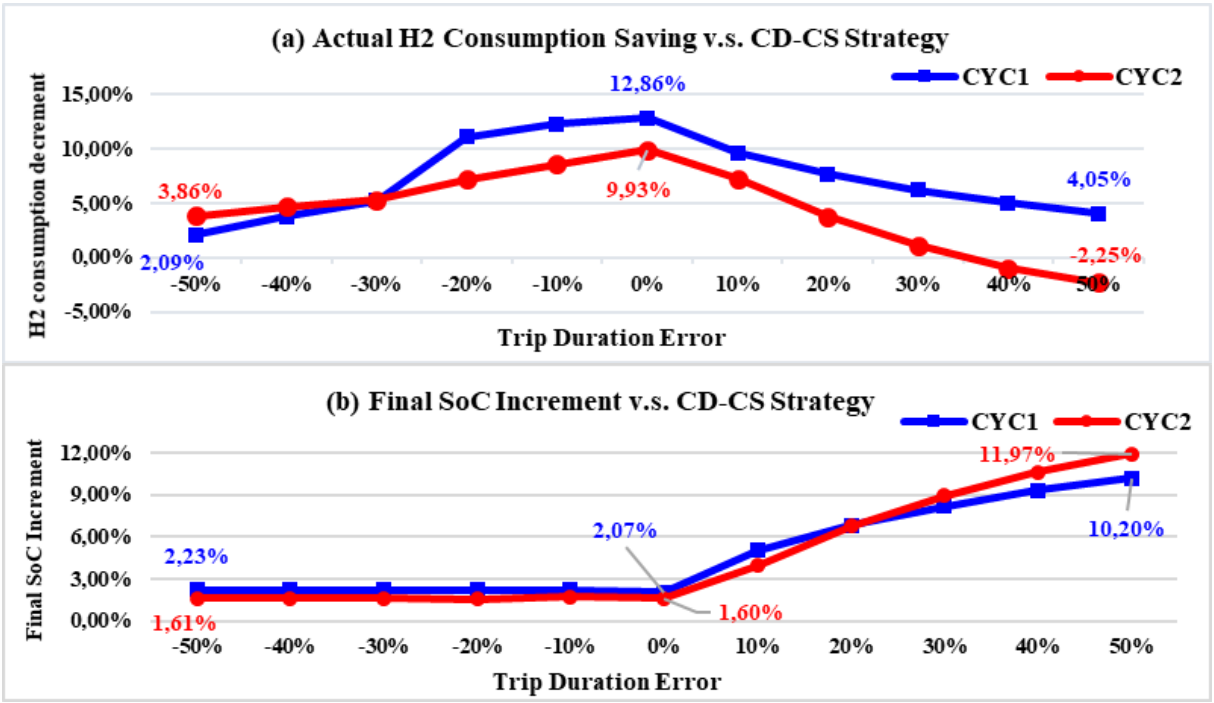


Figure 4.19(a)-(b). MPC-based EMS performance deviations against CD-CS strategy under different $T_{trip}$ errors.

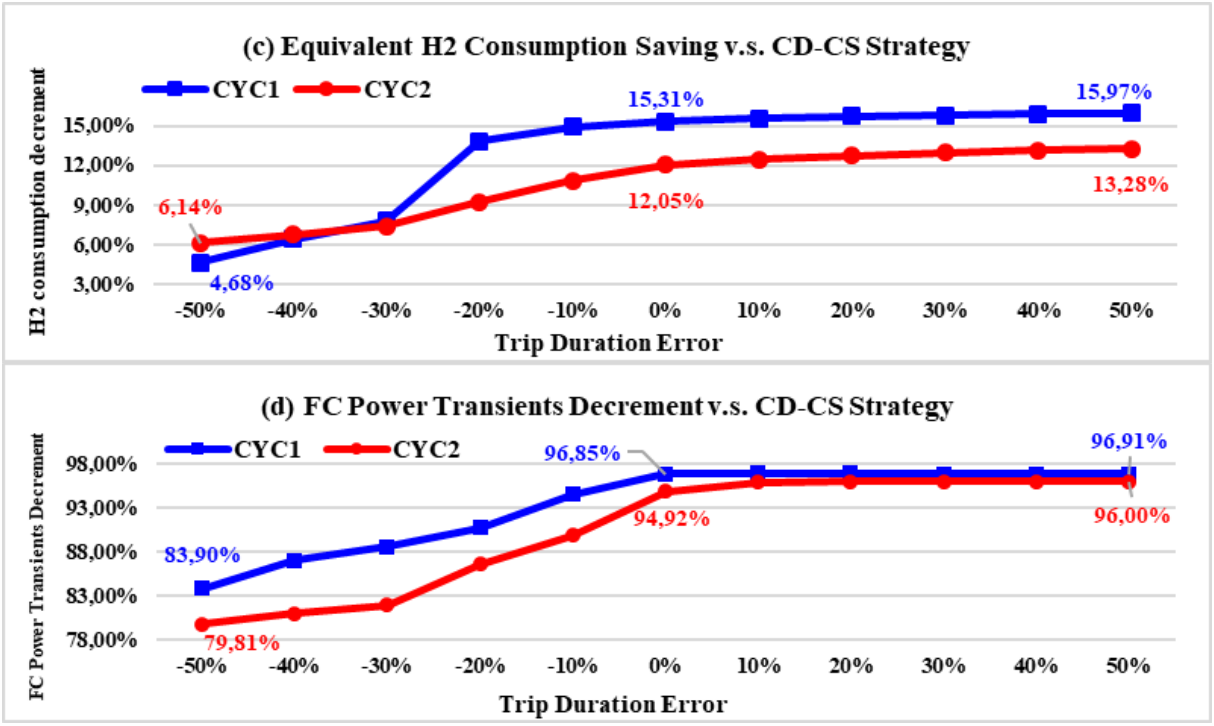


Figure 4.19(c)-(d). MPC-based EMS performance deviations against CD-CS strategy under different $T_{trip}$ errors.

In summary, with the help of OL-MC speed predictor and the adaptive SoC reference generator, the online-learning enhanced PEMS performs close to DP benchmark under multi-pattern testing cycles. In contrast to CD-CS benchmark, it can save equivalent H2 consumption by over 12.05% and suppress the average FC power spikes by over 94.40%. Furthermore, in face of the trip the duration errors caused by unpredictable traffic conditions, the proposed EMS could still outperform the CD-CS benchmark, thereby denoting its potential for actual applications.

## 4.5. Integrated predictive energy management strategy for mail-delivery vehicle

This subsection will focus on the development of an integrated predictive energy management strategy (PEMS) for a light-duty plug-in fuel cell electric vehicle dedicated to postal delivery. Compared to the PEMSs in two previous subsections, the vehicle model has been changed to the prototype developed in the "Mobypost" project [2], with key specifications given in TABLE 4.1 (**config. III**). Accordingly, the driving cycles for EMS performance validation have been changed to the speed profiles collected by GPS on the real delivery routes. In addition, due to the sizing configuration of the "Mobypost" vehicle, battery becomes the primary energy-provider for vehicle propulsion, while the FCS, as the range-extender, is used to charge the battery for extending the driving mileage.

The system-level block diagram of the presented hierarchical PEMS is depicted in figure 4.20. In supervisory level, the upcoming speed profile ($V^*$) is generated by the fuzzy C-means enhanced Markov Chain (FCM-MC) predictor. Subsequently, with the estimated trip duration ($T_{trip}$), the SoC reference ($SoC_{ref}$) is estimated for planning the electricity energy usage. Combined with the velocity prediction

results and SoC reference, MPC generates the control policies ($U_{opt}$) by minimizing the multi-objective cost function within each rolling optimization horizon, where the sampling period $\Delta T$ is set to 1s.

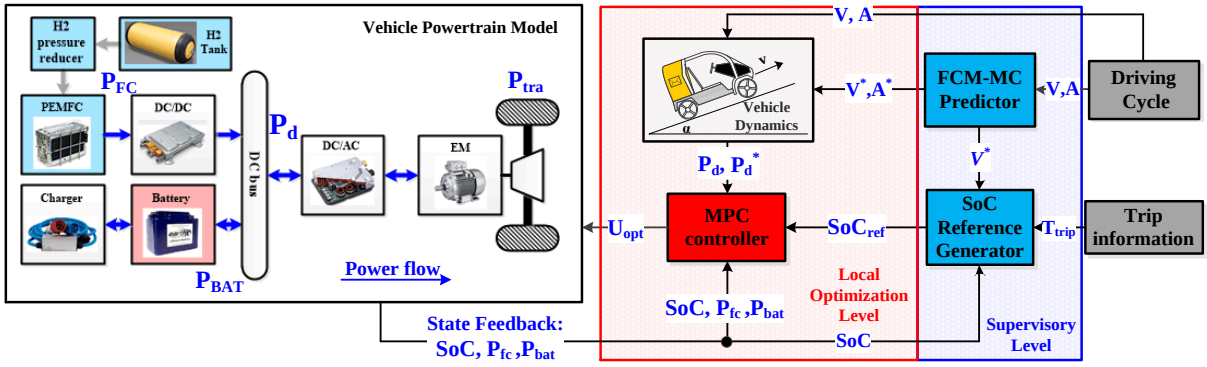


Figure 4.20. Schematic diagram of the proposed PEMS.

### 4.5.1. Energy distribution using model predictive control

This subsection presents the formulation of model predictive control for real-time power allocation.

#### 4.5.1.1. Control-oriented model formulation

Considering the limited resources of the onboard electronic control units, a linear-quadratic MPC model (with $\Delta T = 1s$) is adopted. Specifically, given the state vector $\boldsymbol{x} \in R^{2\times1}$, the manipulated variable $\boldsymbol{u} \in R^{1\times1}$, the output vector $\boldsymbol{y} \in R^{2\times1}$, the reference $\boldsymbol{r} \in R^{2\times1}$ and the disturbance $\boldsymbol{w} \in R^{1\times1}$ of the studied system, the control-oriented model can be defined by Eq. (4.32) and Eq. (4.33)

$$\begin{aligned} &x(k+1) = A(k)x(k) + B_u(k)u(k) + B_w w(k) \quad (a) \\ &y(k) = Cx(k) \quad (b) \end{aligned} \tag{4.32}$$

$$\text{with} \begin{cases} x(k) &= [SoC(k)\ P_{FC}(k-1)]^T \\ u(k) &= \Delta P_{FC}(k) = \frac{P_{FC}(k)-P_{FC}(k-1)}{\Delta T} \\ y(k) &= [SoC(k)\ P_{FC}(k-1)]^T \\ w(k) &= P_d(k) \end{cases} \tag{4.33}$$

Besides, the reference vector $r(k) = [SoC_{ref}\ P_{fc_{ref}}]^T$ includes the reference values for SoC and fuel cell power. Moreover, combine Eq. (4.32) and Eq. (4.33) with the first-order differential approximation of SoC dynamics Eq. (4.20) and the DC power balance relationship Eq. (4.21), the studied system matrices can be given as:

$$\begin{aligned} &A(k) = \begin{bmatrix} 1 & \frac{\Delta T\cdot\eta_{DC/DC}\cdot\eta_{BAT}}{U_d(k)\cdot Q_{BAT}} \\ 0 & 1 \end{bmatrix} \quad B_u(k) = \begin{bmatrix} \frac{\Delta T\cdot\eta_{DC/DC}\cdot\eta_{BAT}}{U_d(k)\cdot Q_{BAT}} & 1 \end{bmatrix}^T \\ &B_w(k) = \begin{bmatrix} -\frac{\Delta T\cdot\eta_{DC/DC}\cdot\eta_{BAT}}{U_d(k)\cdot Q_{BAT}} & 0 \end{bmatrix}^T \quad C = \begin{bmatrix} 1 & 0 \\ 0 & 1 \end{bmatrix} \end{aligned} \tag{4.34}$$

#### 4.5.1.2. Formulation of multi-criteria objective function and constraints

Fuel efficiency and FCS durability are two major optimization objectives. In parallel, MPC should be able to track the battery SoC reference. Besides, the identical lengths for both MPC control and preview horizon are adopted. Hence, within the $k^{th}$ rolling optimization horizon, the desirable control sequence $U^*(k) = \left[u_1^*(k), \dots, u_{H_p}^*(k)\right]$ is derived via minimizing Eq. (4.35) with regard to Eq. (4.36). In this case study, the fuel cell reference working point $P_{ref}$ is extracted based on the historical data in real world driving conditions, thus ensuring a more accurate reference extraction, which is also the major difference between the cost functions Eq. (4.35) and Eq. (4.29).

$$J(k) = \sum_{i=1}^{H_p} \left[ \omega_1 \cdot \underbrace{\left( \frac{P_{FC}(k+i-1) - P_{ref}}{P_{FC}^{max}} \right)^2}_{C_1} + \omega_2 \cdot \underbrace{\left( \frac{\Delta P_{FC}(k+i-1)}{\Delta P_{FC}^{max}} \right)^2}_{C_2} \right] + \omega_3 \cdot \underbrace{\left( \frac{SoC(k+H_p) - SoC_{ref}}{SoC_{max} - SoC_{min}} \right)^2}_{C_3} \tag{4.35}$$

$$\begin{cases} \underline{SoC} \le SoC(k+i) \le \overline{SoC} & \text{(a)} \\ \underline{P_{FC}} \le P_{FC}(k+i-1) \le \overline{P_{FC}} & \text{(b)} \\ \underline{\Delta P_{FC}} \le \Delta P_{FC}(k+i-1) \le \overline{\Delta P_{FC}} & \text{(c)} \\ \underline{P_{BAT}} \le P_{BAT}(k+i) \le \overline{P_{BAT}} & \text{(d)} \\ w(k+i) = P_d^*(k+i), i \ge 1 & \text{(e)} \end{cases} \tag{4.36}$$

where $P_{FC}^{max} = 1200\ W$, $\Delta P_{FC}^{max} = 40\ W/s$, $SoC_{max} = 0.9$, $SoC_{min} = 0.3$. Three constant penalty coefficients $\omega_1, \omega_2, \omega_3$ are adjusted manually with the help of the global optimal control effects extracted by DP, as introduced in subsection 4.3.1.3. As a result, $\omega_1, \omega_2, \omega_3$ are respectively set to 1, 30 and 80000 in this study. In addition, the functions of $C_1, C_2, C_3$ are given as follows:

- $C_1$ enforces FC operating towards the preset reference point. Please note that the selection of fuel cell reference working point $P_{ref}$ is achieved using the historical data in real world, where the selection of $P_{ref}$ will be introduced in the following part.
- $C_2$ enables a punishment on the large FC power spikes to decelerate the FCS performance degradations owing to frequent load changes.
- $C_3$ is adopted to narrow the discrepancy between the actual and reference SoC, where $SoC_{ref}$ is provided by the SoC reference generator, namely $SoC_{ref} = SoC_{ref}^*(k + H_p)$. By setting $C_3$ as a terminal cost term, there will be additional room for MPC controller to suppress the FC power spikes owing to speed mis-predictions.

Considering the battery operation safety, constraint (4.36a) defines the permissible SoC variation range, where $\underline{SoC} = 0.25$, $\overline{SoC} = 0.95$. If SoC > 0.9 or SoC < 0.3, $\omega_1, \omega_2$ are set to zero so that the cost term $C_3$ could force SoC back to the normal operation range [0.3, 0.9]. Moreover, due to the physical limitations, (4.36b)-(4.36d) specify the operating boundaries for both energy sources, where $\underline{P_{FC}} = 0$ W, $\overline{P_{FC}} = 1.2$ kW, $\underline{\Delta P_{FC}} = -\overline{\Delta P_{FC}} = 40$ W/s, $\underline{P_{BAT}} = -10$ kW, $\overline{P_{BAT}} = 30$ kW. Constraint (4.36e)

specifies the $k^{th}$ disturbance sequence as $\left[P_d^*(k+1), \ldots, P_d^*(k+H_p)\right]$. Due to the use of quadratic performance index Eq. (4.35), such a quadratic optimization problem can be solved by ***quadprog*** function embedded in the MATLAB optimization Toolbox.

### 4.5.2. Evaluation on predictive energy management strategy

Combined with the FCM-MC predictor and the adaptive SoC reference generator, the functionality and real-time suitability of the MPC-based PEMS is comprehensively verified in this subsection.

#### 4.5.2.1. Selection of fuel cell reference working point

To improve the overall FCS working efficiency, the fuel cell reference working point $P_{ref}$ should be carefully pre-determined. Due to the availability of the historical driving data in real world driving scenarios, the extraction of $P_{ref}$ can be realized using the GPS-collected driving database. To cover the vehicles' daily driving conditions, the speed profiles of 12 mail delivery tasks (which are shown in figure 3.13 of subsection 3.2.4.3) are used for $P_{ref}$ extraction. As a powerful technique in search for the global optima, DP is leveraged to extract the fuel cell working points, with the global optimization problem formulated as to minimize the hydrogen consumption while respecting the constraints given in Eq. (4.37).

$$\begin{cases} 0.3 \le SoC(k) \le 0.9 & (a) \\ 0 \le P_{FC}(k) \le 1200\ W & (b) \\ -40\ W/s \le \Delta P_{FC}(k) \le 40\ W/s & (c) \\ -10\ kW \le P_{BAT}(k) \le 30kW & (d) \\ SoC_0 = 0.45, P_{FC_0} = 0\ W & (e) \\ SoC_N = 0.3 & (f) \end{cases} \tag{4.37}$$

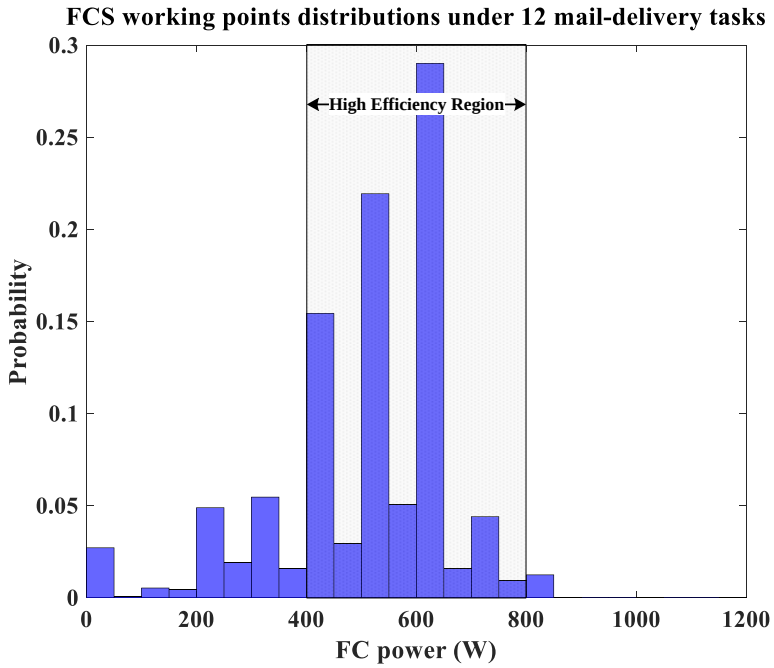


Figure 4.21. The $P_{FC}$ distribution under 12 mail-delivery tasks.

To emphasize the function of FCS as a range extender, $SoC_0$ is set as 0.45 to simulate the situations

when battery is not fully charged. Please note that the fuel cell reference working points under other $SoC_0$ settings can be extracted in the same way. Figure 4.21 depicts the FCS power distribution under 12 mail-delivery missions. Consequently, the median value is selected as the reference FC power for online application, namely $P_{ref} = 550$ W.

#### 4.5.2.2. Analysis of the impacts on EMS performance by different parameters

To explore the potential impacts on EMS performance brought by several parameters (e.g. the SoC reference adjusting boundary $k_\alpha$ and the length of prediction horizon $H_p$ etc.), a postal delivery mission profile is used as the testing cycle, as shown in figure 4.22(a).

- **Battery SoC regulation performance with different $k_\alpha$**

As mentioned in subsection 3.3.2, $\alpha(k) = \frac{k_\alpha}{1+\frac{v_{std}(k)}{v_{ave}(k)}}$ is the adjusting factor of SoC depleting rate, which can help adjust battery energy depleting rates in different driving scenarios. The constant positive numerator $k_\alpha$ defines the upper boundary of $\alpha$. A proper setting on $k_\alpha$ could help fully utilize the onboard electricity, whereas an overlarge $k_\alpha$ would deplete battery energy too fast, leading to the extension of vehicle's charge-sustaining driving mileage.

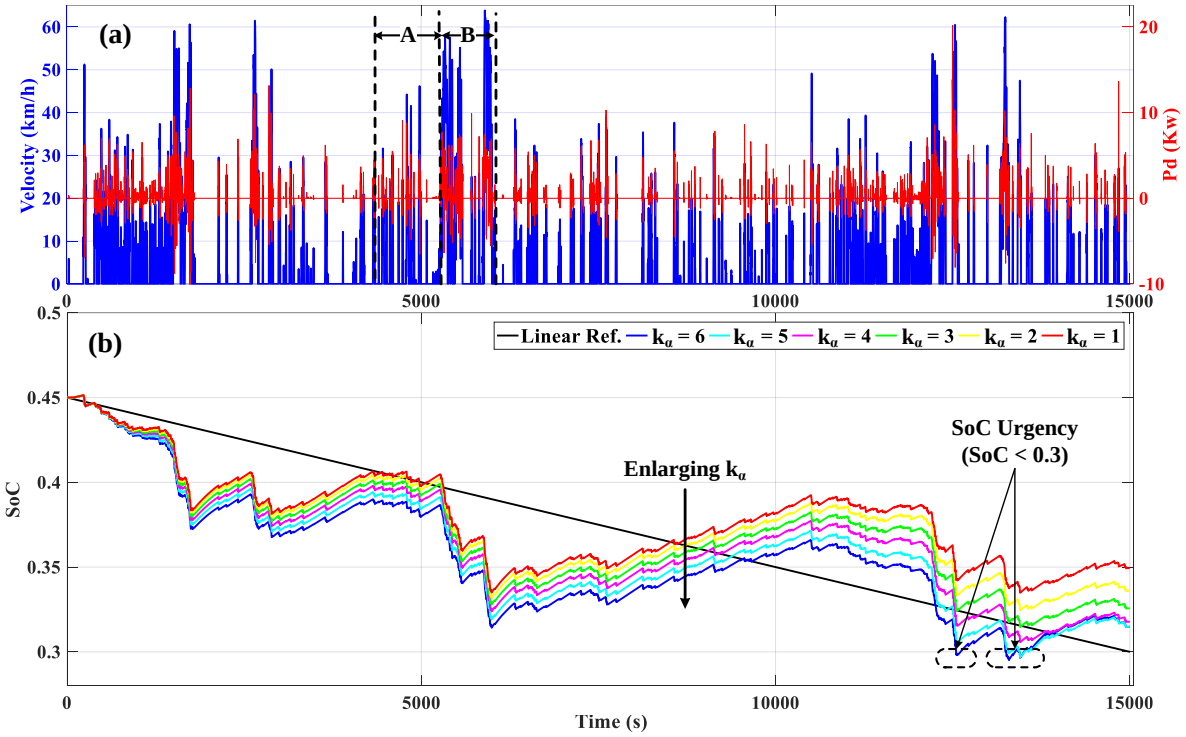


Figure 4.22. EMS performance comparison against various impact factors. (a) The speed (blue) and power demand profiles (red) of the used testing cycle. (b) SoC trajectories with different $k_\alpha$ ($H_p = 5$).

With $H_p = 5$ and different $k_\alpha$ candidates (1 to 6), the proposed MPC-based EMS is verified on the testing cycle and the corresponding battery SoC profiles are depicted in figure 4.22(b). Among

$k_\alpha$ candidates, a larger $k_\alpha$ would accelerate the overall battery energy depletion rate, making the terminal battery SoC closer to the threshold (0.3). However, using an overlarge $k_\alpha$ (e.g. $k_\alpha = 5$ or 6) would lead to the occurrence of SoC urgency event (SoC < 0.3) before the end of the trip, resulting in the prolonged CS driving phase. To tradeoff between the battery energy utilization rate and the battery operation safety, $k_\alpha$ is set to four in this subsection.

- **Comparison between adaptive SoC reference and linear SoC reference**

To compare the SoC regulation performance between the adaptive SoC reference Eq. (3.18) and the linear SoC reference Eq. (3.17), the MPC-based EMS (with $k_\alpha = 4$ and different $H_p$ (3s, 5s and 10s)) is performed on the testing cycle, where the related SoC profiles are shown in figure 4.22(c). Specifically, increasing $H_p$ makes the final SoC closer to the target value (0.3), indicating a deeper battery discharge. Moreover, the linear SoC reference leads to a constant energy depletion rate along the entire cycle. In contrast, the adaptive SoC reference model can regulate the actual SoC depleting rates regarding changeable driving conditions. For example, a lower SoC depleting rate appears under the congested driving conditions (e.g. phase A), while a higher SoC depleting rate occurs during the flowing driving conditions (e.g. phase B). Consequently, the adaptive SoC reference generator enables a flexible battery energy usage towards various power requirements, thus improving the rationality in energy allocation against the linear SoC reference.

- **Comparison between adaptive SoC reference and linear SoC reference**

Figure 4.22(d) and (e) depict the FCS power profiles when tracking the adaptive SoC reference and the linear SoC reference, respectively. When tracking the adaptive SoC reference, increasing $H_p$ would decrease the average of FC power, which is beneficial to reduce the H2 consumption. However, the FCS would work more actively in this case, leading to larger power transients. In contrast, as shown in figure 4.22(e), extremely large FC power spikes and frequent start-stop cycles occur when tracking the linear SoC reference, which would greatly shorten the lifespan of FCS. Additionally, as highlighted in the dashed regions in figure 4.22(c) and (d), when $H_p$ =10 and SoC < 0.3, the SoC emergency mode is activated, where the FCS is working towards its maximum power point (1.2kW) to help SoC back to the safe operation range [0.3, 0.9].

- **Determination of prediction horizon**

Guided by the adaptive battery SoC reference Eq. (3.17), TABLE 4.8 summarizes the EMS performance discrepancies under different $H_p$. Specifically, enlarging $H_p$ could increase $m_{H_2,equ}$ but lead to a deeper battery discharge. Meanwhile, the average FC power transients ($\overline{|\Delta P_{fc}|}$) and the computation time per step ($T_{step}$) would also be increased through a larger $H_p$. Therefore, $H_p$ = 5 is a reasonable choice to tradeoff among the fuel economy, the FC power transients and the computation efficiency.

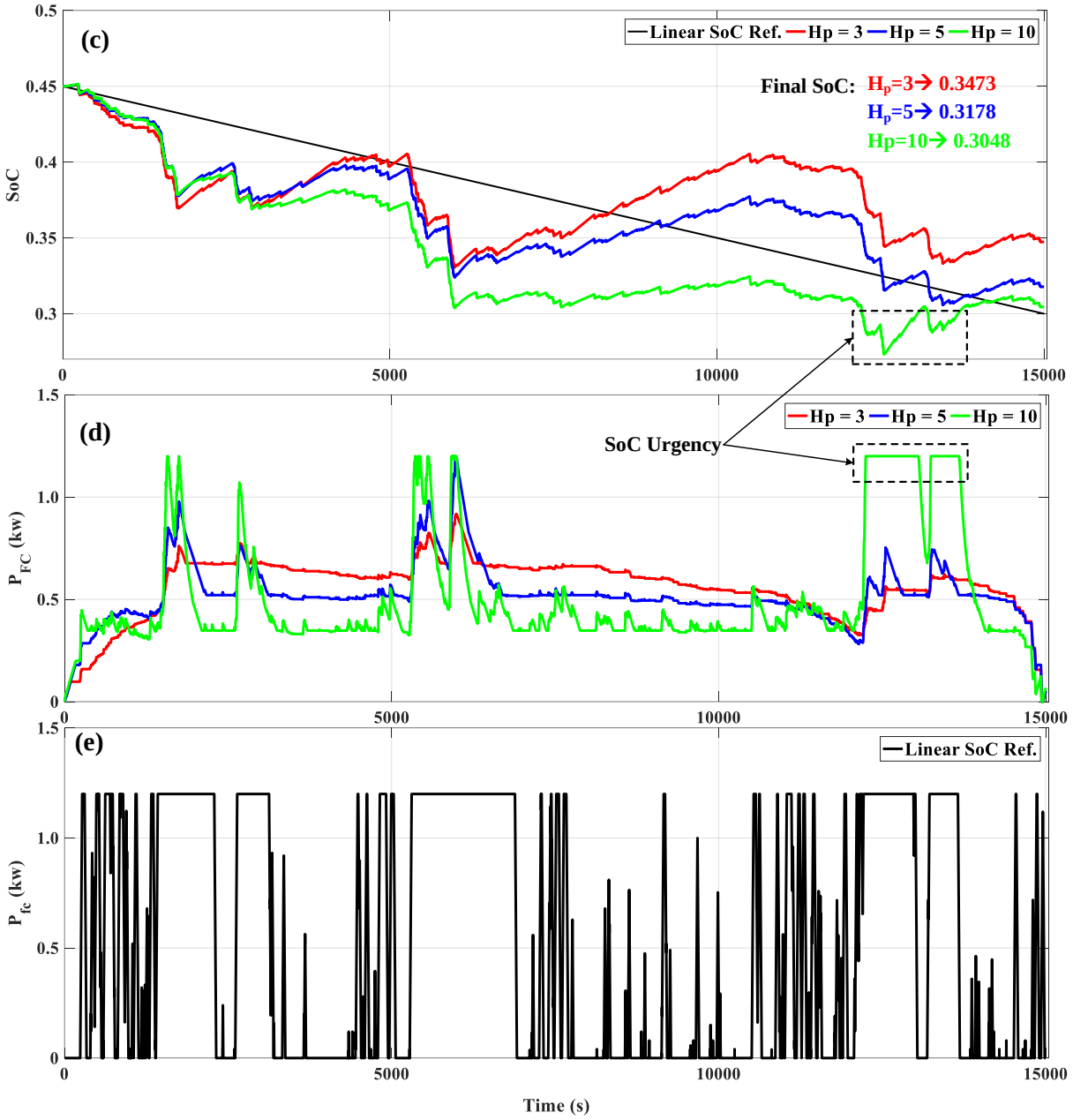


Figure 4.22 (continued). EMS performance comparison against various impact factors. (c) SoC trajectories with different $H_p$ ($k_\alpha = 4$). (d) FC power profiles with the proposed adaptive SoC reference. (e) FC power profile with linear SoC reference.

TABLE 4.8. MPC-based EMS performance under testing cycle with different $H_p$.

| Hp (s) | $m_{H_2}$(g) | $m_{H_2.equ}$(g) | $SoC_N$ | $\overline{\lvert\Delta P_{FC}\rvert}$ (W/s) | $T_{step}$ (ms) |
|---|---|---|---|---|---|
| **3** | 99.4 | 87.2 | 0.3473 | 0.6 | 15.38 |
| **5** | 92.5 | 87.9 | 0.3178 | 1.0 | 16.73 |
| **10** | 90.2 | 89.0 | 0.3048 | 1.8 | 22.04 |

### 4.5.2.3. Comparison with benchmark energy management strategies

To further verify the performance of the integrated PEMS, two benchmark EMSs are introduced. As the

upper benchmark, DP extracts the optimal fuel cell power profiles based on the fully previewed trip information, as formulated by Eq. (4.37). In contrast, the MPC controller with the linear SoC reference is regarded as the lower benchmark, marked as "L-MPC". Besides, the proposed EMS with the adaptive SoC reference is marked as "A-MPC". For both MPC-based strategies, $H_p = 5$ and $k_\alpha = 4$.

- **Evaluation results with respect to benchmark strategies**

Five another GPS-collected speed profiles for mail-delivery are employed for validating the EMSs, where the related comparison results under two mission profiles are detailed in figure 4.23.

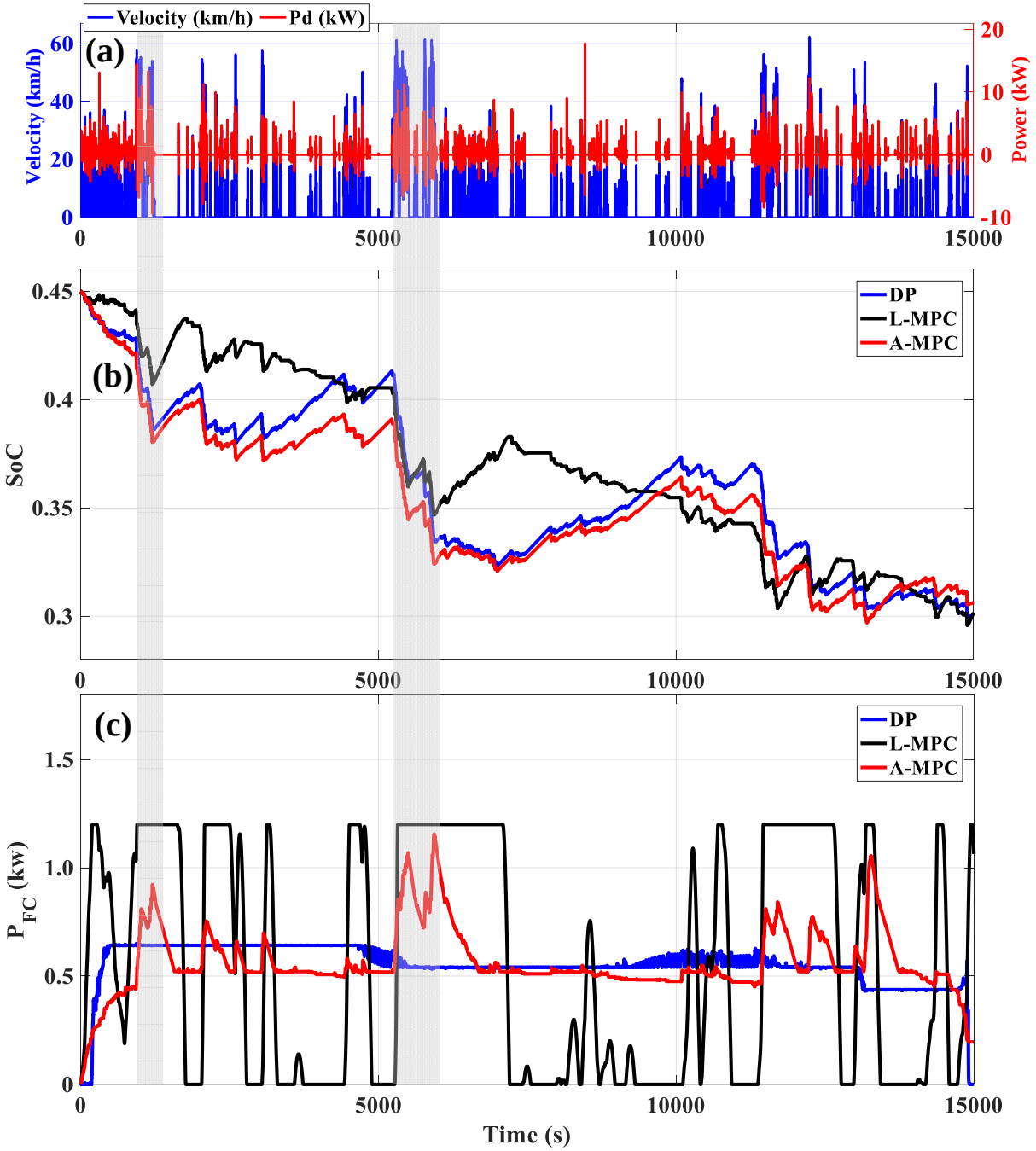


Figure 4.23. EMS performance comparison with benchmark strategies. (a) Speed (red) and power demand (blue) profiles of testing cycle I; (b) SoC profiles of different EMSs; (c) fuel cell power profiles of different EMSs.

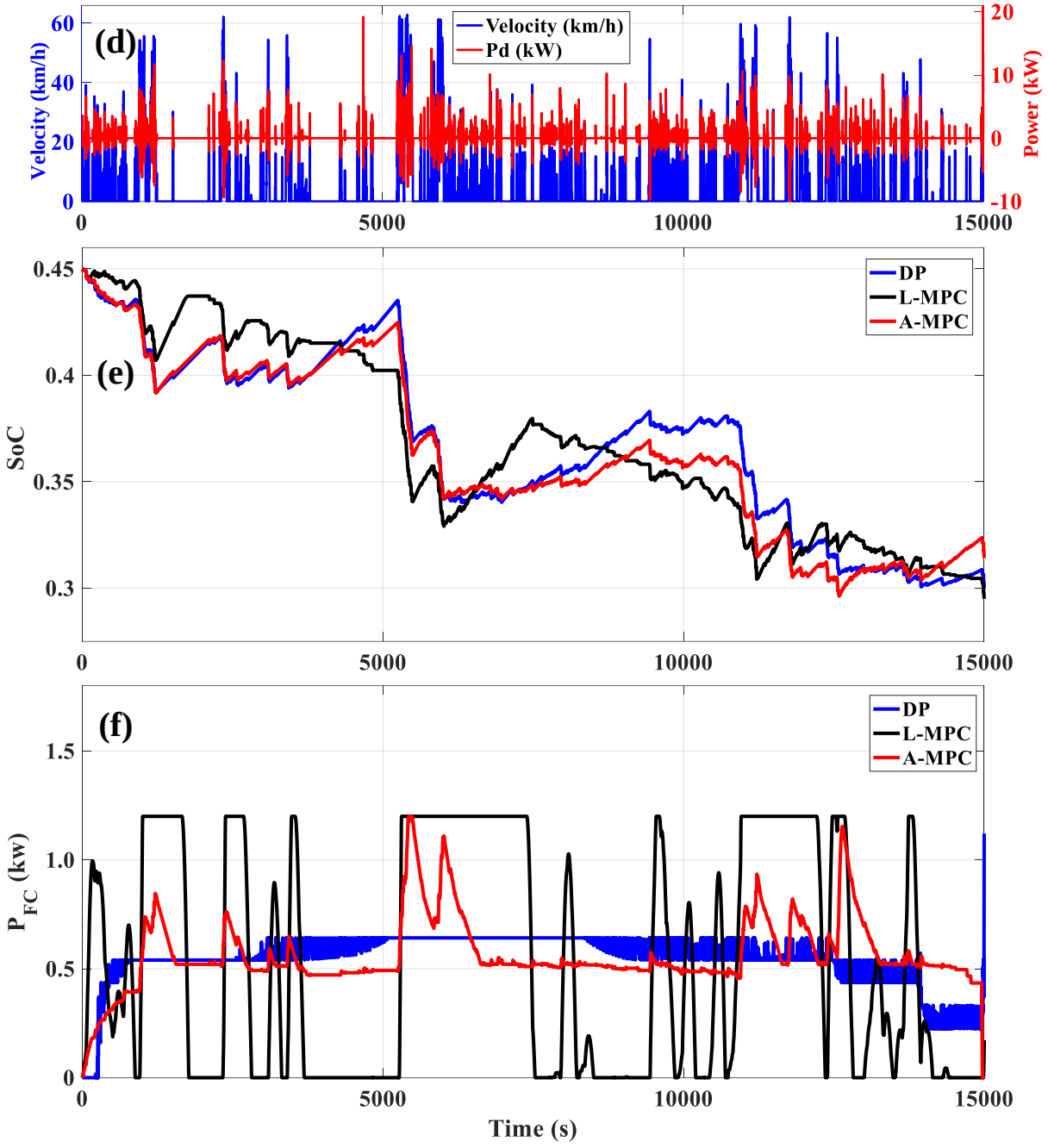


Figure 4.23 (continued). EMS performance comparison with benchmark strategies. (d) Speed (red) and power demand (blue) profiles of testing cycle II; (e) SoC profiles of different EMSs; (f) fuel cell power profiles of different EMSs.

As shown in figure 4.23(b) and (e), under both testing cycles, A-MPC strategy can effectively regulate the SoC depleting rate against the changeable driving conditions, where its SoC profiles are close to the DP-based ones. Besides, given the linear SoC reference, L-MPC strategy tends to maintain the constant SoC depleting rate along the driving cycle. However, due to the maximum FC power limits, the SoC profiles of L-MPC deviate from the linear reference in some peaking power regions (marked with the grey shadow). Moreover, as depicted in figure 4.23(c) and (f), benefiting from the fully previewed trip

information, DP manipulates the output of FCS with the fewest power transients. In contrast, L-MPC regulates the FCS power in an aggressive manner, where much larger power spikes and many start-stop cycles are observed. In contrast, A-MPC is able to smooth the FC power profiles, showing a great potential in mitigating the fuel cell degradation.

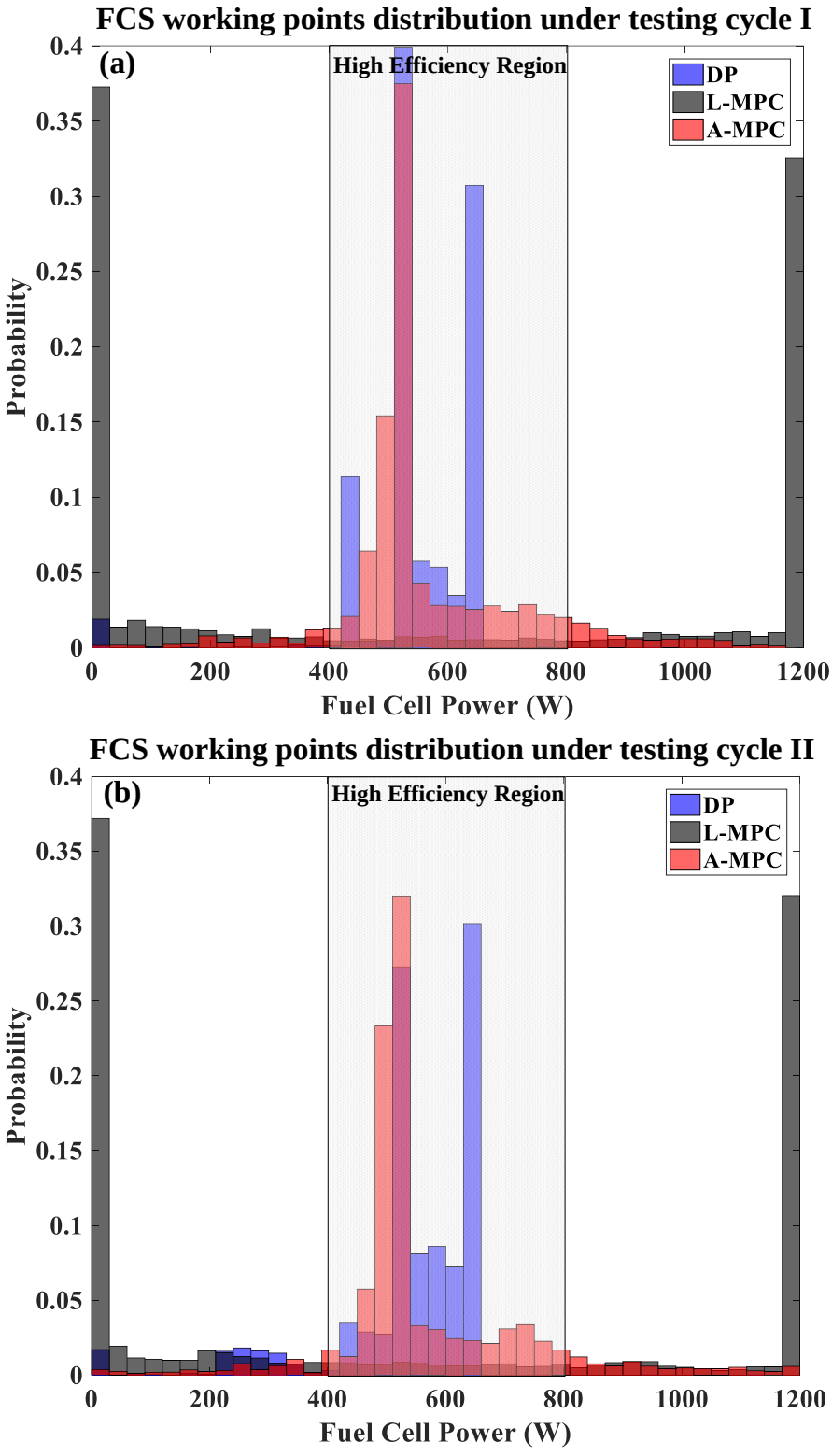


Figure 4.24. FCS working points probability distributions under two testing cycles.

Furthermore, figure 4.24 depicts the FC working point distributions. Specifically, 97.54% (testing cycle I) and 90.66% (testing cycle II) of FC working points for DP are located in the high efficiency region, while this ratio for L-MPC are respectively 7.51% and 9.12%. In contrast, A-MPC can improve this ratio to 86.39% (testing cycle I) and 85.56% (testing cycle II). This indicates the proposed EMS can greatly enhance the FCS working efficiency compared to L-MPC strategy.

TABLE 4.9 summarizes the EMS performances under five testing cycles, where $r_{high}$ is the ratio of fuel cell operating points located in FCS's high efficiency region. Specifically, at least 70.46% FCS working points of A-MPC are distributed in the high efficiency area, where the enhanced working efficiency leads to 3.79% to 5.35% reduction of equivalent H2 consumption ($m_{H_2.equ}$) compared to the L-MPC benchmark. Besides, A-MPC can also decrease the average FC power transients ($\overline{|\Delta P_{FC}|}$) by 40.4% to 54.7% compared to L-MPC, thus enhancing the FCS's durability. Furthermore, A-MPC performs close to DP benchmark under five testing cycles, where the largest performance gap on $m_{H_2.equ}$ and $\overline{|\Delta P_{FC}|}$ are respectively 0.84% (testing cycle II) and 9.18% (testing cycle V). In addition, the online calculation time per step ($T_{step}$) for A-MPC ranges from 16.53 ms to 16.77 ms, which is sufficiently smaller than the sampling time interval (1s), making it suitable for real-time applications.

TABLE 4.9. EMS performance evaluation results under five testing cycles.

| | **Testing cycle I** | | | **Testing cycle II** | | | **Testing cycle III** | | |
|---|---|---|---|---|---|---|---|---|---|
| | **DP** | **L-MPC** | **A-MPC** | **DP** | **L-MPC** | **A-MPC** | **DP** | **L-MPC** | **A-MPC** |
| **$m_{H_2}$(g)** | 96.9 | 102.1 | **99.3** | 95.1 | 98.8 | **99.6** | 73.8 | 78.5 | **80.6** |
| **$m_{H_2,equ}$ (g)** | 96.9 | 101.7 | **97.7** | 95.1 | 100.1 | **95.9** | 73.8 | 78.5 | **74.3** |
| **$SoC_N$** | 0.3000 | 0.3016 | **0.3063** | 0.3000 | 0.2953 | **0.3142** | 0.3000 | 0.2999 | **0.3243** |
| **$\overline{\|\Delta P_{FC}\|}$ (W/s)** | 0.96 | 2.25 | **1.02** | 0.97 | 2.24 | **1.04** | 0.85 | 1.61 | **0.87** |
| **$r_{high}$** | 97.54% | 7.51% | **86.39%** | 90.66% | 9.12% | **85.56%** | 95.39% | 11.69% | **70.46%** |
| **$T_{step}$ (ms)** | --- | 16.97 | **16.63** | --- | 16.67 | **16.58** | --- | 16.75 | **16.62** |
| | **Testing cycle IV** | | | **Testing cycle IV** | | | | | |
| | **DP** | **L-MPC** | **A-MPC** | **DP** | **L-MPC** | **A-MPC** | | | |
| **$m_{H_2}$(g)** | 100.8 | 105.5 | **109.5** | 98.6 | 102.8 | **102.7** | | | |
| **$m_{H_2,equ}$ (g)** | 100.8 | 105.9 | **101.5** | 98.6 | 103.0 | **99.1** | | | |
| **$SoC_N$** | 0.3000 | 0.2983 | **0.3308** | 0.3000 | 0.2993 | **0.3139** | | | |
| **$\overline{\|\Delta P_{FC}\|}$ (W/s)** | 0.98 | 1.71 | **1.02** | 0.98 | 2.33 | **1.07** | | | |
| **$r_{high}$** | 79.75% | 6.65% | **78.87%** | 89.09% | 11.13% | **83.33%** | | | |
| **$T_{step}$ (ms)** | --- | 16.69 | **16.77** | --- | 16.75 | **16.53** | | | |

- **Sensitivity analysis under trip duration estimation errors**

As indicated in subsection 3.3.2, the reference SoC depleting rate $r_{soc}(k) = \frac{SoC(k)-SoC_{final}}{T_{trip}-k}$ is defined by the ratio of the remaining useful SoC ($SoC(k) - SoC_{final}$) and the estimated remaining trip duration ($T_{trip} - k$). To calculate $r_{soc}(k)$, it is assumed that the trip duration $T_{trip}$ can be estimated before

departure with the help of the modern telematics systems (e.g. GPS, ITS). To explore the impacts on EMS performance by $T_{trip}$ estimation errors, under ± 30% $T_{trip}$ estimation errors, the integrated PEMS is evaluated under testing cycle I and II, with the numerical results given in TABLE 4.10. Note $r_{high}$ is the percentage of fuel cell operating points located in the high efficiency area of fuel cell system. Specifically, the trip duration errors would bring different impacts on following performance metrics:

TABLE 4.10. EMS performance under -30% to 30% trip duration errors.

| Testing cycle I | | | | | | Testing cycle II | | | | | |
|---|---|---|---|---|---|---|---|---|---|---|---|
| **Error** | **$m_{H_2}$ (g)** | **$m_{H_2,equ}$ (g)** | **$SoC_N$** | **$\overline{\lvert\Delta P_{FC}\rvert}$ (W/s)** | **$r_{high}$** | **Error** | **$m_{H_2}$ (g)** | **$m_{H_2,equ}$ (g)** | **$SoC_N$** | **$\overline{\lvert\Delta P_{FC}\rvert}$ (W/s)** | **$r_{high}$** |
| -30% | 99.4 | 99.0 | 0.3015 | 1.35 | 53.69% | -30% | 96.4 | 97.5 | 0.2958 | 1.34 | 54.50% |
| -20% | 98.9 | 98.5 | 0.3013 | 1.48 | 63.05% | -20% | 95.9 | 97.0 | 0.2960 | 1.57 | 62.96% |
| -10% | 98.4 | 98.2 | 0.3010 | 1.32 | 77.93% | -10% | 95.3 | 96.7 | 0.2947 | 1.24 | 73.92% |
| 0% | 99.3 | 97.7 | 0.3063 | 1.02 | 86.39% | 0% | 99.6 | 95.9 | 0.3142 | 1.04 | 85.55% |
| 10% | 99.8 | 97.6 | 0.3086 | 0.98 | 86.90% | 10% | 99.9 | 95.9 | 0.3129 | 0.97 | 86.49% |
| 20% | 100.6 | 97.6 | 0.3102 | 0.98 | 86.60% | 20% | 100.0 | 95.8 | 0.3164 | 0.98 | 86.22% |
| 30% | 101.1 | 97.6 | 0.3143 | 0.98 | 86.50% | 30% | 100.6 | 95.8 | 0.3185 | 0.98 | 87.86% |

- **Fuel economy**

If positive errors are applied when planning battery energy usage, the actual SoC depleting rate would be reduced by the enlarged $T_{trip}$, leading to the larger $SoC_N$ under both testing cycles. In this case, larger portion of power demand would be supplied by the FCS, thus increasing the amount of actual H2 consumption ($m_{H_2}$). Besides, $r_{high}$ remains almost the same under positive errors, indicating the relatively stable FCS working efficiency. Therefore, compared to the zero-error working conditions, the discrepancies on the equivalent H2 consumption ($m_{H_2,equ}$) are insignificant. In contrast, negative trip duration estimation errors would accelerate the SoC depletion, making the electricity energy fully depleted before the trip end, resulting in the smaller $SoC_N$. However, the prolonged CS driving phases would greatly reduce the average FCS working efficiency and thus increase the amount of equivalent H2 consumption. Overall, in face of $\pm$ 30% trip duration estimation errors, the proposed EMS (A-MPC) can still save over 2.65% (testing cycle I) and 1.32% (testing cycle II) $m_{H_2,equ}$ than the L-MPC strategy.

- **FCS durability**

When positive trip duration estimation errors appear, $\overline{|\Delta P_{FC}|}$ slightly decreases compared to the zero-error conditions. This is because the enlarged $T_{trip}$ would shorten or eliminate the CS driving phases, making FCS working more stably, thus reducing the average power transients. In contrast, the extended CS driving phases caused by the negative errors require FCS working more actively to cope with the occurrence of SoC urgency events, thus increasing the fuel cell power transients. As a result, compared to the L-MPC strategy, over 34.22% (testing cycle I) and 29.91% (testing cycle II) decrement on the $\overline{|\Delta P_{FC}|}$ can be achieved by the A-MPC strategy even with $\pm$ 30% trip duration estimation errors.

In summary, the proposed integrated PEMS (A-MPC) can effectively bring down the vehicle's operation costs via saving H2 consumption (by at least 3.79%) and limiting the FC power spikes (by at least 40.4%) in contrast to the benchmark L-MPC strategy, implying the improved fuel economy and FCS durability. Additionally, the proposed EMS performs close to upper benchmark (DP), where the largest optimality gaps are respectively 0.84% (fuel economy) and 9.18% (fuel cell power transients). Moreover, it is verified that the proposed strategy is robust to certain level of trip duration estimation errors, which is favorable for its real applications.

## 4.6. Vehicle's operating cost analysis under different sizing configurations

Combined with driving prediction techniques, several predictive energy management strategies (PEMS) are presented in previous subsections. However, it should be mentioned that the powertrain design of a fuel cell hybrid electric vehicle (FCHEV) would also generate profound impacts on the vehicle's drivability and economic performance. Specifically, the mutual affecting mechanism between vehicle sizing and control strategy design is currently one of important topics in the literature, thus deserving substantial attention when devising PEMSs for FCHEVs.

Therefore, this subsection intends to present a supplementary discussion regarding the operating costs of a fuel cell/battery-based PHEV under different sizing configurations. Specifically, the size of fuel cell system is kept as constant while the capacity of battery is altering. Dynamic programming (DP) is then adopted to extract the vehicle's operational cost induced by the consumption of hydrogen fuel and electricity power. Afterwards, a numerical analysis of the impacts on fuel economy, fuel cell durability, battery energy utilization rate is conducted, so as to provide useful guidelines to facilitate the powertrain design and the development of corresponding EMSs.

Please note this subsection focuses on a midsize sedan model with plug-in property (see TABLE 4.1), and the baseline powertrain sizing configuration is composed of a 30kW FCS and a 6.4 kWh battery.

### 4.6.1. Vehicular operation cost extraction

This subsection presents the way of extracting the vehicle's operating cost via dynamic programming.

#### 4.6.1.1. Vehicle operational cost definition

Under the powertrain topology shown in figure 4.1(c), since both FCS and battery can directly propel the vehicle, the total operating cost ($C_{Total}$) comprises two parts: the cost owing to hydrogen fuel consumption ($C_{H_2}$) and the cost owing to electricity consumption ($C_{elec}$), as given by Eq. (4.38). The unit for the cost term is in USD.

$$\begin{aligned} C_{Total} &= C_{H_2} + C_{elec} \\ &= p_{H_2} \cdot M_{H_2} + p_{elec} \cdot E_{elec} \end{aligned} \tag{4.38}$$

where $p_{H_2}$ denotes the H2 price, $p_{elec}$ the electricity price. Moreover, $M_{H_2}$ is the H2 mass consumption (in kg) over a trip, and $E_{elec}$ the electricity power consumption (in kWh), which can be calculated by Eq. (4.39) and Eq. (4.40), respectively, where $\bar{\eta}_B$ is the average battery working efficiency.

$$M_{H_2} = \frac{1}{1000}\int_{t=0}^{N} \frac{P_{FC}(t)}{\eta_{FCS}(P_{FC})\cdot LHV}\,dt \tag{4.39}$$

$$E_{elec} = \frac{1}{3600\cdot 1000}\int_{t=0}^{N} \frac{P_B(t)}{\bar{\eta}_B}\,dt \tag{4.40}$$

To explore whether the geographical locations would generate essential impacts on vehicle's operating costs, this paper uses two sets of $p_{H_2}$ and $p_{elec}$ from China and Europe for evaluation. In China, as indicated in [18], the electricity price for EVs is about 1 yuan/kWh (0.14 USD/kWh) and the hydrogen price is 40 yuan/kg (5.68 USD/kg). Moreover, in Europe, as reported in [19], the hydrogen fuel cost for FC-based passenger vehicles is around 10 to 12 USD per kilogram at the pump, while the average electricity price (e.g. in France) is around 0.15 Euro/kWh (0.16 USD/kWh). Based on these figures, the parameters for operation cost evaluation are summarized in TABLE 4.11.

TABLE 4.11. Parameters for calculating vehicle's operation cost.

| Region | Parameter | Value | Unit | Data source |
|---|---|---|---|---|
| **China** | $\mathbf{P_{H_2}}$ | 5.68 | USD/kg | [18] |
| | $\mathbf{P_{elec}}$ | 0.14 | USD/kWh | |
| **Europe** | $\mathbf{P_{H_2}}$ | 11.00 | USD/kg | [19] |
| | $\mathbf{P_{elec}}$ | 0.16 | USD/kWh | |
| **LHV** | | 120000 | J/g | [10] |
| $\bar{\eta}_B$ | | 0.9 | N/A | Assumption |

#### 4.6.1.2. Dynamic programming

To avoid the impacts on vehicle's economic performance imposed by different control strategies, DP is adopted to find the optimal operation cost under each sizing configuration. Specifically, the global optimization problem is formulated as follows:

$$\begin{aligned} &\min_{\Delta P_{FC}\in\mu_{FC}} \sum_{k=0}^{N-1}\left[p_{H_2}\cdot \dot{M}_{H_2}(k) + p_{elec}\cdot \dot{E}_{elec}(k)\right]\cdot \Delta T \\ &\text{with} \quad \dot{M}_{H_2}(k) = \frac{1}{1000}\cdot\frac{P_{FC}(k)}{\eta_{FCS}(P_{FC})\cdot LHV} \\ &\qquad\quad \dot{E}_{elec}(k) = \frac{1}{3600\cdot 1000}\cdot\frac{P_B(k)}{\bar{\eta}_B} \end{aligned} \tag{4.41}$$

Subject to

$$\begin{cases} 0.3 \le SoC(k) \le 1.0 & (a) \\ 0 \le P_{FC}(k) \le 30\ kW & (b) \\ -1\ kW/s \le \Delta P_{FC}(k) \le 1\ kW/s & (c) \\ -25\ kW \le P_{BAT}(k) \le 50\ kW & (d) \\ SoC_0 = SoC_{ini}, P_{FC\_0} = 0\ W & (e) \\ SoC_N = 0.3 & (f) \end{cases} \tag{4.42}$$

where $\Delta P_{FC}$ is selected as the control variable in DP problem. $\mu_{FC}$ is the discretized feasible domain for $\Delta P_{FC}$, with the grid resolution of 1 W/s. Constraints (4.42a)-(4.42d) respectively specify the operation boundaries for SoC, $P_{FC}$, $\Delta P_{FC}$ and $P_{BAT}$. Besides, (4.42e) indicates the initial states of battery SoC and FC power. Different depth of discharge ($DOD = SoC_0 - SoC_N$) can be realized via altering $SoC_{ini}$. Constraint (4.42f) ensures the final SoC ($SoC_N$) reaching the predefined threshold 0.3 to guarantee the full utilization of battery energy. To approximate daily driving scenarios, a combined testing cycle is established using different standard driving cycles from ADVISOR [1], including urban, suburban and highway driving patterns, as depicted in figure 4.25.

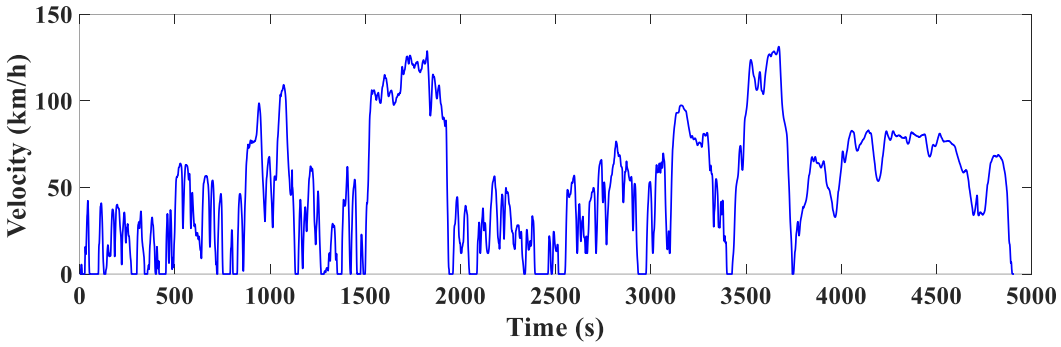


Figure 4.25. Speed profile of the multi-pattern testing cycle (68.5 km).

### 4.6.2. Vehicle's operation costs under different sizing configurations

A quantitative evaluation on the vehicle's operating costs under different sizes of battery capacity, initial SoC value and driving distance is conducted in subsection 4.6.2.

#### 4.6.2.1. Operation cost analysis under different battery capacity and initial SoC

Based on the 30 kW FCS and the battery with different nominal energy capacities ($E_B =$ 1.0 kWh to 15.0 kWh), a quantitative evaluation regarding the vehicle's operation costs under multiple $SoC_{ini}$ candidates is conducted in this subsection, where $SoC_{ini} = [0.3, 0.4, \ldots, 1.0]$. TABLE 4.12 and 4.13 respectively summarize the related costs under Chinese and European cases when $SoC_{ini} = 1.0$ and 0.4, so as to respectively simulate a fully charged battery and a non-fully-charged one.

In TABLE 4.12, when $SoC_{ini} = 1.0$, if $E_B \geq 12.8$ kWh, the energy stored in the battery pack is sufficient to cover the energy required by the entire driving cycle, where, of course, the operation cost mainly comes from the electricity consumption. In this case, although no FC power is delivered to propel the vehicle, there still exists H2 consumption cost (0.36 USD). This is because an "always-on" strategy is adopted to limit the times of FCS on-off cycles for better system durability, and thus a minimal H2 flow rate is needed to supply the compressor and other auxiliaries, with this operational state termed as fuel cell "idle" [20]. If $E_B$ becomes smaller than 12.8 kWh, the FCS gradually becomes the primary energy source for vehicle propulsion, leading to the higher amount of H2 consumption. Consequently,

$C_{H_2}$ enlarges up to 7.44 times (from 0.36 USD to 3.04 USD), while $C_{Total}$ enlarges up to 84.21% (from 1.71 USD to 3.15 USD). The significant cost increment is due to hydrogen fuel is much expensive than electricity power.

If the battery pack is not fully charged at the trip beginning ($SoC_{ini}$ = 0.4), the amount of energy stored in the battery is insufficient to cover the energy demand over the entire driving cycle even with the largest $E_B$. Compared to the fully charged conditions, $C_{H_2}$ shares a dominant ratio in total cost (over 90%), which leads to a higher $C_{total}$ under the same size of battery capacity. Such cost increment becomes significant especially when a large battery capacity is used (e.g. $E_B \geq 6.4$ kWh), compared to fully charged conditions. With the decrement of $E_B$, $C_{H_2}$ enlarges up to 20.82% (from 2.69 USD to 3.25 USD), while $C_{Total}$ increases up to 11.64% (from 2.92 USD to 3.26 USD). In addition, similar results can also be observed under European cases, as shown in TABLE 4.13.

TABLE 4.12. Operation cost comparison with different battery capacity: Chinese case

| $E_B$ (kWh) | $SoC_{ini}$ | DoD | $C_{H_2}$ (USD) | $C_{elec}$ (USD) | $C_{Total}$ (USD) | $SoC_{ini}$ | DoD | $C_{H_2}$ (USD) | $C_{elec}$ (USD) | $C_{Total}$ (USD) |
|---|---|---|---|---|---|---|---|---|---|---|
| 15.0 | 1.0 | 0.57 | 0.36 | 1.35 | 1.71 | 0.4 | 0.10 | 2.69 | 0.23 | 2.92 |
| 12.8 | | 0.67 | 0.36 | 1.35 | 1.71 | | 0.10 | 2.77 | 0.20 | 2.97 |
| 10.0 | | 0.70 | 0.81 | 1.10 | 1.91 | | 0.10 | 2.88 | 0.15 | 3.04 |
| **6.4 (baseline)** | | 0.70 | 1.65 | 0.71 | 2.36 | | 0.10 | 3.02 | 0.10 | 3.12 |
| 5.0 | | 0.70 | 2.00 | 0.55 | 2.55 | | 0.10 | 3.08 | 0.08 | 3.16 |
| 3.2 | | 0.70 | 2.46 | 0.35 | 2.81 | | 0.10 | 3.15 | 0.05 | 3.20 |
| 1.0 | | 0.70 | 3.04 | 0.11 | 3.15 | | 0.10 | 3.25 | 0.01 | 3.26 |

TABLE 4.13. Operation cost comparison with different battery capacity: European case.

| $E_B$ (kWh) | $SoC_{ini}$ | DoD | $C_{H_2}$ (USD) | $C_{elec}$ (USD) | $C_{Total}$ (USD) | $SoC_{ini}$ | DoD | $C_{H_2}$ (USD) | $C_{elec}$ (USD) | $C_{Total}$ (USD) |
|---|---|---|---|---|---|---|---|---|---|---|
| 15.0 | 1.0 | 0.57 | 0.70 | 1.52 | 2.22 | 0.4 | 0.10 | 5.21 | 0.27 | 5.48 |
| 12.8 | | 0.67 | 0.70 | 1.52 | 2.22 | | 0.10 | 5.37 | 0.23 | 5.60 |
| 10.0 | | 0.70 | 1.56 | 1.24 | 2.81 | | 0.10 | 5.58 | 0.18 | 5.76 |
| **6.4 (baseline)** | | 0.70 | 3.19 | 0.80 | 3.99 | | 0.10 | 5.85 | 0.11 | 5.97 |
| 5.0 | | 0.70 | 3.87 | 0.62 | 4.50 | | 0.10 | 5.96 | 0.09 | 6.05 |
| 3.2 | | 0.70 | 4.75 | 0.40 | 5.15 | | 0.10 | 6.09 | 0.06 | 6.15 |
| 1.0 | | 0.70 | 5.89 | 0.12 | 6.02 | | 0.10 | 6.29 | 0.02 | 6.31 |

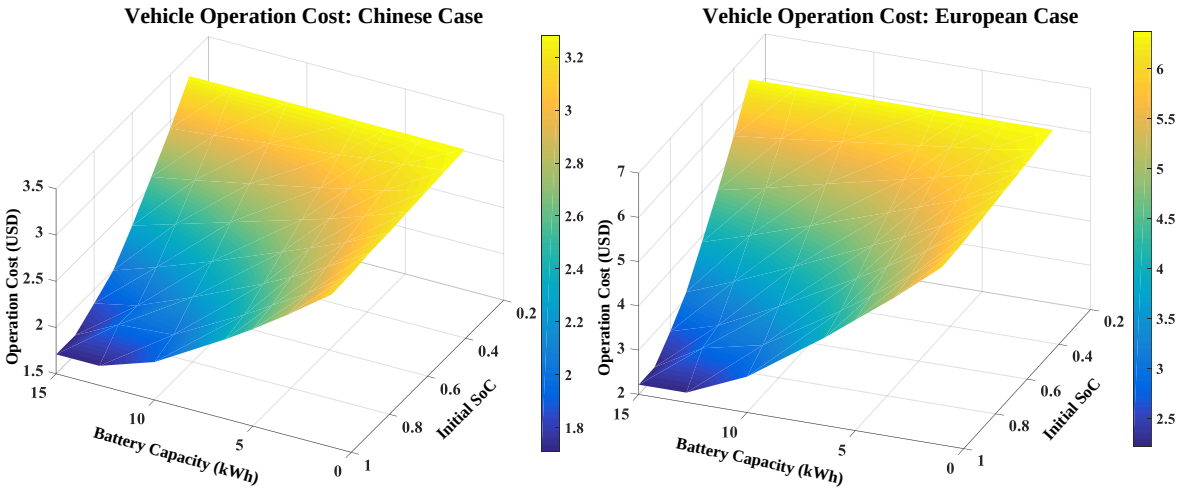


Figure 4.26. Vehicle's operational costs under Chinese and European cases.

Figure 4.26 summarizes the vehicle's operation costs ($C_{Total}$) under all $SoC_{ini}$ candidates in Chinese and European cases. In both regions, when battery has a large $E_B$ and a high $SoC_{ini}$, $C_{Total}$ becomes relatively low, since the cost-effective electricity power accounts for the majority of vehicular propulsion energy. With the decrement of $E_B$ and $SoC_{ini}$, $C_{Total}$ increases significantly, since the expensive hydrogen fuel gradually becomes primary propulsion energy source. Moreover, in European case, $C_{Total}$ is higher compared to that in Chinese case. This is because the discrepancy in electricity price in both regions are insignificant, whereas the hydrogen price in Europe is much higher than that in China, as indicated in TABLE 4.11.

Besides, taken Chinese case as an example, the average FCS working efficiency ($\bar{\eta}_{FCS}$) and average cell voltage ($\bar{U}_{cell}$) with different $E_B$ and $SoC_{ini}$ are given in figure 4.27. The red percentage is the operation time ratio when the cell voltage is above 0.85 V, implying the FCS's over-low loading conditions.

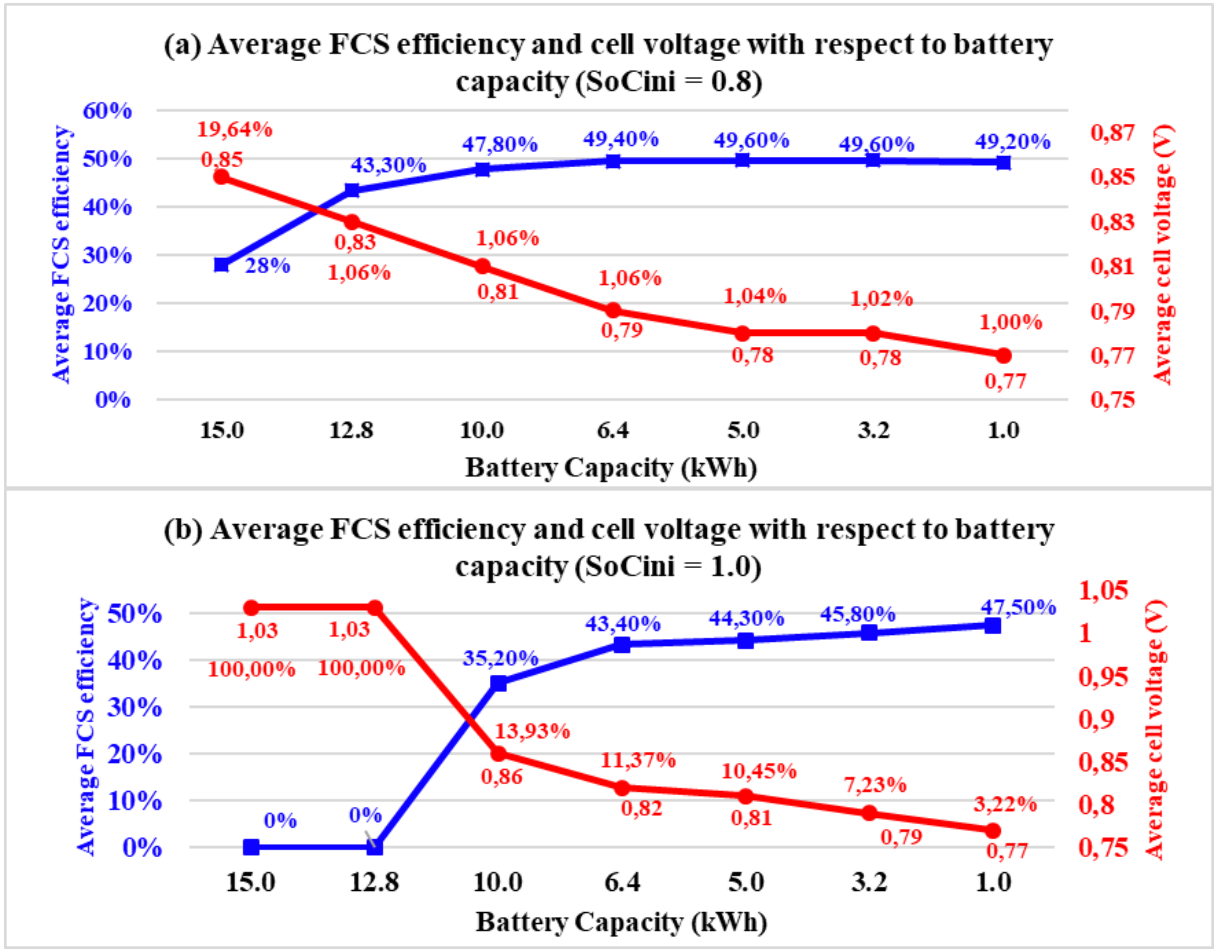


Figure 4.27. Average FCS working efficiency and cell voltage with respect to different sizes of battery capacity and different $SoC_{ini}$ (Remark: the red percentage denotes the operation time ratio when $\bar{U}_{cell}$ > 0.85V).

As can be seen, $\bar{\eta}_{FCS}$ decreases with the growth of $E_B$ and $SoC_{ini}$. This is because a larger $E_B$ and a higher $SoC_{ini}$ imply the larger amount of useful battery energy. When there is sufficient low-cost electricity energy for vehicle propulsion, more FCS operating points tend to distribute towards its low

power region, thus leading to the decrement of $\bar{\eta}_{FCS}$ since the FCS efficiency drops significantly at low power region (see figure 4.5). In addition, as depicted in figure 4.27(b), when battery is fully charged ($SoC_{ini}$ = 1.0), zero FCS efficiency occurs when $E_B \geq 12.8$ kWh. This is because the vehicle operates under the pure electric mode with no output electrical power from FCS for vehicle propulsion (FCS idle state).

Moreover, as given by the red curves in figure 4.27, $\bar{U}_{cell}$ increases with the growth of $E_B$ and $SoC_{ini}$, since in this case the FCS tends to work under low loading conditions. As a result, the high cathode potentials caused by extremely low loadings would increase the surface oxides on the platinum particles, eventually intensifying the catalyst layer degradation of a PEMFC [21].

#### 4.6.2.2. Operation cost analysis under different battery capacity and driving distance

With different battery capacities, vehicle's operation costs and FCS working efficiency is evaluated on the concatenated driving cycles (1 to 3 testing cycles), with the evaluation results summarized in TABLE 4.14 and TABLE 4.15. In all simulations, a fully charged battery is used ($SoC_{ini}$ = 1.0). Moreover, $C_{FE}$ is the total cost per kilometer (USD/km).

TABLE 4.14. Fuel economy comparison with different $E_B$ and driving length: Chinese case

| $E_B$ (kWh) | Distance (km) | $C_{H_2}$ (USD) | $C_{elec}$ (USD) | $C_{Total}$ (USD) | $C_{FE}$ (USD/km) | $\bar{\eta}_{FCS}$ |
|---|---|---|---|---|---|---|
| 15.0 | 68.5 | 0.36 | 1.35 | 1.71 | 0.026 | 0% |
| | 137.0 | 2.72 | 1.66 | 4.38 | 0.032 | 43.7% |
| | 205.5 | 5.91 | 1.66 | 7.57 | 0.037 | 46.5% |
| 12.8 | 68.5 | 0.36 | 1.35 | 1.71 | 0.026 | 0% |
| | 137.0 | 3.26 | 1.41 | 4.67 | 0.034 | 45.0% |
| | 205.5 | 6.47 | 1.41 | 7.88 | 0.038 | 47.0% |
| 10.0 | 68.5 | 0.81 | 1.10 | 1.91 | 0.028 | 35.2% |
| | 137.0 | 3.96 | 1.10 | 5.06 | 0.037 | 46.0% |
| | 205.5 | 7.20 | 1.10 | 8.30 | 0.040 | 47.4% |
| **6.4 (baseline)** | 68.5 | 1.65 | 0.71 | 2.36 | 0.035 | 43.4% |
| | 137.0 | 4.88 | 0.71 | 5.59 | 0.041 | 46.8% |
| | 205.5 | 8.13 | 0.71 | 8.84 | 0.043 | 47.8% |

TABLE 4.15. Fuel economy comparison with different $E_B$ and driving length: European case

| $E_B$ (kWh) | Distance (km) | $C_{H_2}$ (USD) | $C_{elec}$ (USD) | $C_{Total}$ (USD) | $C_{FE}$ (USD/km) | $\bar{\eta}_{FCS}$ |
|---|---|---|---|---|---|---|
| 15.0 | 68.5 | 0.70 | 1.52 | 2.22 | 0.032 | 0% |
| | 137.0 | 5.27 | 1.87 | 7.13 | 0.052 | 43.6% |
| | 205.5 | 11.44 | 1.87 | 13.31 | 0.065 | 46.7% |
| 12.8 | 68.5 | 0.70 | 1.52 | 2.22 | 0.032 | 0% |
| | 137.0 | 6.30 | 1.59 | 7.89 | 0.058 | 45.1% |
| | 205.5 | 12.52 | 1.59 | 14.11 | 0.069 | 47.2% |
| 10.0 | 68.5 | 1.56 | 1.24 | 2.81 | 0.041 | 35.3% |
| | 137.0 | 7.66 | 1.24 | 8.90 | 0.065 | 46.4% |
| | 205.5 | 13.92 | 1.24 | 15.16 | 0.074 | 47.9% |
| **6.4 (baseline)** | 68.5 | 3.19 | 0.80 | 3.99 | 0.058 | 43.8% |
| | 137.0 | 9.45 | 0.80 | 10.24 | 0.075 | 46.9% |
| | 205.5 | 15.74 | 0.80 | 16.54 | 0.081 | 48.0% |

In TABLE 4.14, if $E_B \leq 10.0$ kWh, $C_{elec}$ is not affected by the driving distance, meaning the stored battery energy is fully utilized over the trip. If $E_B > 10.0$ kWh, battery energy is fully depleted only when

the driving distance ≥ 137.0 km. Moreover, under the same driving distance, enlarging $E_B$ would contribute to the reduction of $C_{FE}$, since more low-cost electricity power can be used for vehicle propulsion. However, with the increment of driving distances, the $C_{FE}$ reduction ratios brought by battery capacity enlargement (from 6.4 kWh to 15.0 kWh) are shrinking, namely 26.0% for 68.5 km, 22.0% for 137.5 km and 14.0% for 205.5 km, respectively.

Furthermore, $\bar{\eta}_{FCS}$ grows with the increment of driving distance, especially obvious when $E_B \geq 10.0$ kWh. This is because, for a long-distance trip, the amount of energy required by the driving cycle is much larger than the amount of energy stored in the battery. To bridge such energy gap, larger portion of propulsion power will be supplied by FCS. Therefore, more FCS operating points will move towards its higher power region, leading to the improved $\bar{\eta}_{FCS}$ and better FCS utilization rate. In addition, escaping from the extremely low loadings conditions is beneficial for extending the lifetime of FCS [21].

In addition, since the hydrogen price is much higher in European case (11 USD/kg) in contrast to that in Chinese case (5.68 USD/kg), $C_{FE}$ under all driving distances are more expensive in European case, as shown in TABLE 4.15. For example, the $C_{FE}$ in European case is up to 1.88 times of the $C_{FE}$ in Chinese case (e.g. when $E_B = 6.4$ kWh, driving distance is 205.5 km). This indicates that the fuel economy of FCHEVs is closely related to the hydrogen price, especially for long-distance driving. To further reduce the operation costs of fuel cell vehicles, it is required to bring down the price of hydrogen fuel in a region.

### 4.6.3. Summary of impacts on vehicle's performance by sizing discrepancies

Based on the aforementioned analyzes, the major findings are summarized as below:

- On the one hand, with a fixed size of 30 kW FCS, increasing battery capacity would enlarge the amount of available onboard electricity energy, indicating a longer all-electric-range. Moreover, since the electricity price is much cheaper than hydrogen price in some regions of the world (e.g. China and Europe), this measure would be helpful to reduce the vehicle's overall operation cost, since more low-cost electricity power can be used for vehicle propulsion, and battery can be recharged by external grid power when trip ends.
- On the other hand, increasing battery capacity would reduce the average FCS working efficiency. This is because if there is sufficient low-cost battery energy for vehicle propulsion, the FCS is more likely to work under low power region (or idle condition), meaning the average FCS power level would be reduced, thus leading to the significant drop of FCS efficiency. Moreover, working under extremely low loadings would also shorten the lifetime of FCS, thus increasing the powertrain maintenance cost.
- We also found that the operation cost of a FCHEV is very sensitive to the price of hydrogen, which is likely to be affected by the vehicle's operating locations. Therefore, the related techniques and

local policies that facilitate reduction of the hydrogen price in production, storage and distribution processes would be beneficial for further enhancing the economic potential of FCHVEs.

To sum up, with a 30 kW FCS, if the size of battery capacity in the baseline configuration is slightly increased (e.g. to 10.0 kWh), it would be favorable for achieving a more balanced performance among the vehicle's operation cost, the FCS efficiency, durability and the battery energy utilization rate.

## 4.7. Conclusion

Assisted by the driving prediction techniques proposed in **Chapter 3**, **Chapter 4** presents several solutions to realize the predictive energy management for fuel cell/battery-based HEVs. Specifically, the modelling of vehicular hybrid powertrain is introduced at first. Subsequently, the development of a multi-mode predictive energy management strategy (PEMS) for midsize non-plug-in FCHEV, an online-learning enhanced PEMS for midsize plug-in FCHEV, and an integrated PEMS for light-duty mail-delivery FCHEV is presented, with their performance validated through simulation studies. Finally, a vehicle's operational cost analysis under different powertrain-sizing configurations is conducted, so as to explore the potential fuel economy enhancement imposed by altering vehicle configurations.

Overall, in comparison with benchmark strategies, the effectiveness of the proposed PEMSs in enhancing fuel efficiency and avoiding fuel cell degradation by harsh transients has been verified in this Chapter. Moreover, the proposed strategy has certain level of robustness against the trip duration estimation errors, which is favorable for their real implementations. In addition, the online computation time per step of the proposed strategies is sufficiently smaller than the sampling time interval, thus demonstrating the possibility of being integrated into the onboard ECUs.

Next chapter will focus on running the proposed strategies in the software-in-the-loop (SIL) platform to further validate its functionality and real-time practicality.

## References


[1]. ADVISOR. Advanced Vehicle Simulator [online]. Available at: http://adv-vehicle-sim.sourceforge.net/.

[2]. C. Higel, F. Harel, D. Candusso, S. Faivre, et al, Part 1: Mobypost vehicle's powertrain modeling, simulation and sizing. ***Conference on Fundamentals and Development of Fuel Cells (FDFC 2013)***, Apr. 2013, Germany.

[3]. L. Guzzella, A. Sciarretta. ***Vehicle Propulsion Systems: Introduction to Modeling and Optimization***. Berlin: Springer-Verlag, pp. 14-18, 2005.

[4]. A. Ravey, N. Watrin, B. Blunier, D. Bouquain, A. Miraoui, "Energy-Source-Sizing Methodology for Hybrid Fuel Cell Vehicles Based on Statistical Description of Driving Cycles," in ***IEEE Transactions on Vehicular Technology***, vol. 60, no. 9, pp. 4164-4174, Nov. 2011. doi: 10.1109/TVT.2011.2158567.

[5]. Y. Liu, J. Li, Z. Chen, D. Qin, Y. Zhang, Research on a multi-objective hierarchical prediction energy management strategy for range extended fuel cell vehicles, ***Journal of Power Sources***, Volume 429, 2019, Pages 55-66, https://doi.org/10.1016/j.jpowsour.2019.04.118.

[6]. A. Ravey, B. Blunier, A. Miraoui, "Control Strategies for Fuel-Cell-Based Hybrid Electric Vehicles: From Offline to Online and Experimental Results," in ***IEEE Transactions on Vehicular Technology***, vol. 61, no. 6, pp. 2452-2457, July 2012. doi: 10.1109/TVT.2012.2198680..

[7]. Squadrito, G., Maggio, G., Passalacqua, E., Lufrano, F. and Patti, A. An empirical equation for polymer electrolyte fuel cell (PEFC) behaviour. ***Journal of Applied Electrochemistry*** 29, 1449–1455 (1999). https://doi.org/10.1023/A:1003890219394.
[8]. F. Laurencelle, R. Chahine, J. Hamelin, B. Agbossou, M. Fournier, T.K. Bose Characterization of Ballard MK5-E proton Exchange membrane fuel cell stack J. ***Fuel Cells***, 1 (2001), pp. 66-71. https://doi.org/10.1002/1615-6854(200105)1:1%3C66::AID-FUCE66%3E3.0.CO;2-3.
[9]. K. Kordesch, G. Simader. Fuel Cells and Their Applications,WILEY-VCH, ***Weinheim***, 1996. https://doi.org/10.1002/bbpc.19961001128.
[10]. M.C. Péra, D. Hissel, H. Gualous, C. Turpin. Electrochemical Components, ***John Wiley & Sons, Inc***, 2013.
[11]. F. Gao, B. Blunier, A. Miraoui, A. El Moudni, "A Multiphysic Dynamic 1-D Model of a Proton-Exchange-Membrane Fuel-Cell Stack for Real-Time Simulation," in ***IEEE Transactions on Industrial Electronics***, vol. 57, no. 6, pp. 1853-1864, June 2010. doi: 10.1109/TIE.2009.2021177.
[12]. J. Larminie A. Dicks, Fuel Cell Systems Explained, ***John Wiley & Sons Ltd***, 2003, DOI:10.1002/9781118878330.
[13]. Y. Zhou, A. Ravey, M.C. Péra, Multi-mode predictive energy management for fuel cell hybrid electric vehicles using Markov driving pattern recognizer, ***Applied Energy***, Volume 258, 2020, 114057, https://doi.org/10.1016/j.apenergy.2019.114057.
[14]. Y. Zhou, H. Li, A. Ravey, M.C. Péra, An integrated predictive energy management for light-duty range-extended plug-in fuel cell electric vehicle, ***Journal of Power Sources***, Volume 451, 2020, 227780 https://doi.org/10.1016/j.jpowsour.2020.227780.
[15]. L. Lu, X. Han, J. Li, J. Hua, M. Ouyang, A review on the key issues for lithium-ion battery management in electric vehicles, ***Journal of Power Sources***, Volume 226, 2013, Pages 272-288, https://doi.org/10.1016/j.jpowsour.2012.10.060..
[16]. C.H. Zheng, G.Q. Xu, Y.I. Park, W.S. Lim, S.W. Cha, Prolonging fuel cell stack lifetime based on Pontryagin's Minimum Principle in fuel cell hybrid vehicles and its economic influence evaluation, ***Journal of Power Sources***, Volume 248, 2014, Pages 533-544, https://doi.org/10.1016/j.jpowsour.2013.09.110.
[17]. D. Zhou, A. Al-Durra, F. Gao, A. Ravey, I. Matraji, M. G. Simões, Online energy management strategy of fuel cell hybrid electric vehicles based on data fusion approach, ***Journal of Power Sources***, Volume 366, 2017, Pages 278-291, https://doi.org/10.1016/j.jpowsour.2017.08.107.
[18]. X. Wu, X. Hu, X. Yin, L. Li, Z. Zeng, V. Pickert, Convex programming energy management and components sizing of a plug-in fuel cell urban logistics vehicle, ***Journal of Power Sources***, Volume 423, 2019, Pages 358-366, https://doi.org/10.1016/j.jpowsour.2019.03.044.
[19]. Path to hydrogen competitiveness: A cost perspective, Jan. 2020. https://hydrogencouncil.com/en/path-to-hydrogen-competitiveness-a-cost-perspective/.
[20]. B. Geng, J. K. Mills, D. Sun, "Two-Stage Energy Management Control of Fuel Cell Plug-In Hybrid Electric Vehicles Considering Fuel Cell Longevity," in ***IEEE Transactions on Vehicular Technology***, vol. 61, no. 2, pp. 498-508, Feb. 2012. doi: 10.1109/TVT.2011.2177483.
[21]. T. Fletcher, R. Thring, M. Watkinson, An Energy Management Strategy to concurrently optimise fuel consumption & PEM fuel cell lifetime in a hybrid vehicle, ***International Journal of Hydrogen Energy***, Volume 41, Issue 46, 2016, Pages 21503-21515, https://doi.org/10.1016/j.ijhydene.2016.08.157.

# Chapter 5. Performance Validation via Online Simulation

## 5.1. Introduction

**Chapter 4** presents the design and offline simulation results of several predictive energy management strategies (PEMSs) for fuel cell/battery-based hybrid electric vehicles (FCHVEs). Nevertheless, considering the limited resources of vehicular electronic control units (ECUs), whether the proposed strategies can be properly integrated into the embedded systems and executed in real-time still remain a questionable issue. To this end, **Chapter 5** sets up an online-simulation platform, which allows the proposed strategies to be tested in the dSPACE hardware (MicroAutoBox II), thereby further validating their functionality and real-time suitability. The online-simulation platform is made up of hardware and software subsystems, wherein the hardware subsystem includes a DC power supply, a host PC and a dSPACE MicroAutoBox II real-time system. The software subsystem contains the vehicular powertrain model and the control algorithms (PEMS) developed in the Matlab/Simulink environment, which are compiled into the executable C code by the Microtec PowerPC C/C++ (PPC) compiler V3.7 and downloaded into the MicroAutoBox II. Besides, the dSPACE ControlDesk V4.2NG software is installed in the host PC as the human machine interface (HMI) to calibrate the model parameters and to capture the experimental data during the online simulation. The host PC and the MicroAutoBox II is connected via a network cable through the Ethernet interface, and the data communication between them is managed by the dSPACE real-time interface (RTI) module. Figure 5.1 gives the system-level block diagram and the real picture of the online-simulation platform.

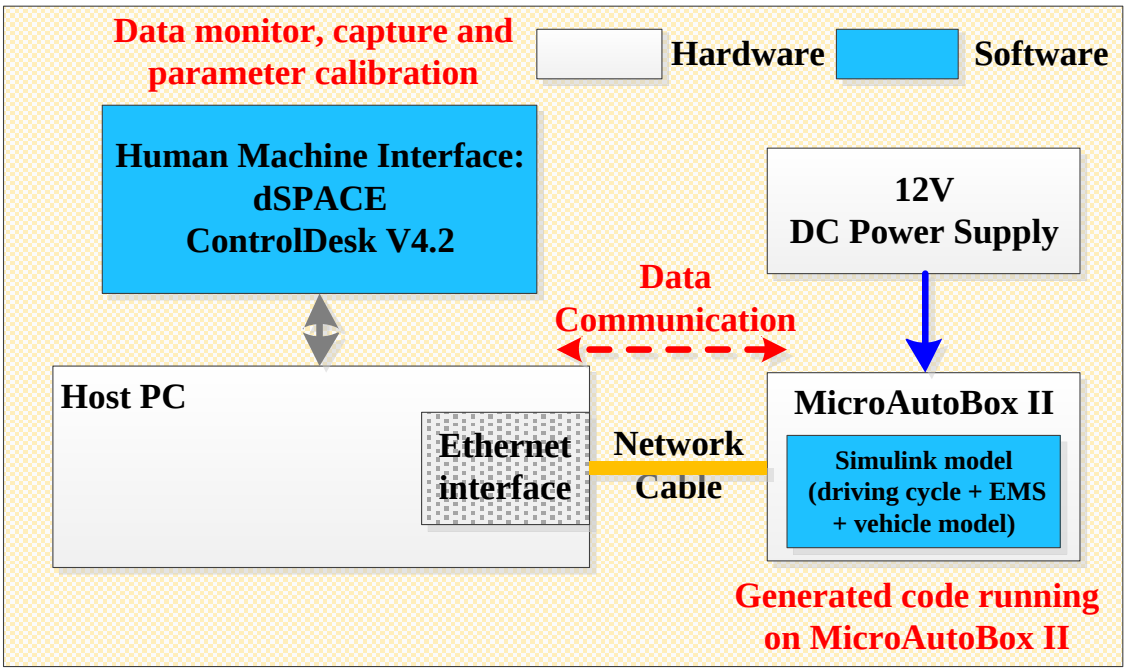


Figure 5.1(a). Block diagram of the online-simulation platform.

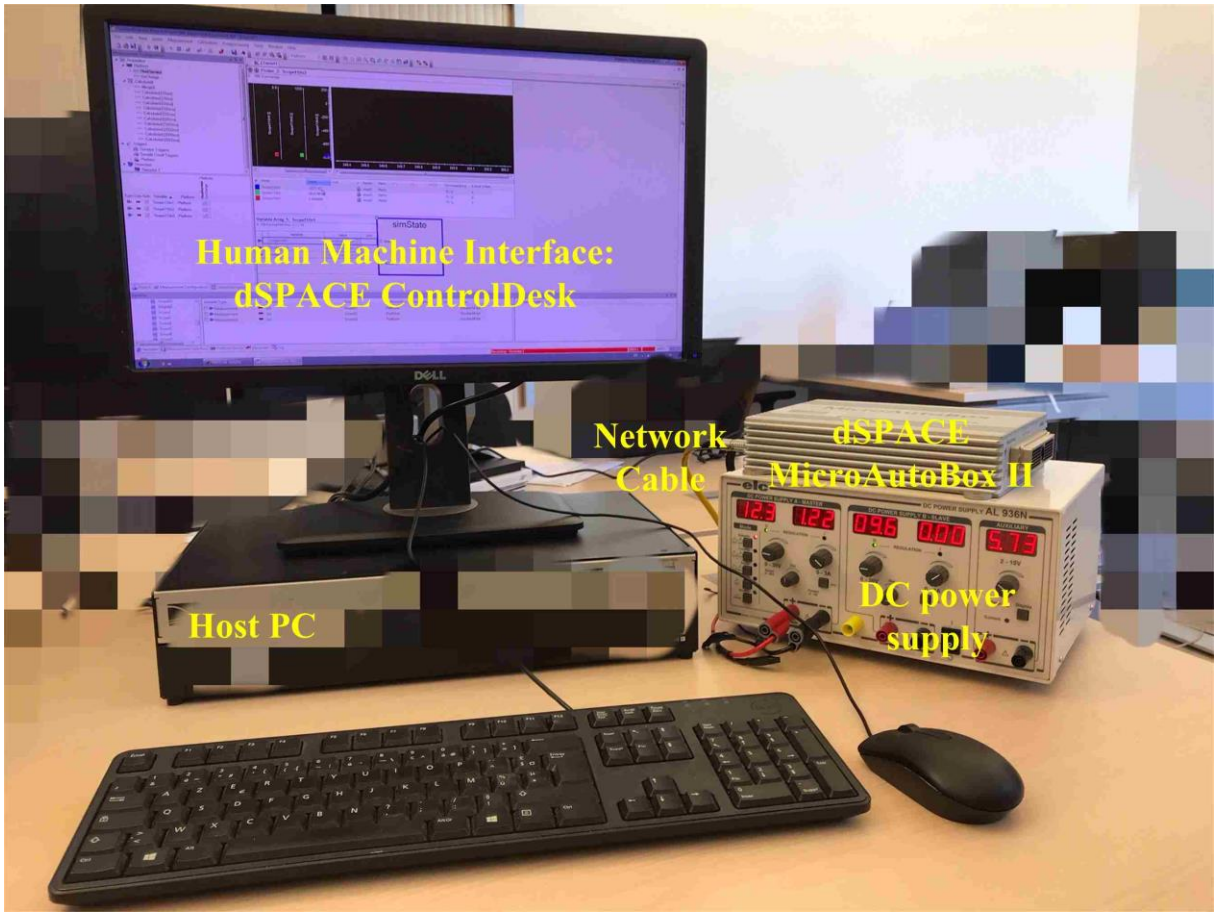


Figure 5.1(b). Real picture of the online-simulation platform.

The rest of this chapter is organized as follows: subsection 5.2 first briefs different simulation-based techniques for control algorithms validation, and then introduces the configuration of the online-simulation platform. Subsection 5.3 presents and analyzes the obtained validation results so as to examine the consistency against the offline-simulated results, and to highlight the effectiveness of the proposed strategies running in the embedded hardware. Major findings of this chapter are summarized in subsection 5.4.

## 5.2. Description of the online-simulation platform

This subsection introduces the aim and scope of various simulation-based validation techniques, and the configuration of the online-simulation platform.

### 5.2.1. Software-in-the-Loop Simulation

After the software (e.g. energy management strategies in our case) has been designed, a proper testing methodology is necessary to further validate and verify its functionality and real-time practicality. This could yield the necessity of establishing physical prototypes to test the software performance, which is typically a time-consuming and cost-sensitive procedure. Moreover, conducting such experimental tests may increase the risks of damage to researchers and equipment if the designed software encounters with

unexpected problems during the execution in embedded environment. To tackle such challenging issue and to produce reliable software meeting the predefined demands, almost all modern industrial sectors, like aerospace, automotive and robotic industries, are using the model-based design [1], since it has the following significant benefits [2]:

- Shorten the design-to-market period;
- Detection and elimination of errors in early development stage;
- Cost-saving during the software production;
- Enable iterative code enhancing, modifying and last-minutes changes.

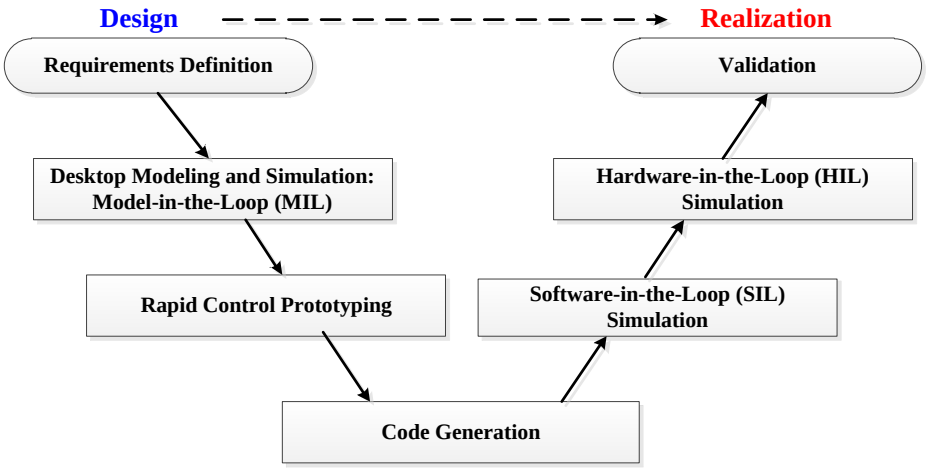


Figure 5.2. The design-to-realization workflow of Model-Based design [3].

As shown in figure 5.2, in the workflow of model-based design, several simulation-based techniques, aiming at evaluating the designed software at different validation stages, are the important tools for initial prototyping before the integration of any actual hardware. Specifically, the aim and scope of these simulation-based techniques are briefed as follows [4]:

- **Model-in-the-Loop** (MIL): MIL testing is often conducted in the offline-simulation environment (e.g. MATLAB/Simulink) with the whole system (controller and plant) being simulated, so as to evaluate the correctness regarding the functionality of the control algorithms;
- **Software-in-the-Loop** (SIL): After the control algorithms have been verified in MIL testing, they can be converted into the executable codes (e.g. C/C++ or VHDL depending on the embedded target) and tested with the simulated plant. Usually, the auto-/manually-generated code and the simulated plant are operating in the same hardware (e.g. a desktop PC). Moreover, if the generated code is running in the embedded hardware (e.g. microcontroller), such testing scenario can be further specified as **Processor-in-the-Loop** (PIL) simulation [2]. The major task of SIL testing is to justify the behavior of the generated code (functional), while PIL testing gives the further proofs of the generated code running on the embedded target (operational);
- **Hardware-in-the-Loop** (HIL): In HIL simulation, with the verified controller code, the plant model

is replaced by the actual system or by a real-time simulator representing the actual plant, with the response of sensors and actuators electronically emulated. The actual I/O interface is used for data communication between the embedded target (controller) and the real-time simulator (plant). HIL testing is the last step that allows debugging and evaluation of functional and operational tests in a manageable way in real-time environment [5]. Compared to SIL/PIL simulations, HIL setup is more complicated and requires more hardware and software resources.

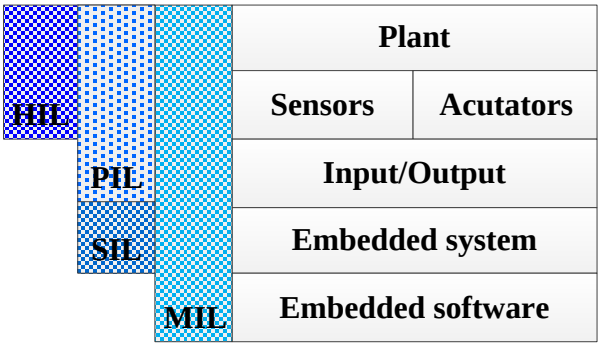


Figure 5.3. Scope of simulation for four validation approaches [6]. MIL: model-in-the-loop, SIL: Software-in-the-Loop, PIL: Processor-in-the-Loop, and HIL: Hardware-in-the-Loop. The scope ranges from the whole system being simulated in MIL to merely the plant in HIL.

Figure 5.3 summarizes the simulation scopes of MIL, SIL (PIL) and HIL testing. In this chapter, an online-simulation platform is established as introduced previously, and the SIL (PIL) testing is conducted to verify the proposed energy management strategies (EMS), where the EMSs are compiled into the executable C code and running on the target hardware: dSPACE MicroAutoBox II system. The setup of the online-simulation platform is detailed in the following parts.

### 5.2.2. Software subsystem of the online-simulation platform

One of the important parts of the software subsystem is the vehicular powertrain model (plant) and the energy management strategies (EMS, controller) developed in the MATLAB/Simulink environment. Figure 5.4 depicts the system-level block diagram of the devised Simulink model.

The EMS receives the input signals and computes the optimal power-allocating control actions. Specifically, the measurement module in the EMS part transforms the feedback signal into the proper format and sends them to a quadratic programming (QP) solver. Besides, the driving prediction module provides with the estimation of upcoming driving conditions (e.g. velocity prediction results, SoC reference profile and driving pattern recognition) according to input information. The development of corresponding driving prediction techniques is detailed in **Chapter 3**. With the updated system states and the forecasted results, QP solver module derives the optimal control action via minimizing the multi-objective cost function. It should be mentioned that the MATLAB-embedded QP solver (e.g. *quadprog* function) is not supported for code generation (since MicroAutoBox II requires discretization of the

optimization solver), and thus cannot be easily embedded into the target hardware. To this end, an open access QP solver, *qpOASES* (Version 3.2.1), developed and supported by ABB Corporate Research, Switzerland and the Interdisciplinary Center for Scientific Computing (IWR) at Heidelberg University, is leveraged in this work for solving the optimization problem. The *qpOASES* solver is programmed in C++ and supports a variety of third-part interfaces, which can be easily integrated with Simulink and dSPACE environment. More details of *qpOASES* solver can be found in [7].

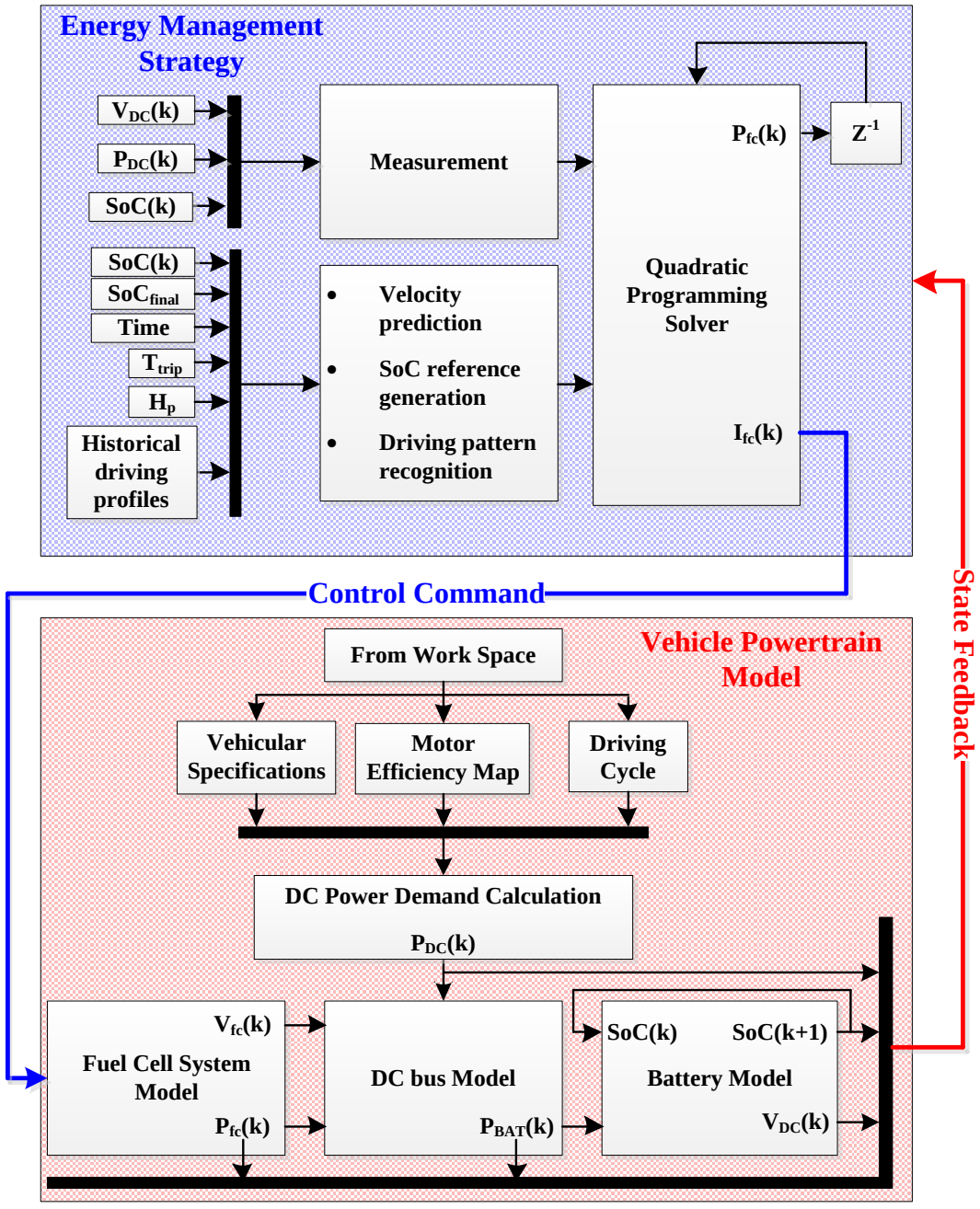


Figure 5.4. System-level block diagram of the Simulink model.

The control command is sent to vehicle powertrain model to evolve the system dynamics, and the updated system states are feedback to the EMS for determining the control actions at the next time step.

Please note the vehicular specifications (e.g. weight, air drag coefficient, etc.), the efficiency map of electric machine and the testing mission profiles (driving cycle) are loaded from MATLAB workspace. Specifically, the DC bus power demand calculation module computes the corresponding DC bus power request based on the vehicular specifications, the efficiency map of electric machine and the driving cycle information. Based on the given fuel cell current command and the polarization curve, the fuel cell system module outputs the corresponding fuel cell voltage and power signal. With the DC bus power request and the fuel cell power signals, the DC bus module derives the battery power signal and sends it to the battery module, where the battery module updates SoC according to the battery power signal and the SoC value at the previous time step. Moreover, the DC bus voltage changes accordingly with the update of SoC. The renewed system states are feedback to the EMS part for power distribution at the next time step.

After the Simulink model has been developed and tested in offline-simulation scenario, it is compiled into the executable C code via the Microtec PowerPC C/C++ compiler and downloaded into the MicroAutoBox II via the dSPACE Real-time interface (RTI). The RTI software is the link between dSPACE hardware and the development software (MATALB/Simulink), and it extends the C code generator Simulink Coder™ for automatically implementing the developed Simulink models on the real-time hardware [8].

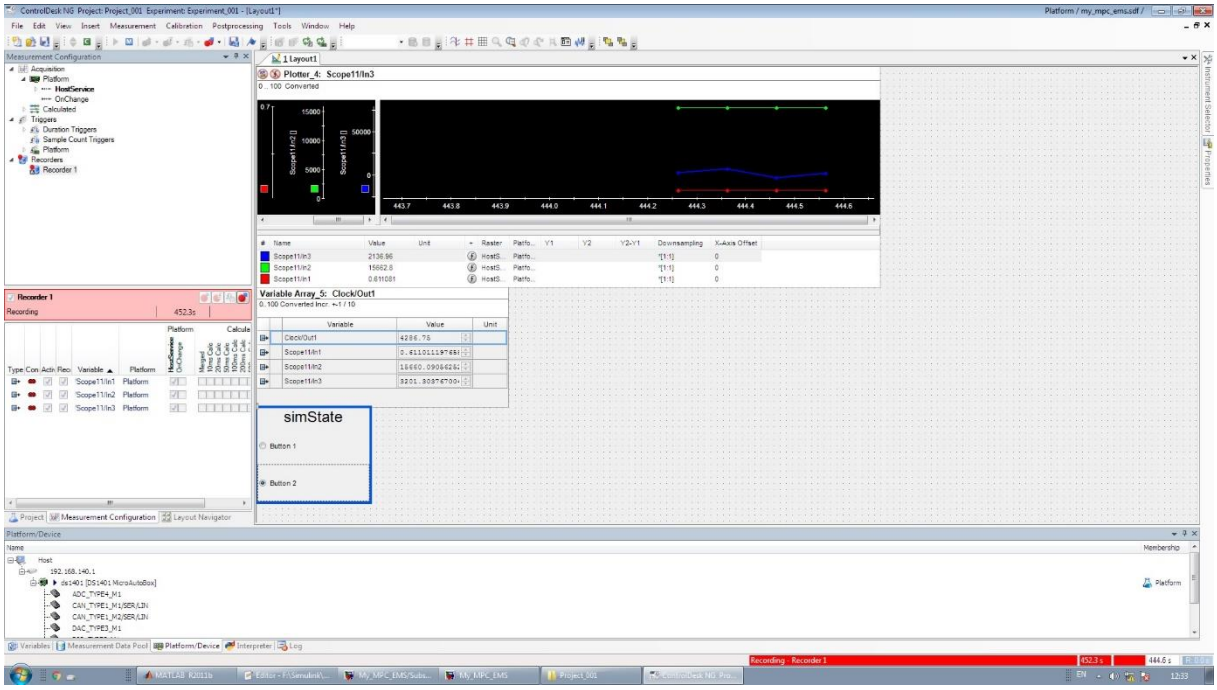


Figure 5.5. Screenshot of the dSPACE ControlDesk v4.2 NG human machine interface.

As shown in figure 5.5, dSPACE ControlDesk 4.2NG is used as a human machine interface (HMI), which is the dSPACE experimental software for ECU development, and it performs all the necessary tasks and gives you a single working environment [9]. With the ControlDesk software, the experimental

interface can be rapidly set up by dragging and dropping a variety of virtual instruments within the embedded library, like plotter, radio button, and switch. In addition, ControlDesk software enables and manages the data communication between the host PC and the MicroAutoBox II, so as to visualize the system state and the measured variables, calibrate model parameters and store the experimental results. In the established online-simulation platform, the major task of the HMI is summarized as follows: (a) send the start signal of simulation to the MicroAutoBox II; (b) monitor the value of multiple variables during the online simulation; and (iii) record and export the experimental results for further analysis.

### 5.2.3. Hardware subsystem of the online-simulation platform

This subsection presents the hardware settings of the online-simulation platform. As illustrated in figure 5.1, three major hardware devices exist in the online-simulation platform: a desktop host PC, a MicroAutoBox II and an associated DC power supply.

The desktop host PC (Dell Precision T1700) is equipped with an Intel Core i5-4590 CPU @ 3.3GHz and a 16G memory. The PC is working under Window 7 OS with the development software, MATLAB R2011b, and the HMI software, dSPACE ControlDesk V4.2, installed in the PC. The major tasks of the host PC are given as follows: (i) establish and modify the Simulink model in the offline environment; (ii) compile the model and download it to the MicroAutoBox II; and (iii) monitor and record the experimental data during the online simulation.

The core hardware of the online-simulation platform, the dSPACE MicroAutoBox II 1401/1511 with an IBM PPC 750GL microprocessor @ 900 MHz (see figure 5.6), is a real-time system for performing fast function prototyping, and it can operate without user intervention [10].

Figure 5.6. Outline of dSPACE MicroAutoBox II (1401/1511) [10].

MicroAutoBox II can be used for many different rapid control prototyping (RCP) applications such as powertrain, chassis, electric drive control and aerospace applications. With the developed Simulink model and the real-time interface library, a PC or a laptop can be easily connected to MicroAutoBox II for application download, model parameterization, and data analysis [10]. More technical details about MicroAutoBox II can be found in its product brochure [11]. A network cable is used to connect the host PC and the MicroAutoBox II via Ethernet interface. Besides, it should be mentioned that a DC power

supply (AL 936N-elc) is used to power the MicroAutoBox II. In this work, the MicroAutoBox II is the hardware container and the operating platform of the auto-generated code from the Simulink model, where the experimental data and signals are feedback to the host PC via the Ethernet during the online simulation.

## 5.3. Results and Discussions

This subsection presents the validation results obtained based on the previously described online-simulation platform. In SIL testing, all the proposed control strategies have been successfully executed in real-time under three different sampling period settings, namely 1.0s, 0.5s and 0.2s.

It should be mentioned that the original sampling period of driving cycles (speed profiles) is 1.0s, meaning the time interval between two consecutive speed samples is 1.0s. When the control strategies are tested under a smaller sampling period, it is equivalent to reducing the original speed sampling period. For instance, if the sampling period of EMS is set to 0.2s, the time interval between two consecutive speed samples is reduced accordingly to 0.2s. From the obtained results, it can be observed that all performance indicators of EMS (e.g. hydrogen fuel consumption, fuel cell power transients, etc.) are the same under three different sampling period settings, meaning reducing the length of sampling period would not change the functionality of control strategies.

Besides, the lower sampling period in SIL testing is 0.2s, meaning the execution of EMSs can be finished within 0.2s, which is 5 times smaller than the original sampling period (1.0s) in offline simulation. This implies the computational hardware demand of the proposed control strategies is far from reaching the upper limits of the target CPU. Consequently, it can be confirmed that the computation burden of the proposed EMSs is acceptable for online applications. To avoid the repetitive illustrations, only the SIL testing results at the sampling period of 1.0s are presented in the following parts.

### 5.3.1. Validation of multi-mode predictive energy management strategy

Firstly, the multi-mode predictive energy management strategy (PEMS) proposed in subsection 4.3 is verified under a multi-pattern testing cycle extracted from ADVISOR [1], where the speed and power demand profiles of the testing cycle are depicted in figure 5.7.

In order to validate the PEMS's performance consistency in both offline simulation and software-in-the-loop (SIL) simulation environment, the multi-mode PEMS designed for a midsize non-plug-in FCHEV is tested under the driving cycle as shown in figure 5.7, where the corresponding testing results of battery SoC, fuel cell power and battery power are depicted in figure 5.8(a)-(d). Please note the prediction horizon ($H_p$) is set as 5s in both testing scenarios, where the sampling period is 1s. As shown in figure 5.8, the SIL testing results are very similar to offline-simulation results. In fact, the numerical discrepancy of the PEMS performance (SoC, fuel cell power and battery power) under two testing scenarios is displayed in figure 5.9. As can be seen, the order of discrepancy ($10^{-10}$ to $10^{-15}$) is much

smaller than the magnitude of the original signals, and, hence, such performance difference can be neglected. Hence, the PEMS's performance consistency under both testing scenarios is verified.

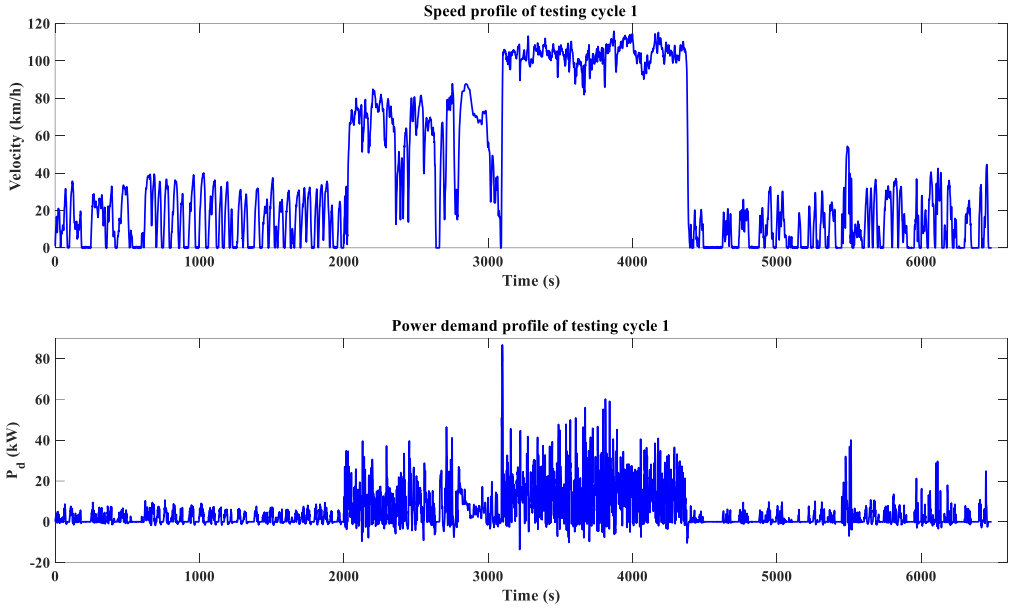


Figure 5.7. Speed and power demand profiles of the multi-pattern testing cycle.

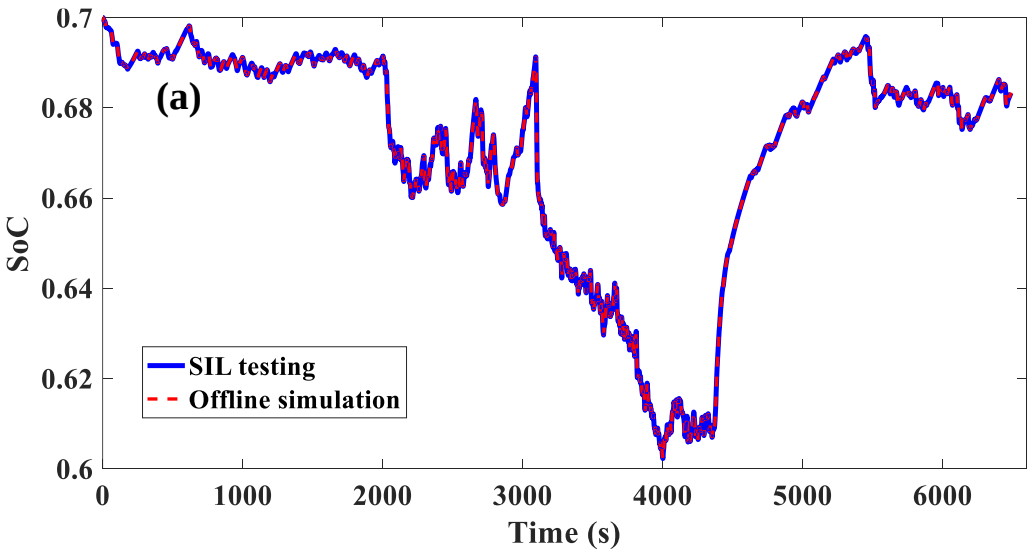


Figure 5.8(a). Battery SoC comparison under SIL and offline simulation scenarios.

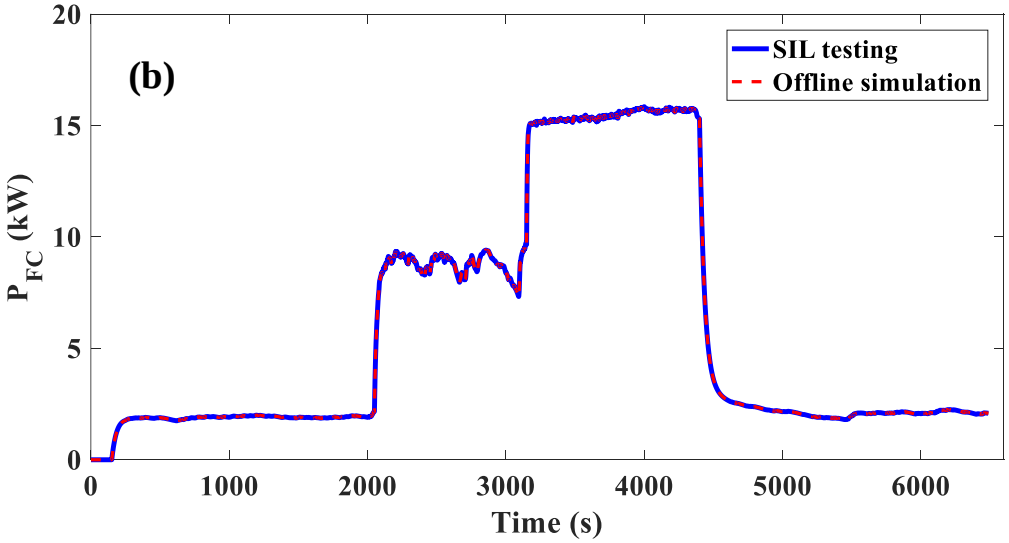


Figure 5.8(b). Fuel cell power comparison under SIL and offline simulation scenarios.

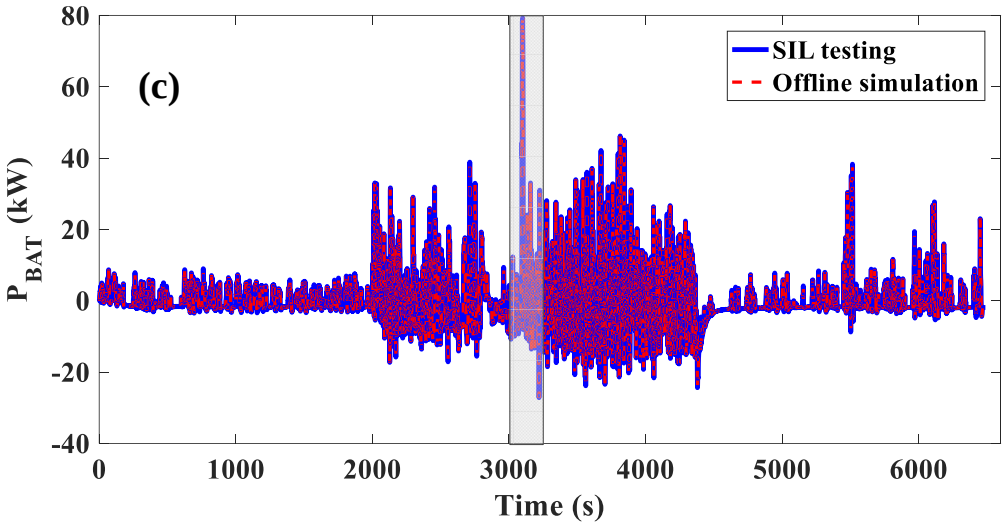


Figure 5.8(c). Battery power comparison under SIL and offline simulation scenarios (global view).

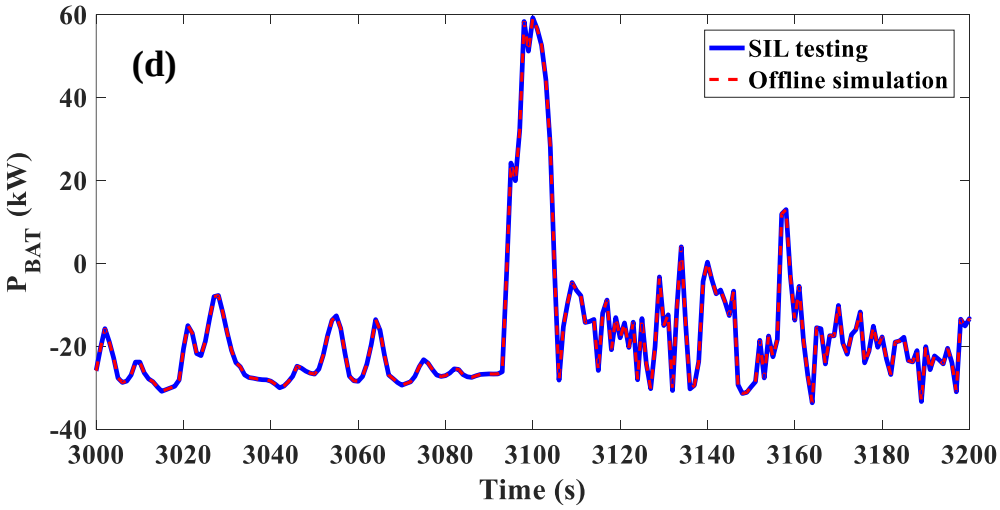


Figure 5.8(d). Battery power comparison under SIL and offline simulation scenarios (Local view: 3000s to 3200s).

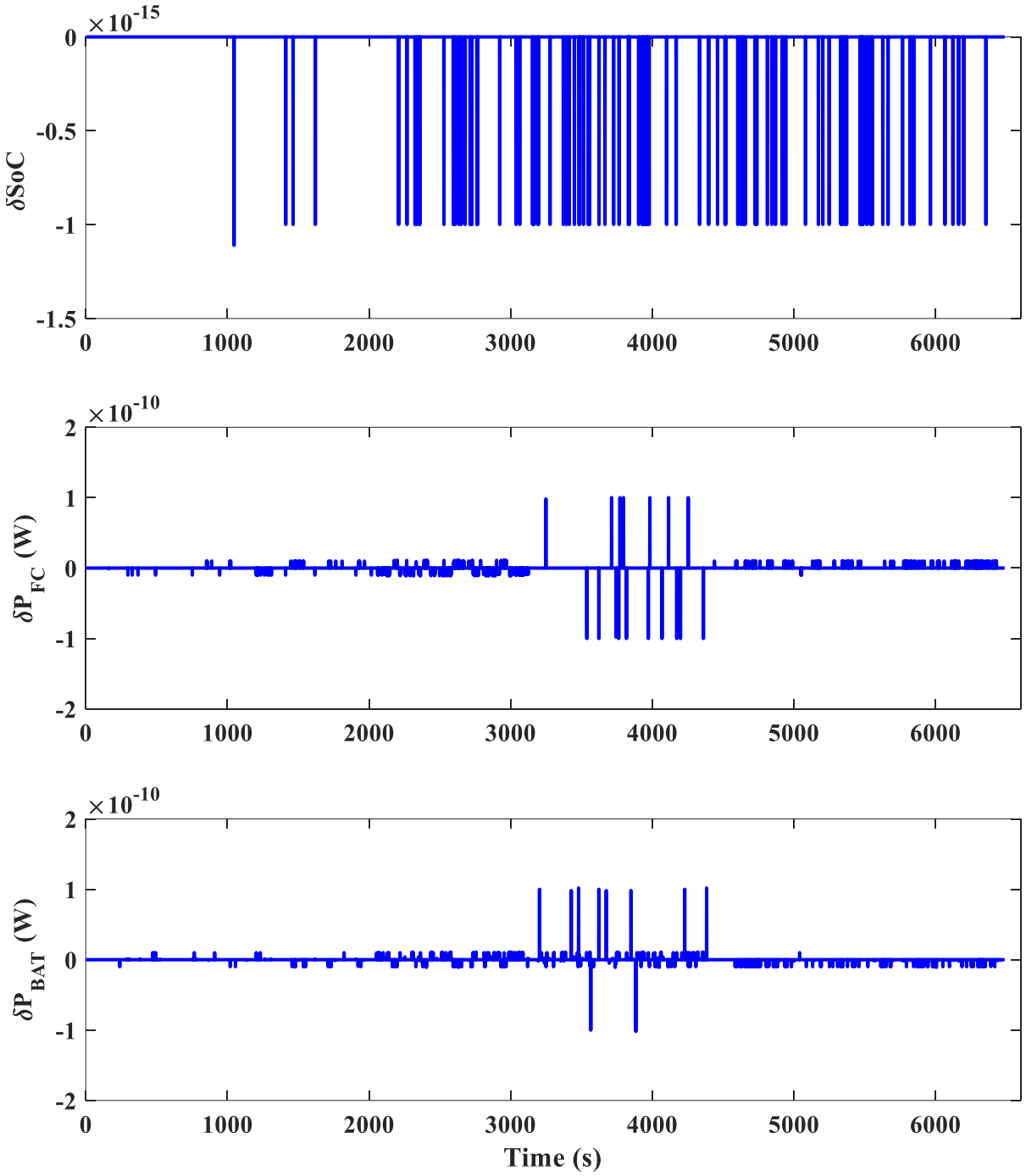


Figure 5.9. Performance discrepancy on SoC, fuel cell power and battery power under SIL and offline-simulation scenarios.

After the performance consistency between the SIL testing results and the offline-simulation results has been validated, the multi-mode PEMS (multi-mode MPC) is compared with benchmark strategies in the following parts. A single-mode model predictive control-based strategy (single-mode MPC) is regarded as the lower benchmark. The performance of dynamic programming (DP) is regarded as the upper benchmark. More details regarding the benchmark strategies can be found in subsection 4.3.2.1. Please note the prediction horizon for MPC-based strategies is set as 5s. Moreover, both MPC-based strategies

are executed in SIL platform, while DP results are obtained in offline environment. Figure 5.10 presents the corresponding comparative results. As shown in figure 5.10(a), DP strategy charges battery in urban driving scenarios (the SoC increases), sustains the SoC in suburban scenarios and depletes battery energy in highway driving conditions, while the single-mode MPC keeps SoC around the initial SoC (0.7) under all driving scenarios. In contrast, multi-mode MPC restricts SoC strictly around 0.7 in urban driving patterns while the battery energy can be used in a flexible manner in other driving patterns.

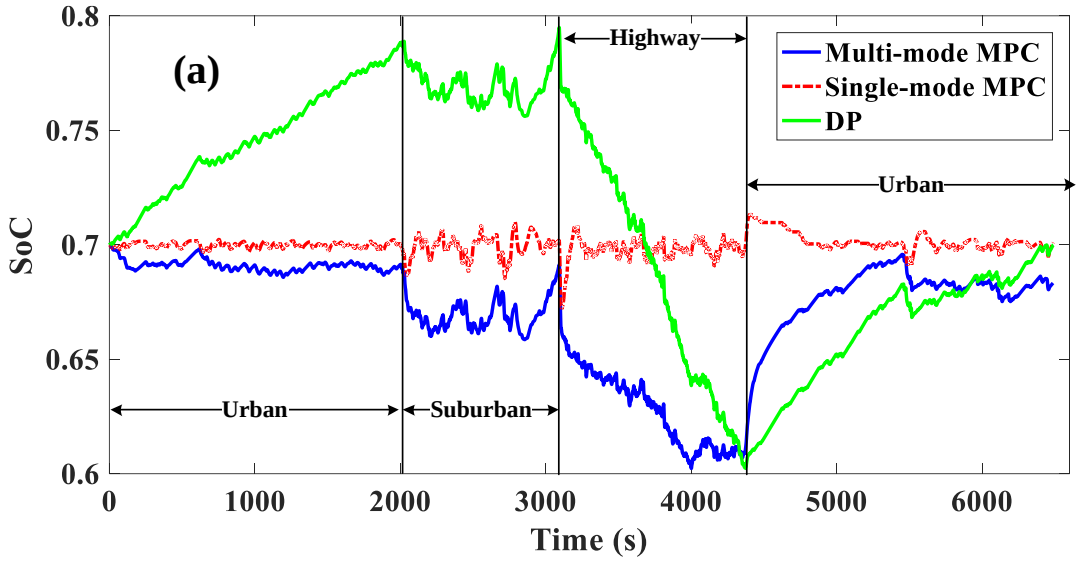


Figure 5.10(a). Battery SoC performance comparison of multi-mode MPC (SIL), single-mode MPC (SIL) and DP (offline-simulation).

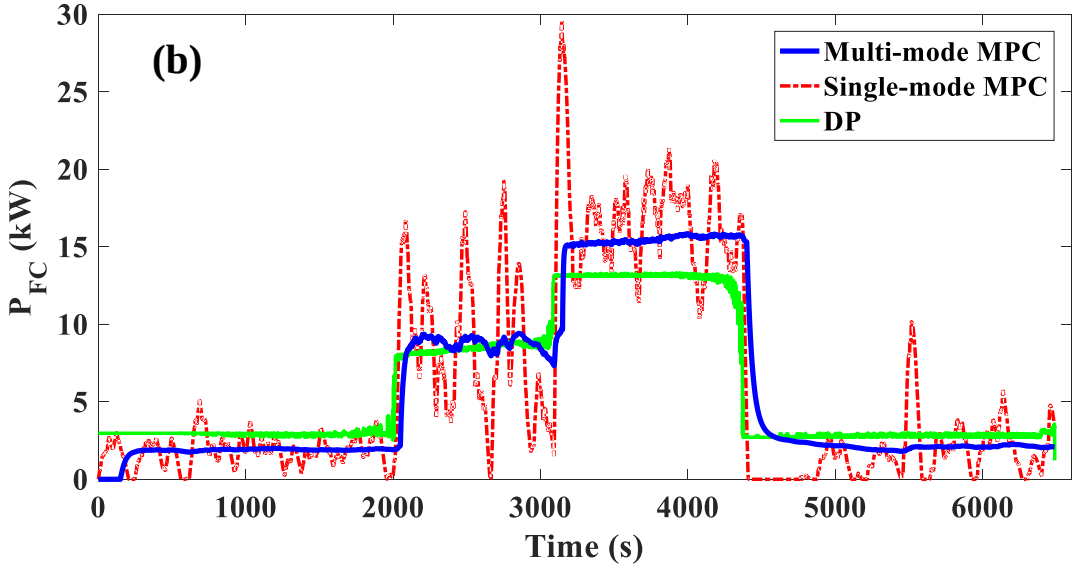


Figure 5.10(b). Fuel cell power performance comparison of multi-mode MPC (SIL), single-mode MPC (SIL) and DP (offline-simulation).

Figure 5.10(b) depicts the corresponding fuel cell power comparison results. DP strategy manipulates fuel cell power with the fewest transients, and the fuel cell output power level alters accordingly with

the change of driving patterns. In contrast, the average fuel cell power of multi-mode MPC in urban scenario is lower than DP strategy, and it becomes higher than DP strategy in highway driving pattern. Single-mode MPC, as the lower benchmark, results in the largest fuel cell power transients and more fuel cell start-stop cycles among three strategies, which would accelerate the degradation of fuel cell. Moreover, figure 5.10(c) and (d) depict the battery power performance discrepancy among three strategies. From figure 5.10(d), it can be clearly seen that the proposed multi-mode MPC performs close to the upper benchmark (DP) strategy in terms of battery output power.

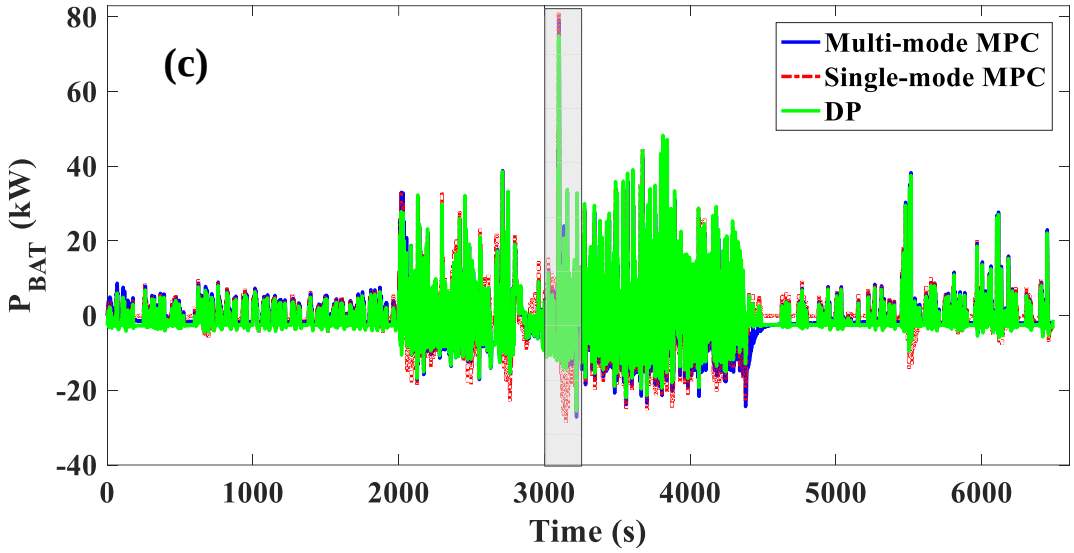


Figure 5.10(c). Global view of battery power performance comparison of multi-mode MPC (SIL), single-mode MPC (SIL) and DP (offline-simulation).

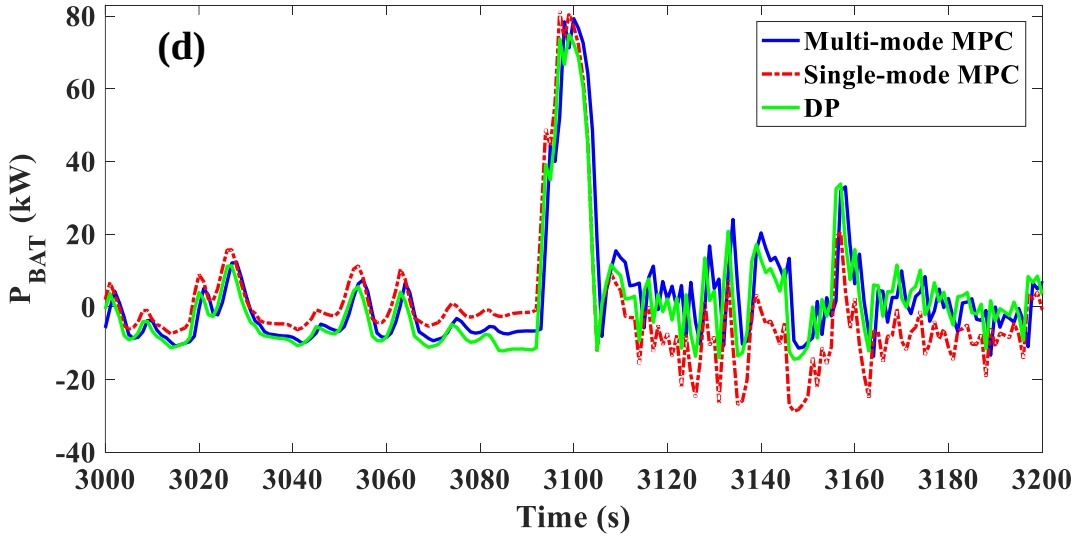


Figure 5.10(d). Local view (3000s to 3200s) of battery power performance comparison of multi-mode MPC (SIL), single-mode MPC (SIL) and DP (offline-simulation).

TABLE 5.1 summarizes the numerical testing results of three different control strategies. Specifically, with the driving pattern recognition method and the offline-optimized control parameters, the multi-

mode strategy can reduce the equivalent hydrogen consumption and the fuel cell power transients by 3.13% and 88.86% compared to single-mode MPC strategy, respectively. Moreover, its performance optimality gap versus DP benchmark is 2.47% (equivalent hydrogen consumption) and 10.14% (fuel cell power transients), respectively. Therefore, the effectiveness of the multi-mode EMS in reducing H2 consumption and fuel cell power transients can be verified via the SIL testing results.

TABLE 5.1. Numerical testing results of three energy management strategies.

| Metrics | DP | Multi-mode MPC | Single-mode MPC |
|---|---|---|---|
| **Final SOC** | 0.7000 | 0.6844 | 0.7010 |
| **Actual H2 consumption (g)** | **474.30** | 480.50 | 502.10 |
| **Equivalent H2 consumption (g)** | | **486.02** | **501.72** |
| **Average fuel cell power transients (w/s)** | **9.07** | **9.99** | **89.71** |

### 5.3.2. Validation of online-learning enhanced predictive energy management strategy

In this subsection, the online-learning enhanced predictive energy management strategy (PEMS), which is designed for a midsize plug-in FCHEV in subsection 4.4, is verified under a multi-pattern testing cycle extracted from ADVISOR [1], where the speed and power demand profiles of the testing cycle are plotted in figure 5.11. This subsection focuses on fuel cell/battery-based hybrid electric vehicles with plug-in property, and thus better fuel economy can be achieved via depleting the low-cost electricity energy for vehicle propulsion.

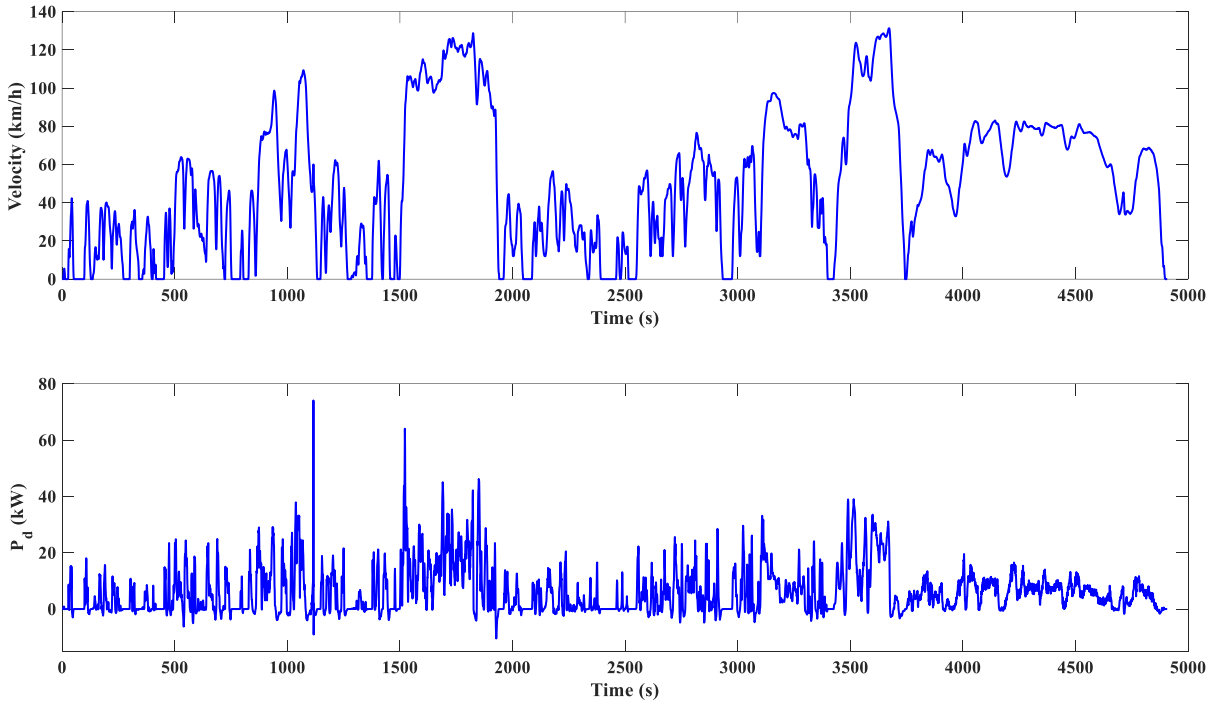


Figure 5.11. Speed and power demand profiles of the combined testing cycle.

Figure 5.12 depicts the comparative results of battery SoC, fuel cell power and battery power in both SIL testing and offline-simulation scenarios. Overall, it can be found that the SIL testing results are very

similar to those of offline-simulation. Moreover, figure 5.13 gives the numerical discrepancy between SIL testing results and offline simulation results. It can be found that the order of performance difference ($10^{-15}$ to $10^{-10}$) is much smaller than the magnitude of original signals, thereby confirming the performance consistency of the SIL testing and offline simulation.

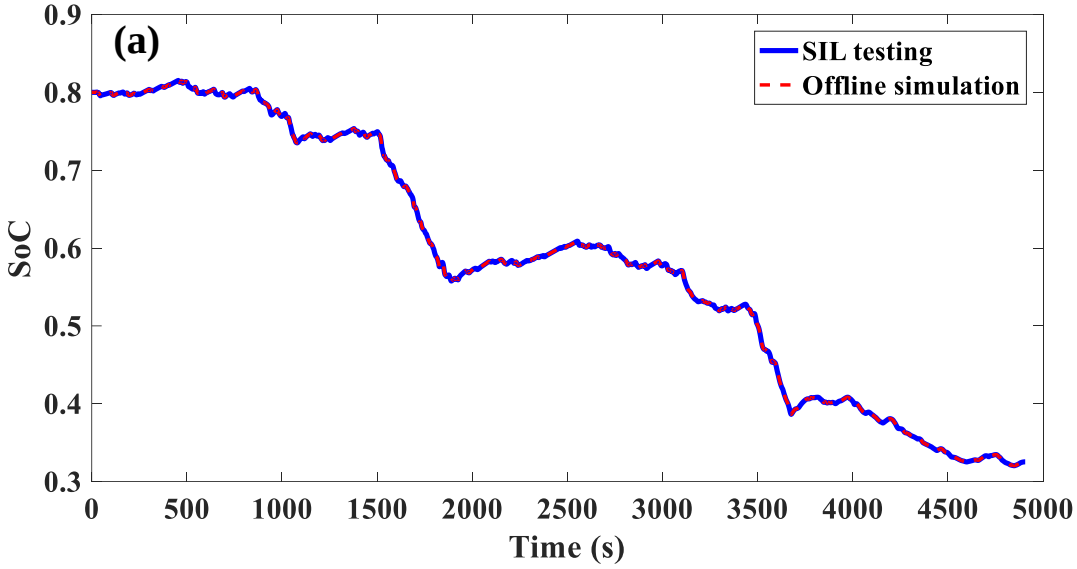


Figure 5.12(a). Battery SoC comparison under SIL and offline simulation scenarios.

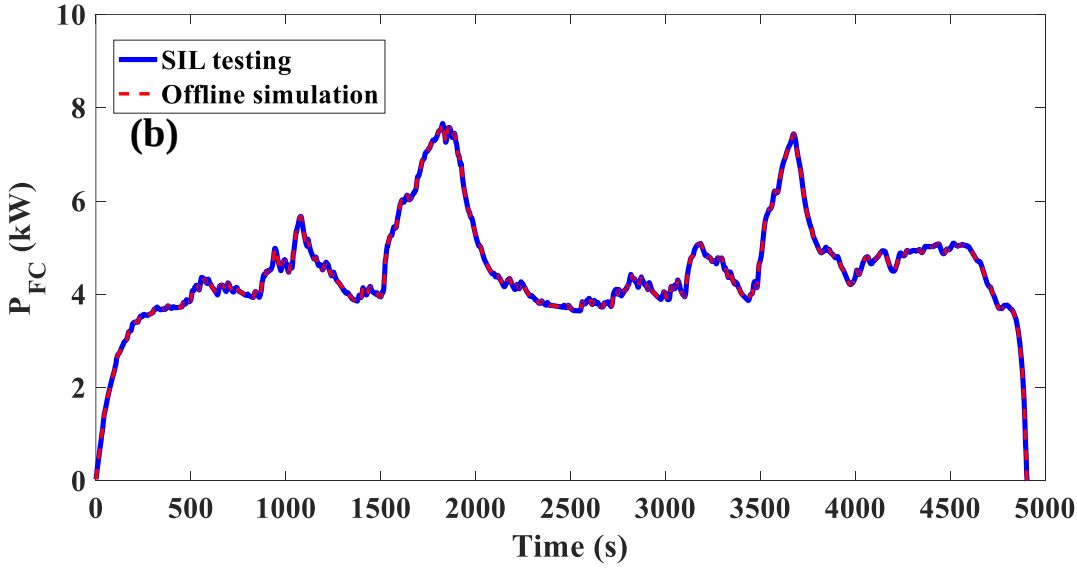


Figure 5.12(b). Fuel cell power comparison under SIL and offline simulation scenarios.

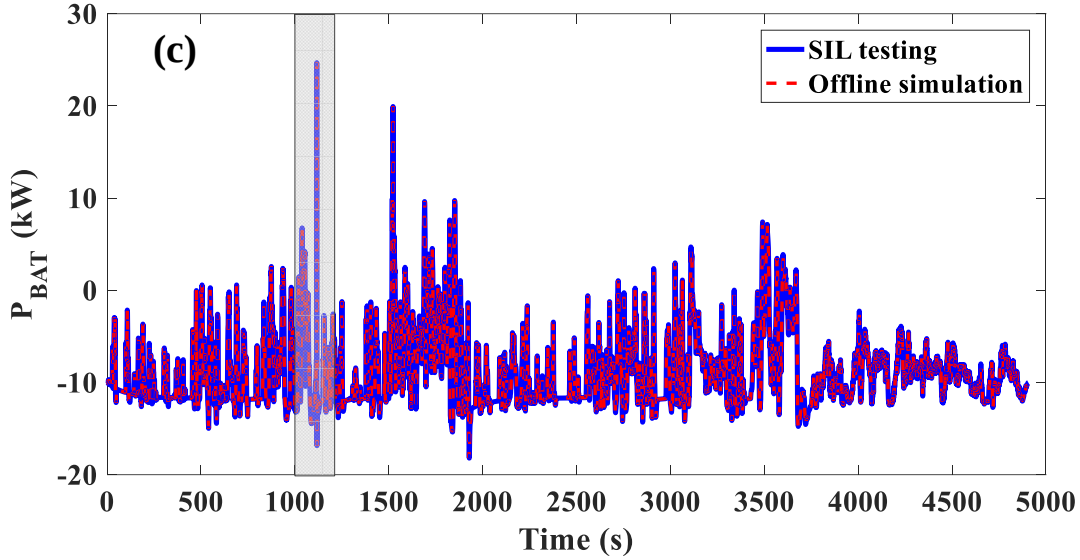


Figure 5.12(c). Battery power comparison under SIL and offline simulation scenarios (Global view).

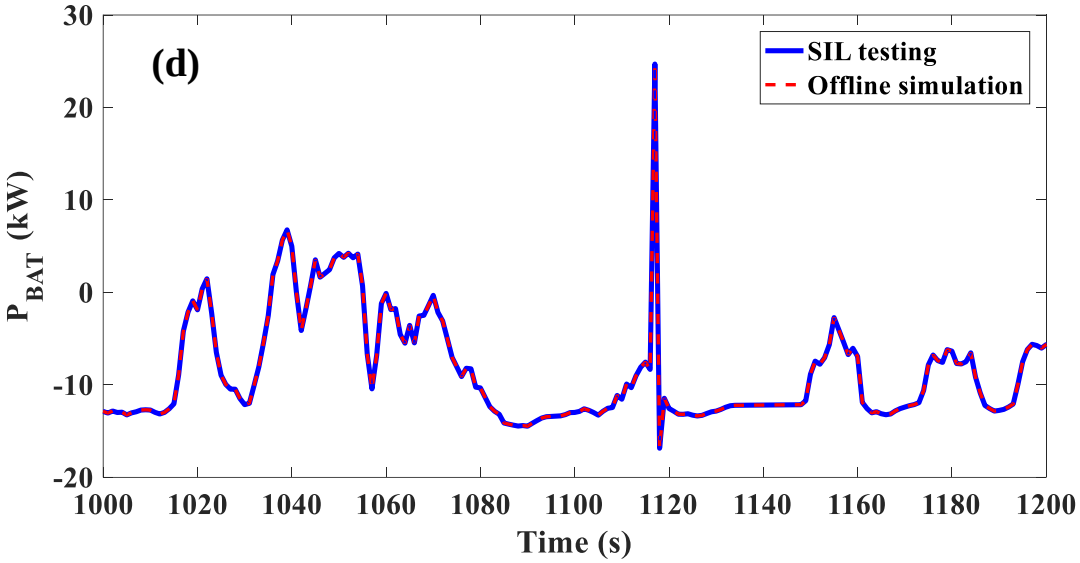


Figure 5.12(d). Battery power comparison under SIL and offline simulation scenarios (Local view: 1000 to 1200s).

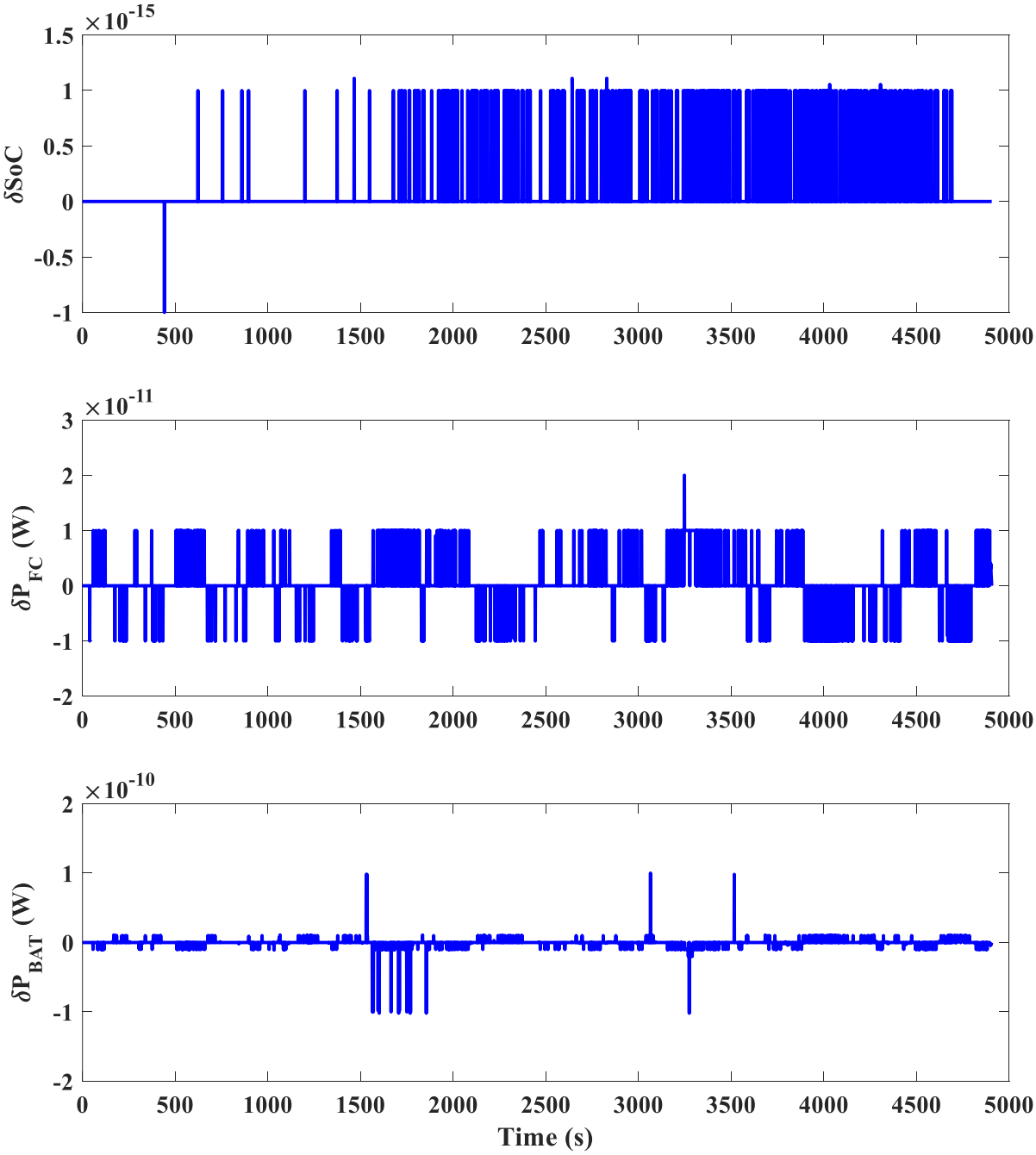


Figure 5.13. Performance discrepancy on SoC, fuel cell power and battery power under SIL and offline-simulation scenarios.

After the performance consistency in SIL testing and offline-simulation scenarios has been verified, the proposed online-learning enhanced PEMS is compared against benchmark strategies in the following parts. Concerning the upper benchmark, dynamic programming (DP), as a global-optima seeking approach, derives the optimal control decisions based on the complete driving cycle knowledge *a priori*. The commonly used charge-depleting/charge-sustaining (CD-CS) strategy is leveraged as the lower benchmark. Detailed description of the benchmark strategies can be found in subsection 4.4.2.2. Please note the prediction horizon for the model predictive control-based strategy is set as 5s, with the sampling

period being 1s. Besides, two real-time strategies, online-learning enhanced PEMS and CD-CS strategy, are tested in SIL platform, while the performance of DP benchmark is obtained in offline simulation.

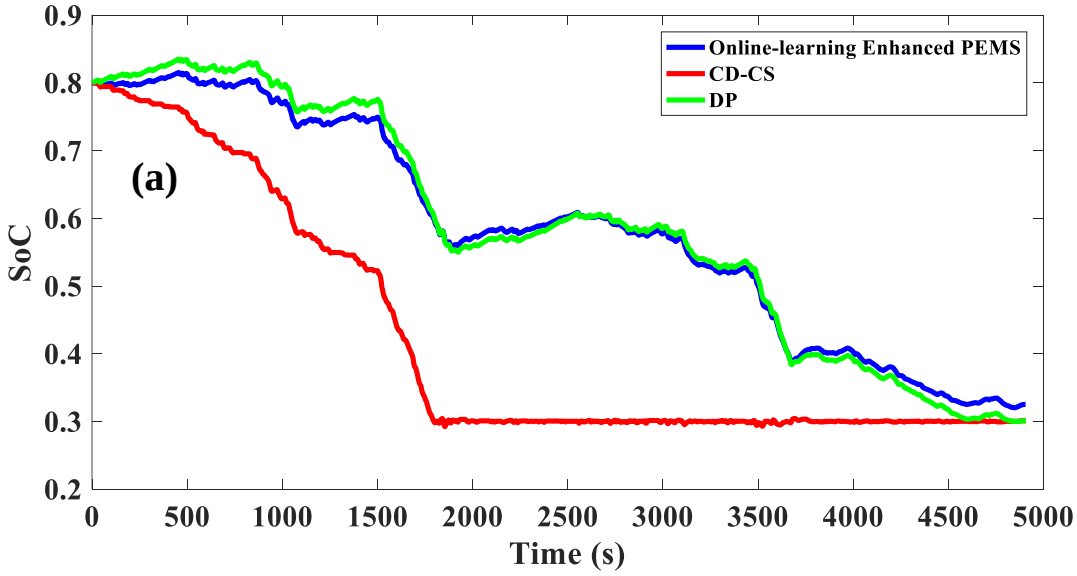


Figure 5.14(a). Battery SoC performance comparison of online-learning enhanced PEMS (SIL), CD-CS (SIL) and DP (offline-simulation).

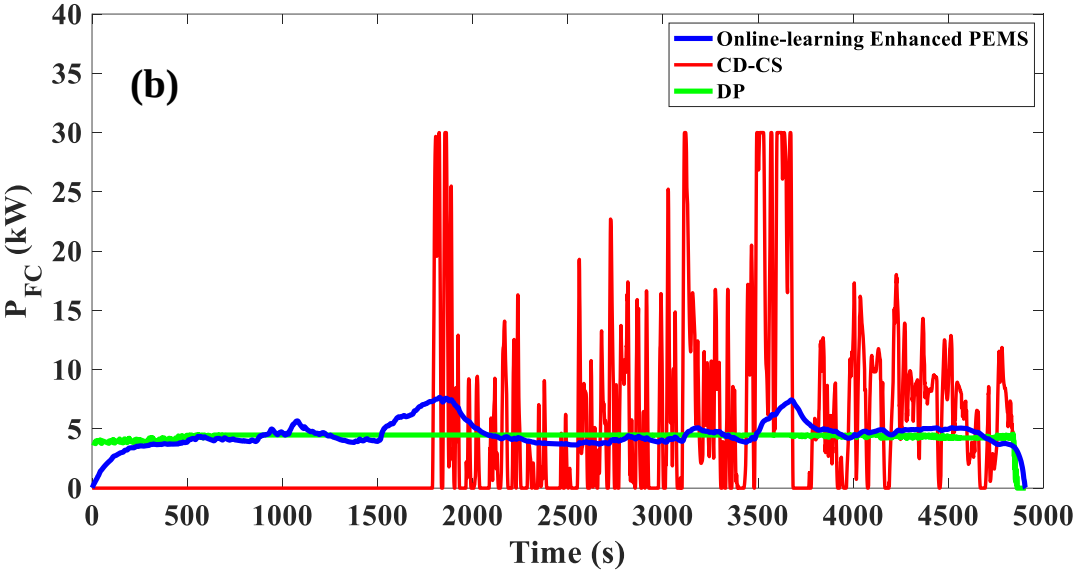


Figure 5.14(b). Fuel cell power performance comparison of online-learning enhanced PEMS (SIL), CD-CS (SIL) and DP (offline-simulation).

Figure 5.14(a) depicts the battery SoC trajectories of three energy management strategies. As can be seen, the online-learning enhanced PEMS performs close to DP benchmark, where its SoC can be depleted at various rates in different driving patterns. In contrast, CD-CS benchmark depletes battery SoC faster than the other two strategies and its SoC is maintained around the lower threshold (0.3) from 1800s until the trip end. As shown in figure 5.14(b), DP strategy results in the fewest fuel cell power

transients among three strategies, where the fuel cell power of online-learning enhanced PEMS is fluctuating around the most efficient working point (~5kW, as shown in figure 4.5). In contrast, the CD-CS strategy brings much larger fuel cell power transients and many fuel cell on-off cycles, which would greatly intensify the performance degradation of fuel cell. Moreover, in figure 5.14(c) and (d), the online-learning enhanced PEMS performs close to DP benchmark in terms of battery power. In contrast, since CD-CS strategy depletes SoC to the lower threshold (0.3) at around 1800s, the battery power of CD-CS strategy is restricted within a limited range since then, compared to other two strategies (as detailed in figure 5.14(d)).

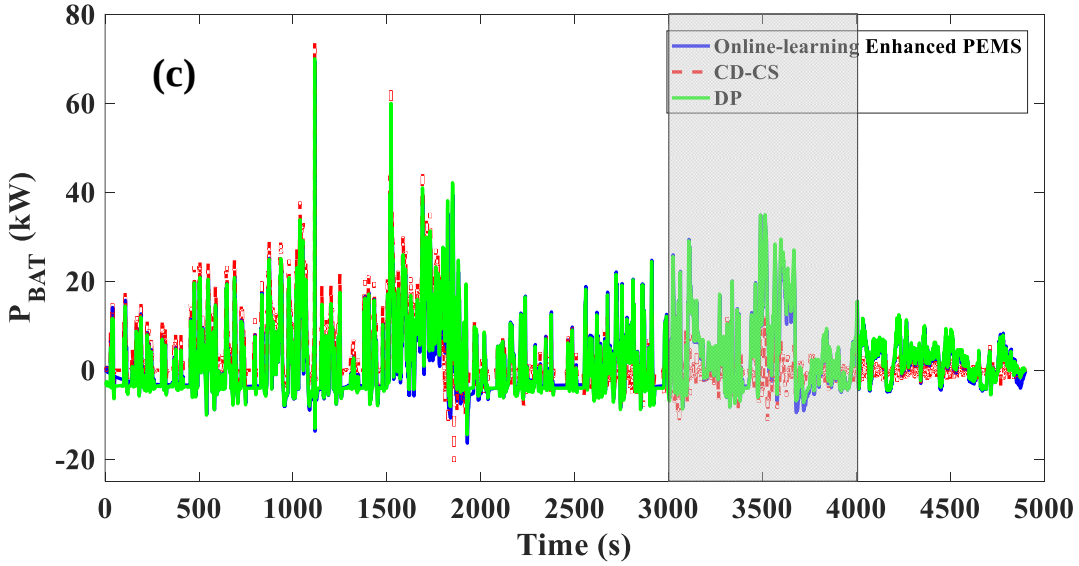


Figure 5.14(c). Global view of battery power performance comparison of online-learning enhanced PEMS (SIL), CD-CS (SIL) and DP (offline-simulation).

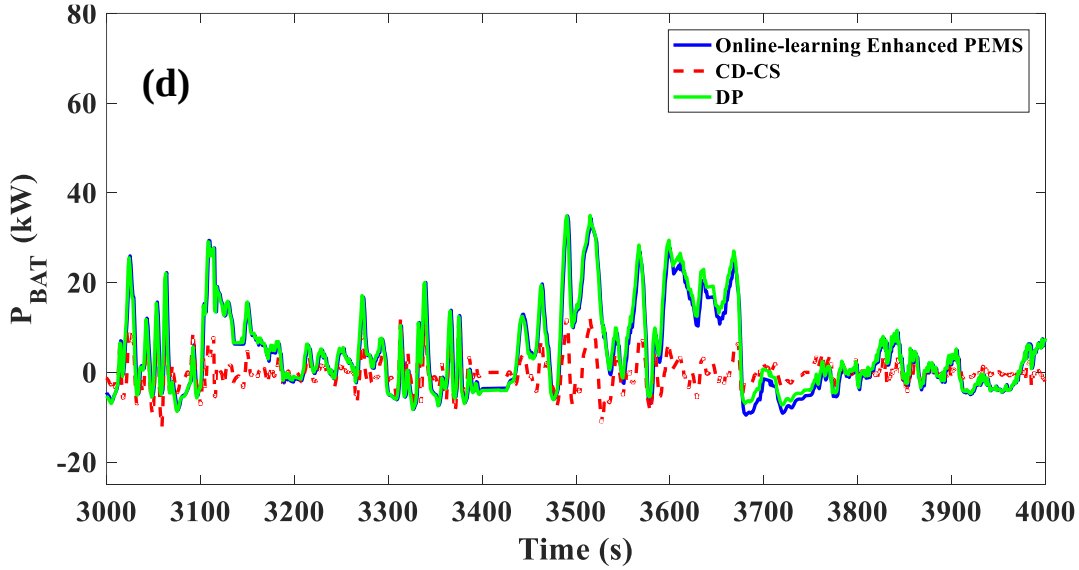


Figure 5.14(d). Local view (3000s to 4000s) of battery power performance comparison of online-learning enhanced PEMS (SIL), CD-CS (SIL) and DP (offline-simulation).

TABLE 5.2. Numerical testing results of three energy management strategies.

| Metrics | DP | Online-learning enhanced PEMS | CD-CS |
|---|---|---|---|
| **Final SOC** | 0.3000 | 0.3218 | 0.3011 |
| **Actual H2 consumption (g)** | **245.9** | 262.8 | 301.6 |
| **Equivalent H2 consumption (g)** | | **255.1** | **301.2** |
| **Average fuel cell power transients (W/s)** | **5.6** | **11.8** | **375.1** |

TABLE 5.2 lists the numerical testing results of three control strategies. As can be seen, the proposed online-learning enhanced PEMS can respectively reduce the equivalent hydrogen consumption and fuel cell power transients by 15.3% and 96.9% versus the CD-CS benchmark. Its hydrogen consumption optimality gap against DP benchmark is 3.7%. Therefore, the effectiveness of the online-learning enhanced PEMS in reducing H2 consumption and fuel cell power transients versus CD-CS benchmark can be verified via the SIL testing results.

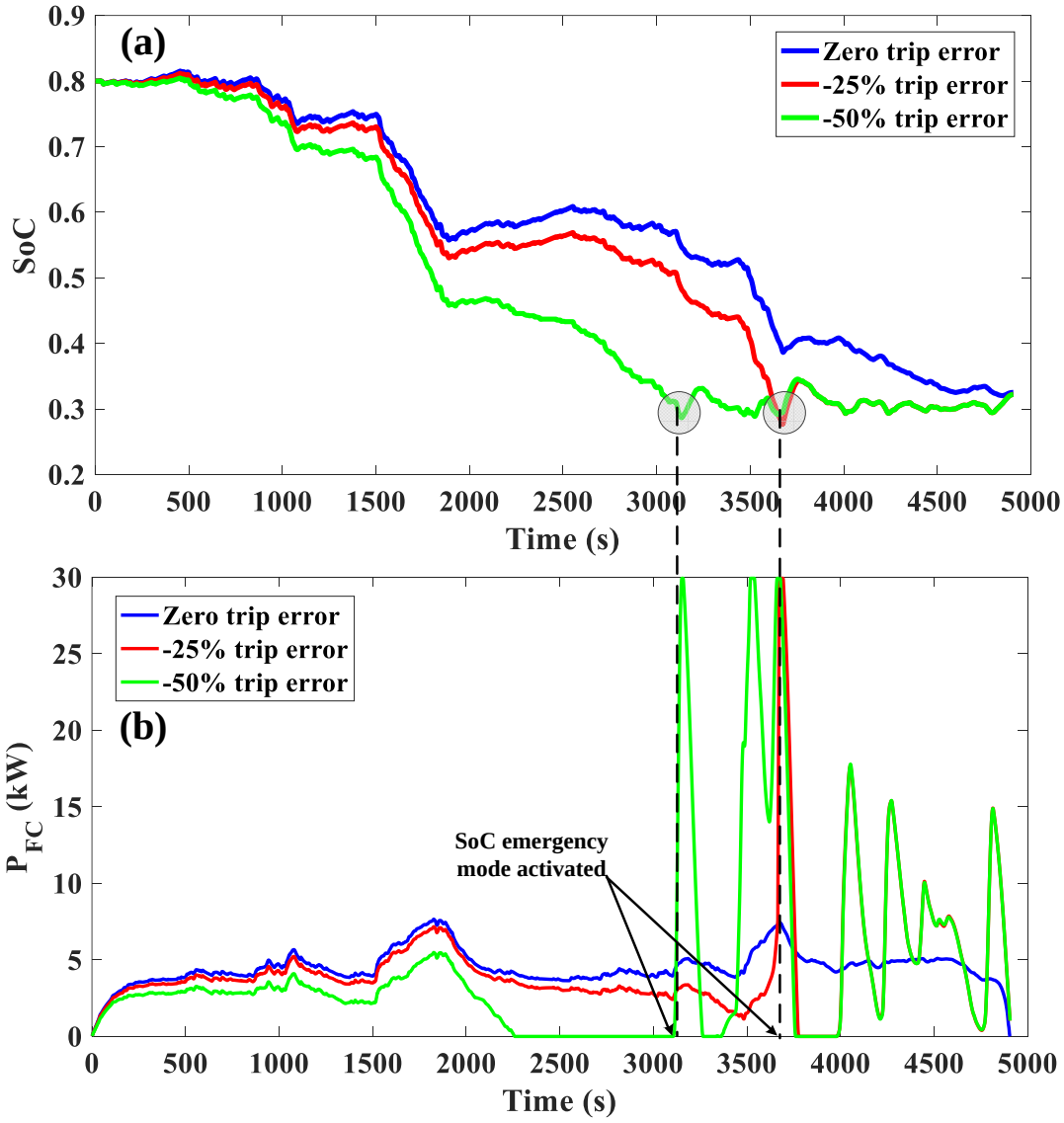


Figure 5.15. SIL testing results of online-learning PEMS under trip duration estimation errors: (a) SoC and (b) fuel cell power.

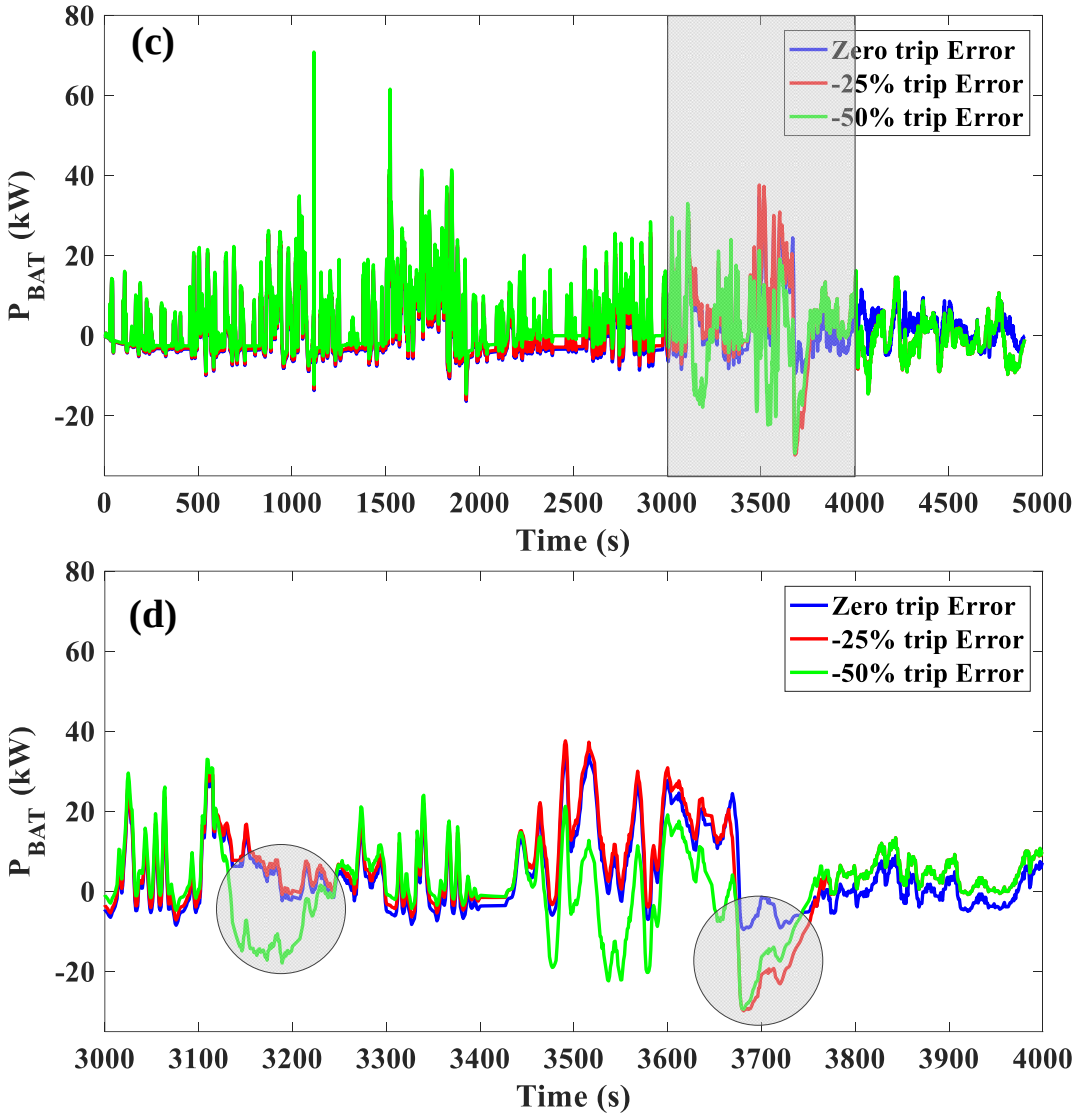


Figure 5.15. SIL testing results of online-learning PEMS under trip duration estimation errors: (c) battery power (global view) and (d) battery power (local view: 3000 to 4000s).

Due to the unpredictable traffic events, there would be difference between the actual trip duration and the estimated one (from telematics systems, like GPS), which would affect the precision of battery SoC reference generation (as detailed in subsection 3.3.2). Figure 5.15 depicts the performance comparison of the proposed PEMS under -25% and -50% trip duration estimation errors. Please note the negative errors here mean that the estimated trip time is shorter than the actual one. As shown in figure 5.15(a), under negative trip duration errors, the depletion of battery SoC is accelerated compared to zero-error case. Moreover, the larger the negative error is, the longer the charge-sustaining driving phase would be. When battery SoC < 0.3, the SoC emergency mode is activated (see figure 5.15(b)) to urge fuel cell working in an aggressive way with larger power transients than in SoC normal mode. As a consequence of that, the battery SoC would not continue to drop but fluctuate around the lower threshold (0.3), meaning the SoC emergency mode can effectively prevent battery over-discharge, thereby ensuring the

operation safety of battery pack. Figure 5.15(c) and (d) depict the battery power profiles under three error scenarios. When SoC emergency mode is activated (SoC<0.3, as highlighted with grey circles in figure 5.15(d)), battery tends to absorb negative power to avoid the further drop of SoC.

### 5.3.3. Validation of the integrated predictive energy management strategy

In this subsection, the integrated predictive energy management strategy (PEMS) proposed in subsection 4.5 is verified under a realistic GPS-collected mail-delivery mission profile [13], where the speed and power demand profiles of the testing cycle are given in figure 5.16. As can be seen, the top speed is around 60 km/h and frequent vehicle start-stops can be observed: this represents a typical city driving scenario. To highlight the functionality of the 1.2kW fuel cell system as a range-extender, the initial SoC is set to 0.55 and the final target SoC is set to 0.4. The reason for choosing such a limited SoC variation range is that the battery of Mobypost is hugely oversized, so the vehicle would work under the all-electric mode if we pick a wider variation range on SoC (e.g. [0.4, 0.8]). In this case, the performance of fuel cell as a range extender cannot be evaluated.

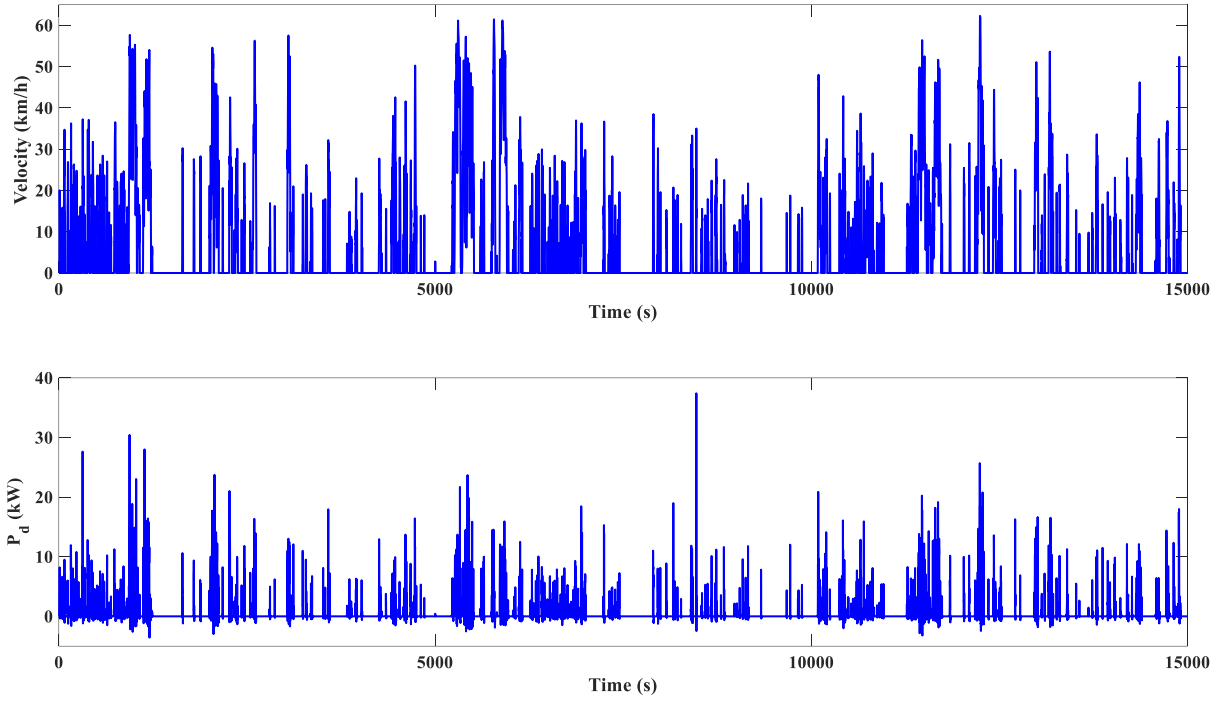


Figure 5.16. Speed and power demand profiles of the mail-delivery mission profile.

Similarly, the performance consistency in both SIL testing and offline simulation is examined firstly. As shown in figure 5.17, the SIL testing results are very similar to those of offline simulation. Moreover, the numerical difference on battery SoC, fuel cell power and battery power under two testing scenarios is given in figure 5.18. It can be observed that the order of difference ($10^{-15}$ to $10^{-11}$) is sufficiently smaller than the magnitude of original signals. Hence, it can be confirmed that the obtained results in both SIL testing and offline simulation are identical.

Thereafter, the proposed integrated PEMS (termed as “A-MPC”) is compared versus two benchmark strategies to further verify its effectiveness. Based on the complete driving information beforehand, dynamic programming (DP) is leveraged to extract the optimal power-allocating effect, where the performance of DP is regarded as the upper benchmark. In contrast, the lower benchmark strategy is established with the help of linear SoC reference and model predictive control (termed as “L-MPC”). More details regarding the formulation of benchmark strategies are available in subsection 4.5.2.3. Please note for MPC-based strategies, the prediction horizon is set as 5s, with the sampling period being 1s. In addition, both A-MPC and L-MPC strategies are executed in the online-simulation platform (MicroAutoBox II), while the DP is performed in offline simulation (host PC). The corresponding comparative results are given in figure 5.19.

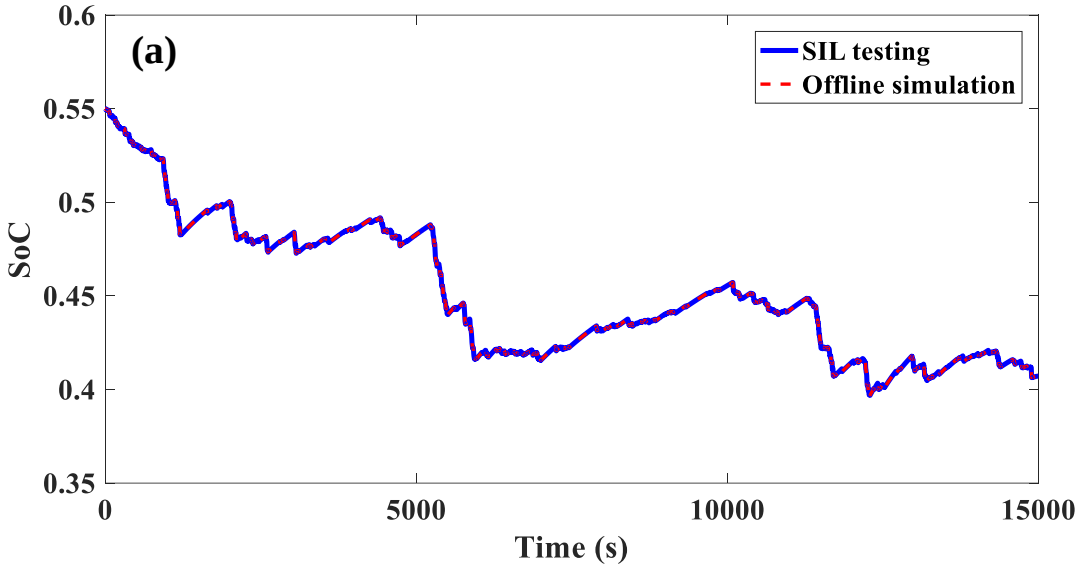


Figure 5.17(a). Battery SoC comparison under SIL and offline simulation scenarios.

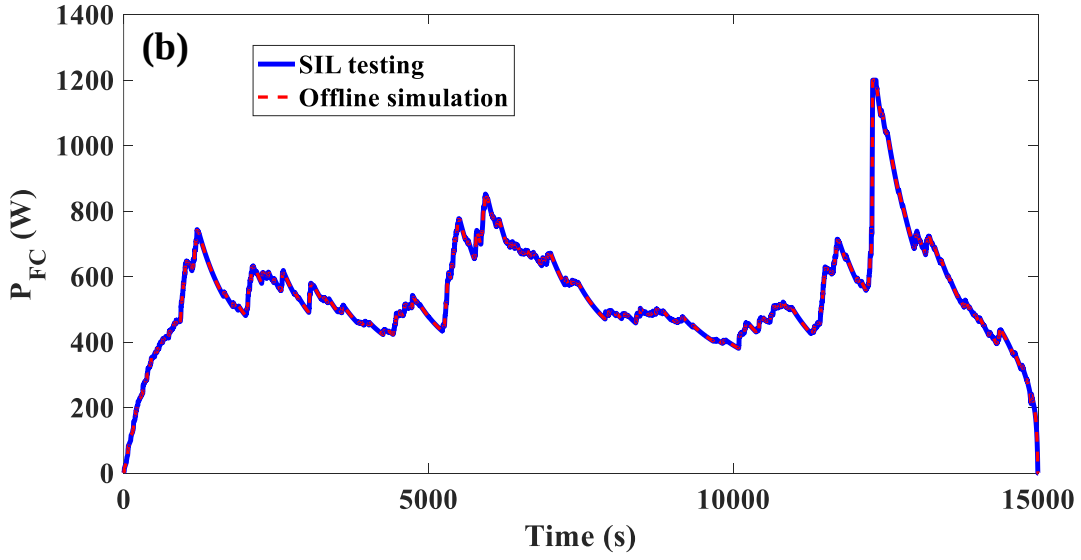


Figure 5.17(b). Fuel cell power comparison under SIL and offline simulation scenarios.

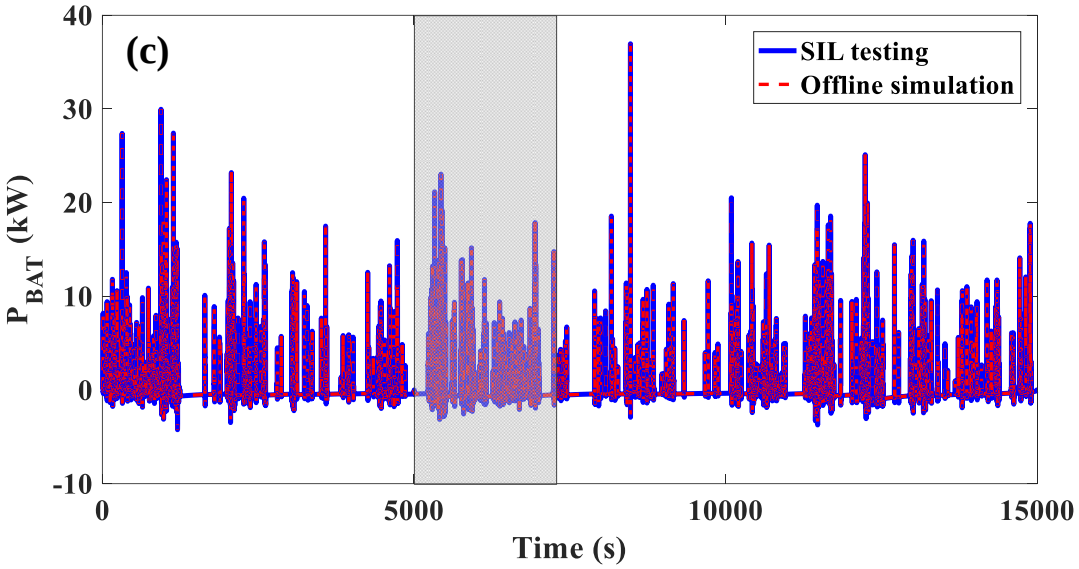


Figure 5.17(c). Battery power comparison under SIL and offline simulation scenarios (global view).

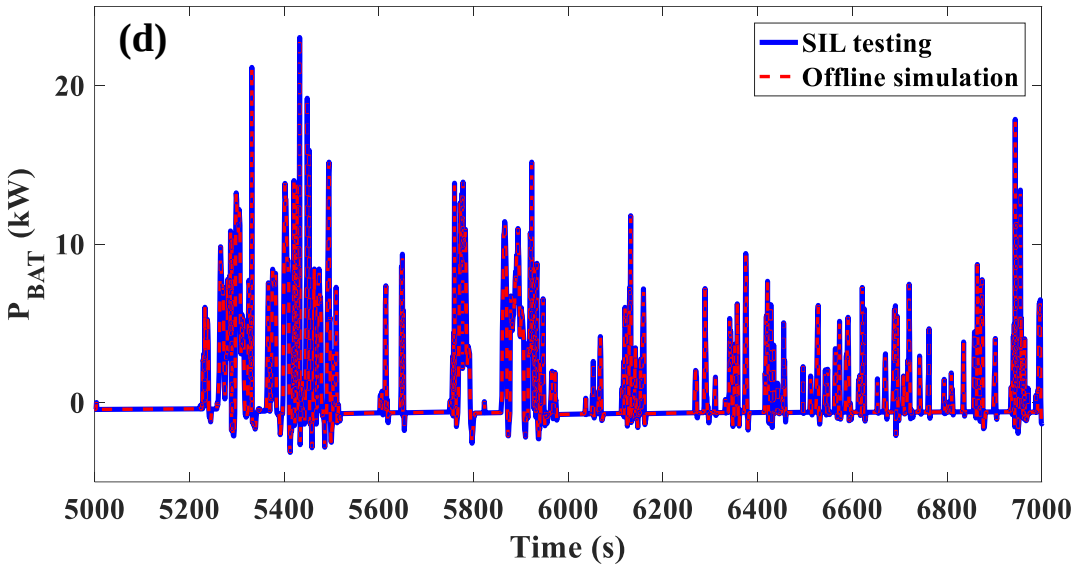


Figure 5.17(d). Battery power comparison under SIL and offline simulation scenarios (local view: 5000 to 7000s).

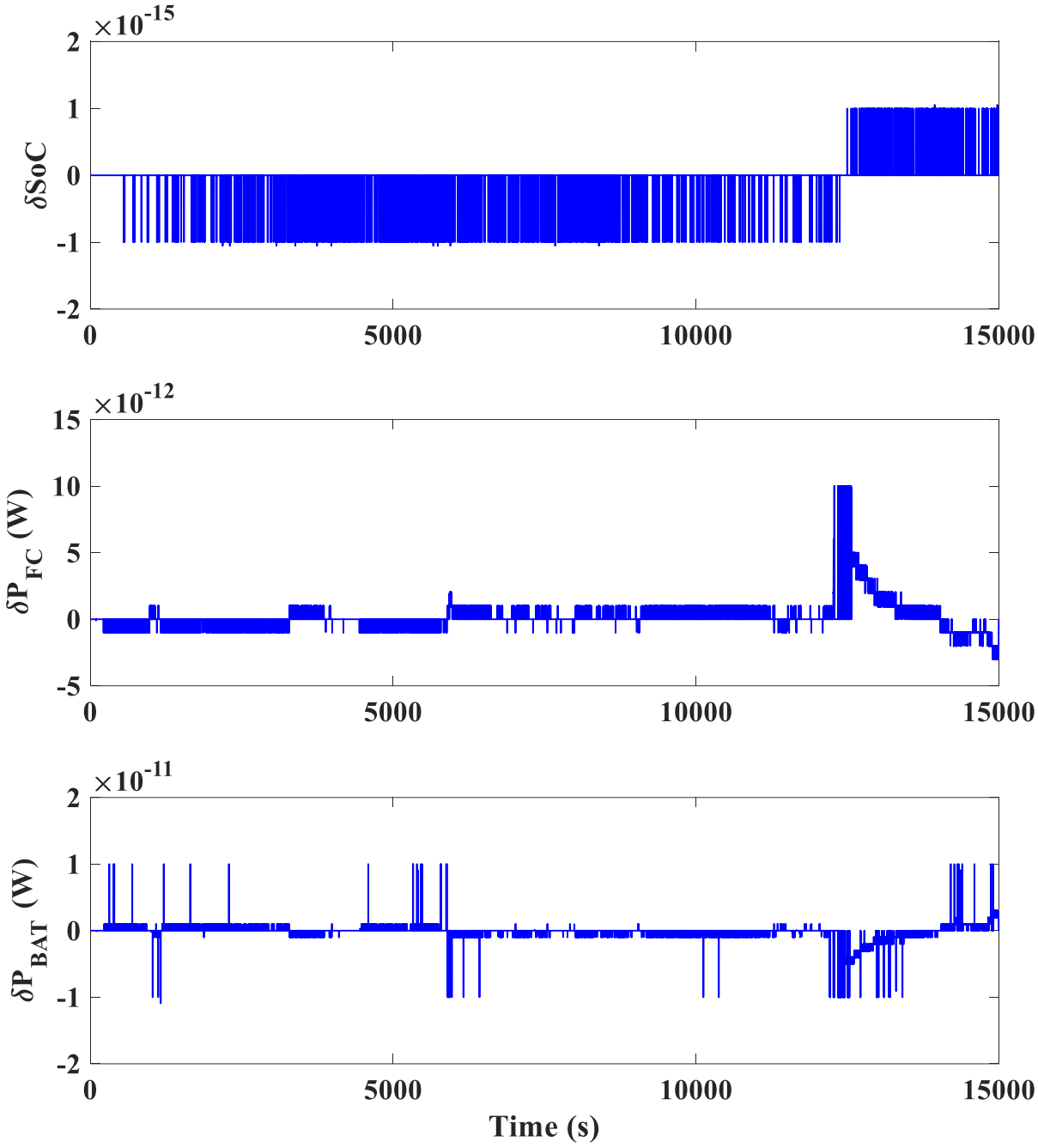


Figure 5.18. Performance discrepancy on SoC, fuel cell power and battery power under SIL and offline-simulation scenarios.

As shown in figure 5.19(a), A-MPC strategy performs close to DP benchmark in terms of battery SoC. In contrast, the lower benchmark L-MPC strategy intends to keep SoC linearly depleting over the testing cycle. Nevertheless, due to the maximal power limits of fuel cell, its SoC trajectory deviates from linear form in some peaking power regions, as highlighted with the grey circles. Three strategies perform similarly in terms of final SoC. As can be observed in figure 5.19(b), DP leads to the most smoothed fuel cell power profile among three strategies, where most of the fuel cell working points are distributed around the most efficient point (~ 550W, as shown in figure 4.6). In contrast, A-MPC strategy can

maintain the most of fuel cell working points around the most efficient point, but the fuel cell power transients are larger compared to DP benchmark. Compared to other strategies, the lower benchmark L-MPC strategy brings larger fuel cell power transients and more frequent fuel cell on-off cycles. On this basis, the fuel cell working points are no longer distributed around the most efficient point. As a result, L-MPC strategy would lead to the drop of average fuel cell efficiency and the compromise of fuel cell durability, compared to other two strategies. Besides, as shown in figure 5.19(c) and (d), the performance discrepancy in terms of battery power among three strategies is insignificant.

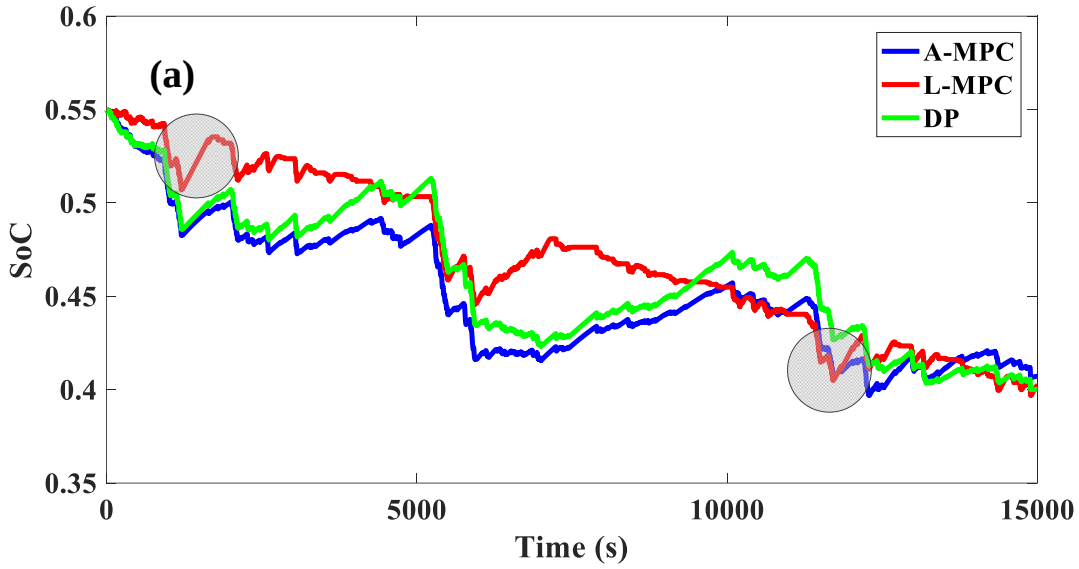


Figure 5.19(a). Battery SoC performance comparison of A-MPC (SIL), L-MPC (SIL) and DP (offline-simulation).

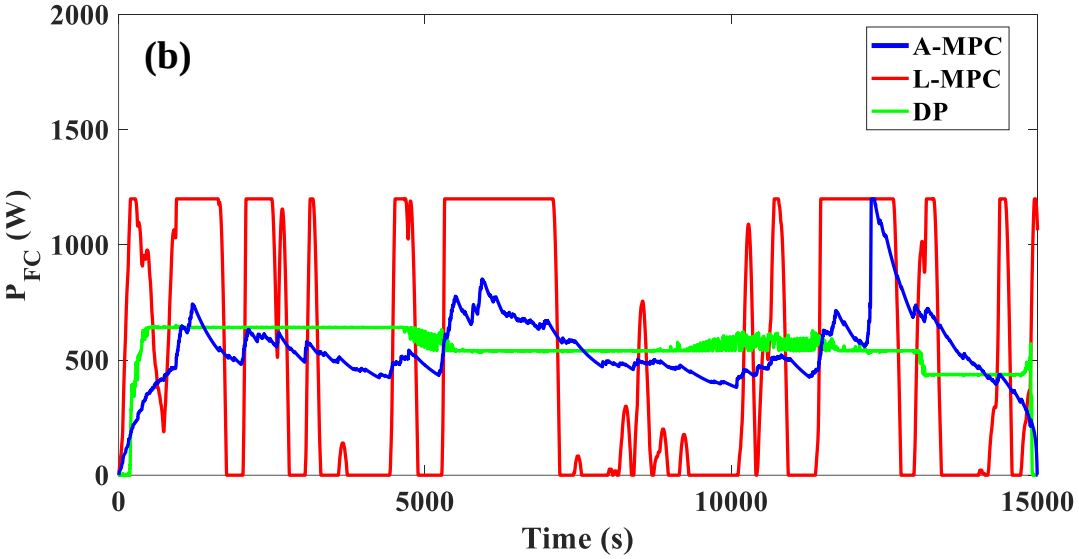


Figure 5.19(b). Fuel cell power performance comparison of A-MPC (SIL), L-MPC (SIL) and DP (offline-simulation).

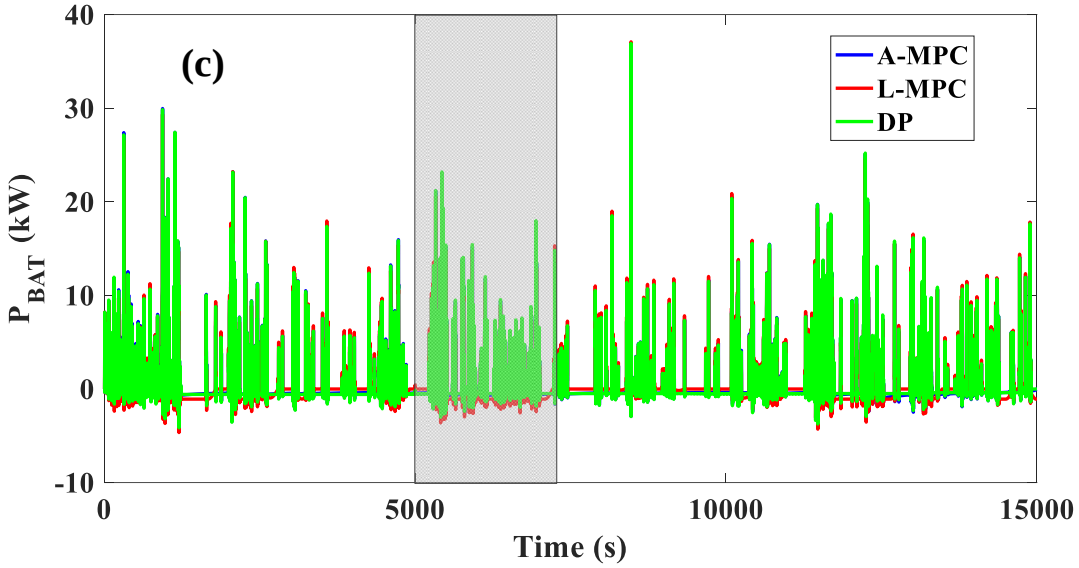


Figure 5.19(c). Global view of battery power performance comparison of A-MPC (SIL), L-MPC (SIL) and DP (offline-simulation).

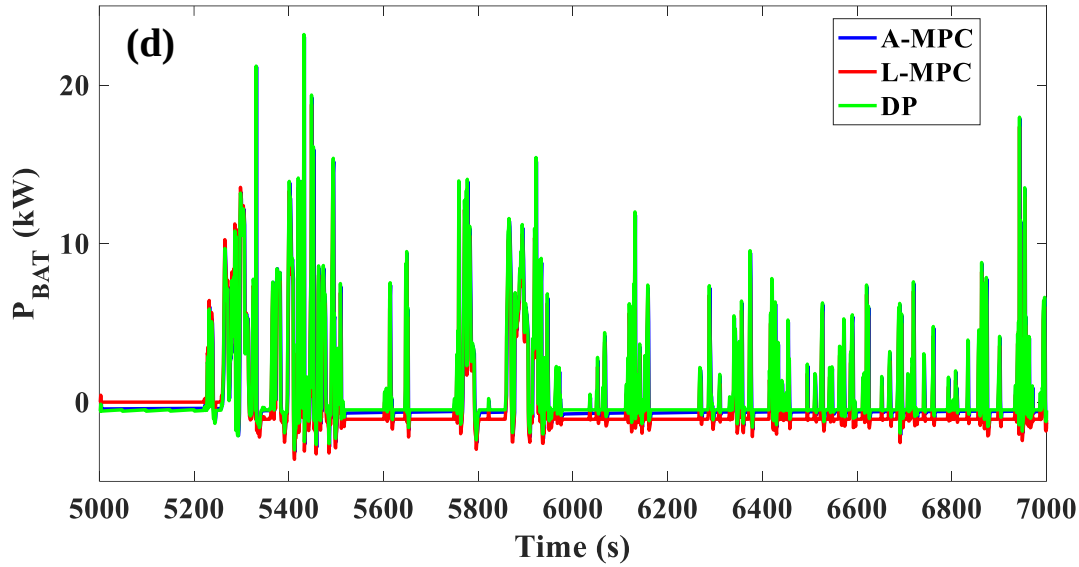


Figure 5.19(d). Local view (5000 to 7000s) of battery power performance comparison of A-MPC (SIL), L-MPC (SIL) and DP (offline-simulation).

TABLE 5.3. Numerical testing results of three energy management strategies.

| Metrics | DP | A-MPC | L-MPC |
|---|---|---|---|
| **Final SOC** | 0.4000 | 0.4063 | 0.4016 |
| **Actual H2 consumption (g)** | **96.9** | 99.3 | 102.1 |
| **Equivalent H2 consumption (g)** | | **97.7** | **101.7** |
| **Average fuel cell power transients (W/s)** | **0.96** | **1.02** | **2.25** |
| **Fuel cell high efficiency ratio** | **97.54%** | **86.39%** | **7.51%** |

The numerical testing results of three strategies are summarized in TABLE 5.3. As can be seen, all three energy management strategies can lead to the similar values of final SoC, indicating the similar level of battery depth of discharge. Moreover, the proposed A-MPC strategy can respectively reduce the

equivalent hydrogen consumption and fuel cell power transients by 3.93% and 54.67% compared to lower benchmark (L-MPC), wherein the performance optimality gap against DP benchmark is 0.83% and 6.25% in terms of equivalent H2 consumption and fuel cell power transients, respectively. Besides, it can also be found that, the lower benchmark L-MPC strategy can maintain 7.51% of fuel cell working points distributing in the predefined high efficiency area ([400, 800] W, as shown in figure 4.6), while this ratio is greatly improved to 86.39% after using the A-MPC strategy, which is close to the result of DP (97.54%). From the obtained SIL testing results, it can be confirmed that (i) the proposed integrated PEMS can improve fuel cell working efficiency, save hydrogen consumption and mitigate the fuel cell degradation caused by transient loadings than the lower benchmark strategy; (ii) the corresponding performance optimality gap against DP benchmark is insignificant.

## 5.4. Conclusion

This chapter presents the setup of the online-simulation platform and the Software-in-the-Loop (SIL) validation of predictive energy management strategies. The online-simulation platform is composed of hardware and software subsystems. Specifically, the hardware subsystem comprises a host PC, a dSPACE MicroAutoBox II real-time system and an associated DC power supply, where the host PC and the MicroAutoBox II is connected via the Ethernet interface. The software subsystem is made up of the vehicular powertrain model and the control strategies developed in the MATLAB/Simulink environment, the dSPACE real-time interface for linking the MATLAB software to the dSPACE hardware, and the dSPACE ControlDesk V4.2 as the human machine interface during the SIL testing. Based on the established online-simulation platform, the proposed energy management strategies are compiled into C code via PowerPC compiler, downloaded into the dSPACE hardware (MicroAutoBox II), and compared against the benchmark strategies. From the SIL testing results, it can be confirmed that the proposed ready to be embedded EMSs are:

(a) **Operational**: All the devised energy management strategies can be properly embedded into and correctly executed on the target MicroAutoBox II real-time system;
(b) **Consistent**: The control performance discrepancy between SIL testing and offline simulation is neglectable, meaning the obtained results in both testing scenarios are identical;
(c) **Functional**: The proposed control strategies outperform lower benchmark strategies in terms of fuel cell working efficiency, hydrogen fuel consumption and fuel cell durability. Meanwhile, regarding these evaluation metrics, the proposed control strategies result in the similar performance versus the upper benchmark strategies.

To sum up, the SIL testing results have demonstrated that the proposed control strategies are operational in the real-time embedded system with all predefined objectives (e.g. the enhancement of fuel efficiency and fuel cell durability) realized, thereby further validating their functionality and real-time suitability.

## References


[1]. W. Chaaban, M. Schwarz, B. Batchuluun, H. Sheng, J. Börcsök, "A partially automated HiL test environment for model-based development using Simulink® and OPC technology," ***2011 XXIII International Symposium on Information, Communication and Automation Technologies***, Sarajevo, 2011, pp. 1-6, doi: 10.1109/ICAT.2011.6102112.

[2]. J. Mina, Z. Flores, E. López, A. Pérez, J. -. Calleja, "Processor-in-the-loop and hardware-in-the-loop simulation of electric systems based in FPGA," ***2016 13th International Conference on Power Electronics (CIEP)***, Guanajuato, 2016, pp. 172-177, doi: 10.1109/CIEP.2016.7530751.

[3]. Matlab Documentation. What is Hardware-in-the-Loop Simulation? [Online]. ***Available at***: https://www.mathworks.com/help/physmod/simscape/ug/what-is-hardware-in-the-loop-simulation.html

[4]. A. Biswas, A. Emadi, "Energy Management Systems for Electrified Powertrains: State-of-the-Art Review and Future Trends," in ***IEEE Transactions on Vehicular Technology***, vol. 68, no. 7, pp. 6453-6467, July 2019, doi: 10.1109/TVT.2019.2914457.

[5]. P. Waeltermann. Hardware-in-the-Loop: The Technology for Testing Electronic Controls in Vehicle Engineering. [Online]. ***Available at***: https://www.dspace.com/files/pdf1/dspace-paper_hil_overview_waeltermann_e_160405.pdf.

[6]. E. Ágústsson, Hardware-in-The-Loop Simulation of a High Speed Servo System, ***Master of Science Thesis at KTH Industrial Engineering and Management Machine Design***, 2013.

[7]. H. J. Ferreau et al., qpOASES User's Manual, Version 3.2 [Online], Apr. 2017. ***Available at***: https://github.com/coin-or/qpOASES/blob/master/doc/manual.pdf.

[8]. Real-time interface (RTI): Implementation software for running models on dSPACE hardware [Online]. ***Available at***: https://www.dspace.com/en/pub/home/products/sw/impsw/realtimeinterf.cfm.

[9]. ControlDesk: Universal modular experiment and instrumentation software for electronic control unit (ECU) development [Online]. ***Available at***: https://www.dspace.com/en/inc/home/products/sw/experimentandvisualization/controldesk.cfm.

[10]. MicroAutoBox II: Compact and robust prototyping system for in-vehicle applications [Online]. ***Available at:*** https://www.dspace.com/en/pub/home/products/hw/micautob/microautobox2.cfm.

[11]. MicroAutoBox II: Product brochure [Online]. ***Available at***: https://www.dspace.com/shared/data/pdf/2020/dSPACE-MicroAutoBoxII_Product-Brochure_2020-02_EN.pdf.

[12]. ADVISOR. Advanced Vehicle Simulator [online]. Available at: http://adv-vehicle-sim.sourceforge.net/.

[13]. S. Faivre, A. Ravey, D. Guilbert, A. N'Diaye, A. Gaillard, et al.. Part 2- Mobypost vehicle's powertrain design and experimental validation. ***International Conference on Fundamentals and Development of Fuel Cells (FDFC 2013)***, Apr. 2013, Germany.

# Chapter 6. Conclusion

## 6.1. Summary of the research works

To improve the economic and durability performance of fuel cell/battery-based hybrid electric vehicles, the goal of this PhD thesis was to develop an intelligent energy management strategy to coordinate the outputs of multiple energy sources within vehicle's propulsion system. In contrast to traditional control strategies, this thesis especially focused on the possibility of embedding the driving predictive information (e.g. speed profiles, driving pattern, etc.) into the real-time multi-objective decision-making framework, so as to seek further performance improvement (e.g. fuel economy, fuel cell lifetime prolongation, etc.) by predictive knowledge integration.

First of all, the research background, the state-of-the-art development status on fuel cell hybrid electric vehicles (FCHEV), energy management strategies (EMS), and driving prediction techniques were thoroughly reviewed. Then, a comprehensive analysis on the knowledge gaps towards existing studies was conducted. To compensate for the limitations in previous works, the major objectives of this work were indicated, so as to guide the technical development in the following sections. Thereafter, a detailed comparative study on energy management strategies for FCHEVs was conducted, including rule-based and optimization-based strategies. Through comparing the advantages and disadvantages of existing methods, model predictive control (MPC) was selected for real-time decision-making due to its capacity of handling the complex time-varying constrained systems (e.g. hybrid propulsion system). In the end, the general mathematical formulation of MPC was presented, so as to facilitate the development of MPC-based energy management strategies.

Specifically, following effective contributions were introduced via this thesis, so as to attempt to bridge the research gaps against existing studies. First, to provide accurate predictive information for decision-making, several driving prediction techniques were proposed:

- ***Vehicle speed prediction techniques***: to estimate the future behaviors of a dynamic system over each MPC rolling optimization horizon, three vehicle speed predictors were established, including a layer recurrent neural network predictor, an online-learning enhanced Markov Chain predictor and a fuzzy C-means clustering enhanced Markov Chain predictor. Validation results have shown that the proposed speed predictors outperformed the benchmark methods in terms of forecast precision and robustness.
- ***Driving pattern recognition method***: a Markov Chain based driving pattern recognition technique was proposed to differentiate the real-time driving patterns, that is urban, suburban and highway, which thus established a basis for the realization of multi-mode EMS framework.
- ***Battery state-of-charge (SoC) reference planning approach***: an adaptive battery SoC reference estimation approach was devised, which could guide the depletion of battery energy in face of

changeable driving scenarios.

Subsequently, to combine the predictive information for real-time power-allocation, several predictive energy management strategies were developed under different vehicle's sizing configurations:

- ***Multi-mode predictive energy management strategy***: with the assistance of the Markov driving pattern recognizer and the layer recurrent neural network predictor, a multi-mode EMS was developed for a midsize sedan powered by fuel cell and battery, aiming at splitting power demand under changeable driving patterns.
- ***Online-learning enhanced predictive energy management strategy***: based on the online-learning enhanced Markov predictor and the adaptive SoC reference generator, a predictive EMS was designed for a midsize plug-in fuel cell hybrid electric vehicle, so as to effectively control the drop of battery SoC with regard to multiple driving scenarios.
- ***Integrated predictive energy management strategy for urban postal delivery vehicle***: for a light-duty plug-in fuel cell electric vehicle dedicated to postal delivery, an integrated predictive energy management strategy with the help of fuzzy C-means enhanced Markov predictor was built for improving the fuel efficiency and the fuel cell durability.
- ***Operational analysis under different component-sizing configurations***: to further explore the potential impacts on EMS performance by different degrees of hybridization, a numerical analysis regarding the vehicle's operating cost under different powertrain sizing configurations was presented.

In order to further verify the effectiveness of the proposed energy management strategies, an online-simulation platform was established based on the dSPACE MicroAutoBox II real-time system. First of all, the Software-in-the-Loop (SIL) validation results show that all proposed control strategies could be properly embedded into and correctly executed on the target hardware (MicroAutoBox II), thus verifying the functionality and real-time suitability of the proposed strategies. Moreover, it has been proven that the results from both offline-simulation and SIL testing are highly consistent. Overall, the proposed energy management strategies could realize the predefined control objectives in real-time, thus further indicating its possibility of being integrated into the onboard ECUs for real applications.

## 6.2. Future research directions

Despite the progresses regarding the energy management strategies for fuel cell electric vehicles in this thesis, further intensive studies should be conducted to improve the energy allocation performance. Specifically, future works would concentrate on the following aspects:

- This thesis only focused on retarding fuel cell degradation imposed by harsh power (current) transients, whereas other factors that may compromise the durability of fuel cell systems were not considered, such as working at extremely high/low loadings, frequent start-stop cycling, etc.

In future works, it is expected to systematically consider these degrading factors by quantifying them in the multi-objective cost function when making power allocation decisions. In parallel, if more advanced fuel cell and battery models that can represent the actual degrading behaviors of energy sources can be integrated with the control strategies, a long-term evaluation framework regarding the life-cycle economic performance of fuel cell vehicles can be established to help minimizing the vehicle's total ownership costs.

- In addition, this thesis has validated the proposed energy management strategies in software-in-the-loop environment, which focused on verifying the embeddability into the real-time hardware of the control strategies. In the next step, a hardware-in-the-loop (HIL) platform will be established, which would integrate multiple pieces of real hardware (e.g. battery, power load, fuel cell, etc.) into the testing platform. In HIL platform, the proposed control strategies would be further examined with the presence of the actual physical powertrain components, which would be closer to the real vehicle testing scenarios compared to SIL testing. Thereafter, the control performance testing on real vehicle prototype can be considered.
- Due to the abundant historical driving database of the postal-delivery vehicles, the past driving experience is useful in guiding future energy distributions. Therefore, it is expected in future works to develop a data-driven approach (e.g. deep neural networks) to plan the future usage of onboard electricity energy for further improving the fuel economy performance when charge-depleting mode is involved.
- Powertrain component sizing plays an important role in vehicle's drivability and economic performance. In future works, a co-optimization framework for fuel cell/battery-based hybrid electric vehicles considering the component degradations will be developed, which can simultaneously optimize the sizing parameters and the vehicle's total ownership cost given the desired driving profiles.
- Reinforcement-learning-based control strategies have gained substantial attentions in recent years. The self-adaptive feature makes them capable of updating the control policies towards global optimality via the action-reward interaction between the learning agent (controller) and the environment, which is deeded as another research direction in our future works.
- The evolution of state-of-health (SoH) of energy sources (e.g. battery and fuel cell) indicate the accumulative degrading impacts brought by loading conditions, which would greatly affect the performance of energy sources. Thus, in future works, health-conscious energy management strategies combined with advanced prognostic and diagnostic technologies would be another research direction, so as to properly govern the health states of multiple energy sources, contributing to the enhanced durability of fuel cell-based hybrid propulsion system.

# List of Figures

(offline-simulation). (c). Global view of battery power performance comparison of A-MPC (SIL), L-MPC (SIL) and DP (offline-simulation). (d). Local view (5000 to 7000s) of battery power performance comparison of A-MPC (SIL), L-MPC (SIL) and DP (offline-simulation).

# List of Tables

# Nomenclature

| | |
|---|---|
| **EV** | Electric Vehicle |
| **HEV** | Hybrid Electric Vehicle |
| **PHEV** | Plug-in Hybrid Electric Vehicle |
| **FC** | Fuel Cell |
| **FCS** | Fuel Cell System |
| **ICE** | Internal Combustion Engines |
| **FCHEV** | Fuel Cell Hybrid Electric Vehicles |
| **EMS** | Energy Management Strategy |
| **DP** | Dynamic Programming |
| **GA** | Genetic Algorithm |
| **ECMS** | Equivalent Consumption Minimization Strategy |
| **DPT** | Driving Prediction Techniques |
| **PEMS** | Predictive Energy Management Strategy |
| **MPC** | Model Predictive Control |
| **FCM-MC** | Fuzzy C-means enhanced Markov Chain |
| **DPR** | Driving Pattern Recognition |
| **SIL** | Software-in-the-loop |
| **PEMFC** | Proton Exchange Membrane Fuel Cell |
| **SOFC** | Solid-oxide Fuel Cell |
| **SC** | Supercapacitor |
| **CD-CS** | Charge-Depleting Charge-Sustaining |
| **QP** | Quadratic Programming |
| **CP** | Convex Programming |
| **PSO** | Particle Swarm Optimization |

| | |
|---|---|
| **NN** | Neural Network |
| **PMP** | Pontryagin's Minimum Principle |
| **SDP** | Stochastic Dynamic Programming |
| **RL** | Reinforcement Learning |
| **MC** | Markov Chain |
| **FTP-75** | Federal Test Procedure-75 |
| **UDDS** | Urban Dynamometer Driving Schedule |
| **GPS** | Global Positioning System |
| **TPM** | Transition Probability Matrix |
| **ITS** | Intelligent Transportation System |
| **V2V** | Vehicle-to-Vehicle |
| **SVM** | Support Vector Machine |
| **KNN** | K-nearest neighbor algorithm |
| **ARIMA** | Auto-regressive integrated moving average |
| **PSVM** | Probabilistic Support Vector Machine |
| **ECU** | Electronic Control Unit |
| **OL-MC** | Online learning-enhanced Markov Chain |
| **SoC** | State-of-Charge |
| **LRNN** | Layer Recurrent Neural Network |
| **WT** | Wavelet Transform |
| **LP** | Linear Programming |
| **SA** | Simulated Annealing |
| **EF** | Equivalence Factor |
| **KKT** | Karush-Kuhn-Tucker |
| **HIL** | Hardware-in-the-loop |
| **ESM** | Extremum Seeking Method |

**SoH** State-of-health

**BPNN** Back Propagation Neural Network

**RBF-NN** Radial Basis Functional Neural Network

**NARNN** Nonlinear Autoregressive Neural Network

# Annex. Modeling of power consumptions by auxiliary devices in fuel cell system

According to the fuel cell system model in subsection 4.2.2, the fuel cell net power ($P_{FC}$) is derived as the difference between the electrical power generated from the stack ($P_{st}$) and the power used by auxiliary devices ($P_{AUX}$). The auxiliary power is composed of power consumption from air compressor ($P_{cp}$) and other devices ($P_{other}$).

$$P_{FC} = P_{st} - P_{AUX} = N_{cell} \cdot U_{cell} \cdot I_{FC} - P_{cp} - P_{other} \quad \text{(a1)}$$

According to literature [20], the power consumption of the compressor is calculated by:

$$P_{cp} = \frac{C_p T_{amb}}{\eta_m \eta_{cp}} \left[ \left( \frac{p_{cp}}{p_{amb}} \right)^{\frac{\gamma-1}{\gamma}} - 1 \right] \dot{m}_{cp} \quad \text{(a2)}$$

Where $p_{cp}$ is the pressure at the compressor outlet, $p_{amb}$ is the atmospheric pressure, $C_p$ is the specific heat capacity of air, $\gamma$ is the ratio of the specific hears of air, $T_{amb}$ is the ambient temperature, $\eta_m$ is the compressor motor efficiency, $\eta_{cp}$ is the compressor efficiency, and $\dot{m}_{cp}$ is the compressor air flow rate, which can be calculated as:

$$\dot{m}_{cp} = \frac{\lambda_{O_2} N_{cell} M_{air} I_{FC}}{4 \omega_{O_2} F} \quad \text{(a3)}$$

Where $M_{air}$ is the molar mass of air, $\omega_{O_2}$ is the molar fraction of oxygen in the air, $\lambda_{O_2}$ is the excess oxygen ratio and F is the Faraday constant (96485 C/mol).

The power consumption of other auxiliaries ($P_{other}$) is assumed to be constant in this thesis.

Based on equations (a1)-(a3), figure a1 gives the modeling results of a 30-kw PEMFC system: net power ($P_{FC}$), stack power ($P_{st}$), compressor power ($P_{cp}$) and other auxiliaries' power ($P_{other}$) as a function of fuel cell current ($I_{FC}$).

Moreover, figure a2 depicts the relationship between fuel cell net power ($P_{FC}$) and H2 mass flowrate ($\dot{M}_{H_2}$). It can be seen that a non-zero H2 mass flowrate (~ 0.006 g/s) exists even though no external load drives current from fuel cell ($P_{FC} = 0$W). This is because a minimal H2 mass flow rate is indispensable to maintain the normal operation of PEMFC, where, in this phase, all electrical power (current) generated by the stack is consumed in auxiliaries, with this operational state termed as "idle".

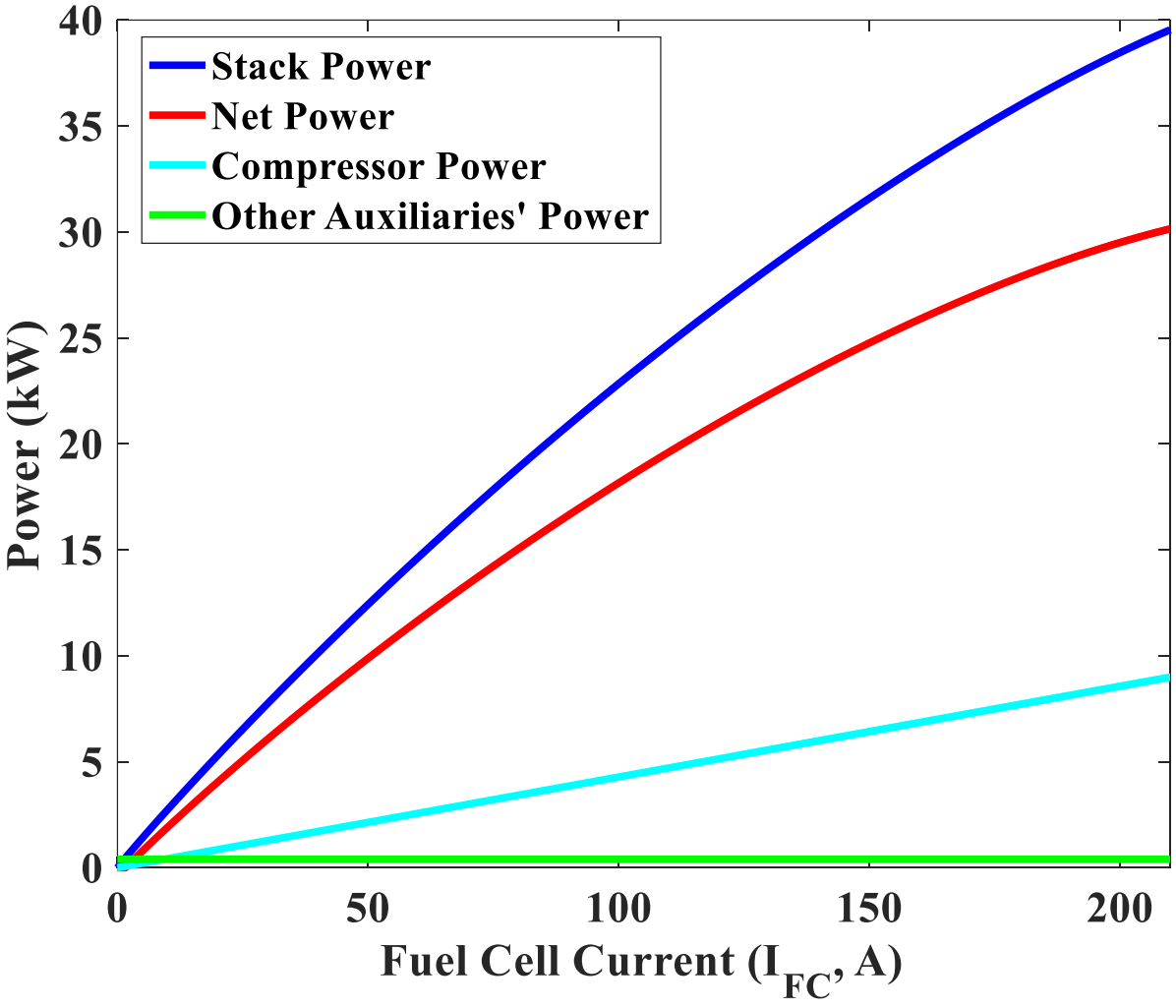


Figure a1. Modeling results of a 30-kW PEMFC system: stack power, net power, compressor power and other auxiliaries' power as a function of fuel cell current.

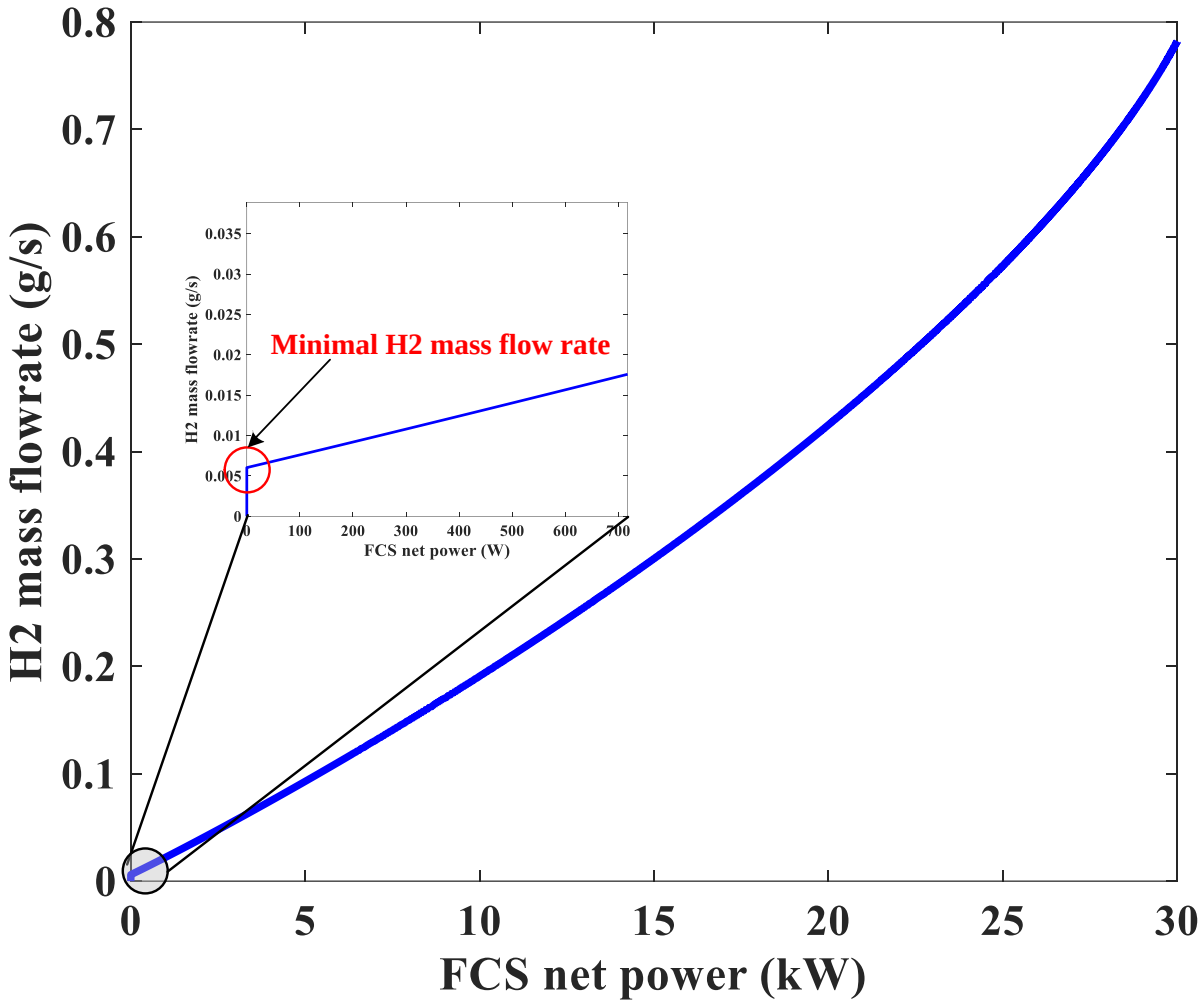


Figure a2. Modeling results of a 30-kW PEMFC system: H2 mass flowrate as a function of FCS net power.